A STABLE ISOTOPE STUDY ON FLUID SOURCE AND TEMPERATURE OF THE MURGUL DEPOSIT

by

STEPHANIE NICHOLE FOCHTMAN

Under the Direction of Doug Crowe

ABSTRACT

The Murgul deposit is a copper-rich VMS system at Murgul, Turkey. It has been interpreted as a Kuroko-type VMS system, and is one of several VMS and vein deposits throughout the Eastern Pontides. The massive sulfide of the Murgul deposit has been removed by mining, but remains profitable because the underlying stockwork is significantly mineralized. Little isotopic research has been conducted on this deposit or others located in the region. Sulfur and oxygen stable isotope data constrain fluid temperature and source for a better understanding of the deposit's origin. Chalcopyrite-pyrite pairs yield equilibrium temperatures of approximately 350^{o}C. Quartz and illite were determined to be in disequilibrium and unable to provide temperature data, but the illite permits calculation of a fluid source $\delta^{18}O$ of 8-11$^{o}/_{oo}$. These data suggest that the fluids that produced Murgul were likely derived from seawater, and the deposit is best interpreted as a VMS deposit.

INDEX WORDS: VMS, copper deposit, sulfur isotope, oxygen isotope, fluid source

A STABLE ISOTOPE STUDY ON FLUID SOURCE AND TEMPERATURE OF THE MURGUL DEPOSIT

by

STEPHANIE NICHOLE FOCHTMAN

BS, State University of New York at Potsdam, NY, 2012

A Thesis Submitted to the Graduate Faculty of The University of Georgia in Partial Fulfillment of the Requirements for the Degree

MASTER OF SCIENCE

ATHENS, GEORGIA

2014

A STABLE ISOTOPE STUDY ON FLUID SOURCE AND TEMPERATURE OF THE MURGUL DEPOSIT

by

Stephanie Nichole Fochtman

Major Professor:	Doug Crowe
Committee:	Paul Schroeder
	Mike Roden

Electronic Version Approved:

Maureen Grasso
Dean of the Graduate School
The University of Georgia
May 2014

ACKNOWLEDGEMENTS

I would like to thank the Society of Economic Geologists, the Watts-Wheeler Fund, Dr. Emin Çiftçi and the Istanbul Technical University, and all the people at the Murgul Mine for their great assistance in my fieldwork in Murgul, Turkey. I would like to thank Julie Cox for her help and supervision in the isotope lab; Dr. Paul Schroeder of my committee for his help and insight with the XRD and my thesis; and Chris Fleisher for spending countless days teaching me the magic of the microprobe and regaling me with stories, only for me to never use his teachings.

Special thanks go to Dr. Hasan Kolayli from the Black Sea University for his help and patience, taking me into his home and making me feel like I found a second home in Turkey, despite a language barrier. Special thanks also go to Ahmet Ozbek, for sacrificing a week of his summer to take care of my sanity and me while in the field. Extra special thanks to my fellow graduate students, Voary Ny, for providing experience and wisdom and no small amount of laughs to help me through the day, and Frank (Tripp) Waters for always reminding me of how much I love rocks, even when they do not cooperate.

It would be remiss of me not to thank Dr. Doug Crowe, for his immense amount of patience and guidance, especially in transforming my English major style writing to scientific, and always providing a calm and chill attitude when I needed it most; despite him being so stressed out at times you could measure it on a Richter scale.

Last but certainly not least I must thank my committee member Dr. Mike Roden, for being very patient with my all-too-often ‘deer in the headlights’ look, teaching me to never simply trust an author on their word, and that there are still plenty of big mysteries in the world.

TABLE OF CONTENTS

LIST OF TABLES

Page

LIST OF FIGURES

Page

CHAPTER 1

INTRODUCTION

Volcanogenic massive sulfide (VMS) deposits occur over a wide range of geologic ages, from Archaen to the present. Although there are several different types of VMS deposits (Kuroko, Besshi, Cyprus), all tend to share several common physical characteristics. They all consist of silicate and sulfide minerals and are a significant source for Cu, Pb, Zn, Ag, and Au throughout the world. The way in which they are formed is also very similar, if not the same in detail. VMS deposits are formed on or near the seafloor via the circulation and release of metal-rich hydrothermal fluids through a stockwork zone, which is rarely economic itself (Çiftçi et al., in press). The stockwork zone acts as a plumbing system, through which fluids flow into the ocean (via some vent or black smoker at the surface). The fluids quickly cool when mixed with seawater, lowering the solubility of the metals, and in some instances deposit a large, solid blanket of sulfide minerals around the vents over time.

The Murgul mine is an Upper Cretaceous copper rich VMS (Çiftçi et al., in press). It is located in northeastern Turkey, near the border of Georgia and the Black Sea (figure 1). The deposit is one of many found within the Eastern Pontides of Turkey, which is part of the overall Pontide belt that runs along the coast of the Black Sea. The Pontide belt is part of the Alpine-Himalayan chain that runs from the Western Mediterranean through Romania and Turkey, and ends on the eastern side of Afghanistan at the Hindu Kush mountain range (Karakaya et al., 2012).

The Murgul mine has been operating since 1907 and has been owned by several different companies at different times, though records have not been kept. As of 2012, it is owned by Etibank and a private company, with an annual production of 2,970,000 tons at 1.31% copper. Annual copper concentrate production is 208,267 tons, 17% of which is copper. The majority of the copper mined from Murgul is used within Turkey (Koz et al., 2012), making it an invaluable resource to the country.

Purpose

The purposes of this study are 1) to evaluate the origin of the Murgul deposit by determining the fluid source, and 2) evaluating the distribution of calculated temperatures within the well-exposed stockwork zone. Both VMS and vein-type deposits are abundant in the Eastern Pontides (figure 2), and the high-grade copper ore has long been mined away. No records have been kept from the beginning of the mine and there have been few geologic studies on it. This study has been conducted to gather data and information about the Murgul deposit by examining what appears to be an intact stockwork zone and the host rock immediately surrounding the deposit. Specifically, we have determined the temperature(s) of the ore forming fluids and the source(s) of the fluids that created this deposit via stable oxygen and sulfur isotopic data.

Further significance of this paper is that besides the recent study by Çiftçi et al. there is, unfortunately, little isotopic data, on any of the other putative VMS deposits in the Eastern Pontides, and that at Murgul we are able to thoroughly examine the stockwork zone, which is intact and well exposed from mining activity, an uncommon occurrence. Ore deposit discovery and exploration is dependent on ore deposit models, thus the more information there is about a type of deposit and the more we understand it, the better the chance we have of finding more deposits of this type.

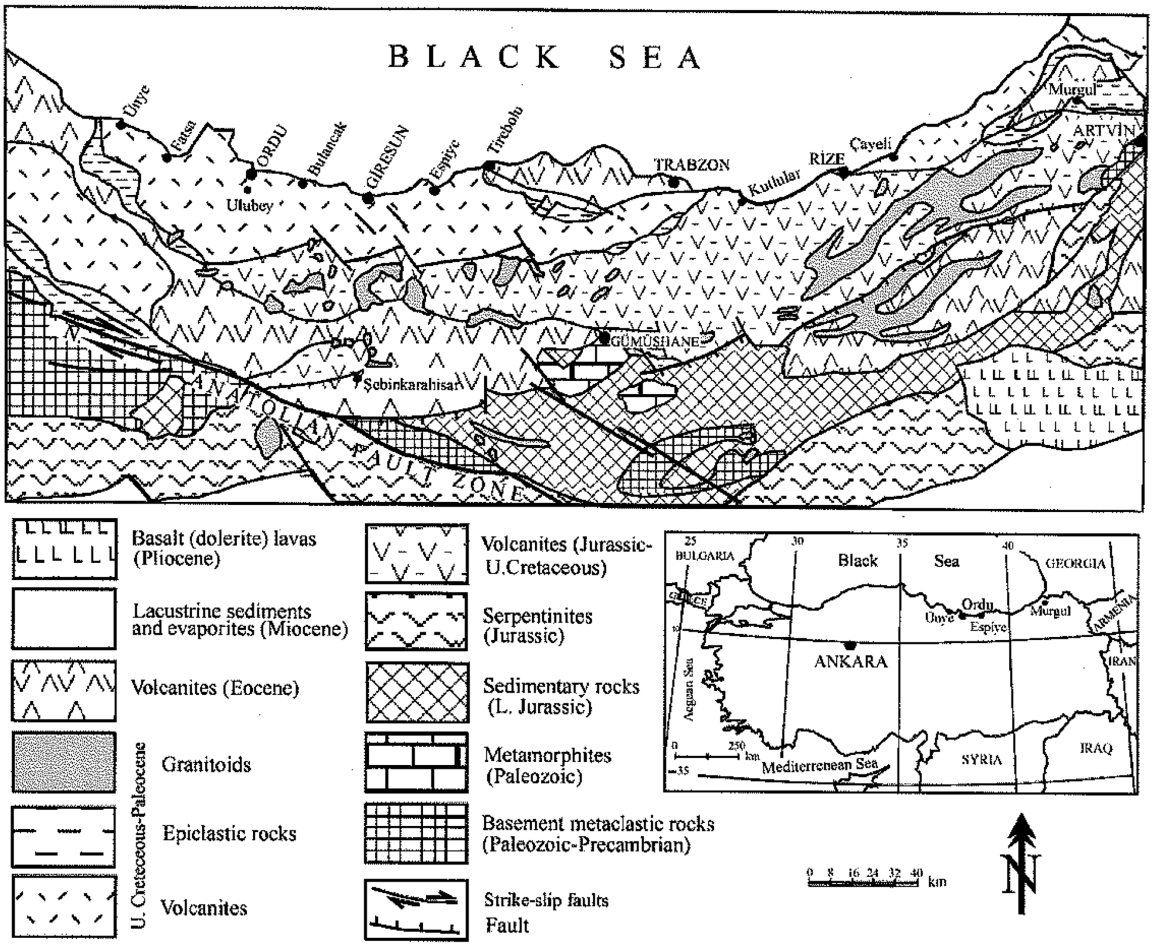

Fig 1. Location and regional geology map, taken from Karakaya et al., (2012).

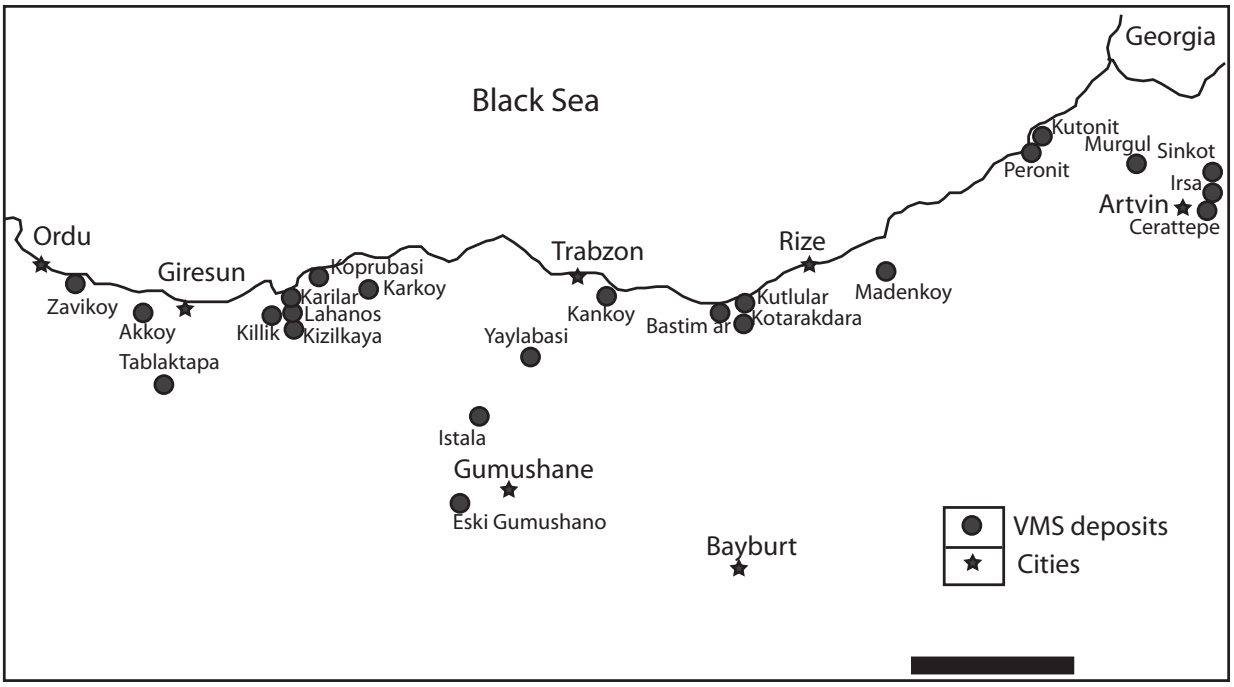

Fig 2. General distribution of major VMS deposits in the Eastern Pontides. (Modified from Çiftçi et al., in press.)

CHAPTER 2

REGIONAL GEOLOGY

Turkey is divided tectonically into 4 major blocks, separated by suture zones and faults (figure 3). The Rhodope-Pontide block is composed of the Pontide arc that runs E-W along the northern end of Turkey. The Pontide arc makes up much of this block, and is a volcanic arc formed from northward subduction of the Neo-Tethys Sea beneath the Eurasian plate during the Late Cretaceous, and abundant flysch deposits from collision. To the east, this block also contains the East Anatolian High Plateau and the Bitlis-Pütürge massif (microcontinent) to the south. The plateau is composed of ophiolites that have been uplifted via a complicated series of continental collisions, volcanism, folding, faulting, and crustal shortening during the Eocene and mid-Miocene.

South of the Pontides, separated by the Northern Anatolian Fault (NAF) is the Sakarya Block (also called the Sakarya Continent) that runs parallel to the Pontides. The Sakarya Block is composed of Paleozoic crystalline basement, Carboniferous sedimentary cover, and Triassic ophiolitic and mélange units. The Sakarya Block also contains Oligocene-Miocene granitoid plutons and a metamorphic core complex, the Kazdag massif, to the west. The Central Anatolian Crystalline Complex (CACC) lies in the middle of Turkey bounded to the north and south by the Izmir-Ankara suture zone (IASZ) and the Inner-Tauride suture zone (ITSZ), respectively, and pinches out to the West and East. The CACC is composed of several metamorphic massifs, including the Kirsehir, Akdag, and Nigde. It is also composed of felsic-mafic plutons, and ophiolites (ranging from the Cretaceous to Miocene). To the south are the Anatolian and Tauride

blocks, bounded to the south by the East Anatolian Fault (EAF) and Arabian plate in the east, and the Mediterranean Sea in the west. To the west, the Anatolian block is separated from the Sakarya Block to the north by the IASZ, and is composed of ophiolites and a metamorphic core complex, the Menderes massif, that was exhumed during the Late Cenozoic and intruded by granitic plutons in the Miocene. The Tauride block lies south of the Anatolian Block and runs E-W. It is composed of carbonate and volcano-sedimentary rocks ranging in age from Cambrian to Upper Cretaceous, and is overlain by ophiolites (Dilek & Sandvol, 2009).

The Pontides are subdivided into 3 sections: Western, Central, and Eastern, though there is no obvious geographical or geological separation. This belt runs along the entire Black Sea coast in Turkey and is bordered to the south by the NAF and the Anatolian High Plateau in the Eastern portion of the belt. The Pontide belt is a magmatic island arc that was formed during the closing of the Paleotethys Ocean during the Upper Jurassic and has since been molded into shape by collision with the Bitlis-Pütürge massif during the Late Eocene, which added abundant sedimentary flysch. The Pontides are home to many large VMS deposits as well as less abundant vein deposits (Karakaya et al., 2012).

The Eastern Pontides lie north of the Anatolian High Plateau, south of the Black Sea, and east of the CACC (Arslan & Aslan, 2006; Dilek & Sandvol, 2009). The basement of the Eastern Pontides is composed of Late Carboniferous granitoids, early Carboniferous metamorphic rocks, and shallow marine-terrestrial sedimentary rocks of Carboniferous-early Permian age (Karsli et al., 2012; Karsli et al., 2011). The Eastern Pontides are split into two sections, the Northern and Southern Sections. The North Section is composed of volcanic and volcaniclastic rocks from the Late Cretaceous-Early Eocene. The South Section is composed of rocks older than the Late Cretaceous that were part of a fore-arc and have been more severely deformed over time than

those of the North section (Arslan & Aslan, 2006; Okay & Şahintürk, 1997). The tectonic setting of the Murgul deposit is very similar to that of Kuroko deposits, which is described by Cathles, et al., (1983). The Murgul deposit is located in the Northern section of the Eastern Pontides, which is interpreted as being formed in a back-arc extensional setting (Karakaya et al., 2012, Koz, B., et al., 2012). During subduction and volcanic arc formation, heat flow in the back arc region causes thinning and extension of the overlying crust, which drives upwelling of warm fluids. Magmatism in this region is typified by intermediate to mafic rocks, including the production of dacite dome complexes.

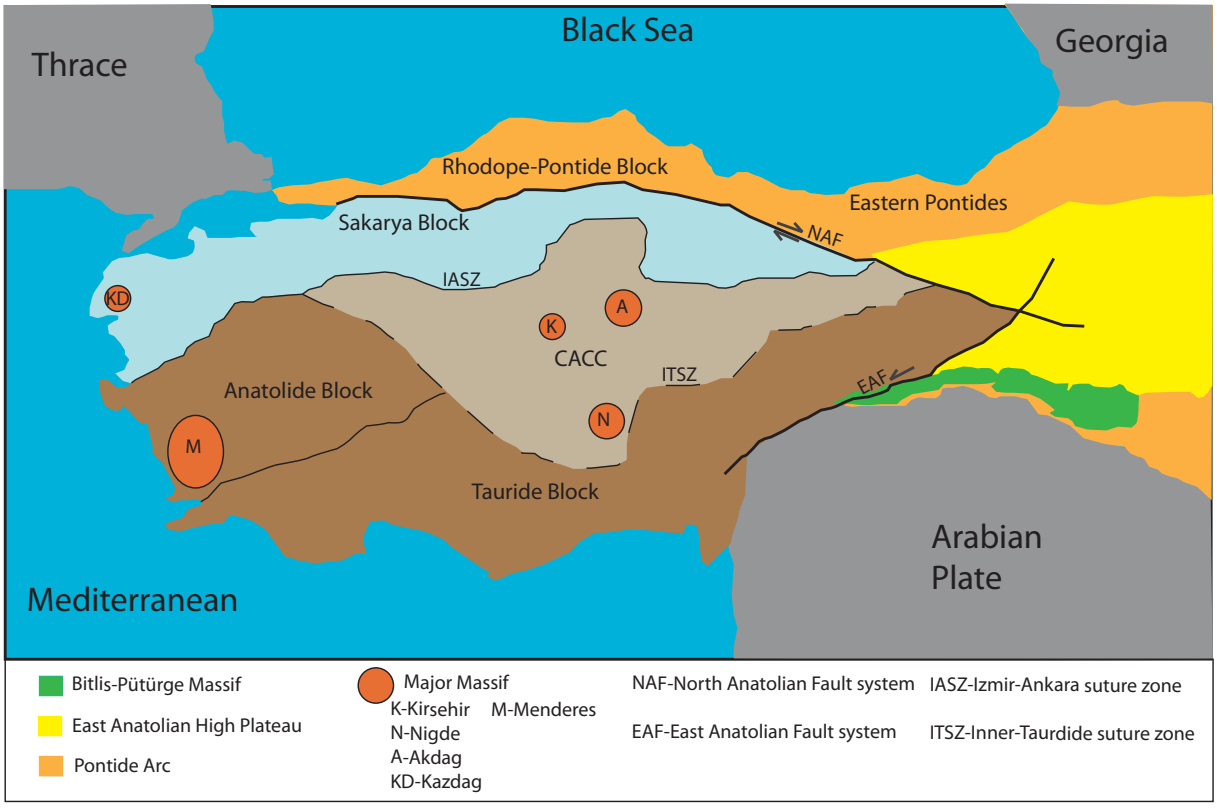

Fig 3. Tectonic overview of Turkey, (modified from Dilek & Sandvol, 2009).

CHAPTER 3

SITE GEOLOGY

Previous Work

Çiftçi et al. (in press) have done previous stable isotope and fluid inclusion work in this area in an attempt to constrain the specific type (e.g. Kuroko, Cyprus) of several VMS deposits that occur in the Eastern Pontides. In their study Dr. Çiftçi et al. determined formation temperatures, fluid salinity, and paragenesis of several major VMS deposits, including Murgul. Using fluid inclusions Dr. Çiftçi et al. measured homogenization temperatures of 160-320 ^{o}C, with the majority of temperatures for massive ores ranging between 200 ^{o}C and 320 ^{o}C (figure 4). The temperatures determined for the Murgul massive ore range from 260 ^{o}C-320 ^{o}C and those for the stockwork zone range from 160 ^{o}C-295 ^{o}C (figure 5). Salinities were calculated to be 0.5-6 wt% NaCl eq.

Çiftçi et al. (in press) propose a four-stage paragenesis of the deposits. Stage 1 is the formation of colloform and coarse-grained pyrite as well as the formation of chalcopyrite. Stage 2 is characterized by the formation of sphalerite and galena, and stage 3 by galena+sulfosalts. Stage 4 is characterized by a second generation of chalcopyrite and bornite. In Murgul the $\delta^{34}S_{CDT}$ of pyrite ranges from +3.3 $^{0}/_{00}$ to +3.7 $^{0}/_{00}$ and the $\delta^{34}S_{CDT}$ of chalcopyrite range similarly from +3.3 $^{0}/_{00}$ to +3.7 $^{0}/_{00}$ (Çiftçi et al., in press).

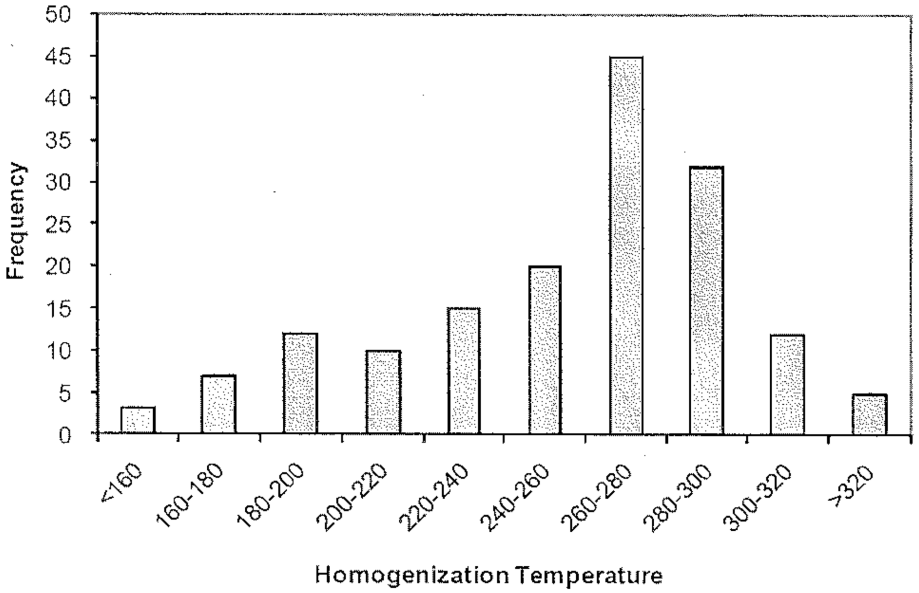

Fig 4. Homogenization temperatures from fluid inclusions in Murgul, Köprübaşi, and Lahanos deposits, taken from Çiftçi et al., (in press).

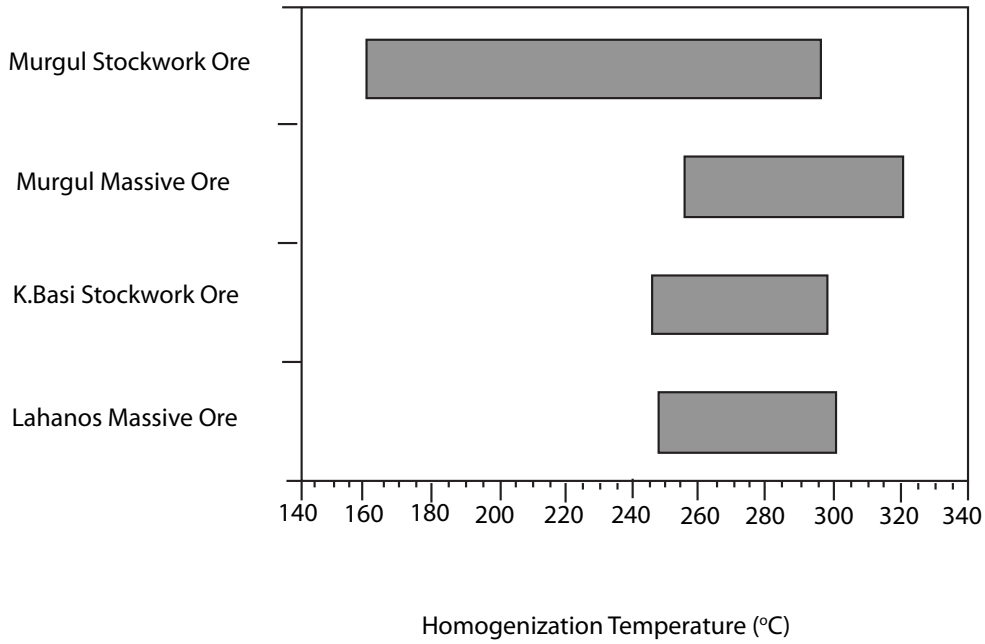

Fig 5. Range of homogenization temperatures found in each of the three deposits analyzed for temperatures, modified from Çiftçi et al., (in press).

Detailed petrographic and geochemical descriptions of Murgul have been done by Sipahi et al., (2013) and Eyuboglu et al., (2014). Sipahi et al., (2013) studied enclaves within the footwall and hanging wall dacites. Both dacites are enriched in LILE and LREE and have similar $^{87}Sr/^{86}Sr$ values, at approximately 0.704-0.705. Eyuboglu et al., (2014) examined the dynamics of the formation of ore within the arc system of the Eastern Pontides and suggests that while some VMS deposits formed in a magmatic arc system, others formed in a continental arc system. The $^{206}Pb/^{238}U$ age of the host dacite at Murgul is 91 Ma, while the host dacite of other VMS deposits, measured by zircon age dating, ranges from 83-87 Ma.

Previous work done in the Eastern Pontides not focusing on the Murgul deposit includes Akçay & Gündüz (2004), Arslan & Aslan (2006), Demir et al., (2013), Karakaya et al., (2012), Karsli et al., (2012), Karsli et al., (2011), Okay & Şahintürk (1997). Akçay & Gündüz (2004), examined the mineralization of a copper-gold porphyry deposit near Gümüşhane, Turkey (figure 2). The mineralization here occurs as veins and disseminations and is composed of chalcopyrite, pyrite, magnetite, pyrrhotite, hematite, molybdenite, sphalerite, and galena. Hydrothermal alteration zones are prominent and are composed primarily of K-feldspars, K-silicates, and quartz. Arslan & Aslan (2006) examined the mineralogy and geochemistry of granitic intrusions within the Eastern Pontides. The geochemistry suggests these granitoids formed in either a post-collisional setting or a volcanic arc setting. The granitic intrusions include monzonites and monzodiorites in the Northern zone of the Eastern Pontides, with monzogranites and granodiorites in the Southern zone. Demir et al., (2013) examined the mineralization of the Istala deposit, near Gümüşhane, Turkey (figure 2). The ore at the Istala deposit is separated into massive black zinc ore, massive barite ore, and massive brecciated ore, in order from bottom to top, stratigraphically. The black ore is composed of sphalerite and galena, with minor amounts of

pyrite and chalcopyrite. The barite ore is composed of massive barite layers, with galena and tetrahedrite/tennantite. The brecciated ore is composed of barite fragments from the underlying barite ore with disseminated sulfides. Karakaya et al., (2012) examined the geochemical behavior of trace elements in the VMS deposits of the Eastern Pontides. The deposits have similar REE patterns, being enriched in LREE and having a negative Eu anomaly, suggesting that they came from similar felsic sources. Some HFSE (Hg, Se, Bi, etc.) could be used as pathfinder elements to discover new VMS deposits, as they are strongly enriched in hematitic-altered samples. Karsli et al., (2012) and Karsli et al., (2011) examined an A-type granitoid, the Pirnalli pluton, and adakite-like granitoids in the Eastern Pontides. The Pirnalli is a hybrid magma, formed via mixing of a more mafic magma, from the melting of the lower crust of the Pontides, and one from an enriched lithospheric mantle. These magmas were formed via back-arc extension caused by northward subduction of the Neotethys. The adakite-like granitoids were formed by partial melting of the lower crust via asthenosphere upwelling, due to slab-break off at a subduction zone. Okay & Şahintürk (1997) review the geology of the entire Eastern Pontides. Although this paper is outdated by more modern studies, it provides a general overview of the geology and tectonic evolution of the Eastern Pontides.

Field Work

The Murgul mine is composed of two pits, the larger main pit of Damar and the smaller secondary pit of Çakmakkaya (figure 6). Çakmakkaya ranges from 1020-1070 ft (310.5-326.1 m) above sea level, but most has been filled with water and so only the 1060-1070 ft (323.0-326.1 m) level is accessible. Accessible areas of Damar range from 950-1070 ft (389.6-326.1 m) above sea level. The overlying massive ore has long since been mined away and the stockwork zone from Damar has been exposed, mined, and stockpiled for processing. Operations are

currently working on mining a 2nd stockwork zone found in Çakmakkaya that is also economic. Unfortunately, this active mining made most of the Çakmakkaya pit inaccessible for sampling. Geologically, both pits are very similar, and so they will only be mentioned separately if there is a significant difference between them.

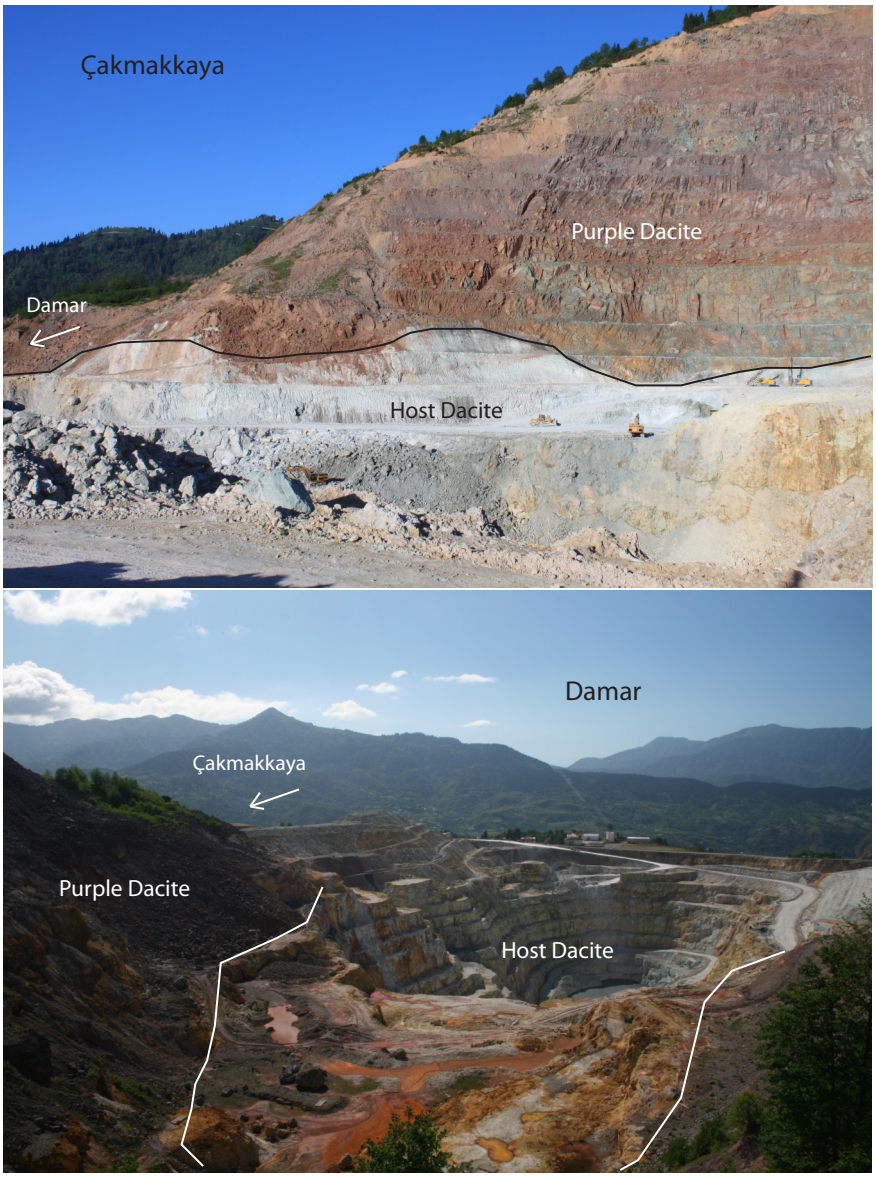

Fig 6. Murgul open pits. Top: Çakmakkaya pit, facing SW. This pit is currently being mined, removing the stockwork zone. Bottom: Damar pit, facing NE. The stockwork zone of this pit has been completely mined and it is being refilled with water. The massive ore was located between the purple dacite and the host rock, but an exact location is unavailable.

A simplified cross section of the deposit is shown in figure 7. Above the deposit lies a distinct hanging wall purple dacite, which contains abundant quartz 'eyes' (phenocrysts). The footwall host rock is composed of dacite that has been thoroughly altered by hydrothermal fluids related to ore emplacement and from present day weathering processes. This alteration causes a change in color in the dacite to white/yellow. This color change marks the contact between the hanging wall and footwall dacites (figure 6 and 7). Both dacites are highly siliceous. The footwall dacite contains abundant kaolinite on rock surfaces, as a result of low temperature weathering. Original macroscopic igneous textures are mostly destroyed.

Alteration

Host rocks were collected at depths ranging from 950-1070 ft above sea level and include both open pits (figure 8). The alteration mineralogy of the host rock consists of abundant silica plus illite related to circulation of hydrothermal fluids, and kaolinite from low temperature weathering. Occurring in smaller amounts as a weathering product is jarosite, occurring in isolated 'balls' with grain sizes of 3-8mm in diameter. Also present in small amounts is magnesite, which is very fine-grained and disseminated. The silica occurs as massive silicification, veins, and veinlets. The clays occur as a weathering product over weathered surfaces (kaolinite) and as a hydrothermal product within the rock (illite). Commonly found in the host rock in smaller quantities are fine-grained chlorite, calcite and dolomite, fine-grained disseminated pyrite, and remnant quartz 'eyes' (phenocrysts) ranging from 0.5-1.0cm in diameter.

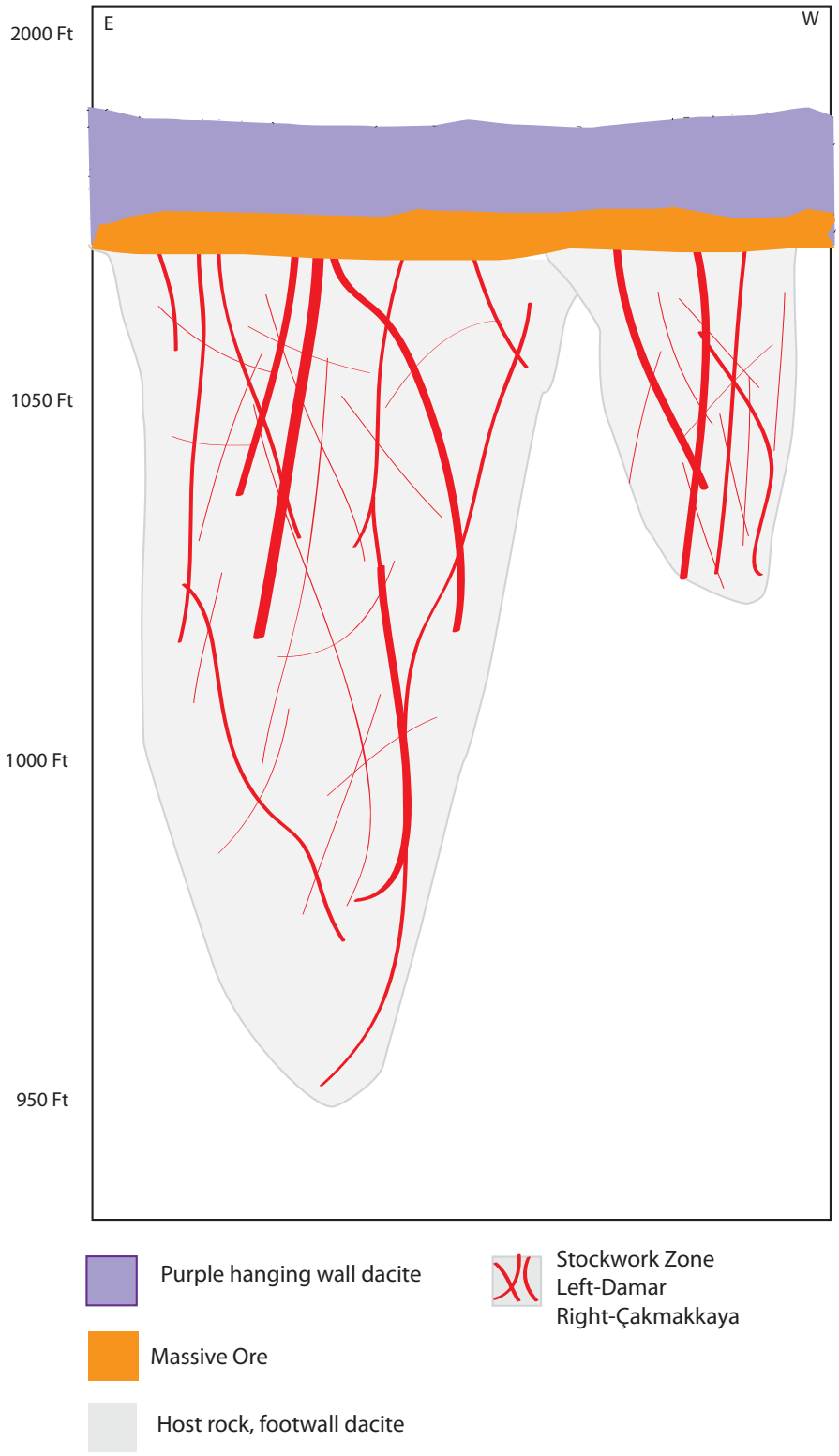

Figure 7. Simplified cross section of the deposit, facing SW. Elevations are feet above sea level.

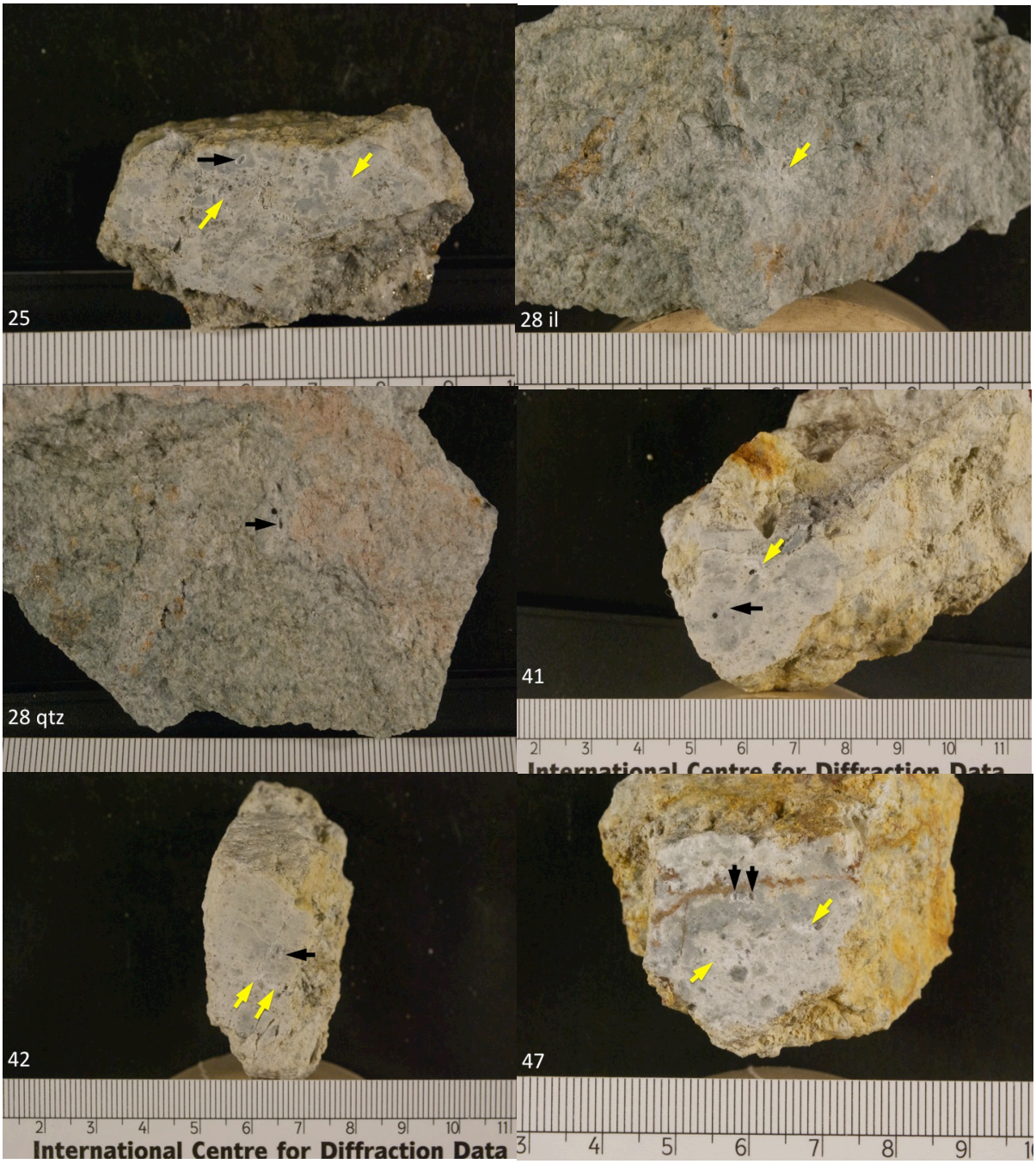

Figure 8. Examples of typical host rocks. Sample numbers are given in the corners. Cm bar for scale, split into mm. Black arrows point to quartz, yellow arrows point to illite. Note the abundance of silica and clay, and the degree of weathering.

In some of the host rocks there are also small amounts of chalcocite occurring as a secondary supergene sulfide phase. The chalcocite is fine-grained. The quantity of chalcocite is higher in those rocks with abundant pyrite, suggesting chalcocite forms via pyrite weathering. Some host rocks are very green from an abundance of chlorite/sericite, mixed with quartz and clay (figure 9). These chlorite rich rocks are very common and occurred at depths ranging from approximately 1010-1030 ft above sea level, in the pit Damar. They are the only ones that do not contain visible pyrite. One of these green rocks contains a thin (.5cm thick) gypsum vein, and this is the only occurrence of gypsum seen in this system.

A second 'host rock' is dacite that occurs not surrounding the deposit but within the stockwork zone itself, hosting the sulfide veins (figure 10). This host rock dacite is different from the main host rock in that it has not been so severely weathered and thus has less kaolinite, both surficial and pervasive, giving it a less 'crumbly' texture. Some of these rocks do not contain any clay. It is possible that these rocks have not been exposed to the surface as long as the main host rock, since they have been recently mined, explaining this difference. It is also possible that these rocks were silicified to a higher degree than the main host rocks, and thus never contained much clay. Another difference is that these host rocks rarely contain disseminated, fine-grained pyrite and then only in trace amounts. These rocks were collected from a stockpile, but were originally mined from the Damar pit at the 950-900ft level.

Silicate-rich veins occur as well. These are not easily seen and they are distinguished by their difference in appearance compared to the host rock (e.g. slight differences in color and having a more massive texture). The mineralogy of these veins is quartz, calcite, dolomite, disseminated fine-grained pyrite, kaolinite (on exposed surfaces), and illite.

Mineralization

Ore mineralization at Murgul occurs as sulfide veins, ranging from < 1-20 cm in thickness (figure 10). Mineralized samples were collected from the mine's stockpile, taken originally from the 950-900ft level in the Damar pit, as well as the 1000-980 ft level in the Damar pit and the 1070-1060 ft level in the Çakmakkaya pit. The sulfide veins consist primarily of massive chalcopyrite and pyrite, but also calcite, dolomite, magnesite, and quartz. Some veins also have large amounts of supergene chalcocite, occurring as a thin, black layer coating chalcopyrite. Kaolinite and illite are common but occur only in small amounts. Some sulfide veins are found in the periphery of the stockwork zone, within the host rock dacite. These tend to be very small, severely weathered, and contain only fine-grained pyrite. Rare stockwork veins and the peripheral veins show evidence of open space, with subhedral pyrite and sub-euhedral quartz crystals. These small veins were collected both in Damar and Çakmakkaya, at depths of 1000-980ft and 1070-1060 ft above sea level, respectively.

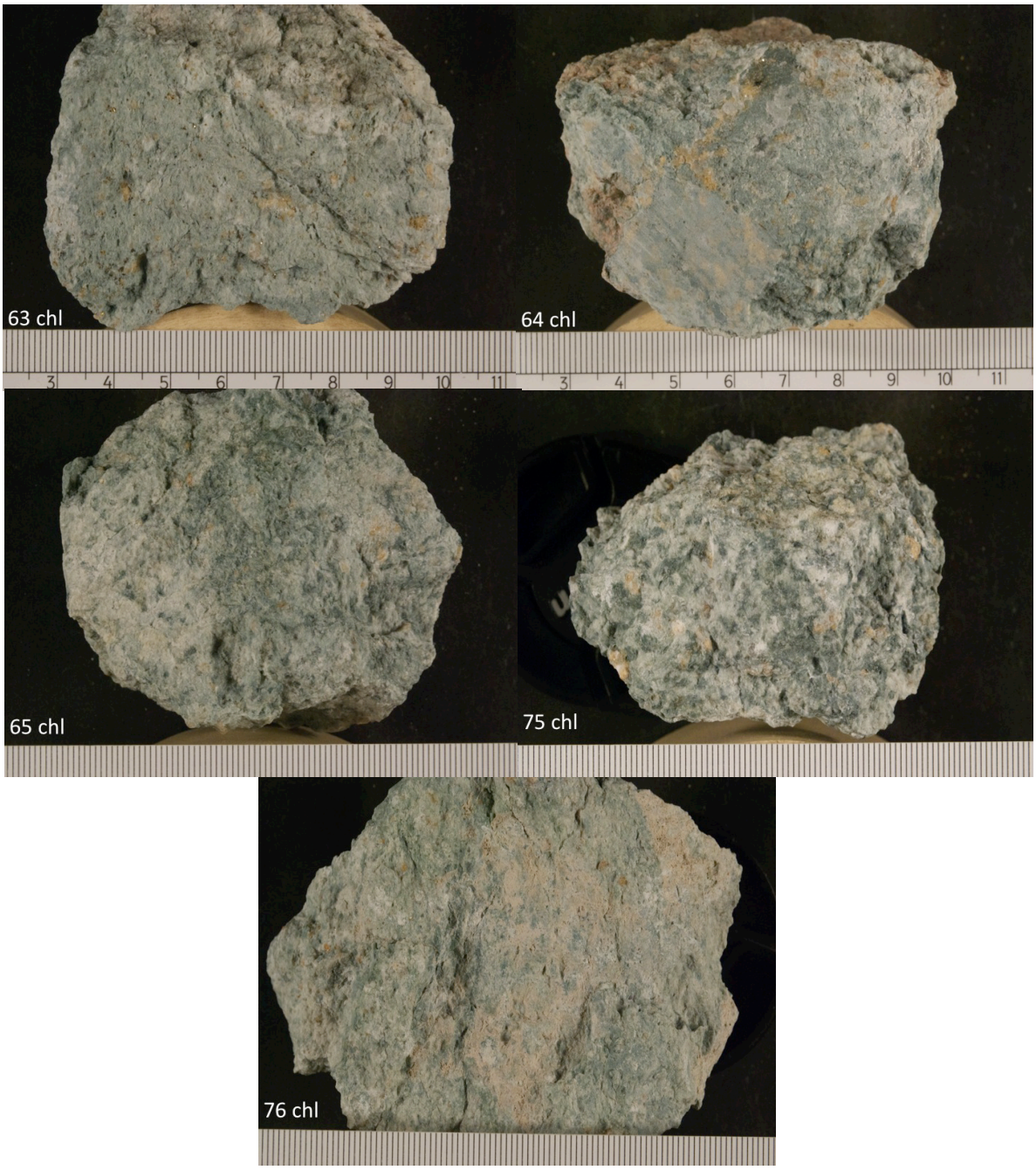

Figure 9. Compilation of 'green rocks' host rocks. '63 chl' denotes sample SF-13-063, chlorite rich. Cm bar for scale, split into mm.

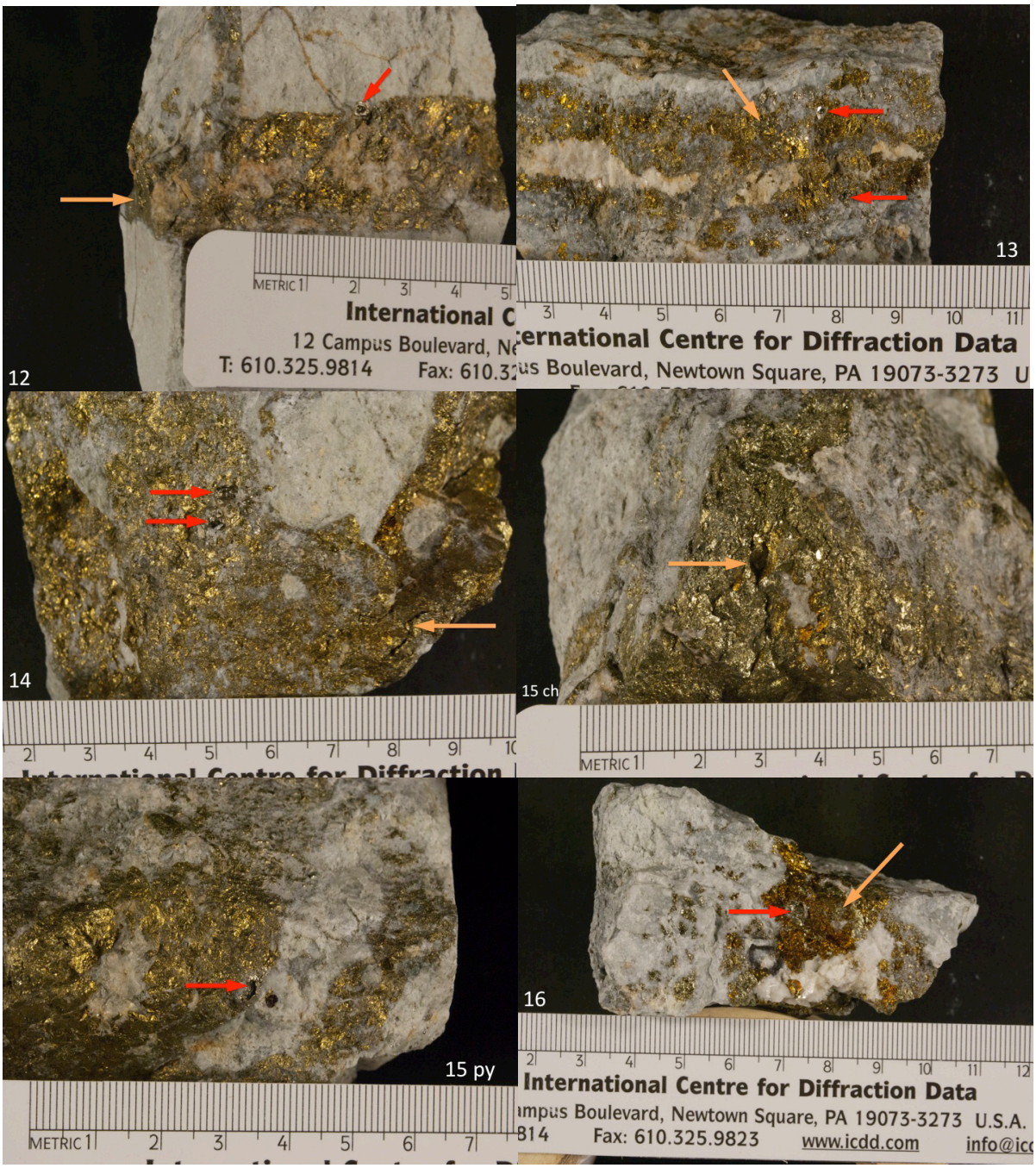

Figure 10. Examples of sulfide veins and the second host rock dacite surrounding them. Sample number is given in the corners. Cm bar for scale, broken into mm. Orange arrows point to chalcopyrite, red arrows point to pyrite. Note the carbonate and quartz occurring in the sulfide vein in samples 12 and 13, and the small veins in sample 12.

CHAPTER 4

METHODS

Sampling

Approximately 100 samples were collected from the Murgul mine. Sample locations include both pits, but most are from Damar due to better access, larger size, and a greater range of depth. The majority of the samples are from the host dacite, but twenty were collected from the main stockwork zone located at the bottom of Damar, 50-100ft deeper than the rest of the samples. At this depth the system may have been at a higher temperature, causing the sulfide veins to be more abundant/concentrated in one area, instead of spreading out near the surface.

X-Ray Diffraction

In order to properly determine the mineralogy of the samples (both host rock and veins), samples were analyzed via X-ray Diffraction (XRD). Powder mounts were made using a McCrone micronizing mill and run on a Bruker D8 Advance XRD from 2-70 degrees 2θ at 0.1 second per step increments, using a 0.6mm slit at the source and CoKα radiation. Data interpretation was done using Eva, which uses a search-match method to qualitatively identify XRD peaks, and is based on preconceived notions of what minerals are present in the icod database.

Stable Isotopes

Minerals were separated via manual drilling using a diamond dental drill bit. Between 1 and 2 mg of quartz or illite were drilled for oxygen isotope analysis. Between 4 and 6 mg of pyrite or chalcopyrite were drilled for sulfur isotope analysis. For silicates, stable isotope data

were obtained via an offline laser fluorination line, using a modified method from Valley et al. (1995). For sulfides, an offline vanadium pentoxide combustion line with variable cryogenic temperature trap was used, employing a modified method from Yanagisawa and Sakai (1983).

For $\delta^{18}O$ analysis, samples were converted to O_2 gas via heating by a 1kW infrared CO_2 laser in the presence of bromine pentafluoride. Excess waste halogeus as well as SiF_4 were removed cryogenically and via exposure to heated mercury. The remaining noncondensible gas and sample were then moved to a platinum filament, graphite rod CO_2 converter, where O_2 reacted with heated carbon to form CO_2. The CO_2 sample is then measured and collected for analysis.

For $\delta^{34}S$ analysis, the samples were combined with elemental copper, quartz, and vanadium pentoxide. This mixture was then heated in a furnace at 1050^{o}C to produce SO_2 and other gases. Water was removed cryogenically using a dry ice-ethanol slush, and the remaining sample was collected in a variable temperature cryogenic trap. After raising the temperature to -145 ^{o}C to remove CO_2, the temperature was raised again to -90 ^{o}C to convert solid SO_2 to gaseous SO_2. This SO_2 was then measured in a manometer and collected for mass spectrometric analysis. Once the gases, CO_2 and SO_2 were extracted, isotope ratios were measured using a Finnigan MAT 252 dual inlet mass spectrometer. An accelerating potential of 8kV was used, and each sample was measured for 8 seconds for 8 standard-sample cycles against the appropriate CO_2 and SO_2 reference gases. The oxygen samples were measured with an 800-100mV signal intensity. The sulfur samples were measured with a 1000-2000mV signal intensity, with an open Variable Ion Source Conductance (VISC) 'sulfur window.' Results are reported relative to SMOW for silicates, and CDT for sulfides.

CHAPTER 5

RESULTS

Mineralogy

All XRD data are presented in appendix A. Minerals present in host rocks are quartz, illite, kaolinite, calcite, dolomite, magnesite, jarosite, pyrite, chlorite, and gypsum. Minerals found in sulfide veins are chalcopyrite, pyrite, quartz, calcite, dolomite, magnesite, illite, and kaolinite. Chalcocite was undetected by the XRD with the scanning parameters used, possibly due to a high level of oxidation during sample preparation. Corundum was detected in all samples, but is an artifact of the sample preparation.

Stable Isotopes

All sulfur isotope data collected for pyrite and chalcopyrite pairs are presented in table 1. All oxygen isotope data collected for illite and quartz pairs are presented in table 2.

Table 1. Total collected sulfur isotope data.

Sample	Mineral	$\delta^{34}S_{CDT}$ Mean	$\delta^{34}S_{CDT}$ Std.Dev.	$\delta^{34}S_{CDT}$
12	pyrite	-10.1	0.03	**4.3**
12	chalcopyrite	-10.9	0.01	**3.4**
13	pyrite	-11.1	0.02	**3.4**
13	chalcopyrite	-10.8	0.03	**3.5**
14	pyrite	-10.5	0.01	**4.0**
14	chalcopyrite	-11.3	0.02	**3.0**
15	pyrite	-10.1	0.01	**4.3**
15	chalcopyrite	-10.0	0.02	**4.4**
16	pyrite	-10.5	0.02	**3.1**
16	chalcopyrite	-9.0	0.03	**5.7**
20	pyrite	-12.1	0.03	**2.3**
20	chalcopyrite	-13.1	0.02	**1.2**
23	pyrite	-15.5	0.03	**-2.4**
23	chalcopyrite	-12.9	0.02	**0.5**
34	pyrite	-12.1	0.03	**2.2**
34	chalcopyrite	-14.4	0.03	**-0.4**
35	pyrite	-12.3	0.02	**2.0**
35	chalcopyrite	-13.8	0.01	**0.3**
36	pyrite	-11.7	0.01	**2.6**
36	chalcopyrite	-12.6	0.02	**1.7**
37	pyrite	-9.4	0.01	**5.0**
37	chalcopyrite	-11.5	0.03	**2.8**
39-5	pyrite	-9.8	0.01	**4.0**
39-5	chalcopyrite	-9.6	0.01	**4.2**
39-7.1	pyrite	-9.9	0.04	**3.8**
39-7.1	chalcopyrite	-10.1	0.01	**3.6**
39-9	pyrite	-9.8	0.03	**4.6**
39-9	chalcopyrite	-11.3	0.02	**3.0**
78	pyrite	-20.8	0.01	**-7.0**
78	pyrite	-23.6	0.01	**-9.9**
78	chalcopyrite	-12.4	0.02	**1.9**
79	pyrite	-10.3	0.03	**4.1**
79	chalcopyrite	-13.6	0.02	**0.6**
80	pyrite	-12.0	0.04	**2.3**
80	chalcopyrite	-13.0	0.02	**1.3**
84	pyrite	-11.8	0.02	**1.7**
84	chalcopyrite	-13.0	0.03	**0.4**
89	pyrite	-10.1	0.02	**4.2**
89	chalcopyrite	-9.9	0.02	**4.5**
90	pyrite	-10.4	0.02	**3.3**
90	chalcopyrite	-9.7	0.02	**4.1**
DC-001	pyrite	-13.9	0.01	**0.3**
DC-001	chalcopyrite	-15.7	0.02	**-1.6**
DC-003	pyrite	-12.7	0.02	**1.5**
DC-003	chalcopyrite	-10.8	0.02	**3.7**

Table 2. $\delta^{18}O_{VSMOW}$ data collected from illite and quartz.

sample ID	$\delta^{18}O_{qtz}$	$\delta^{18}O_{ill}$	$\Delta_{qtz\text{-}ill}$
SNF-13-006	10.2	9.8	0.4
SNF-13-008	10.1	9.6	0.5
SNF-13-025 host	8.2	8.7	-0.6
SNF-13-028	9.6	8.7	0.9
SNF-13-041		7.8	
SNF-13-042		9.4	
repeat	8.7		
SNF-13-047	9.7	8.7	1.0
repeat	10.3		
SNF-13-048	9.2	8.3	0.9
SNF-13-050 host	9.0	7.9	1.0
SNF-13-050 vein	9.3	9.8	-0.5
SNF-13-055		10.2	
SNF-13-062	9.2	8.4	0.8
repeat	10.0		
SNF-13-068		8.4	
SNF-13-069 host	9.0	8.3	0.7
repeat	9.2		
SNF-13-070 host		8.4	
SNF-13-078	9.5	10.9	-1.4
SNF-13-091	9.2	8.9	0.3
SNF-13-092		8.5	
SNF-13-093 host		9.9	
DC-001 host	9.5	10.9	-1.4
DC-001 vein		10.0	

CHAPTER 6

DISCUSSION

Stable Isotopes-Sulfur

To determine the equilibrium temperature of pyrite-chalcopyrite pairs the equation of Kajiwara & Krouse (1971) for temperatures between 250°C-600°C was used (equation 1).

Equation 1

$1000 \ln\alpha_{py\text{-}cpy}=4.5(10^5T^{-2})$

Table 3 shows calculated temperatures using the pyrite-chalcopyrite pair. All calculated temperatures below 250 °C and above 1000 °C are not used for further calculations as they are likely disequilibrium pairs (the two minerals did not precipitate from the same fluid). Chalcopyrite is thermogenically unstable at lower temperatures, and the high-end temperatures would not be produced by this kind of system. Contamination of one phase by the other during sampling could explain the high-end temperatures, but is highly unlikely given the coarse-grained nature of the samples. It is always possible that all calculated temperatures are from disequilibrium pairs, and that some fortuitously yield temperatures within the realistic range.

Table 3. $\delta^{34}S$ data from pyrite and chalcopyrite and calculated temperatures. Calculations were done with the Kajiwara and Krouse (1971) equation. 'Shallow' samples were collected from 1040-1070ft above sea level; 'deep' samples were collected from the stockpile.

	Temp Range	Average
Shallow	315-433	377.8
Deep	397-476	435.3

Sample	Depth	$\delta^{34}S$	KK Temp
36	shallow	0.9	433
80	shallow	1	397
20	shallow	1.1	366
84	shallow	1.3	315
14	deep	1	397
90	deep	0.8	476
12	deep	0.9	433
Disequilibrium			
35	shallow	1.7	241
78	shallow	9.9	-60
34	shallow	2.6	142
79	shallow	3.5	85
37	shallow	2.2	179
23	shallow	1.9	213
89	deep	0.3	951
39-5	deep	0.2	1226
39-7.1	deep	0.2	1226
16	deep	2.6	142
13	deep	0.1	1848
15	deep	0.1	1848
dc-003	deep	2.2	179
dc-001	deep	1.9	213
39-9	deep	1.6	257

It is important to note that the range of temperatures obtained here are ~100 ^{o}C higher than those obtained by Çiftçi et al. (in press), in his fluid inclusion work. This will be discussed further in the next section. Although these data are sparse and not statistically significant, there is a difference of about 60^{o}C across the 100 ft, vertical section of the stockwork zone, suggesting a possible temperature gradient. It could be argued that as this system was convecting that there would be no gradient, and that the temperature of the stockwork zone should be uniform. Although this may be true at depth, modern MOR black smoker systems tend to be leaky near the seawater interface (Koski et al., 1985), with cold seawater entering the system near the interface and producing a temperature gradient.

Stable Isotopes-Oxygen

In order to determine fluid temperature using $\Delta_{quartz\text{-}illite}$, the equation of Eslinger & Savin (1973) for temperatures between 160^{o}C-270^{o}C was used (equation 3).

Equation 3

$$1000\ln \alpha_{quartz\text{-}illite}=0.95\ (10^{6}T^{-2}) + 0.88$$

The calculated temperatures for the illite-quartz pairs are presented in table 4. The temperature calculations show that the illite and quartz are in disequilibrium, meaning that no single fluid phase at any temperature could yield the observed $\delta^{18}O$ values for illite and quartz. It is possible that the quartz present in the samples is either magmatic, such as the remnant phenocrysts, or, more likely, it was formed from some different fluid than the one that formed the illite. Thus we are unable to use the silicate data to determine temperatures of formation.

Typical ore-formation temperatures of volcanogenic massive sulfide deposits range from 200-400^{o}C (Barnes, 1979, Lydon, 1988, Çiftçi et al., in press, and Sato, T., 1977).

Table 4. $\delta^{18}O$ data collected from illite and quartz and calculated temperatures. Calculations using the Eslinger and Savin, 1973, equation. 'N/A' indicates 'no result for -70<T<2000.'

sample ID	$\delta^{18}O_{qtz}$	$\delta^{18}O_{ill}$	$\Delta_{qtz\text{-}ill}$	Temperature (^{o}C)
SNF-13-006	10.2	9.8	0.4	N/A
SNF-13-008	10.1	9.6	0.5	N/A
SNF-13-025 host	8.2	8.7	-0.6	N/A
SNF-13-028	9.6	8.7	0.9	N/A
SNF-13-041		7.8		
SNF-13-042		9.4		
repeat	8.7			
SNF-13-047	9.7	8.7	1.0	N/A
repeat	10.3			
SNF-13-048	9.2	8.3	0.9	N/A
SNF-13-050 host	9.0	7.9	1.0	N/A
SNF-13-050 vein	9.3	9.8	-0.5	N/A
SNF-13-055		10.2		
SNF-13-062	9.2	8.4	0.8	N/A
repeat	10.0			
SNF-13-068		8.4		
SNF-13-069 host	9.0	8.3	0.7	N/A
repeat	9.2			
SNF-13-070 host		8.4		
SNF-13-078	9.5	10.9	-1.4	N/A
SNF-13-091	9.2	8.9	0.3	N/A
SNF-13-092		8.5		
SNF-13-093 host		9.9		
DC-001 host	9.5	10.9	-1.4	N/A
DC-001 vein		10.0		

The temperatures calculated by Çiftçi et al. (in press) are mostly too low for the formation of chalcopyrite, which is the major ore mineral in this deposit (as well as other VMS deposits). However, his calculations were done using fluid inclusion data from quartz. If we trust that the quartz analyzed came from a different fluid and are not remnant phenocrysts, as the lower temperatures suggest, then these temperatures represent a cooler, later stage fluid responsible for the abundant silica in all of the rocks.

The illite data can be used to constrain the fluid source for this system. In order to determine the fluid source the equations by Sheppard & Gilg (1996) (equation 4) and Savin & Lee (1988) (equation 5), were used.

Equation 4

$$1000 \ln \alpha_{illite\text{-}water} = 2.39(10^6 T^{-2}) - 3.76$$

Equation 5

$$1000 \ln \alpha_{illite\text{-}water} = 2.39(10^6 T^2) - 4.19$$

Using the $\delta^{18}O_{ill}$ and a temperature determined by the sulfur isotope data, $\delta^{18}O$ of the fluid from which the illite formed can be determined. These values are presented in table 5 and figure 11, along with various references and data from a previous study (Greene et al., 1983). A temperature of 350 ^{o}C has been chosen to represent the overall temperature of the system for several reasons. This temperature represents the average of calculated temperatures using sulfur stable isotope data (this study), as well as measured fluid inclusion minimum trapping temperatures (Çiftçi et al., in press). Chalcopyrite is stable at this temperature and forms by

reaction of copper in solution with H_2S produced via seawater sulfate reduction (discussed in a later section) (Woodruff and Shanks, 1988). Burnham & Ohmoto (1980) show that at lower temperatures (<300°C) illite is not stable and that kaolin group minerals begin to form.

Table 5. $\delta^{18}O$ collected from illite and calculated water values for a given temperature. 'S+G' refers to calculations done with the Sheppard and Gilg , 1996, equation; 'S+L' refers to those calculated with the Savin and Lee, 1988, equation. Colors correspond to relative depths. 'Deep' samples (white) were collected from the stockpile and from 950-960ft above sea level. 'Middle' (light grey) samples were collected from 960-1030ft above sea level. 'Shallow' (dark grey) samples were collected from 1030-1070ft above sea level.

			At 350 °C, S+G	At 350 °C, S+L	At 250°C, S+G
Sample ID		$\delta^{18}O$ ill	$\delta^{18}O$ H_2O	$\delta^{18}O$ H_2O	
SNF-13-025 host	Deep	8.7	6.3	6.7	3.7
SNF-13-041	Deep	7.8	5.4	5.8	2.8
SNF-13-042	Deep	9.3	6.9	7.3	4.3
DC-001 host	Deep	10.9	8.5	8.9	5.9
DC-001 vein	Deep	10	7.6	8.0	5.0
SNF-13-001	Deep	9.5	7.1	7.5	4.5
SNF-13-005	Deep	8.3	5.9	6.3	3.3
DC-002	Deep	7.8	5.4	5.8	2.8
SNF-13-090	Deep	8.4	6	6.4	3.4
SNF-13-002	Deep	9.4	7	7.4	4.4
SNF-13-006	Middle	9.8	7.4	7.8	4.8
SNF-13-008	Middle	9.5	7.1	7.5	4.5
SNF-13-028	Middle	8.7	6.3	6.7	3.7
SNF-13-047	Middle	8.7	6.3	6.7	3.7
SNF-13-048	Middle	8.3	5.9	6.3	3.3
SNF-13-050 host	Middle	7.9	5.5	5.9	2.9
SNF-13-050 vein	Middle	9.8	7.4	7.8	4.8
SNF-13-055	Middle	10.1	7.8	8.1	5.1
SNF-13-062	Middle	8.3	6.0	6.3	3.3
SNF-13-068	Middle	8.4	6.1	6.4	3.4
SNF-13-069 host	Middle	8.2	5.9	6.2	3.2
SNF-13-070 host	Middle	8.3	6.0	6.3	3.3
SNF-13-078	Shallow	10.8	8.5	8.8	5.8
SNF-13-091	Shallow	8.9	6.5	6.9	3.9
SNF-13-092	Shallow	8.5	6.1	6.5	3.5
SNF-13-093 host	Shallow	9.8	7.5	7.8	4.8
SNF-13-019	Shallow	8.9	6.6	6.9	3.9
SNF-13-081	Shallow	9.6	7.2	7.6	4.6

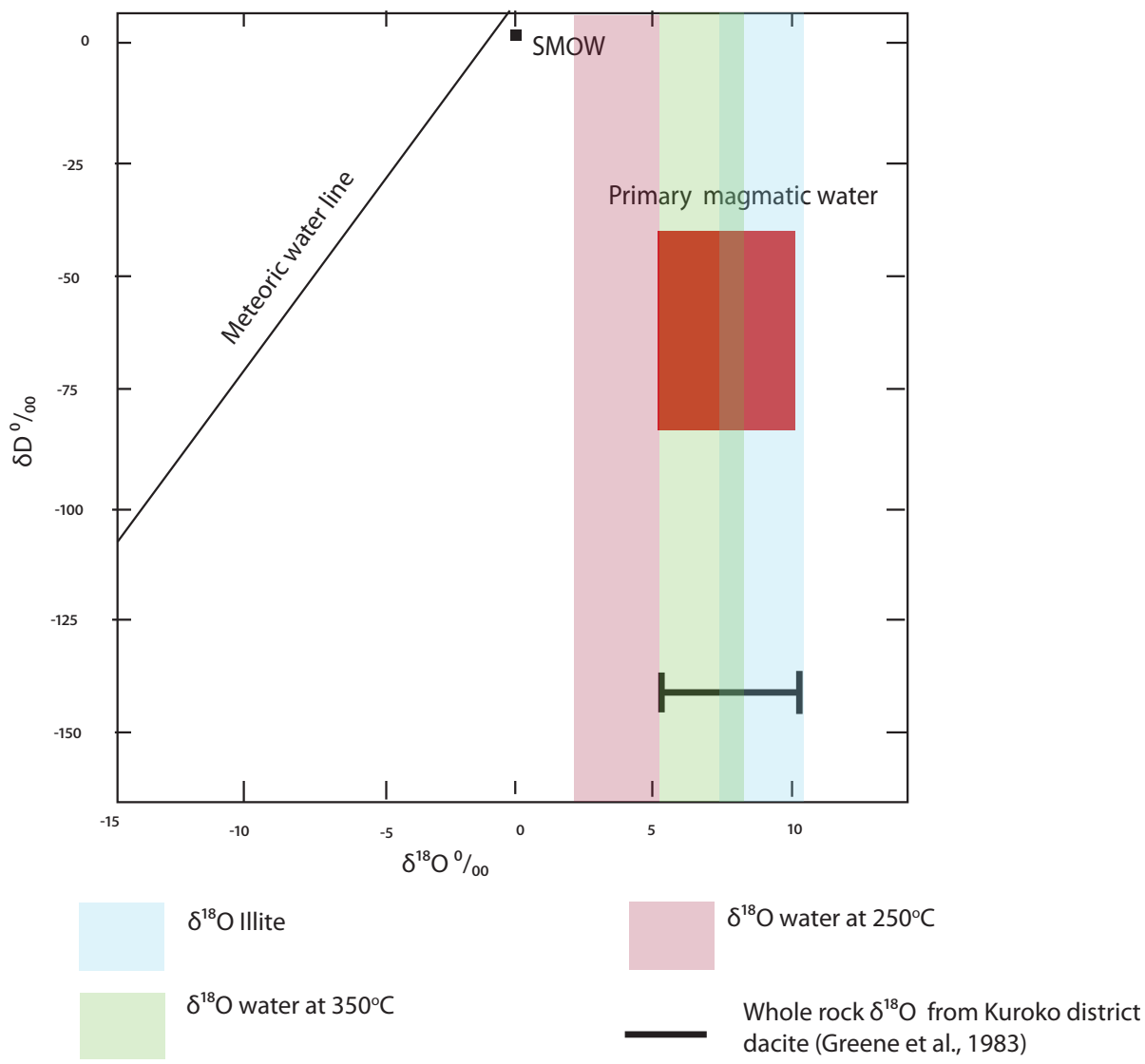

Figure 11. Plot of $\delta^{18}O$ values. Shaded vertical areas show the range of measured illite $\delta^{18}O$ as well as the calculated $\delta^{18}O$ values of water at different temperatures (using the Sheppard and Gilg, 1996, equation) in reference to SMOW, the meteoric water line, and the primary magmatic water box. Note that the range of $\delta^{18}O$ for whole rock analyses of Kuroko district dacites from Greene at al., (1983) shows values that overlaps values for illite.

Formation of Murgul

Oxygen

With these data we are able to confirm how the Murgul deposit was formed and that it is indeed a VMS deposit (figure 12). Seawater sulfate with a $\delta^{18}O$ value of 0 $^{0}/_{00}$ circulates through and exchanges with basalt as well as mixes with convecting hydrothermal fluids. This mixed fluid continues convecting through the basalt and, due to a very low water/rock ratio, takes on the isotopic signature of the basalt. The fluid then exits the system via black smokers or vents with a $\delta^{18}O$ 5-8 $^{0}/_{00}$, the same as the basalt. Due to isotopic fractionation, where the heavier and lighter isotopes of an element are fractionated into different phases (solid, liquid, or gas), the illite formed from this fluid has an enriched isotopic content than the water by +2.39 $^{0}/_{00}$ (using the Sheppard and Gilg, 1996, equation). The isotopic data collected correspond with the values we would expect to see if Murgul was formed at or near the seafloor, 8-11 $^{0}/_{00}$. If it was formed near the Earth's surface (figure 13) as a vein deposit, the resulting $\delta^{18}O$ values of illite would be significantly higher (+3-4 $^{0}/_{00}$) than collected here. The fluid in this system would be a mix of hydrothermal fluids and meteoric water with a negative $\delta^{18}O$ (here we use -5 $^{0}/_{00}$ for demonstrative purposes). Since this system would also have a very low water/rock ratio, the fluid would take on the isotopic signature of the felsic crust ($\delta^{18}O$ 8-11$^{0}/_{00}$) and the resulting $\delta^{18}O$ values of illite would be 11-13 $^{0}/_{00}$.

Whole-rock $\delta^{18}O$ analyses of dacites of the Fukazawa Kuroko VMS deposit (Greene et al., 1983) show a similar $\delta^{18}O$ range when compared to our illite analyses (figures 11 and 12). Samples collected at Murgul for this study are mineralogically analogous to what Greene et al., (1983) call zone III, sericite+chlorite. The $\delta^{18}O$ data collected by Greene et al., (1983), ranges

from 5.5-10.5 $^{o}/_{oo}$, in agreement with the range of data collected in this study for illite and the range of calculated fluid values at 350^{o}C, approximately 6-11 $^{o}/_{oo}$ in total.

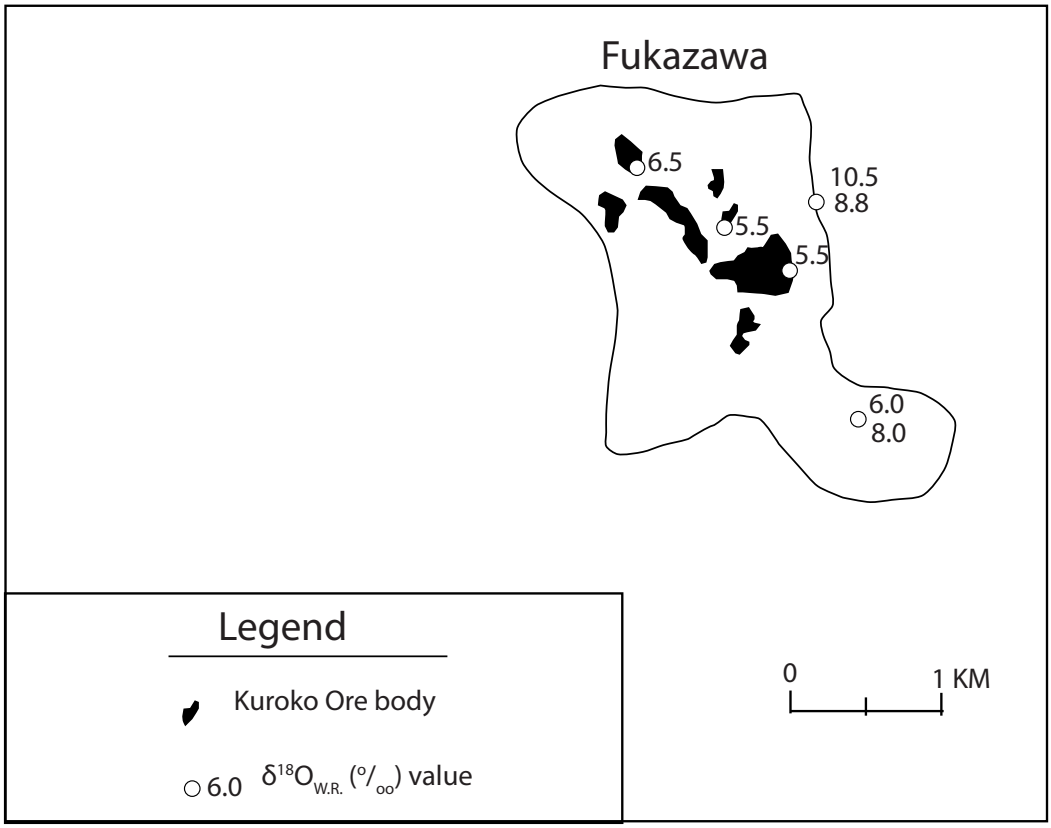

Figure 12. Distribution of whole-rock $\delta^{18}O$ values of dacites in the Fukazawa area, zone III, modified from Greene et al., (1983).

Sulfur

When the seawater sulfate mixes with convecting hydrothermal fluids within the basalt, the sulfate is thermogenically reduced to sulfide and forms H_2S (reaction 1, taken from Woodruff and Shanks, 1988).

Reaction 1

$8Fe^{+2}+10H^{+}+SO^{-2}_{4}<=>8Fe^{+3}+H_2S+4H_2O$

The $\delta^{34}S$ of the sulfide, like the $\delta^{18}O$, takes on the isotopic signature of the basalt as it continues convecting through it. This occurs because the sulfide portion of basalt is highly soluble at 350^{o}C (Woodruff and Shanks, 1988), enabling it to become incorporated into the mixed fluid. When the fluid exits the system via black smokers or vents, water is released into the sea and the massive ore is formed. To form the massive ore, H_2S combines with iron and copper ions to form chalcopyrite (reaction 2, taken from Woodruff and Shanks, 1988), which precipitates due to reduced solubility at colder temperatures.

Reaction 2

$4Cu^{+}+4Fe^{+2}+8H_2S=>4CuFeS_2+2H_2+12H^{+}$

Since the amount of copper is limited, pyrite precipitates as well. If Murgul was a vein-type deposit, meteoric water would enter the system and mix with the hydrothermal fluid. Since there is no seawater sulfate in this system the amount of sulfide is limited to only what is soluble within the crust, so there would not be enough sulfide to form a massive ore or a mineralized stockwork system like we see here.

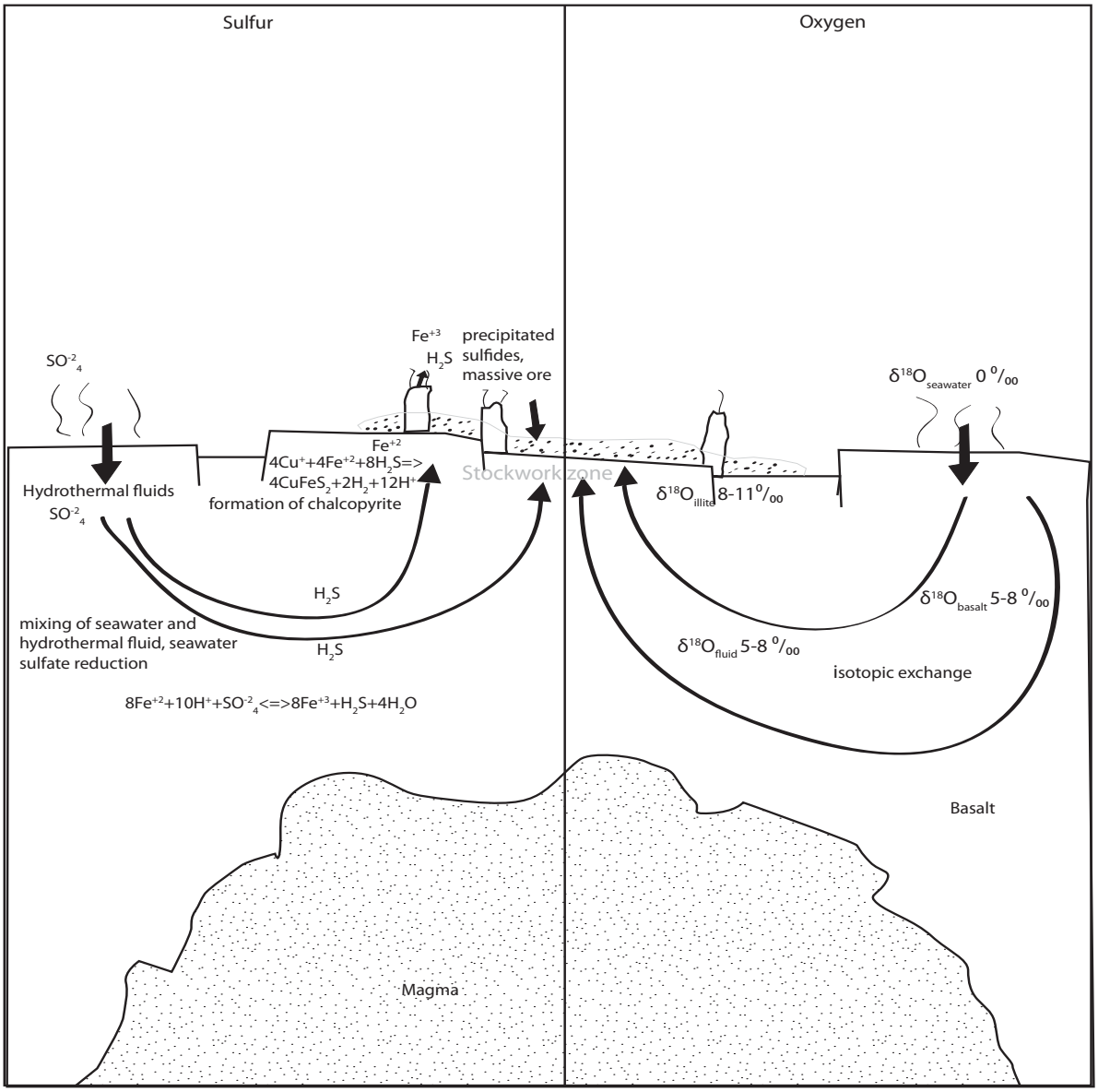

Figure 13. Schematic showing the formation of the Murgul deposit (as a VMS). Right: Oxygen story. Seawater enters the system at $\delta^{18}O$ 0 $^{0}/_{00}$. It circulates and convects through basalt ($\delta^{18}O$ 5-8 $^{0}/_{00}$), taking on the isotopic signature of the basalt via isotopic exchange. The resulting fluid ($\delta^{18}O$ 5-8 $^{0}/_{00}$) cools and deposits illite, which is isotopically enriched compared to the fluid ($\delta^{18}O$ 8-11 $^{0}/_{00}$). Left: Sulfur story. Seawater sulfate enters the system and (via circulation and convection) mixes with hydrothermal fluids. The mixing of these fluids reduces sulfate to sulfide, forming H_2S. As the fluid exits the system it cools, causing the H_2S to combine with (no longer soluble) iron and copper ions, forming chalcopyrite both in the stockwork zone and as the massive ore.

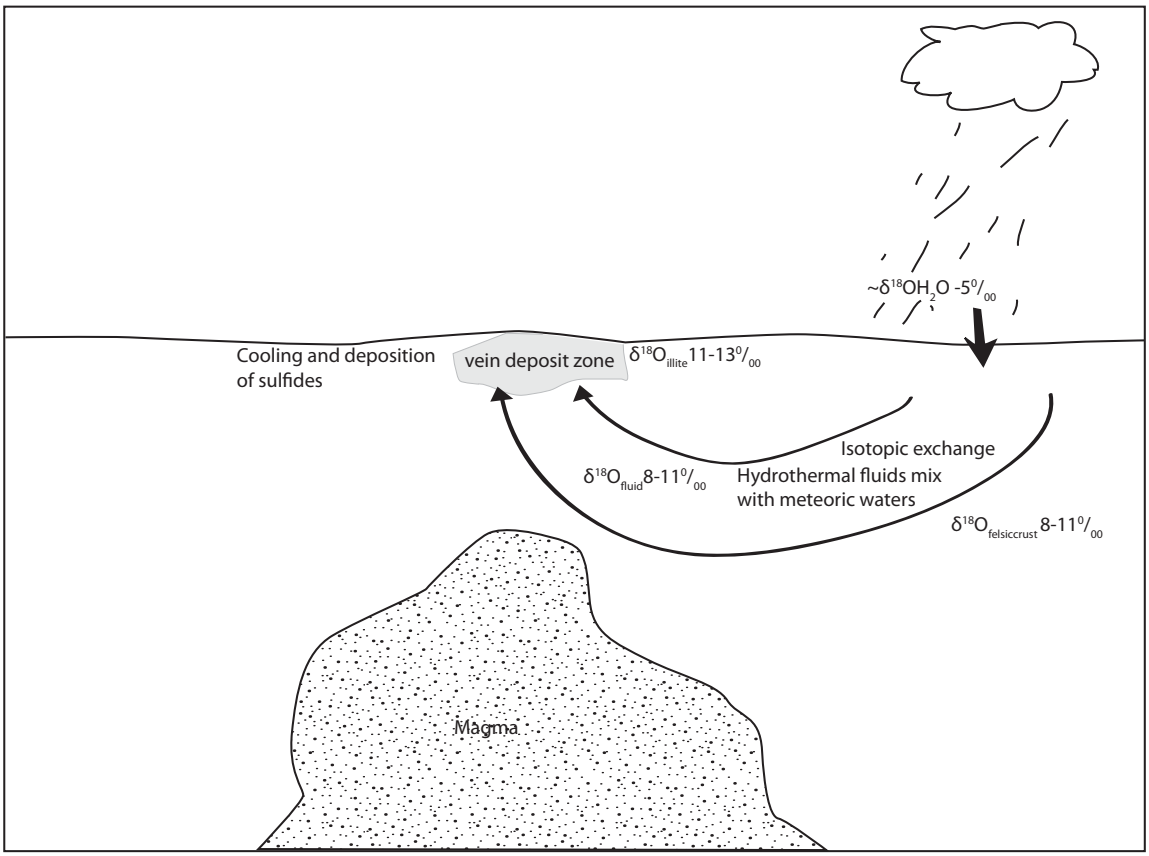

Figure 14. Schematic showing the formation of the Murgul deposit (as a vein deposit). Meteoric water with $\delta^{18}O$ -5 $^{0}/_{00}$ enters the system. It circulates and convects, undergoing isotopic exchange with the felsic crust ($\delta^{18}O$ 8-11 $^{0}/_{00}$) and mixing with hydrothermal fluids. The resulting fluid takes on the isotopic signature of the crust, $\delta^{18}O$ 8-11 $^{0}/_{00}$. As it exits the system it cools, depositing sulfides and an isotopically enriched illite ($\delta^{18}O$ 11-13 $^{0}/_{00}$).

CHAPTER 7

CONCLUSIONS

The isotopic data collected are consistent with ore forming fluid temperatures of 315°C-476°C within the stockwork zone of Murgul. Fluid inclusion data collected by Çiftçi et al. (in press) suggest a secondary, silica-rich fluid with temperatures of 160 °C-295 °C within the stockwork zone. By back-calculating the isotopic values of water that coincide with illite and an average temperature of 350 °C it is clear that the emplacement environment for the Murgul deposit is at or near the seafloor, making it a VMS deposit.

Despite statistically insignificant data, the data do show a temperature variation with depth. The average temperature for shallow samples is 377.8°C and the average temperature for deep samples is 435.3°C. It is possible that there is a temperature gradient throughout this system, but with a lack of data from middle samples it is also possible that there is no gradient.

REFERENCES

Akçay, M., Gündüz, Ö., 2004, Porphyry Cu-Au mineralization associated with a multi-phase intrusion, and related replacement fronts in limestones in an island arc setting near the Gümüşhane village (Artvin) in the Eastern Black Sea Province (Turkey): Chemie der Erde, v. 64, p. 359-383, doi:10.1016/j.chemer.2003.11.001.

Arslan, M., Aslan, Z., 2006, Mineralogy, petrography and whole-rock geochemistry of the Tertiary granitic intrusions in the Eastern Pontides, Turkey: Journal of Asian Earth Sciences, v. 27, p. 177-193, doi:10.1016/j.jseaes.2005.03.002.

Barnes, H.L., 1979, Geochemistry of Hydrothermal Ore Deposits, 2nd ed, Wiley, New York, 1979.

Burnham, C.W. and Ohmoto, H., 1980, Late stage processes of felsic magmatism, p. 1-11, *in* Ishihara, S. and Takenouchi, I., eds., Granitic Magmatism and Related Mineralization, Society of Mining Geologists, Japan, Special Issue v.8, p. 247.

Çiftçi, E., Lermi, A., Yalçinap, B., Carranza, E.J.M., Geochemical and mineralogical characteristics of major Late Cretaceous Kuroko-type VMS deposits in northeastern Turkey (in press).

Demir, Y., Uysal, İ., Sadiklar, M.B., 2013, Mineral chemical investigation on sulfide mineralization of the Istala deposit, Gümüşhane, NE Turkey: Ore Geology Reviews, v. 53, P. 306-317, doi:10.1016/j.oregeorev.2013.01.014.

Dilek, Y., Sandvol, E., 2009, Seismic structure, crustal architecture and tectonic evolution of the Anatolian-African Plate Boundary and the Cenozoic Orogenic Belts in the Eastern Mediterranean Region *in* Murphy, J.B., Keppie, J.D., Hynes, A.J., eds., Ancient Orogens and Modern Analogues, Geological Society, London, Special Publications v. 327, p. 127-160, doi: 10.1144/SP327.8.

Eslinger, E.V., Savin, S.M., 1973, Mineralogy and oxygen isotope geochemistry of the hydrothermally altered rocks of the Ohaki-Broadlands, New Zealand geothermal area: American Journal of Science, v. 273, p. 240-267.

Eyuboglu, Y., Santosh, M., Yi, K., Tuysuz, N., Korkmaz, S., Akaryali, E., Dudas, F.O., Bektas, O., 2014, The Eastern Black Sea-type volcanogenic massive sulfide deposits: Geochemistry, zircon U-Pb geochronology and an overview of the geodynamics of ore genesis: Ore Geology Reviews, v. 59, p. 29-54, doi: 10.1016/j.oregeorev.2013.11.009.

Kajiwara, Y. and Krouse, H.R. (1971). Sulfur isotope partitioning in metallic sulfide systems: Canadian Journal of Earth Sciences, v. 8, pp. 1397-1408.

Karakaya, M.Ç., Karakaya, N., Küpeli, Ş., Yavuz, F., 2012, Mineralogy and geochemical behavior of trace elements of hydrothermal alteration types in the volcanogenic massive sulfide deposits, NE Turkey: Ore Geology Reviews, v. 48, p. 197-224, doi: 10.1016/j.oregeorev.2012.03.007.

Karsli, O., Caran, Ş., Dokuz, A., Çoban, H., Chen, B., Kandemir, R., 2012, A-type granitiods from the Eastern Pontides, NE Turkey: Records for generation of hybrid A-type rocks in a subduction-related environment: Tectonophysics, v. 530-531, p. 208-224, doi: 10.1016/j.tecto.2011.12.030.

Karsli, O., Ketenci, M., Uysal, İ., Dokuz, A., Aydin, F., Chen, B., Kandemir, R., Wijbrans, J., 2011, Adakite-like granitoid porphyries in the Eastern Pontides, NE Turkey: Potential parental melts and geodynamic implications: Lithos, v. 127, p. 354-372, doi: 10.1016/j.lithos.2011.08.014.

Koski, R., Lonsdale, P.F., Shanks, W.C., Berndt, M.E., and Howe, S.S. 1985, Mineralogy and geochemistry of a sediment-hosted hydrothermal sulfide deposit from the Southern Trough of Guaymas Basin, Gulf of California; Jour. Geophys. Res., v. 90, p. 6695-6707.

Koz, B., Cevik, U., Akbulut, S., 2012, Heavy metal analysis around Murgul (Artvin) copper mining area of Turkey using moss and soil: Ecological Indicators, v. 20, p. 17-23, doi: 10.1016/j.ecolind.2012.02.002.

Lydon, John D., 1988, Ore Deposit Models #14: Volcanogenic Massive Sulfide Deposits Part 2: Genetic Models: Geoscience Canada, v. 15 (1), p. 43-65.

Ohmoto, H., Rye, R. O.,1979, Isotope of sulfur and carbon, *in* Barnes, H. L. Ed., Geochemistry of Hydrothermal deposits, John Wiley & Sons, p. 509-567.

Okay, A.I., Şahintürk, Ö., 1997, Geology of the Eastern Pontides, *in* Robinson, A.G., ed., Regional and petroleum geology of the Black Sea and surrounding region, AAPG Memoir, v. 68, p. 291-311.

Sato, T., 1977, Kuroko deposits, their geology, geochemistry, and origin: Geological Society of London, Special Publications, v. 7, p. 153-161.

Savin, S.M., Lee, M., 1988, Isotopic studies of phyllosilicates, *in* Bailey, S.W., ed., Hydrous phyllosilicates, Reviews in Mineralogy, v. 19, p. 189-223.

Sheppard, S.M.F., Gilg, H.A., 1996, Stable Isotope Geochemistry of Clay Minerals: Clay Minerals, v. 31, p. 1-24.

Sipahi, F., Sadiklar, .B., Şen, C., 2013, Geochemical and Sr-Nd isotopic characteristics of Murgul (Artvin) volcanic rocks in the Eastern Black Sea Region (Northeast Turkey): Chemi der Erde (in press), doi: 10.1016/j.chemer.2013.08.005.

Valley et al., 1995, UWG-2, a garnet standard for oxygen isotope ratios: Strategies for high precision and accuracy with laser heating, *Geochimica et Cosmochimica Acta*, v. 59, p. 5223-5231.

Woodruff, L.G. and Shanks III, W.C., 1988. Sulfur isotope study of chimney minerals and vent fluids from 21^{o}N, East Pacific Rise: Hydrothermal sulfur sources and disequilibrium sulfate reduction: Journal of Geophysical Research, v. 93 (B5), p. 4562-4572

Yanagisawa and Sakai, 1983, Thermal decomposition of barium sulfate-vanadium pentaoxide-silica glass mixtures for preparation of sulfur dioxide in sulfur isotope ratio measurements: Analytical Chemistry, v. 55, p. 985-987.

APPENDICES

APPENDIX A

XRD patterns of samples. These are ordered first by depth (shallow, middle, deep), secondly numerically by sample name, and lastly by whether there is a significant amount of sulfide (shown in pattern).

Shallow

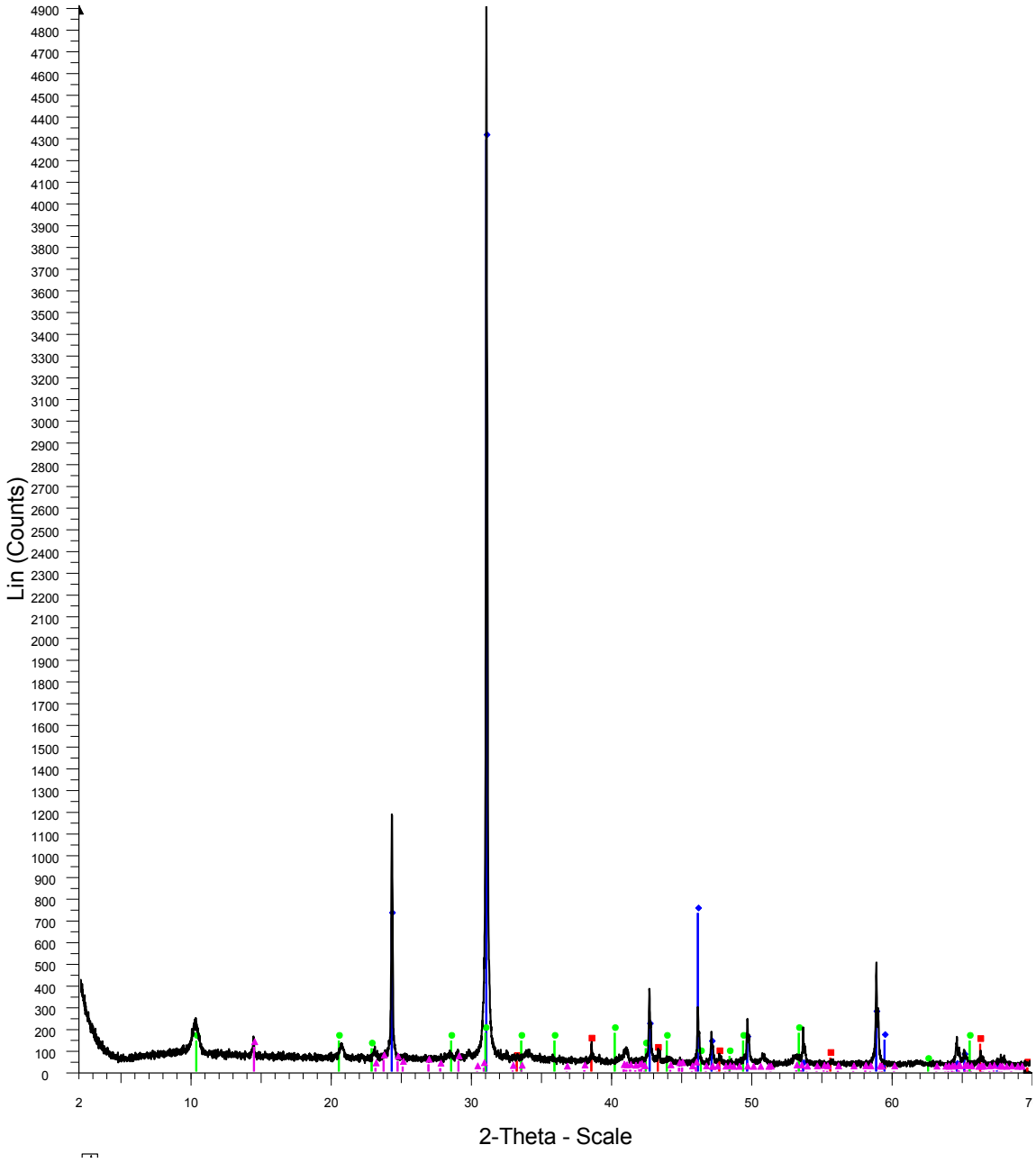

Red-Pyrite
Blue- Quartz
Green-Illite
Pink-Kaolinite

-17host

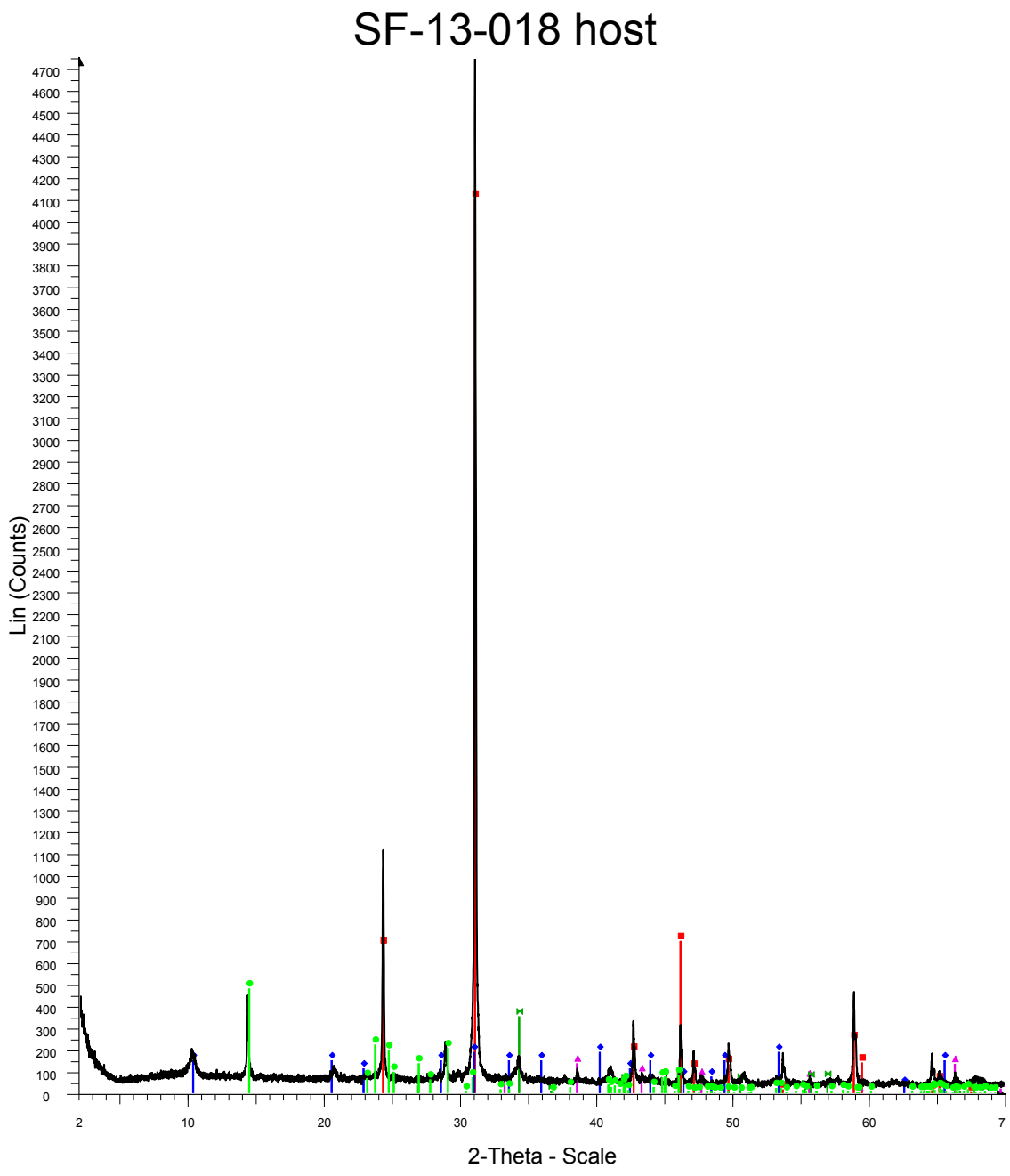

Red-Quartz
Blue- Illite
Pink-Pyrite
Dark Green-Calcite
Green-Kaolinite

-18host

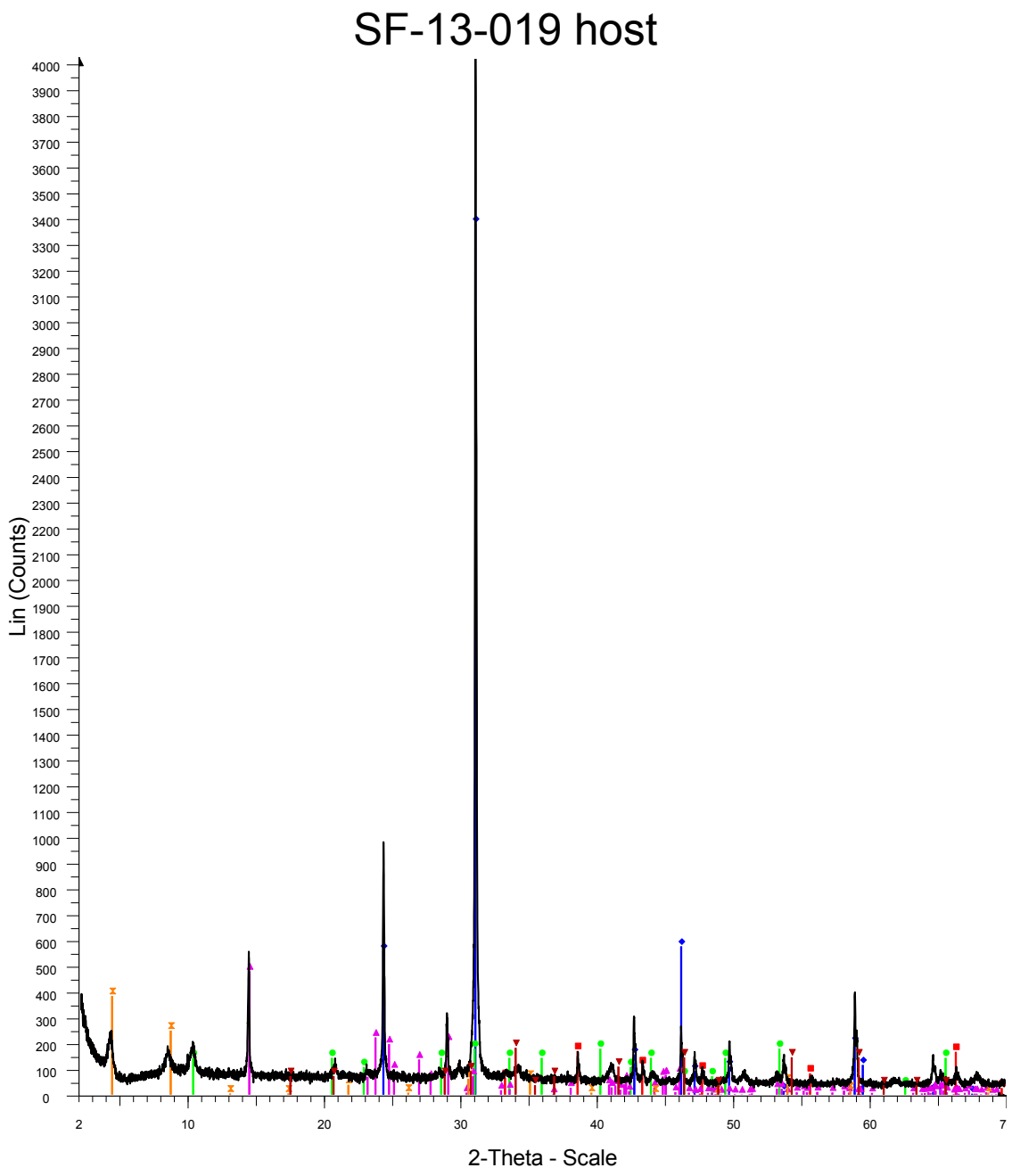

Red-Pyrite
Blue- Quartz
Green-Illite
Pink-Kaolinite
Orange-Rectorite
Dark red-Jarosite

-19host

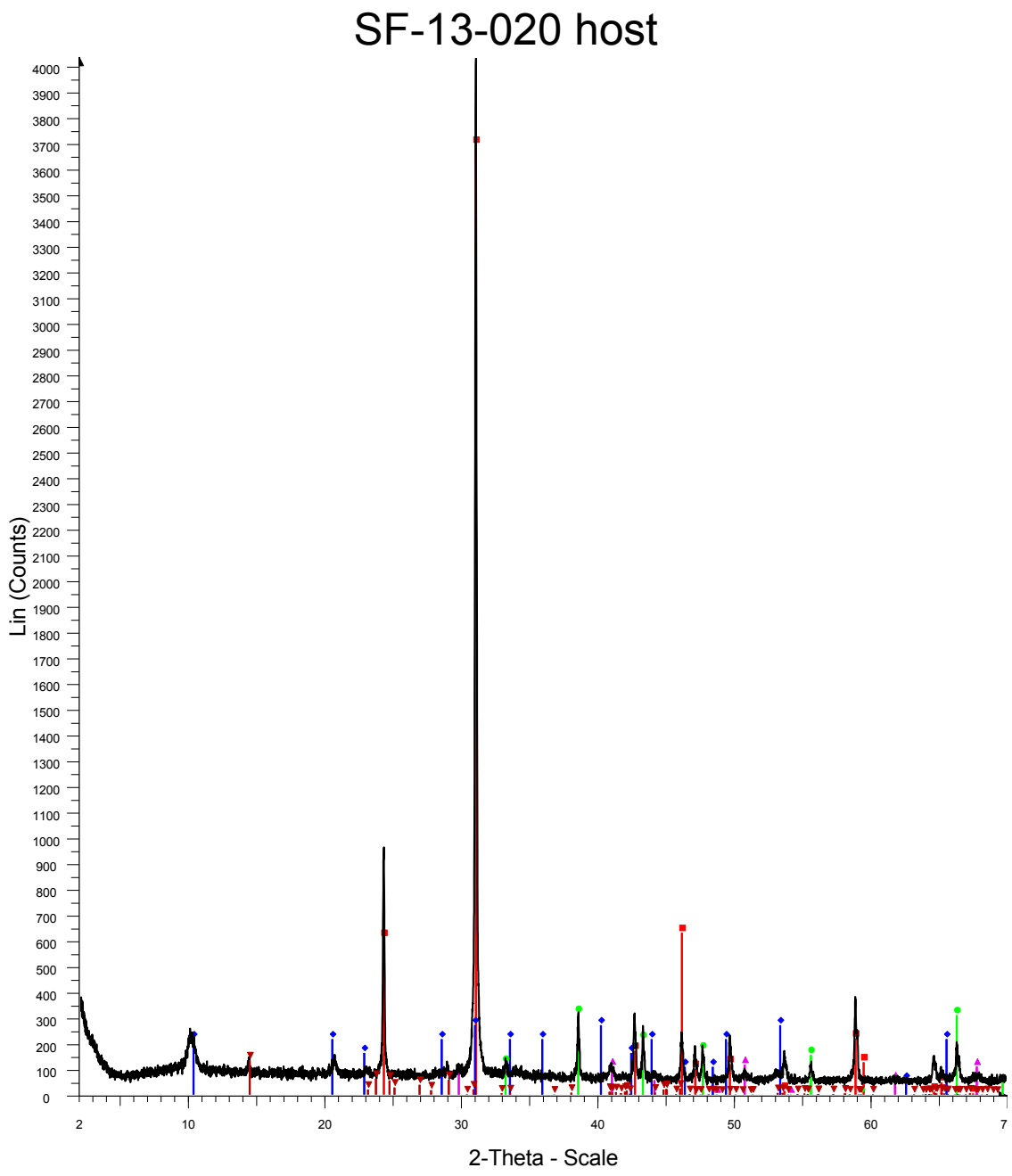

Red- Quartz
Blue- Illite
Green-Pyrite
Pink-Corundum
Dark Red-Kaolinite

-20 host

SF-13-021

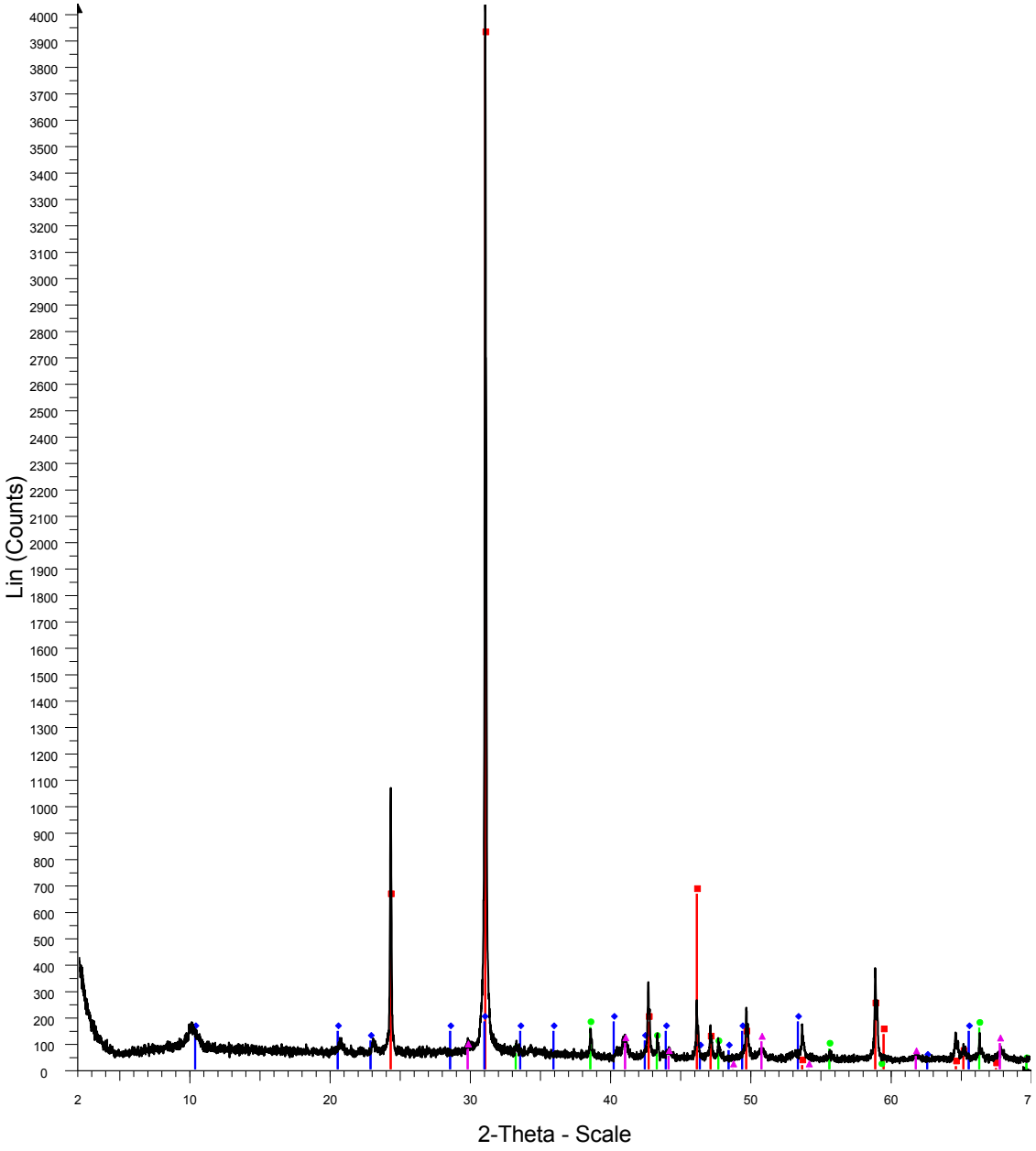

Red- Quartz
Blue- Illite
Green-Pyrite
Pink-Corundum

-21

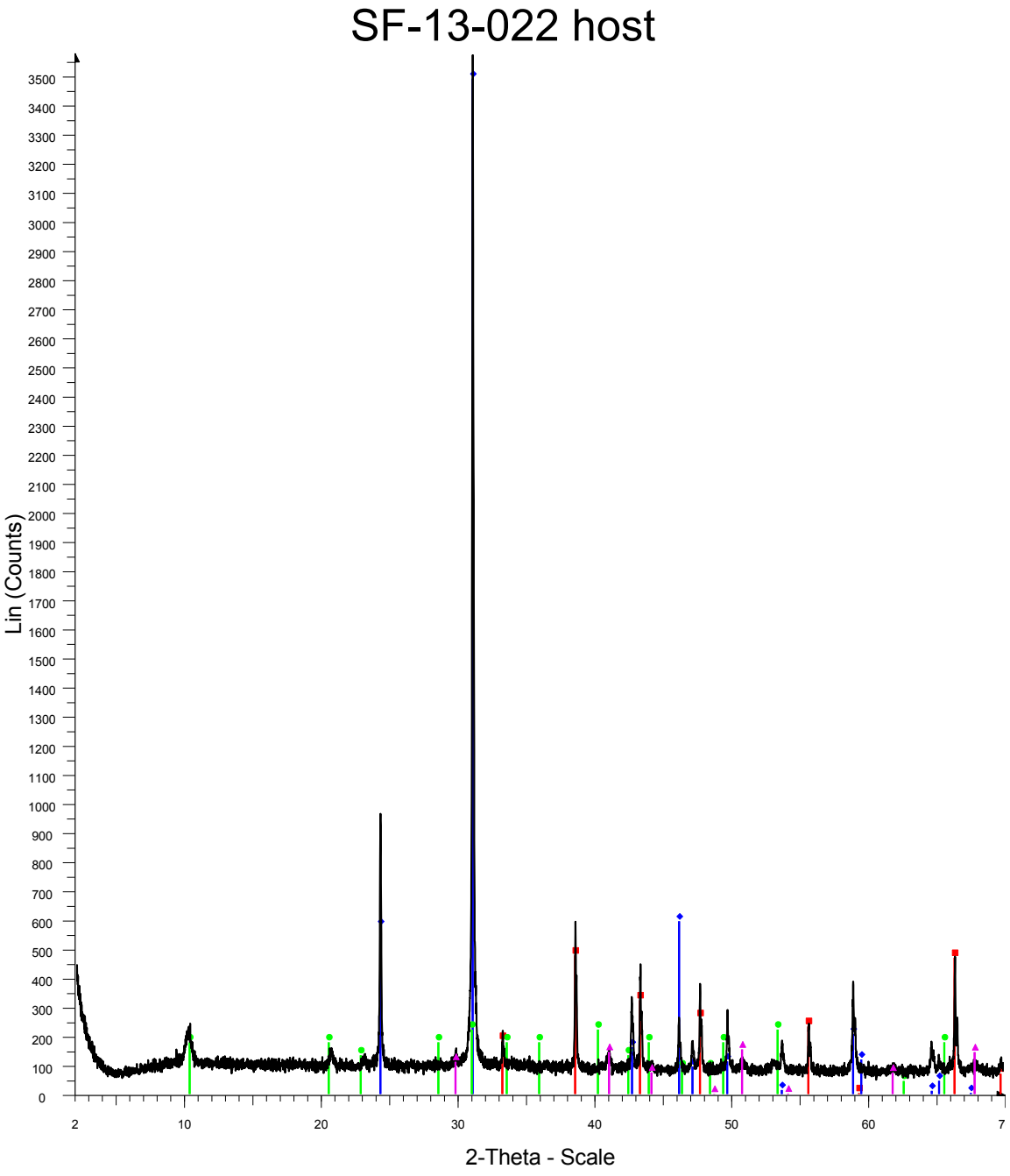

Red- Pyrite
Blue- Quartz
Green-Illite
Pink-Corundum

-22 Host

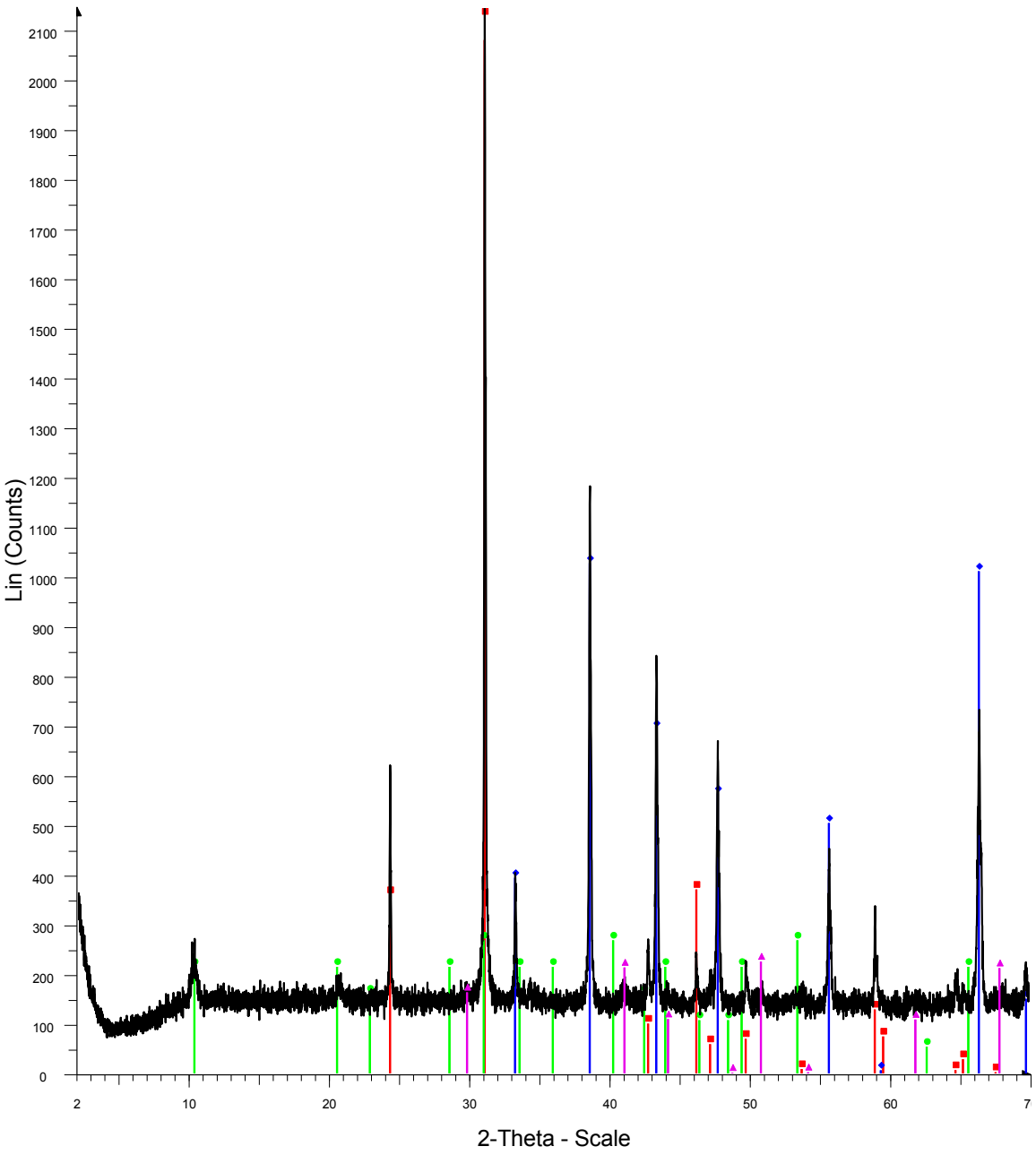

Red- Quartz
Blue- Pyrite
Green-Illite
Pink-Corundum

-22 vein2

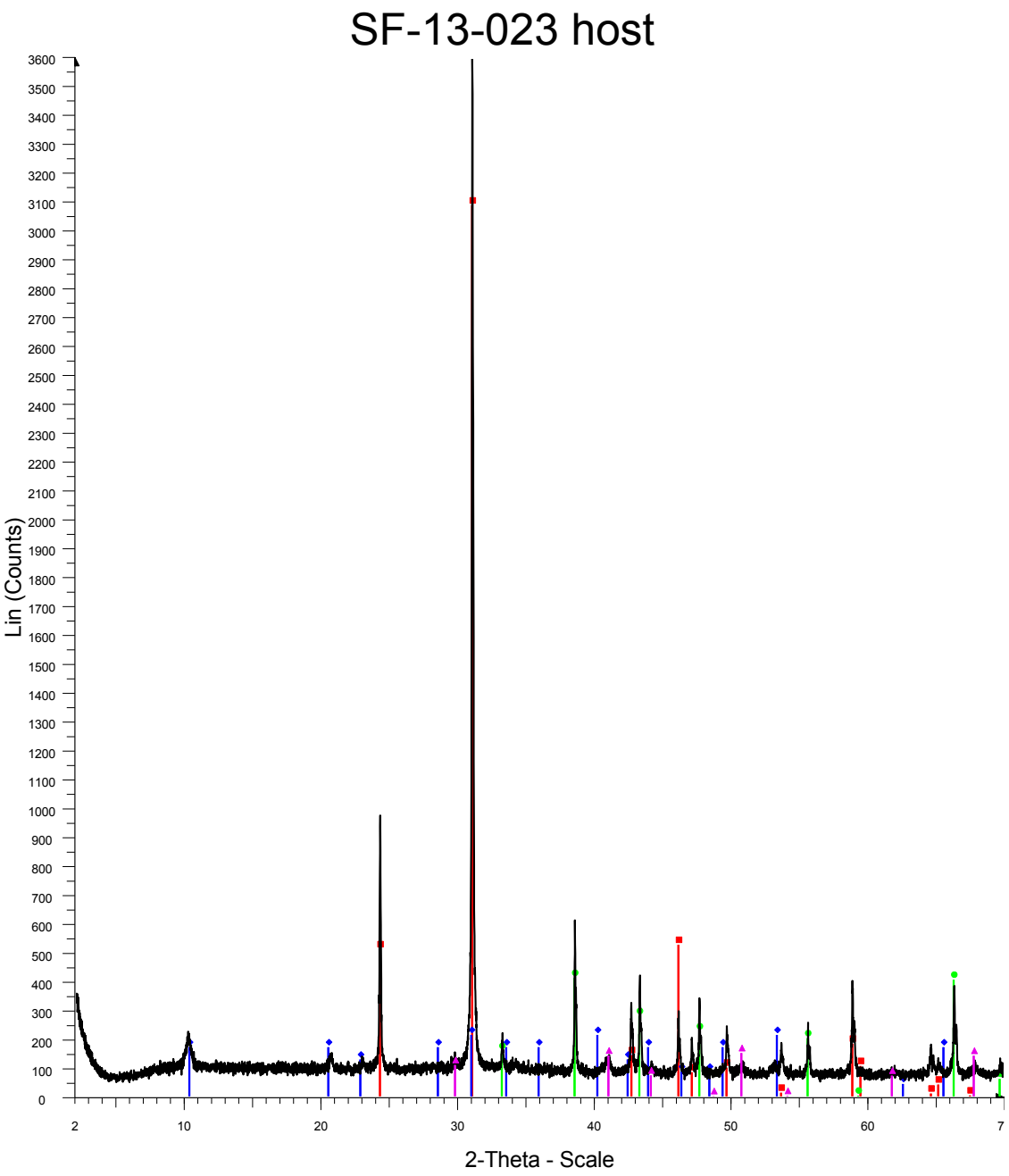

Red- Quartz
Blue- Illite
Green-Pyrite
Pink-Corundum

-23host

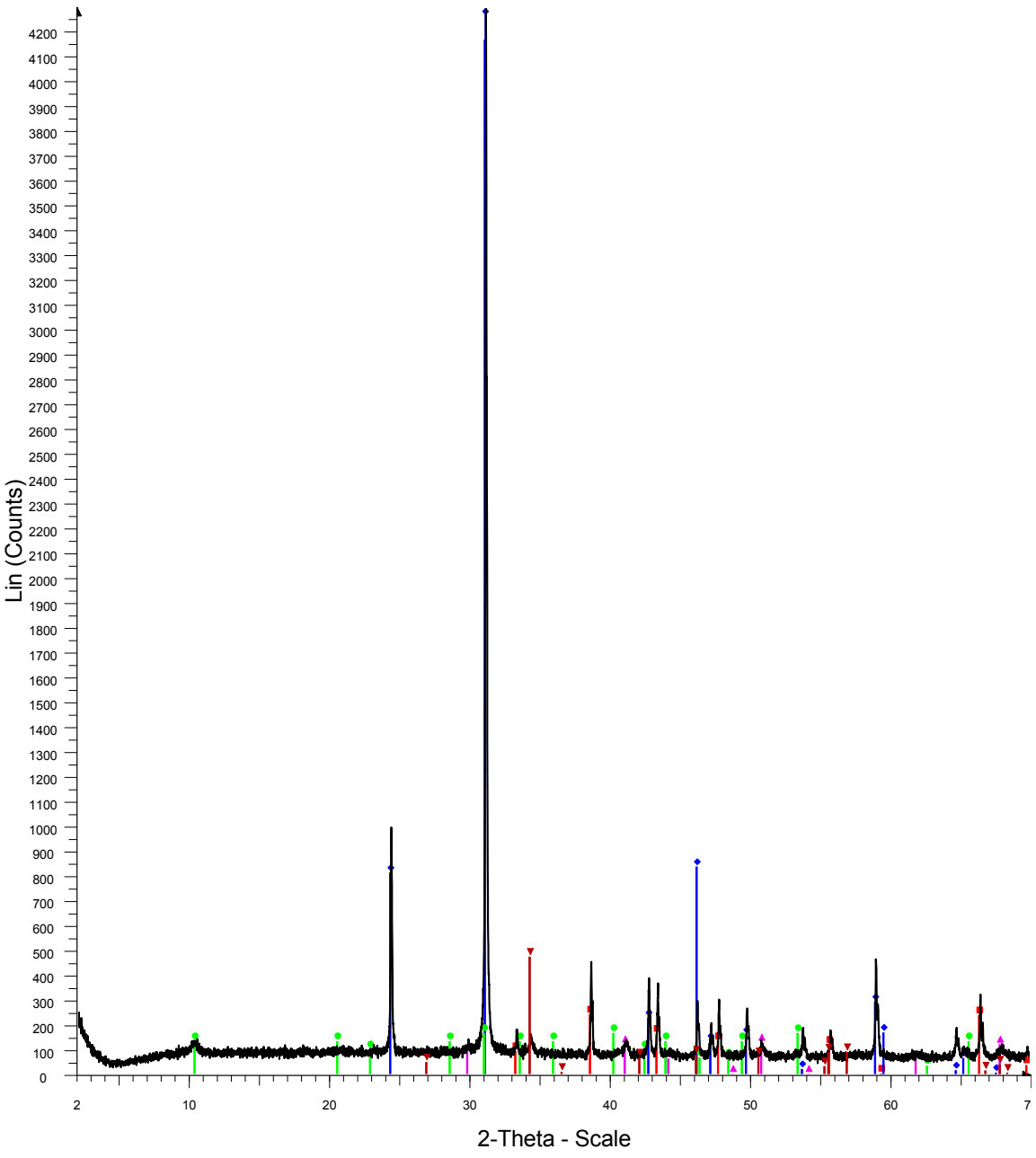

Red- Pyrite
Blue- Quartz
Green-Illite
Pink-Corundum
Dark red-Calcite

-24host

SF-13-033 host

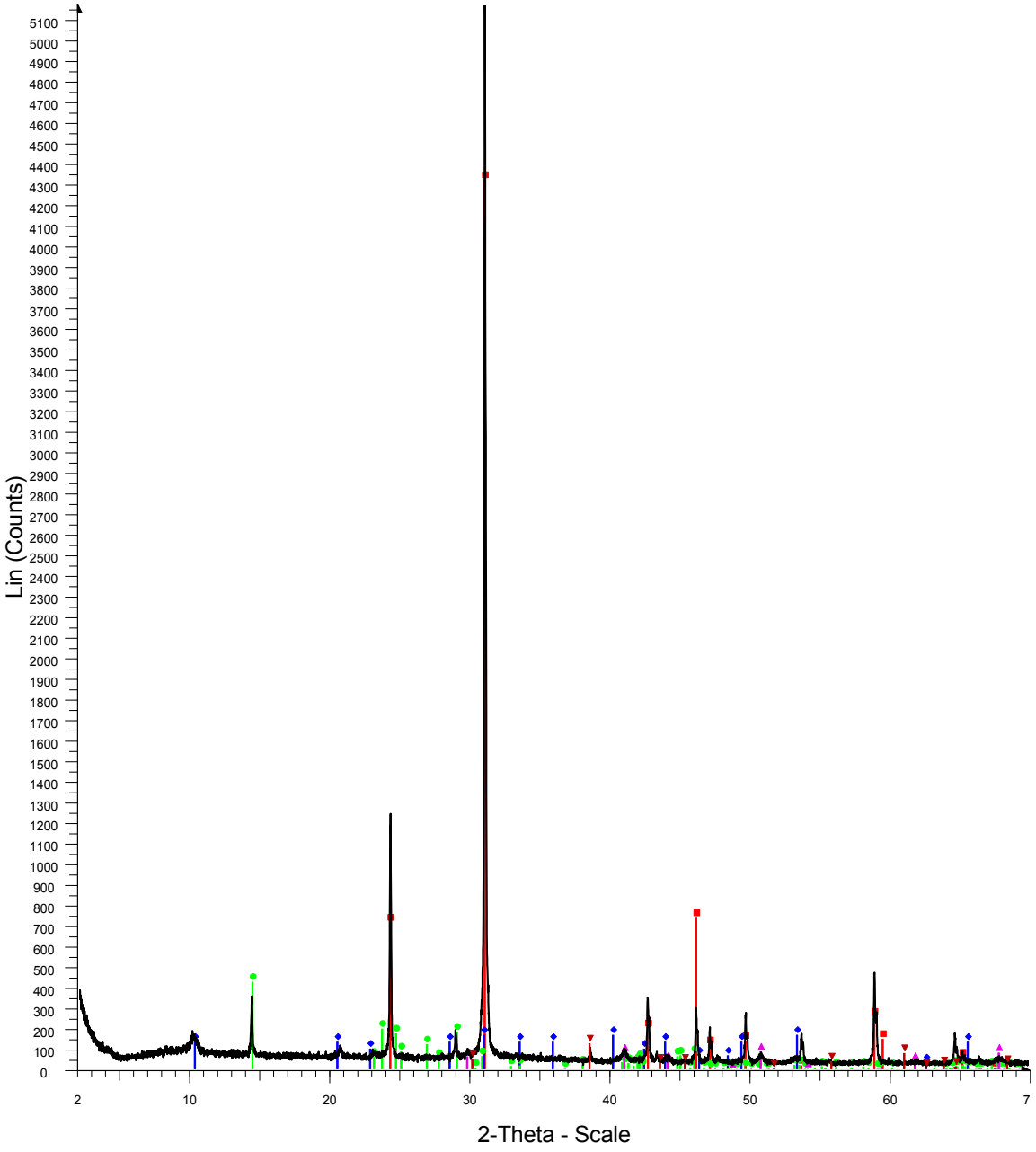

Red-Quartz
Blue- Illite
Green-Kaolinite
Pink-Corundum
Dark red-Marcasite

-33host

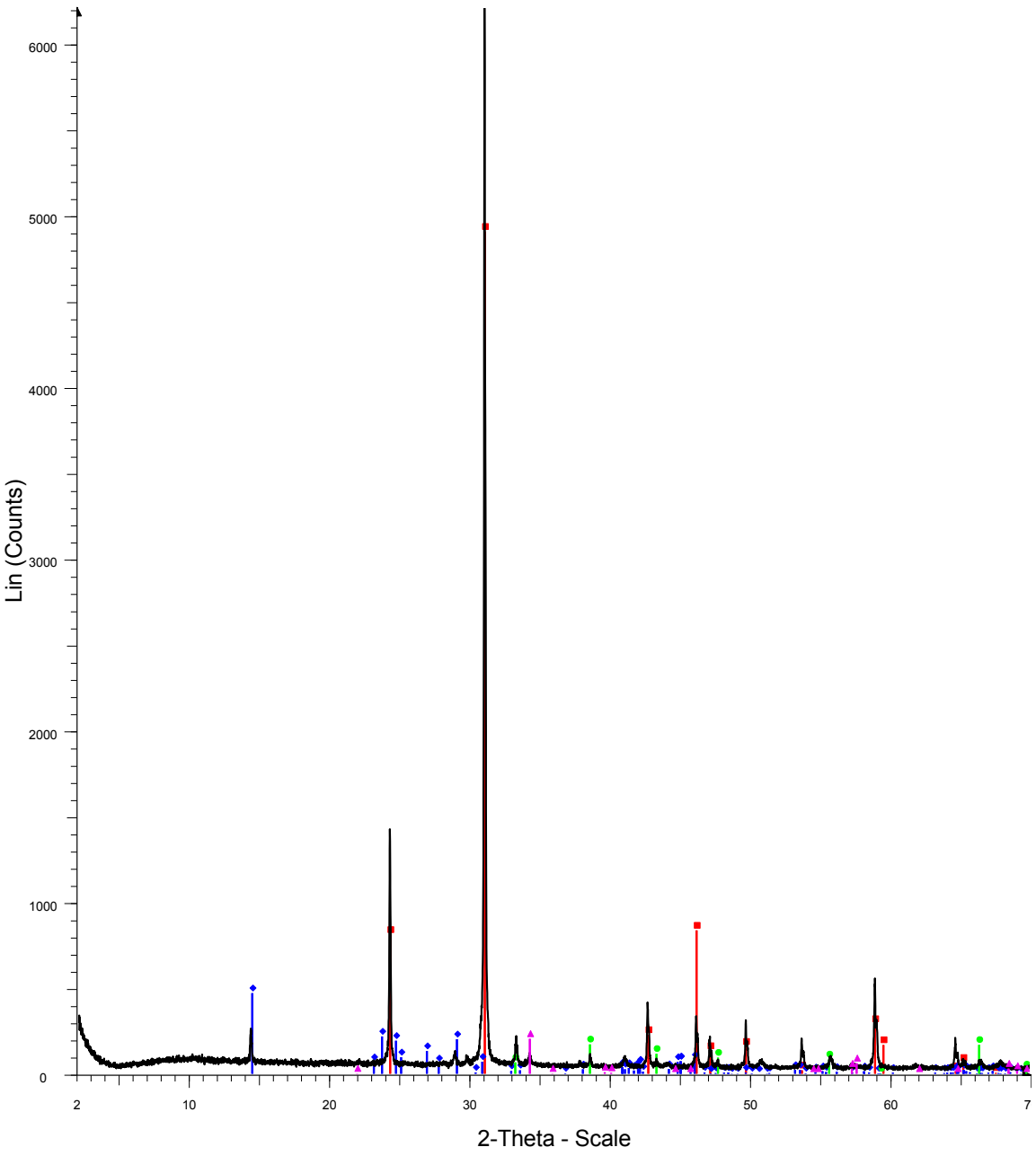

Red-Quartz
Blue- Kaolinite
Green-Pyrite
Pink-Chalcopyrite

-33vein1

SF-13-034 host

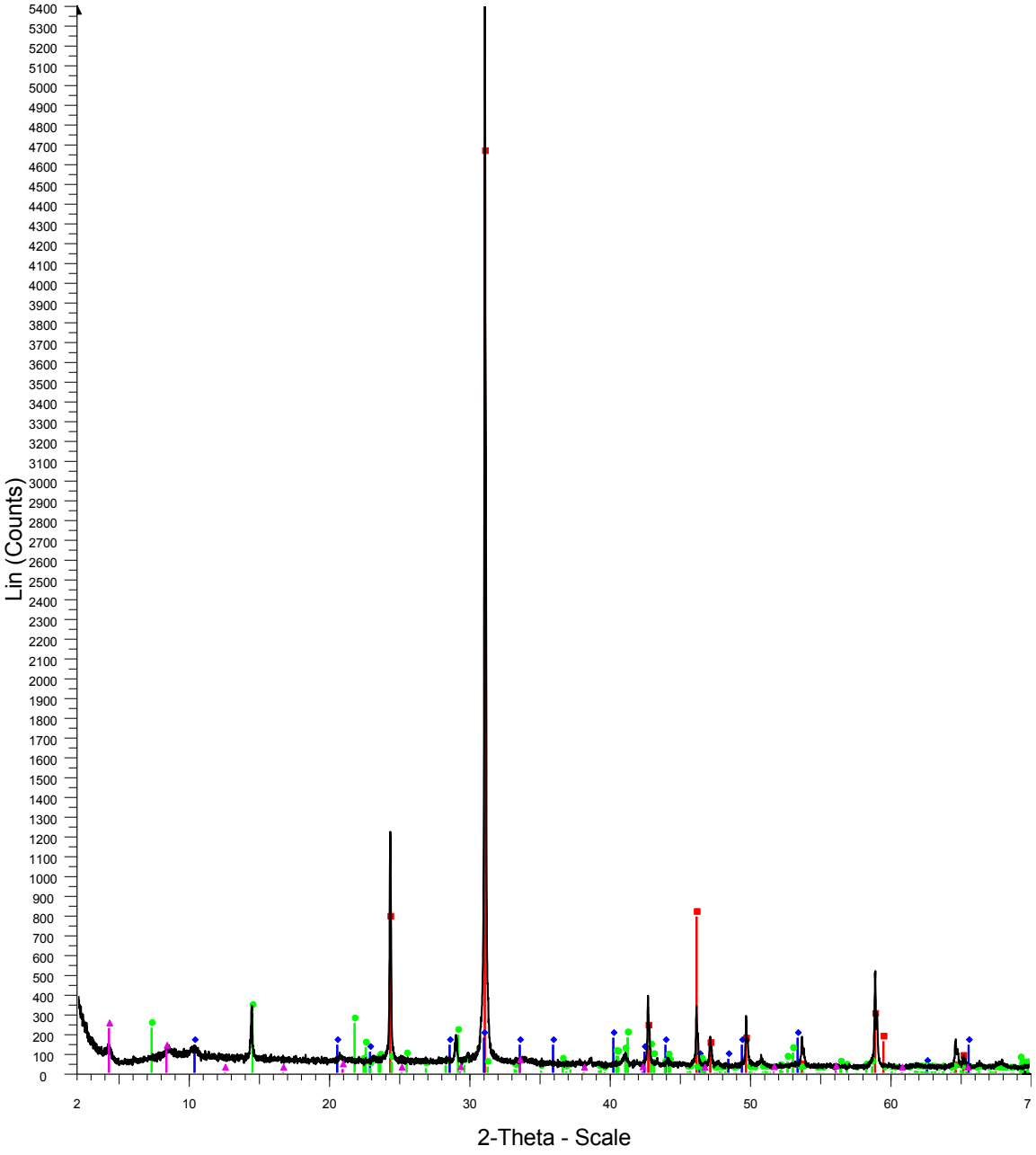

Red-Quartz
Blue- Illite
Green-Chlorite
Pink-Rectorite

-34host

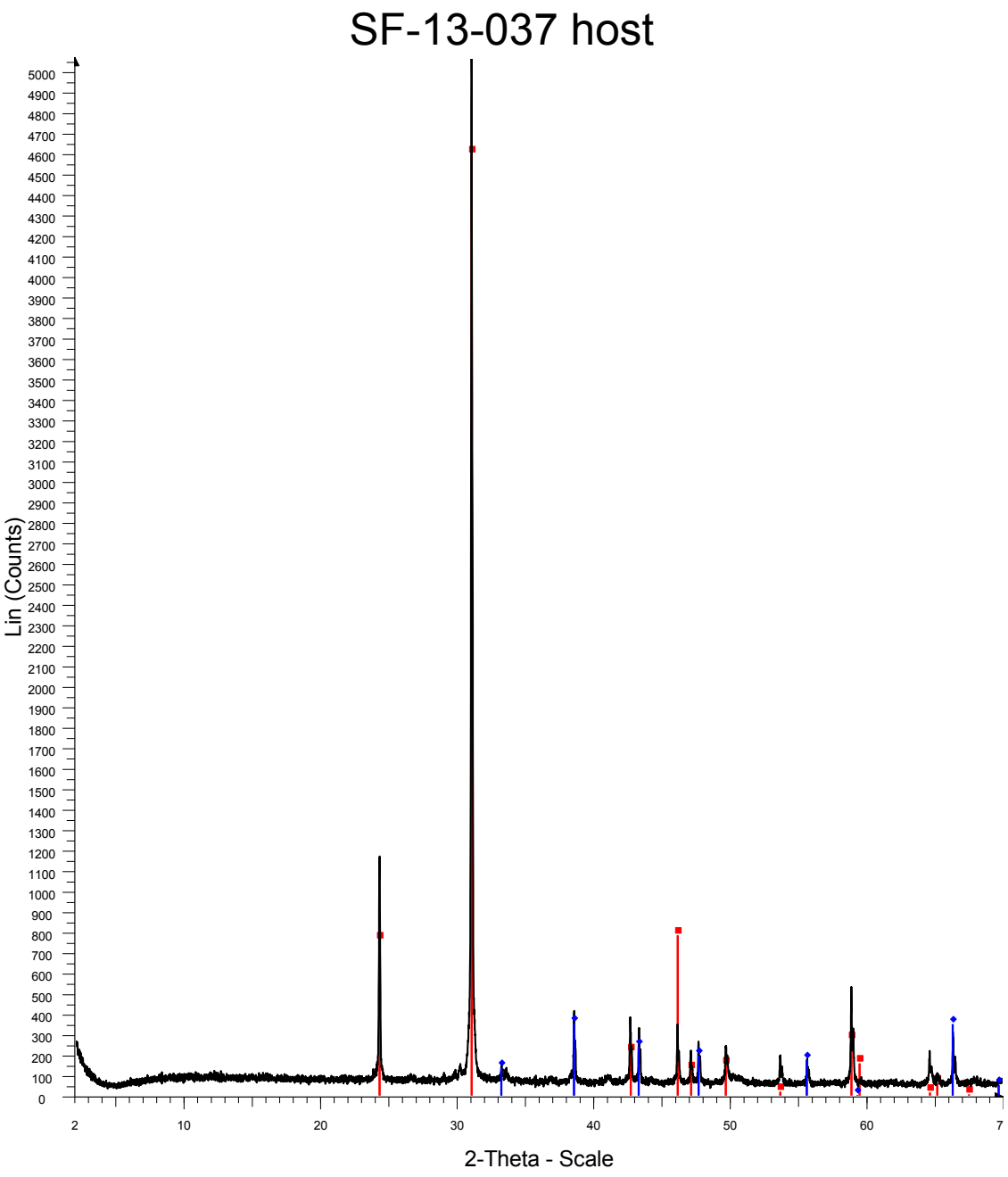

Red- Quartz
Blue- Pyrite
-37host

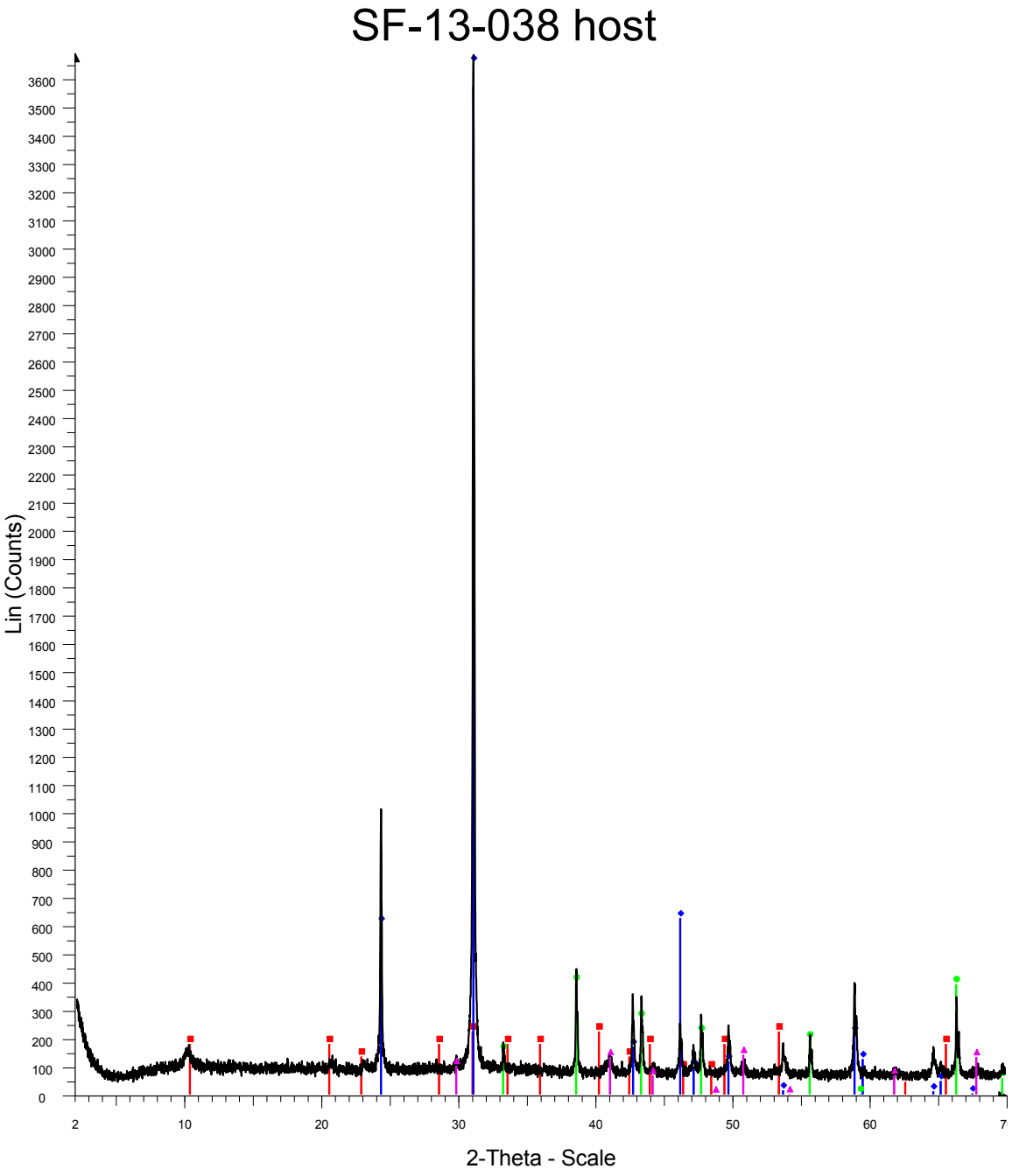

Red- Illite
Blue- Quartz
Green-Pyrite
Pink-Corundum

-38host

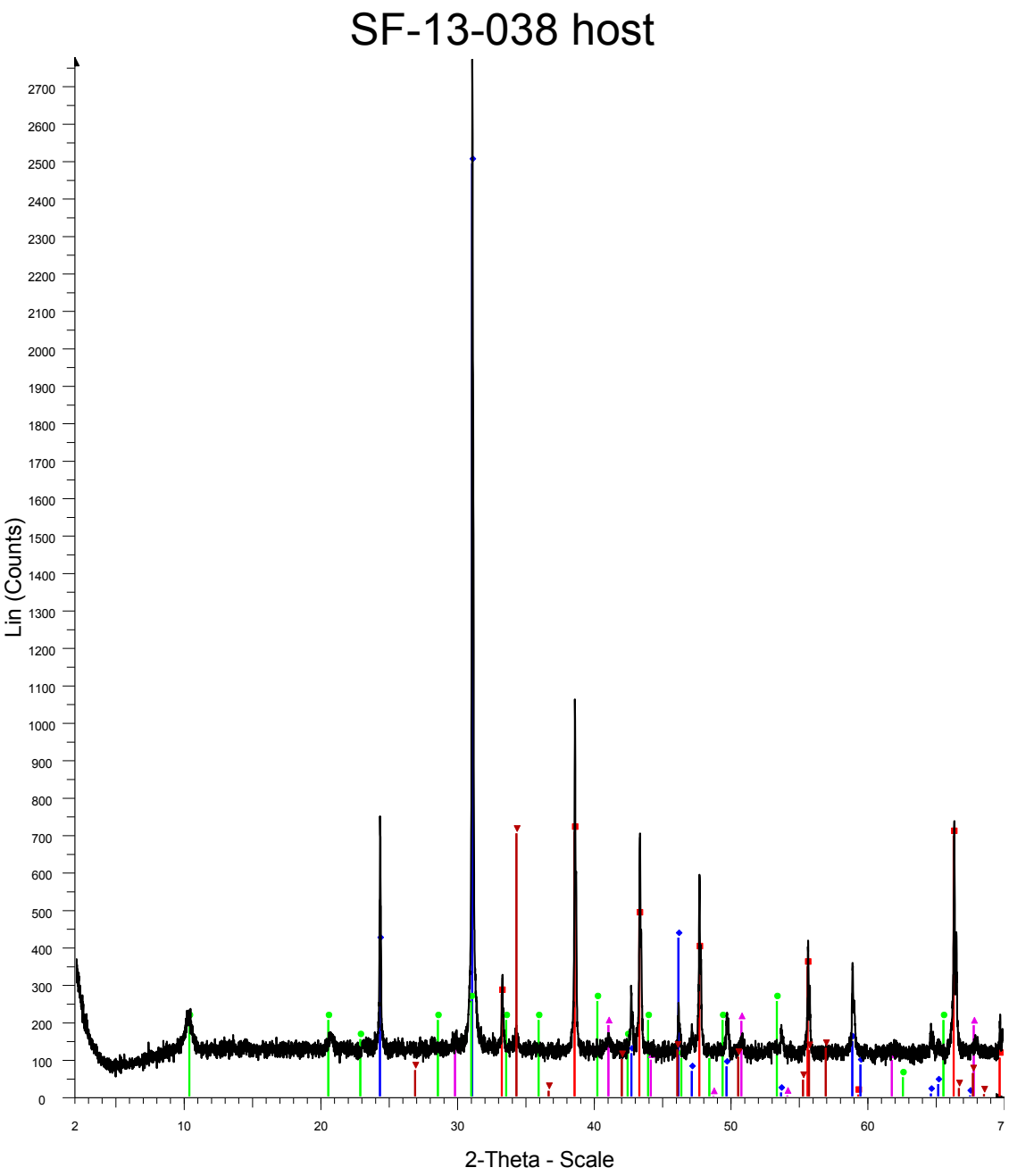

Red-Pyrite
Blue- Quartz
Green-Illite
Pink-Corundum
Dark red-Calcite

-38host2

SF-13-077 host

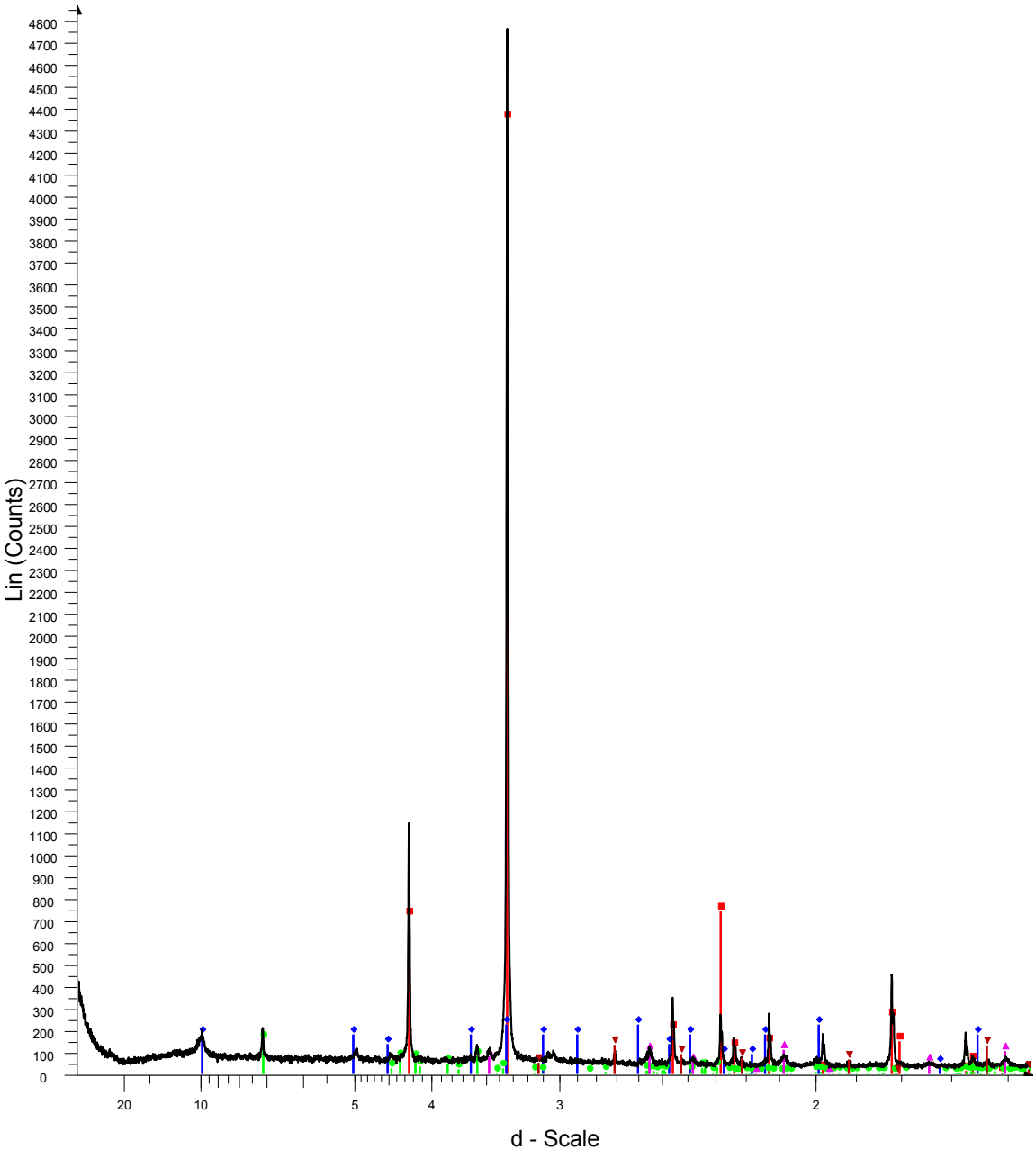

Red-Quartz
Blue- Illite
Green-Kaolinite
Pink-Corundum
Dark red-Pyrite

-77host

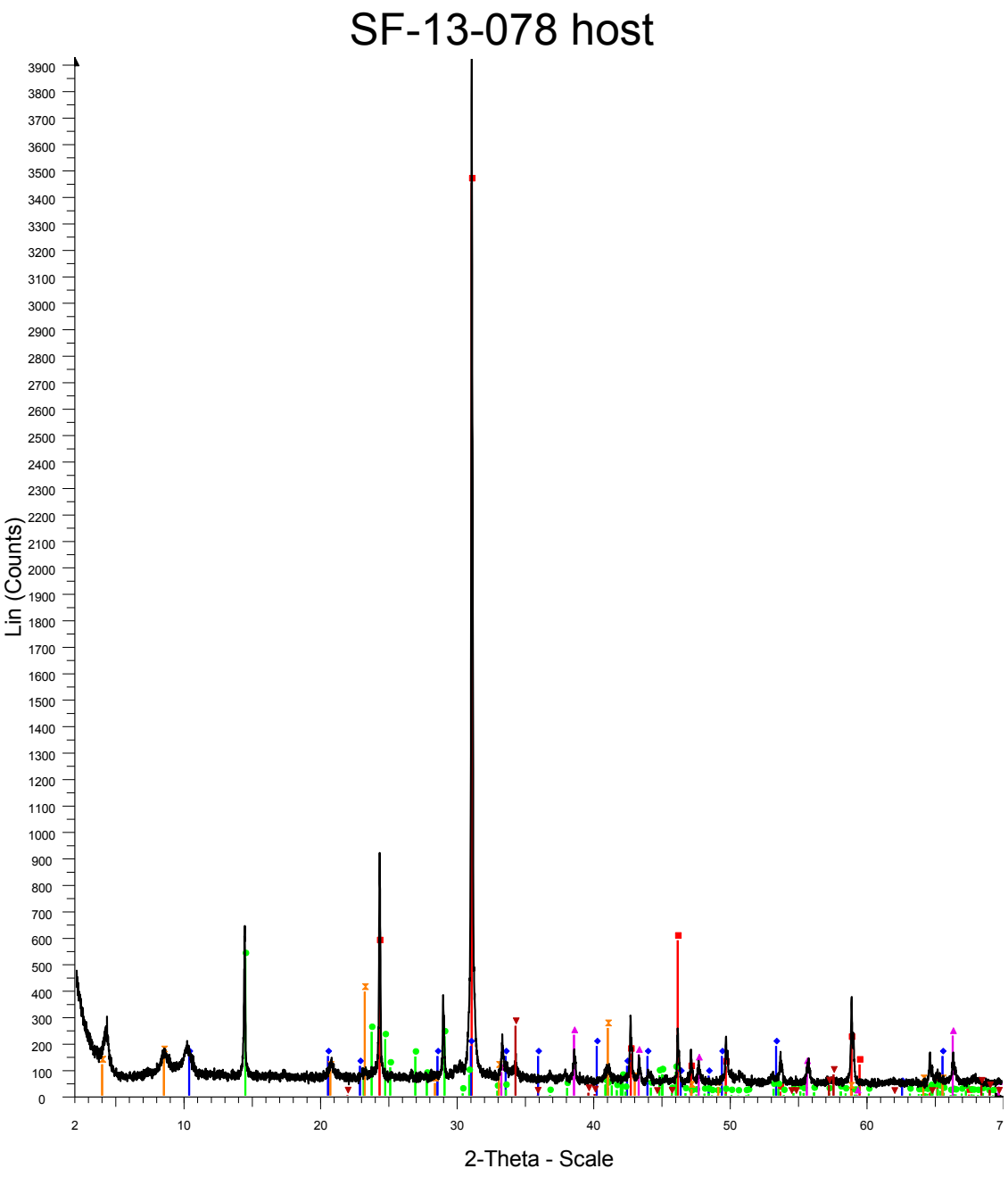

Red-Quartz
Blue- Illite
Green-Kaolinite
Pink-Pyrite
Orange-Rectorite
Dark red-Chalcopyrite
-78host

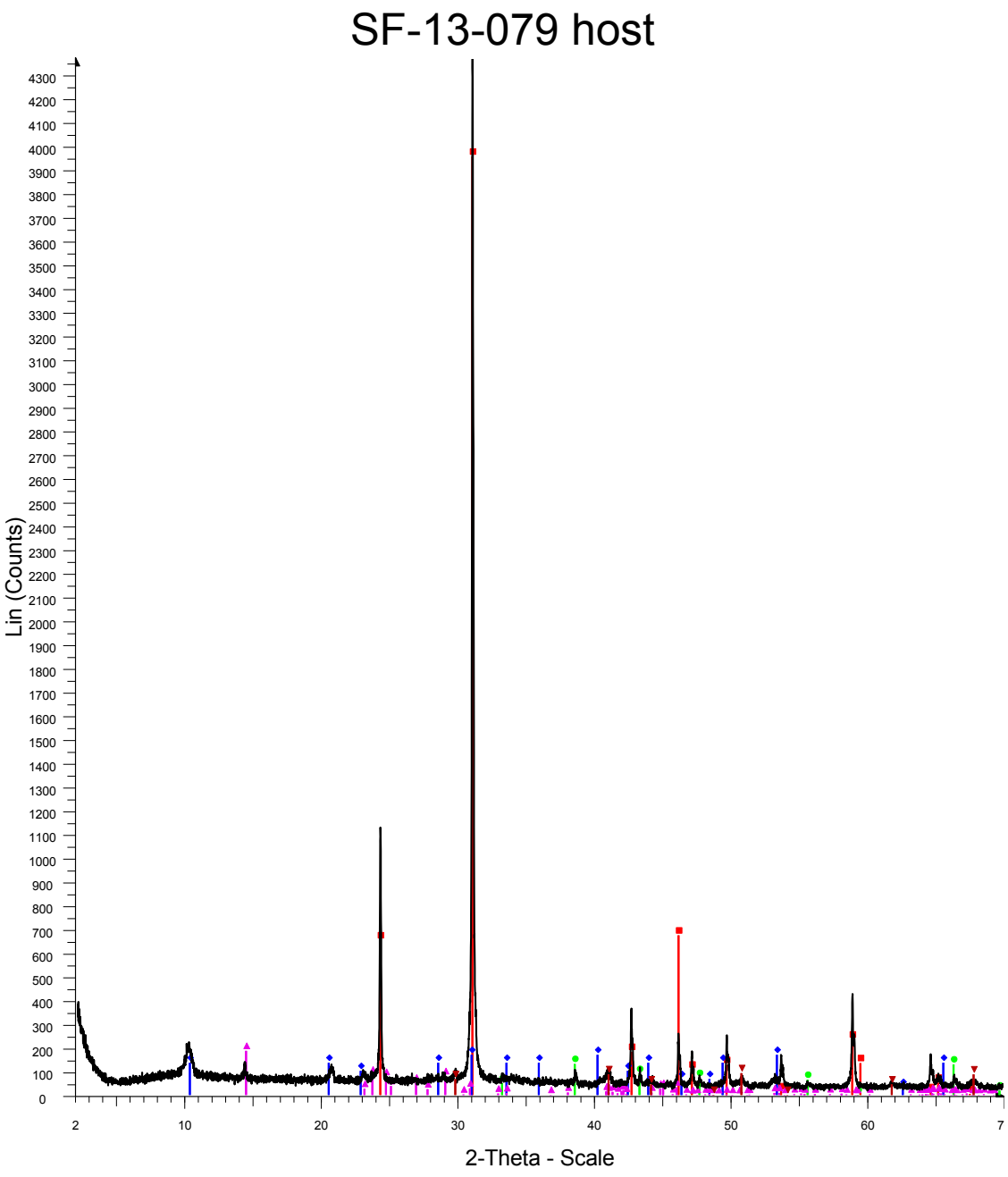

Red-Quartz
Blue- Illite
Green-Pyrite
Pink- Kaolinite
Dark red-Corundum
-79host

SF-13-080 host

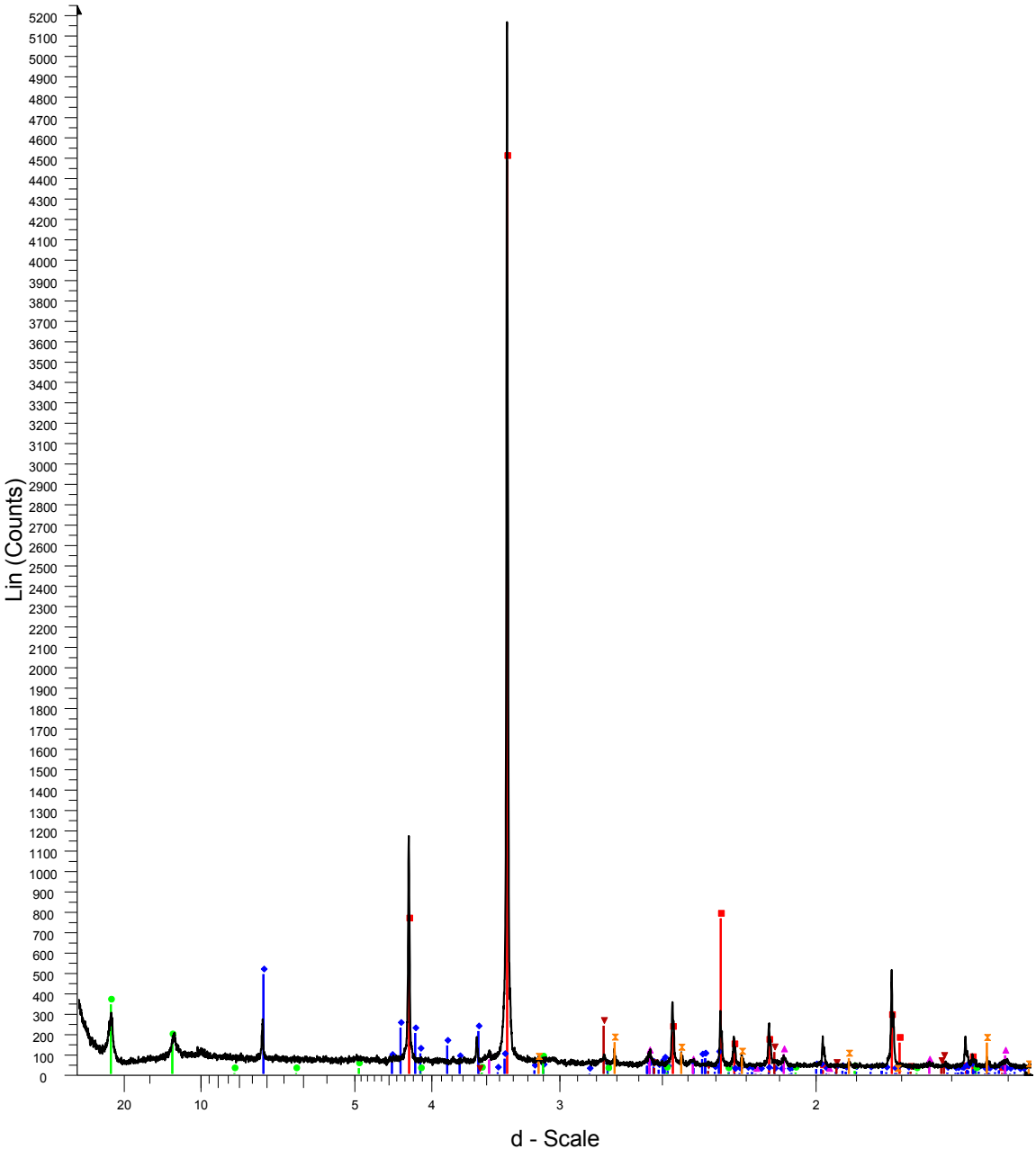

Red-Quartz
Blue- Kaolinite
Green-Rectorite
Pink- Corundum
Dark red-Magnesite
Orange-Pyrite
-80host

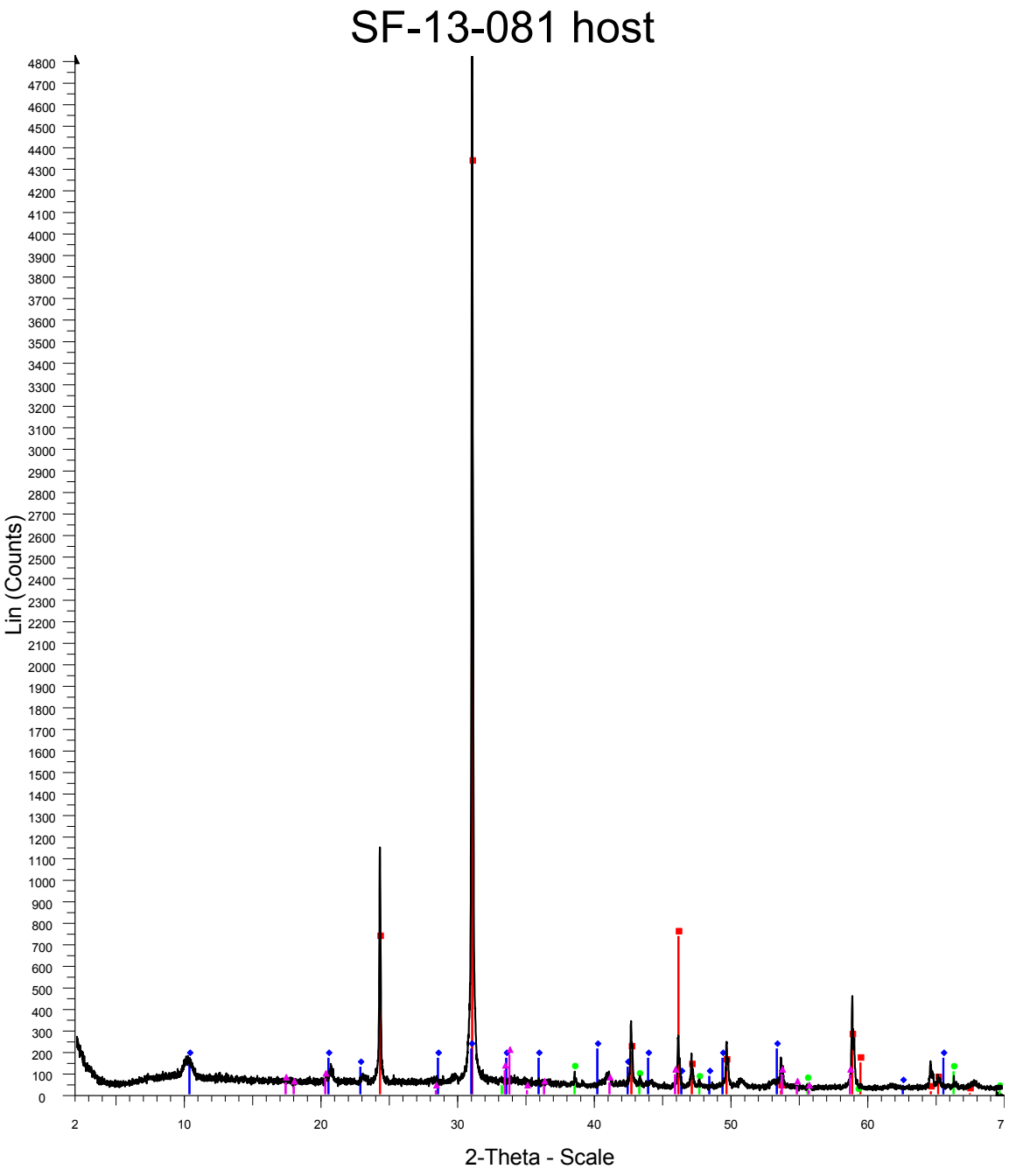

Red-Quartz
Blue- Illite
Green-Pyrite
Pink-Jarosite
-81host

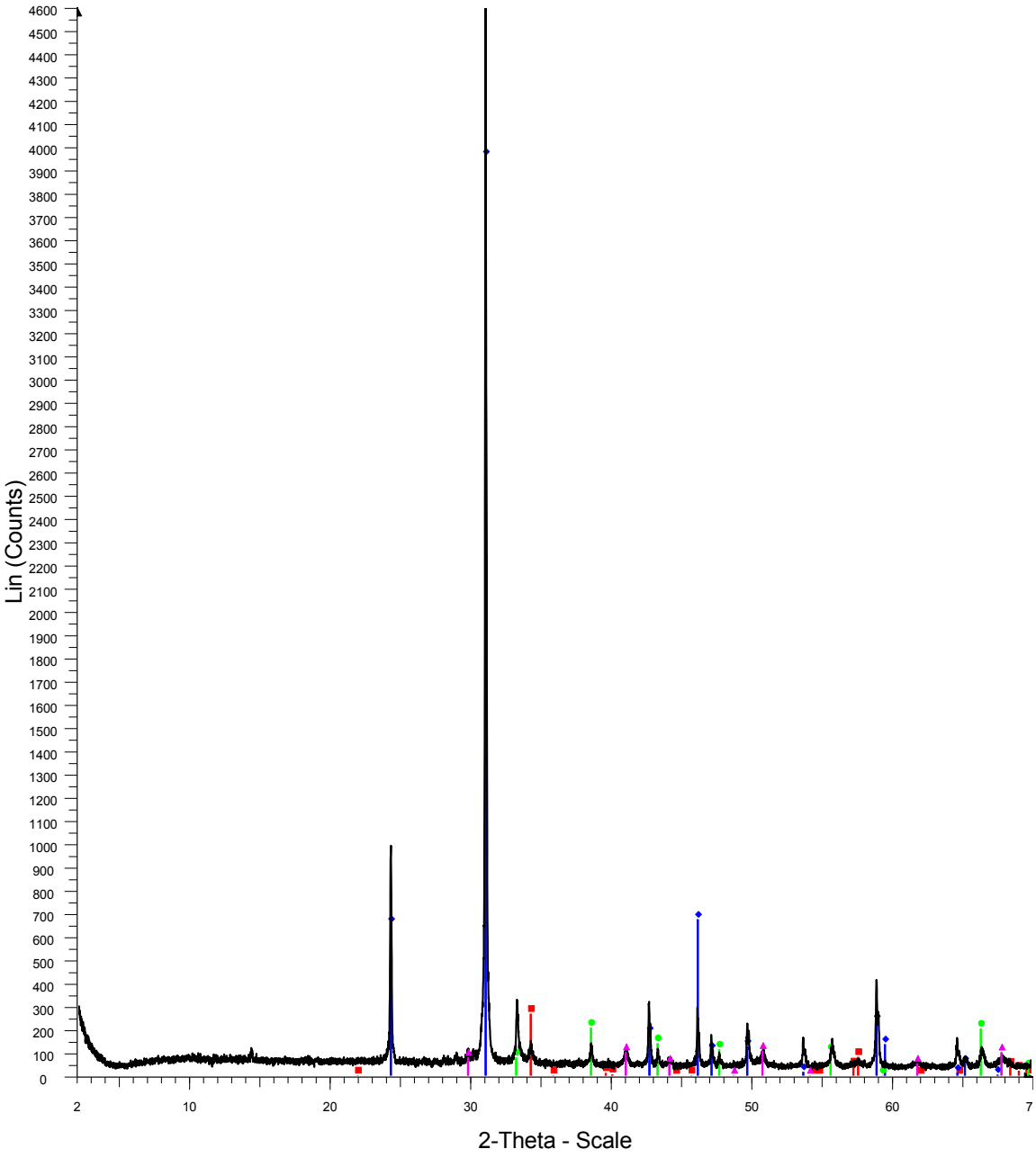

Red-Chalcopyrite
Blue- Quartz
Green-Pyrite
Pink-Corundum
-81vein1

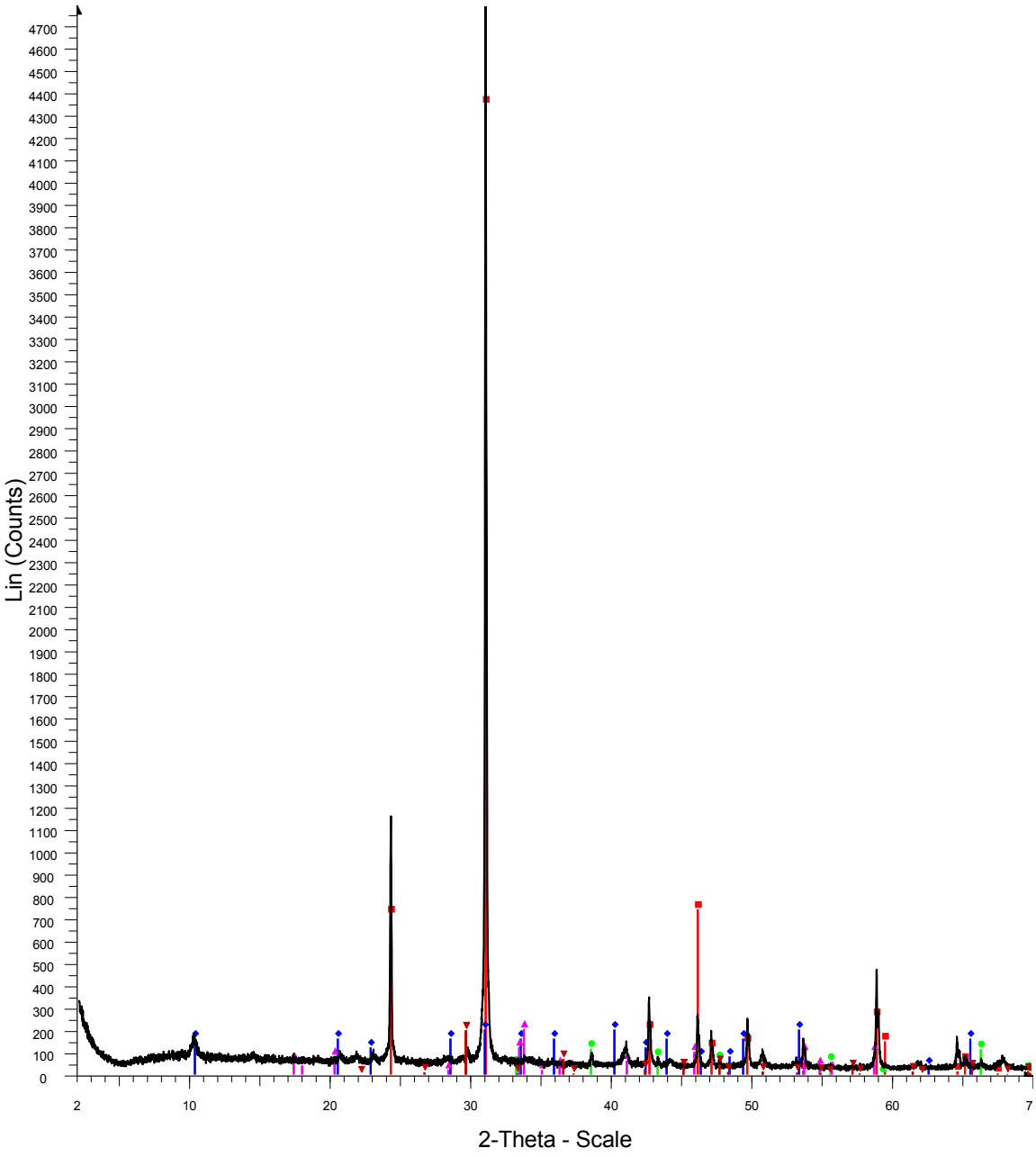

Red-Quartz
Blue- Illite
Green-Pyrite
Pink-Jarosite
Dark red-Anhydrite
-82host

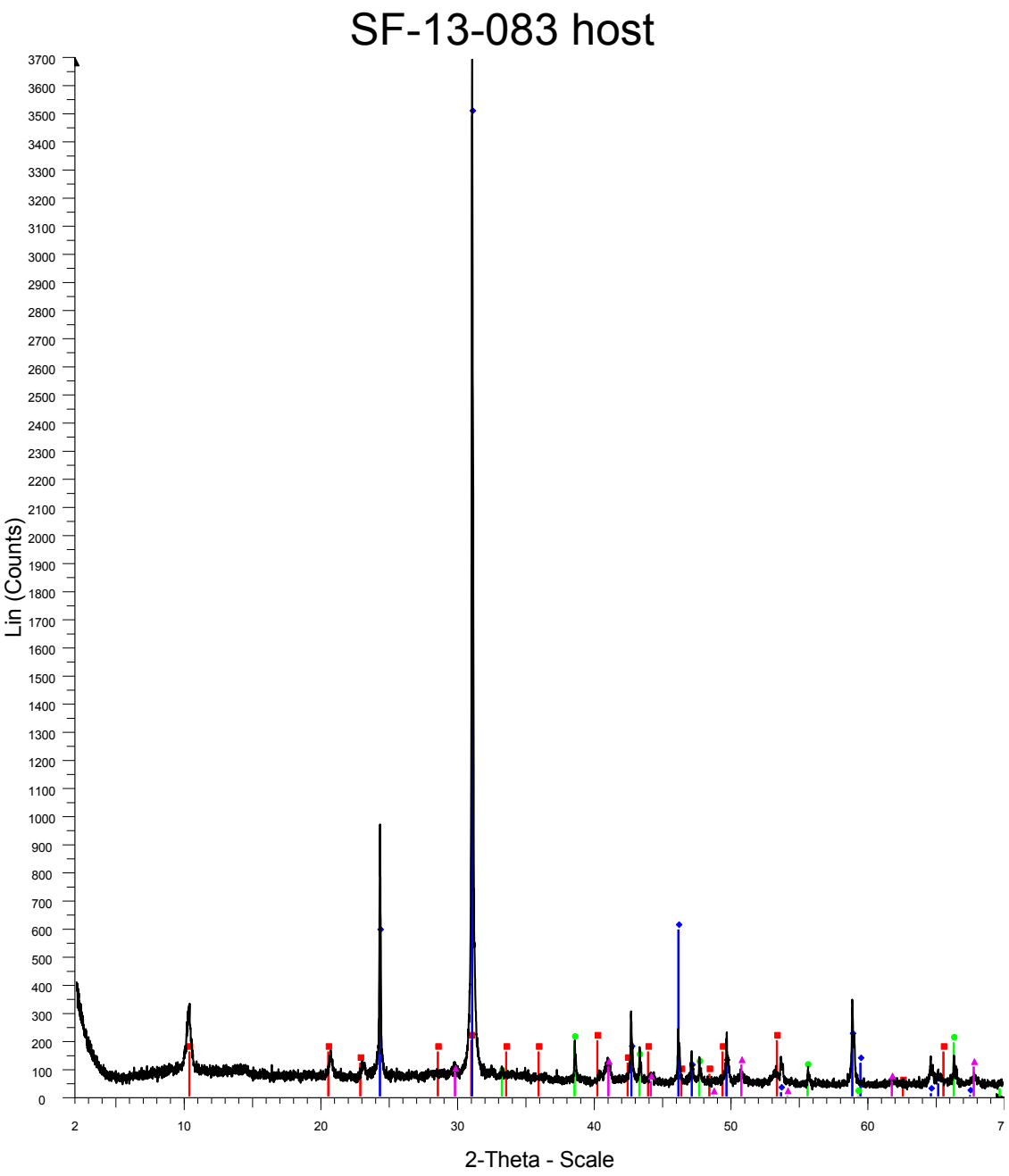

Red-Illite
Blue-Quartz
Green-Pyrite
Pink-Corundum

-83 host

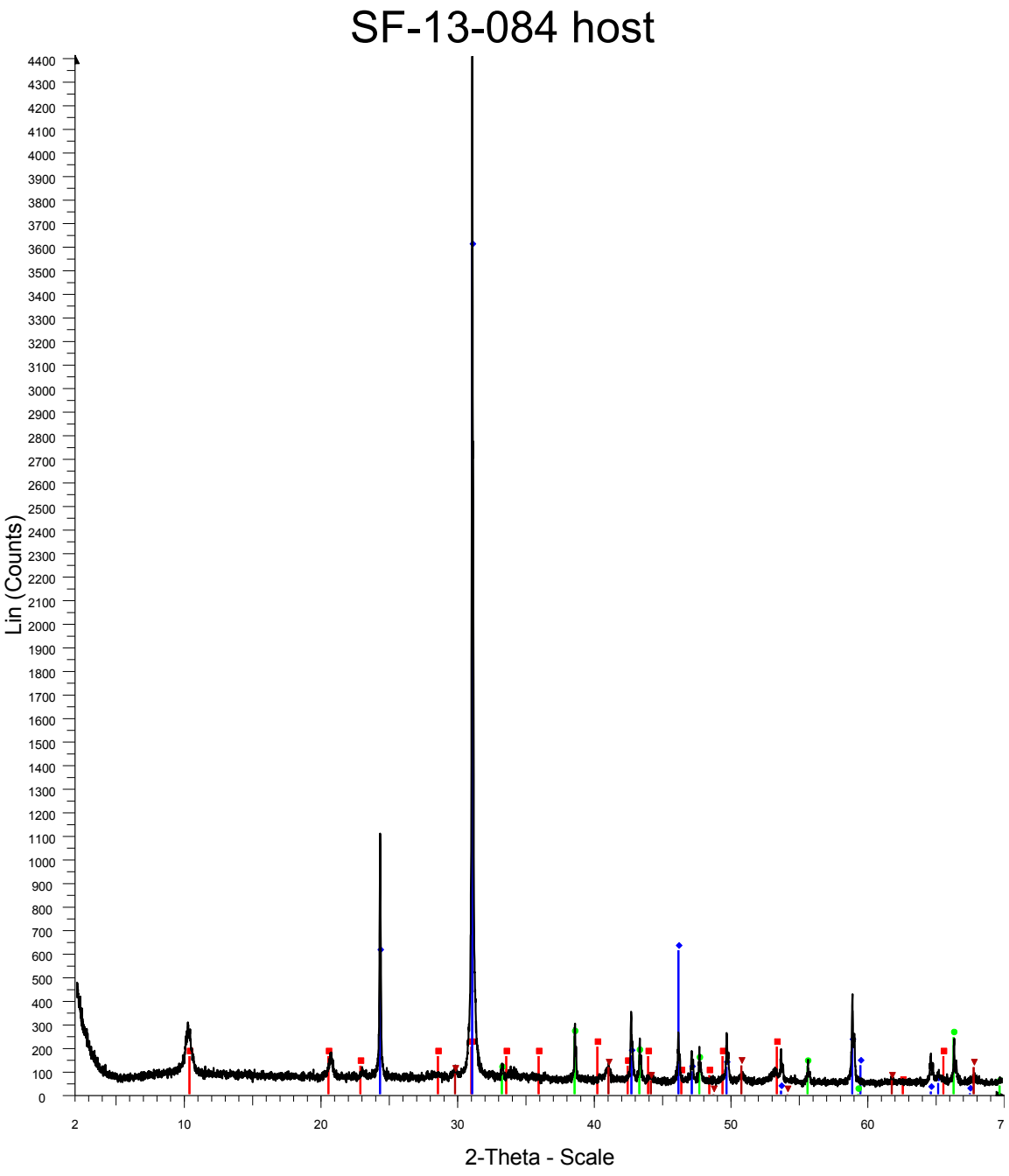

Red-Illite
Blue-Quartz
Green-Pyrite
Dark Red-Corundum

-84 host

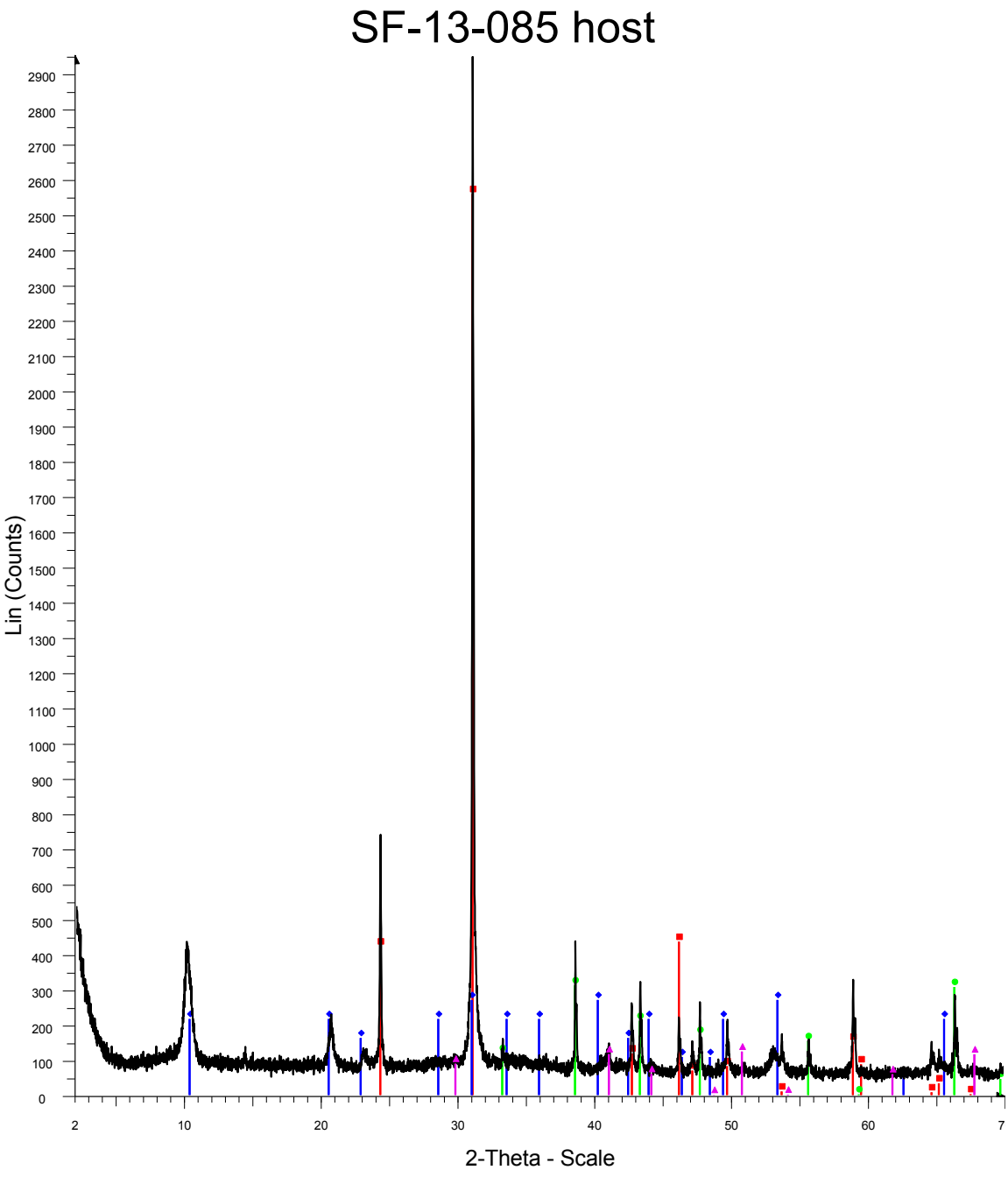

Red-Quartz
Blue- Illite
Green-Pyrite
Pink-Corundum

-85 host

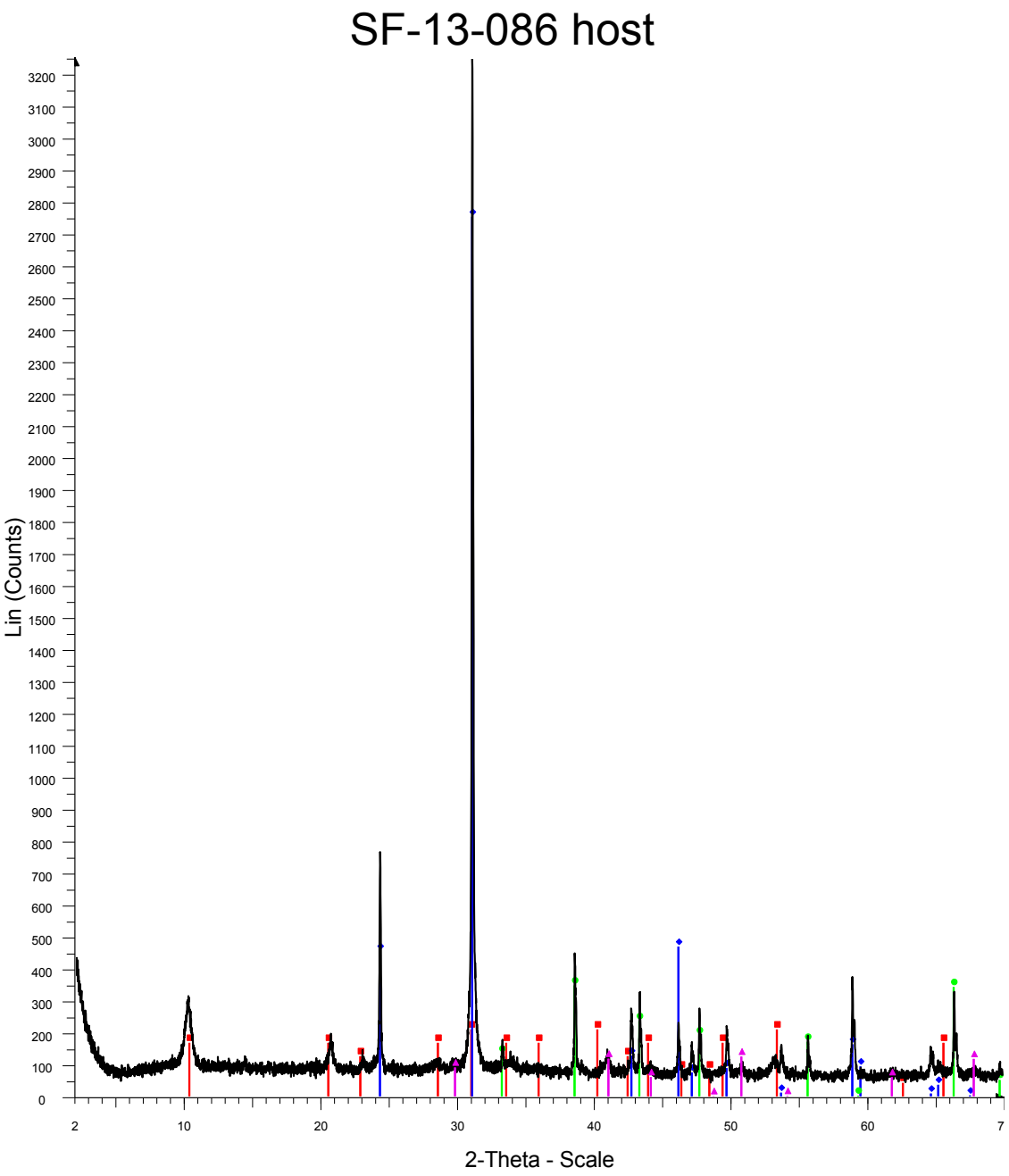

Red- Illite
Blue- Quartz
Green-Pyrite
Pink-Corundum

-86 host

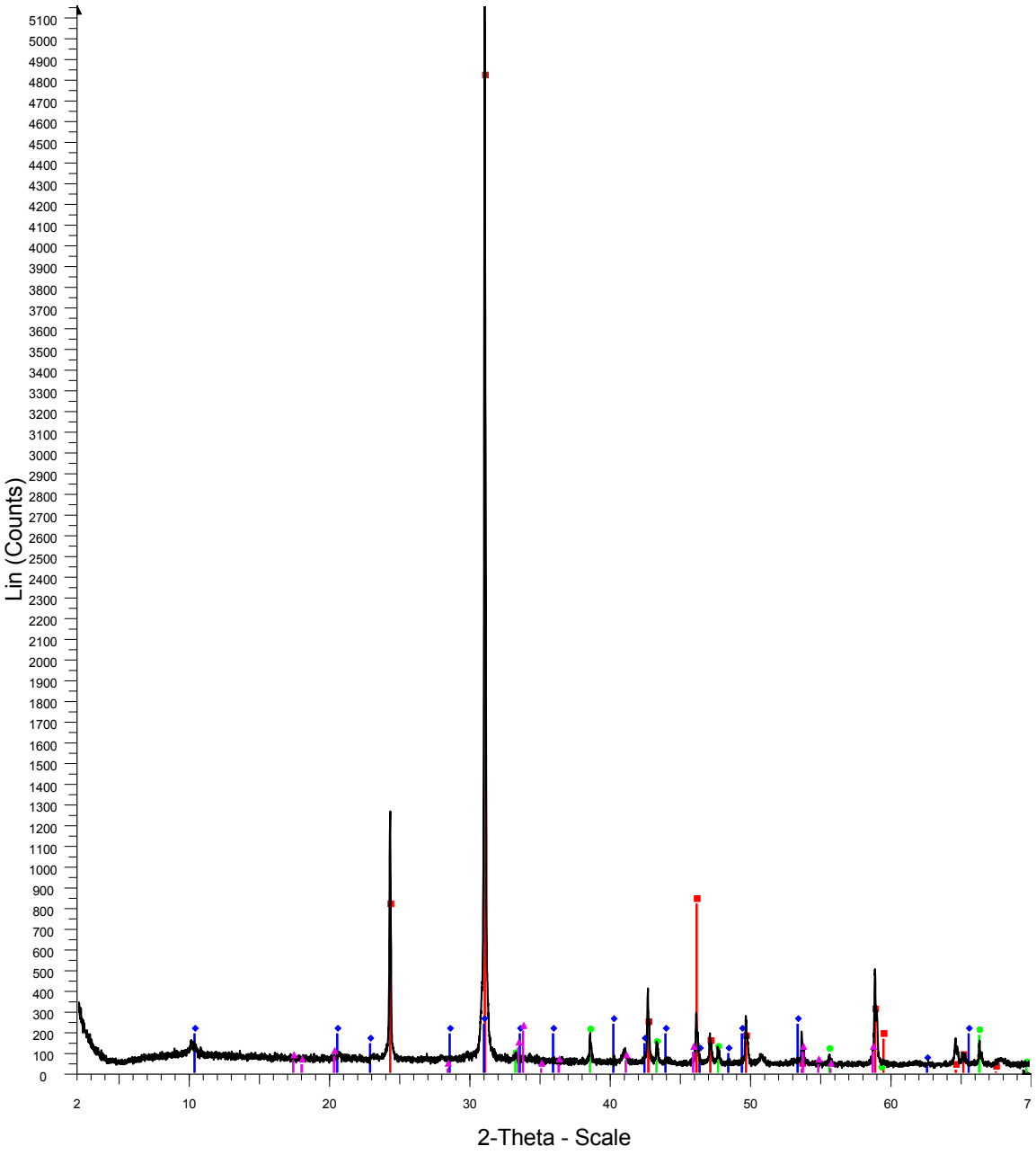

Red-Quartz
Blue- Illite
Green-Pyrite
Pink-Jarosite

-87 host

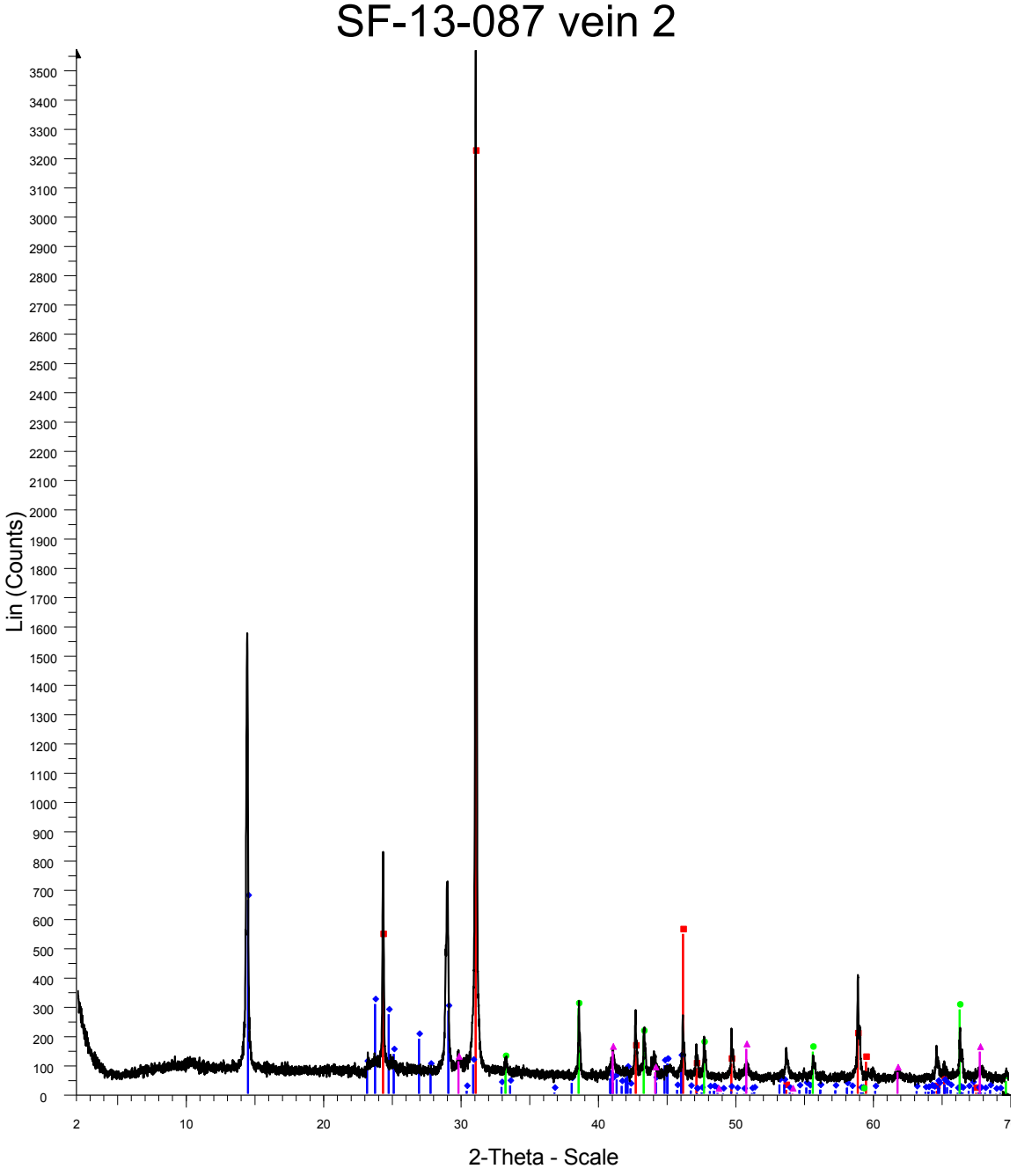

Red- Quartz
Blue- Kaolinite
Green-Pyrite
Pink-Corundum

-87 vein2

SF-13-091

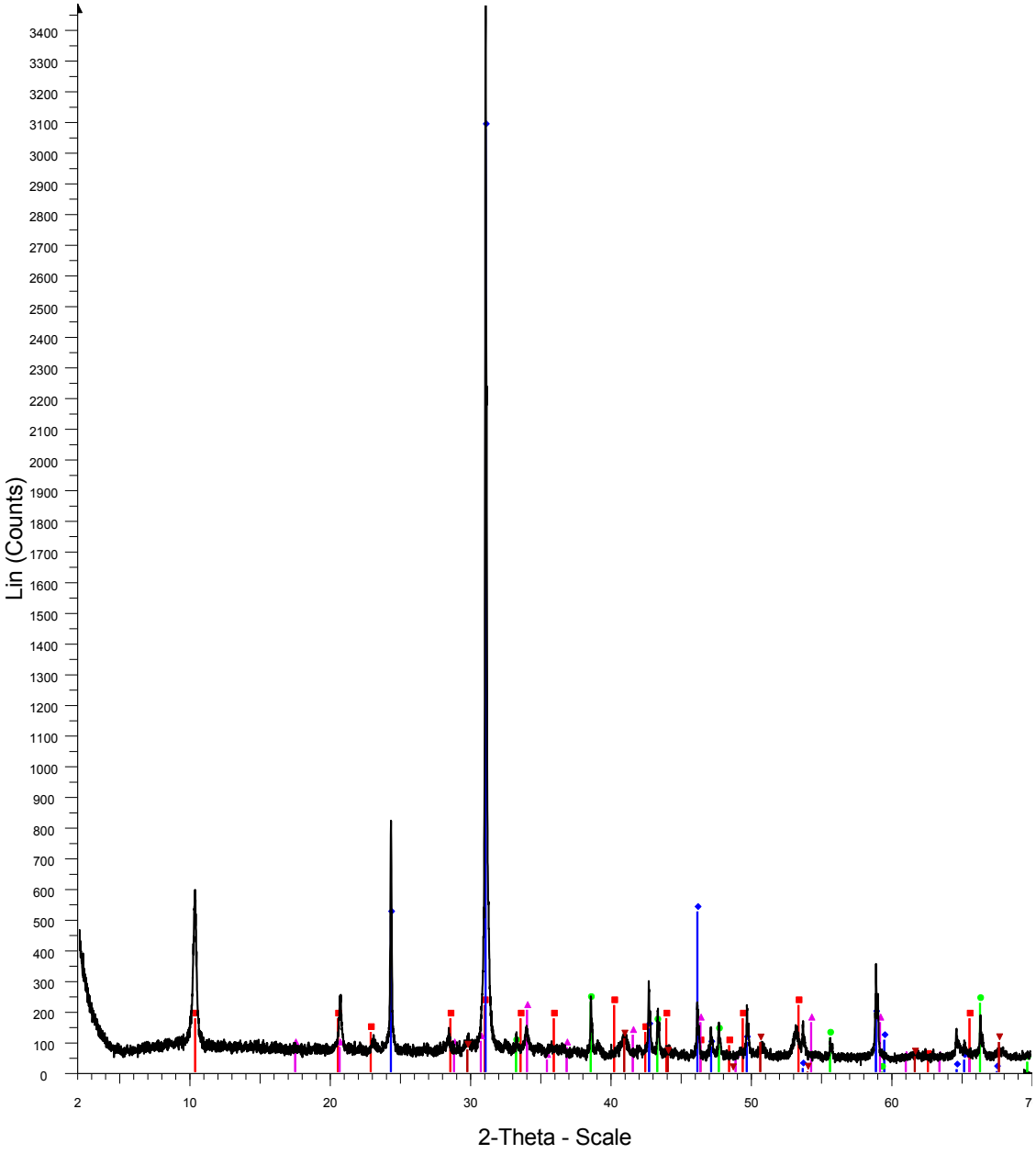

Red-Illite
Blue-Quartz
Green-Pyrite
Pink-Jarosite
Dark Red-Corundum

-91

SF-13-092

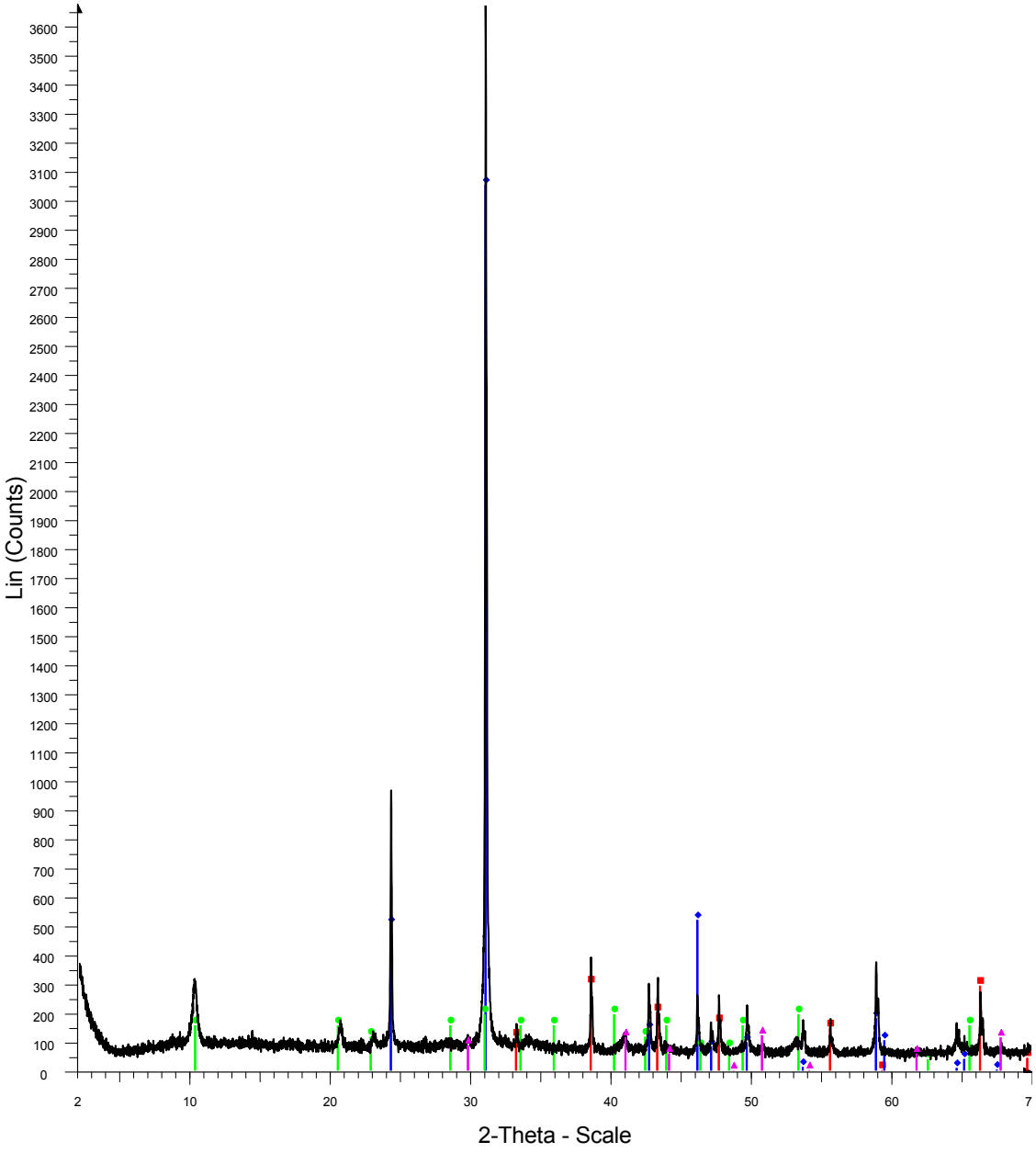

Red-Pyrite
Blue-Quartz
Green-Illite
Pink-Corundum

-92

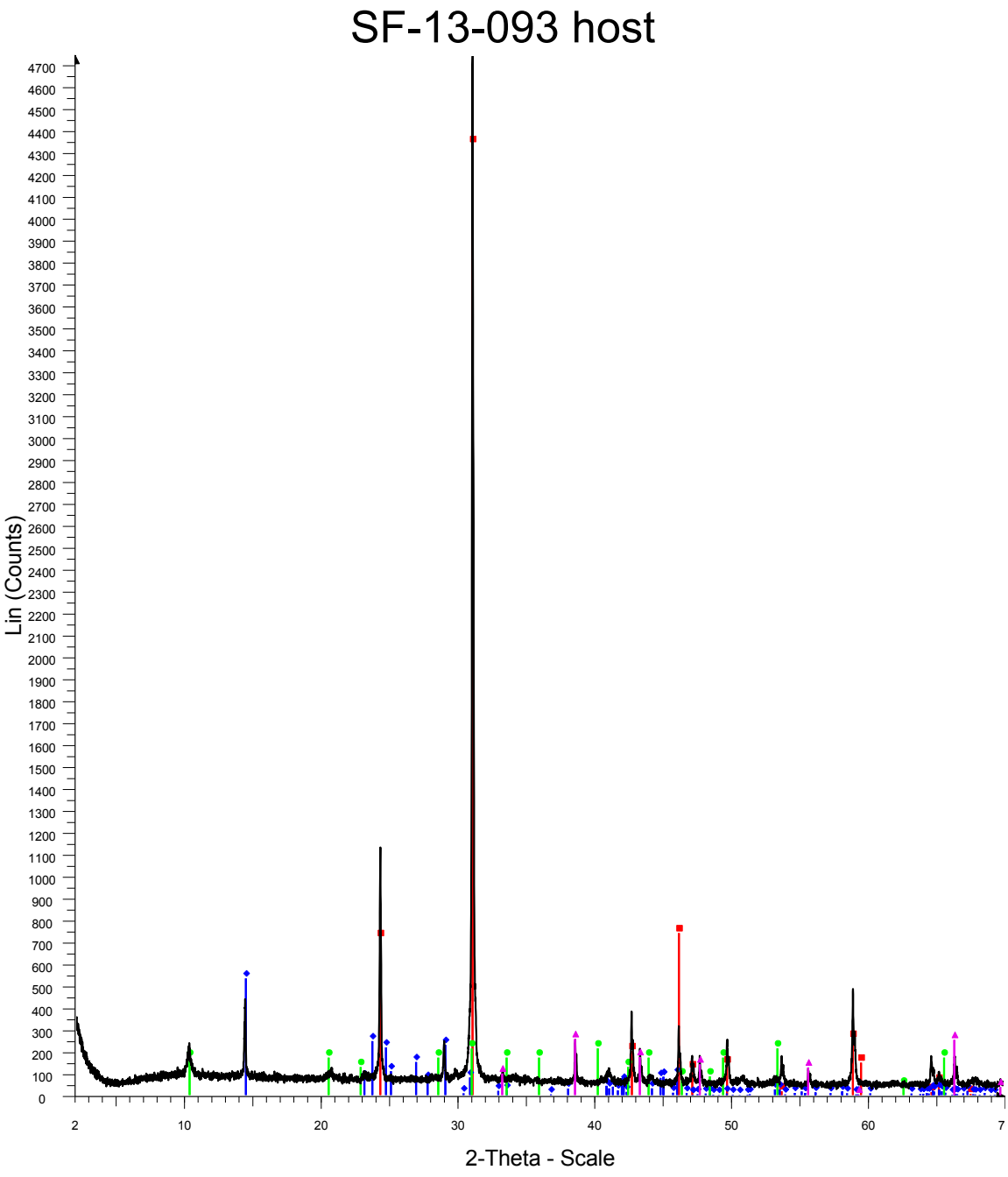

Red-Quartz
Blue-Kaolinite
Green-Illite
Pink-Pyrite

-93 host

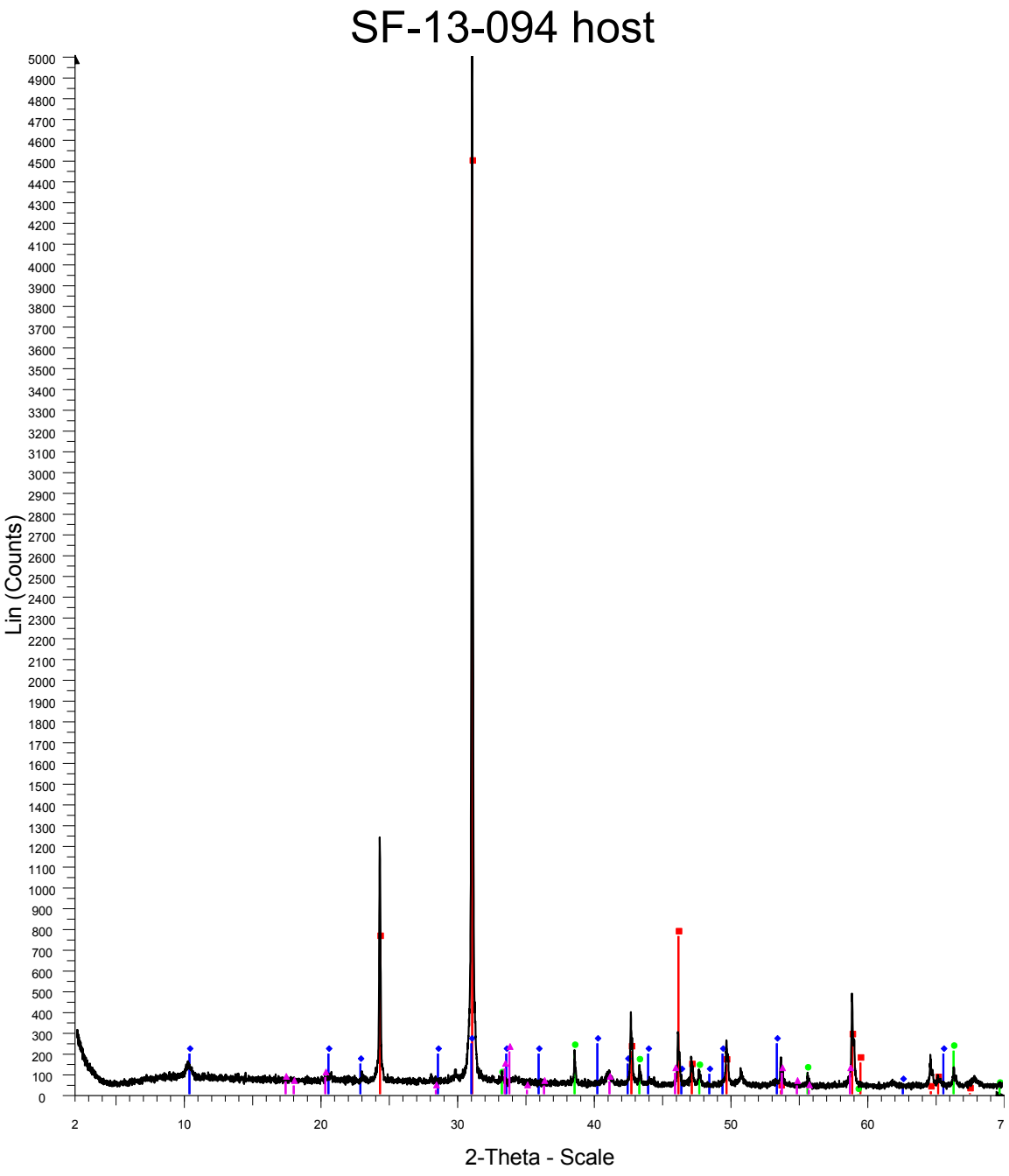

Red-Quartz
Blue-Illite
Green-Pyrite
Pink-Jarosite

-94 host

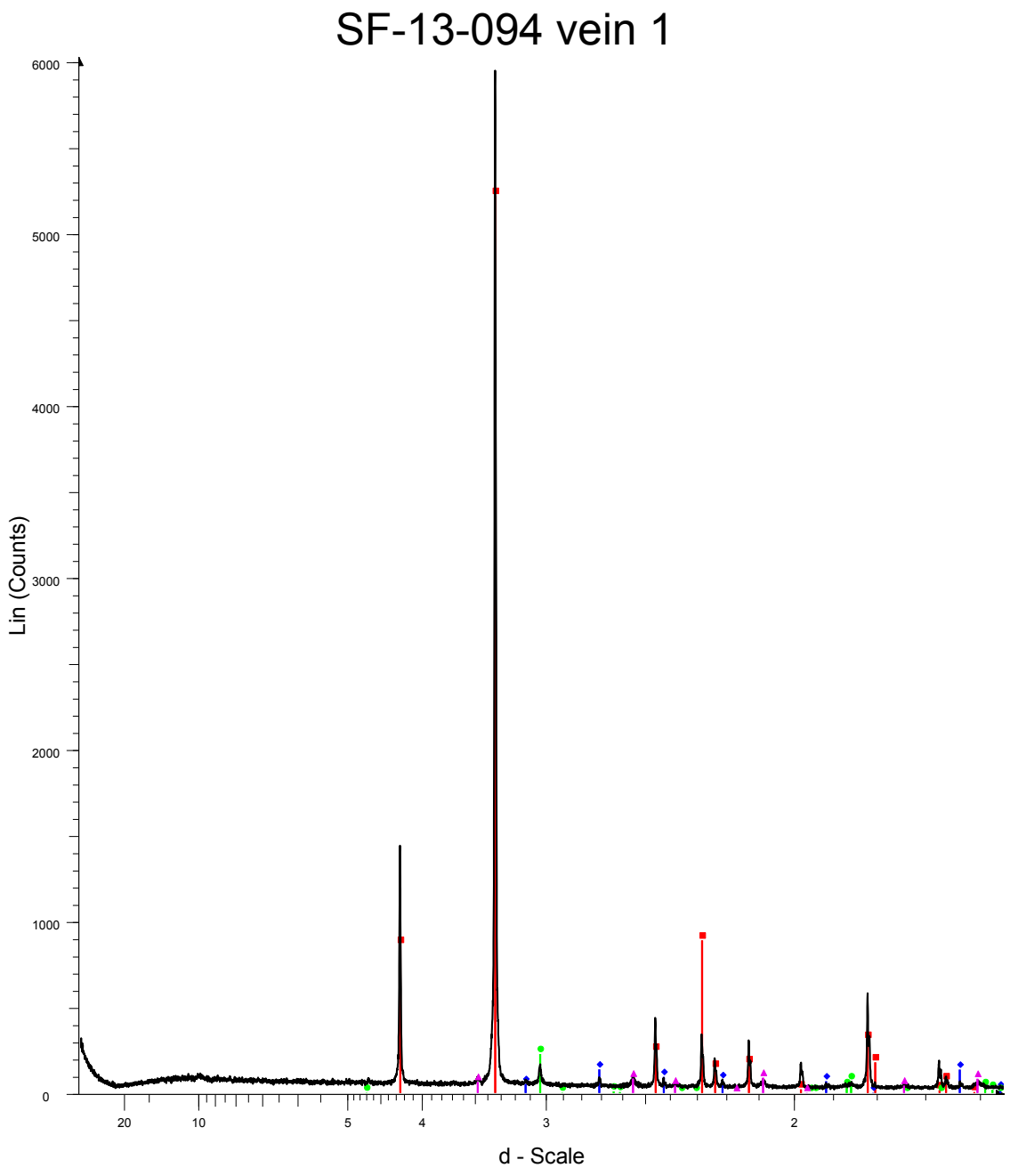

Red-Quartz
Blue-Pyrite
Green-Chalcopyrite
Pink-Corundum

-94 vein1

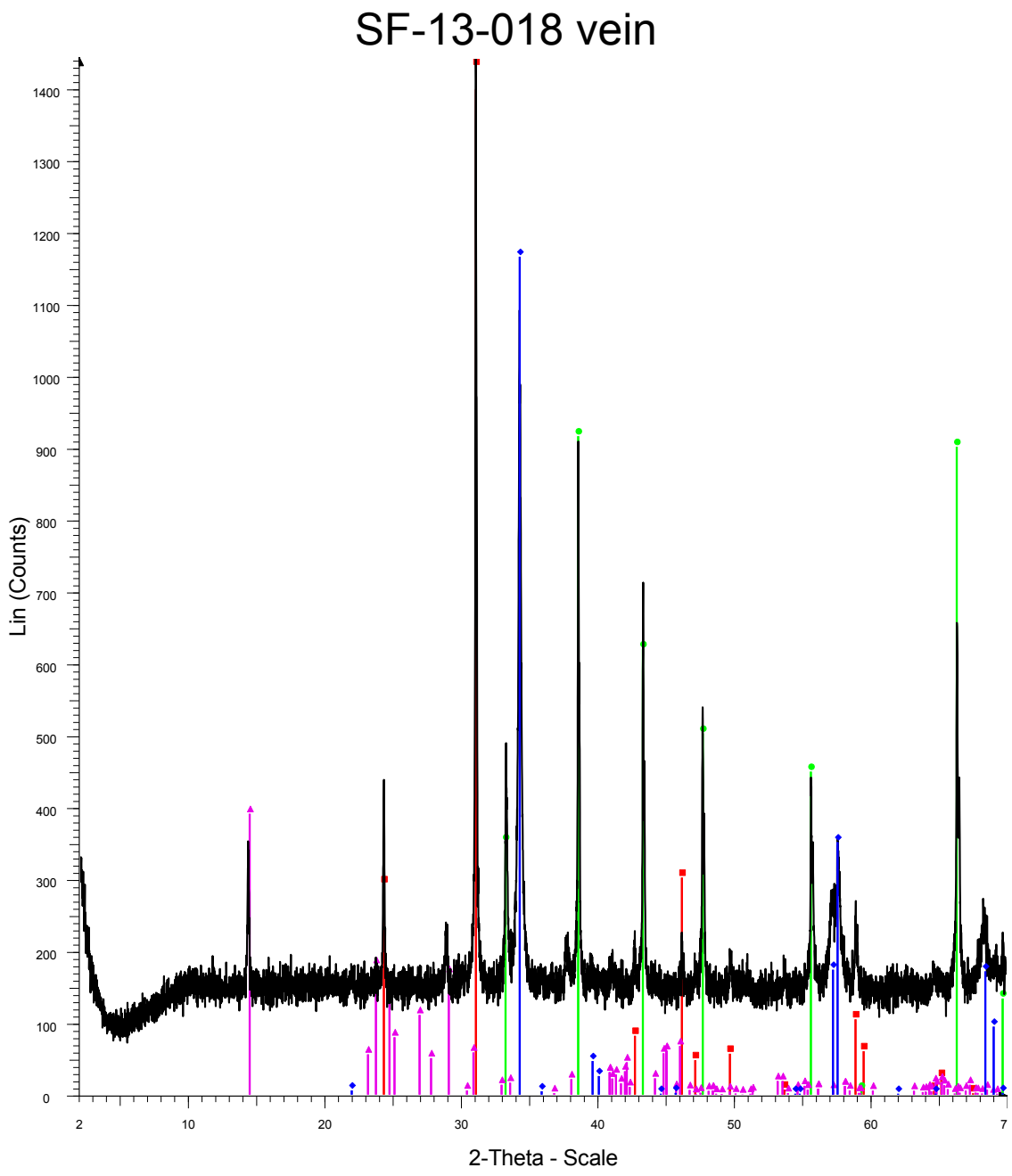

Red-Quartz
Blue-Chalcopyrite
Green-Pyrite
Pink-Kaolinite

18vein

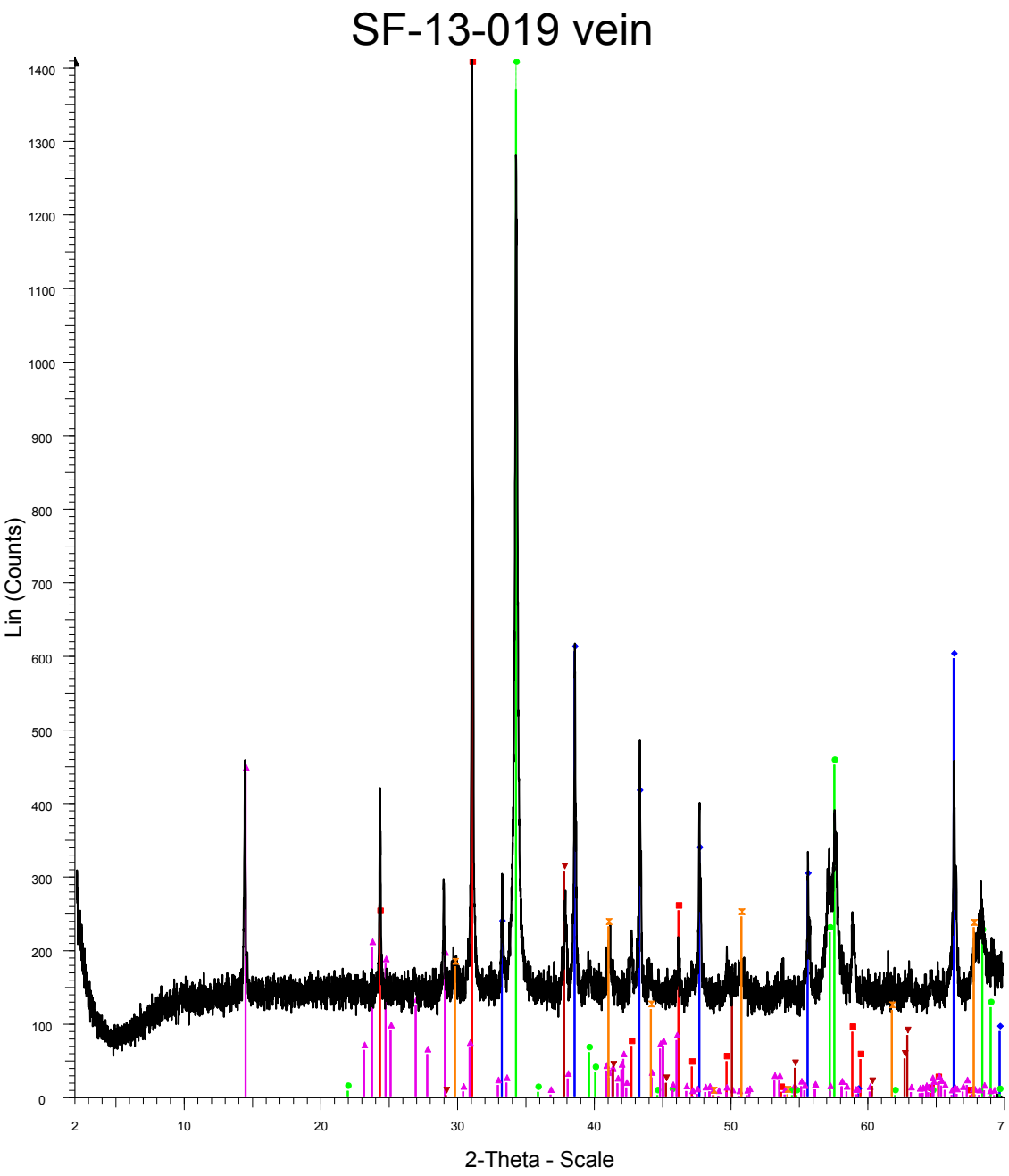

Red-Quartz
Blue-Pyrite
Green-Chalcopyrite
Pink-Kaolinite
Dark red-Magnesite
Orange-Corundum

19vein

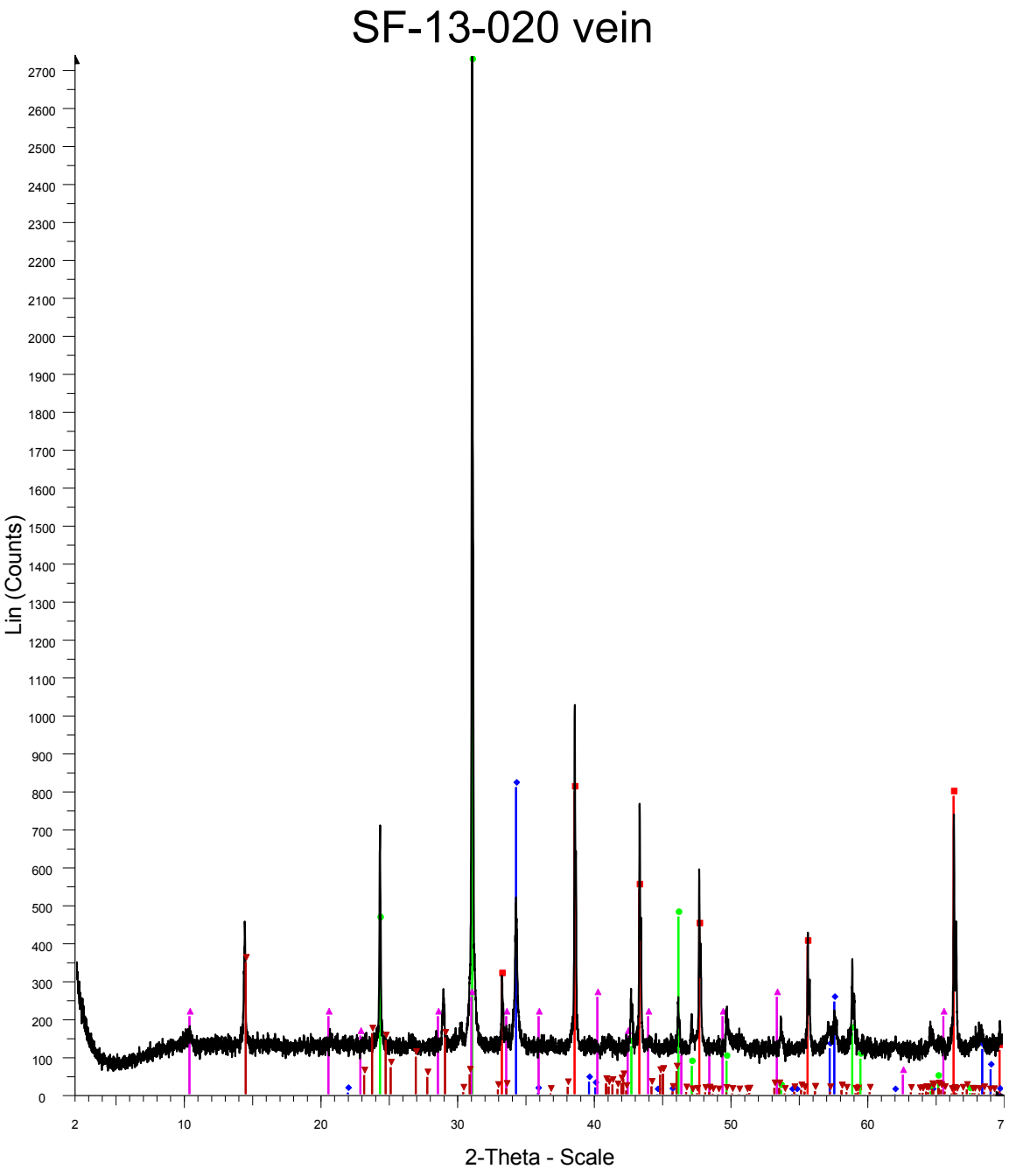

Red-Pyrite
Blue-Chalcopyrite
Green-Quartz
Pink-Illite
Dark red-Kaolinite

20vein

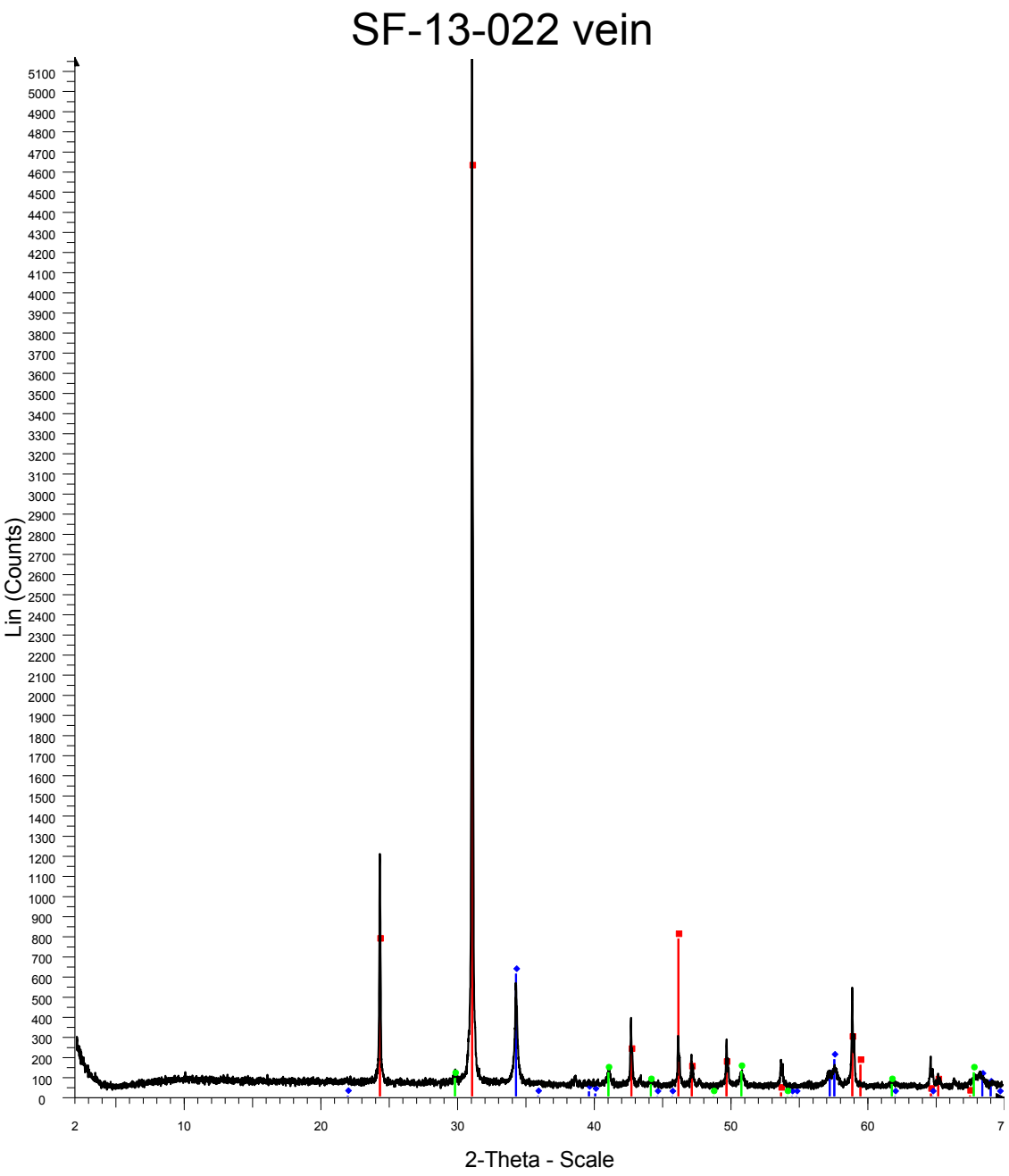

Red-Quartz
Blue-Chalcopyrite
Green-Corundum

22vein

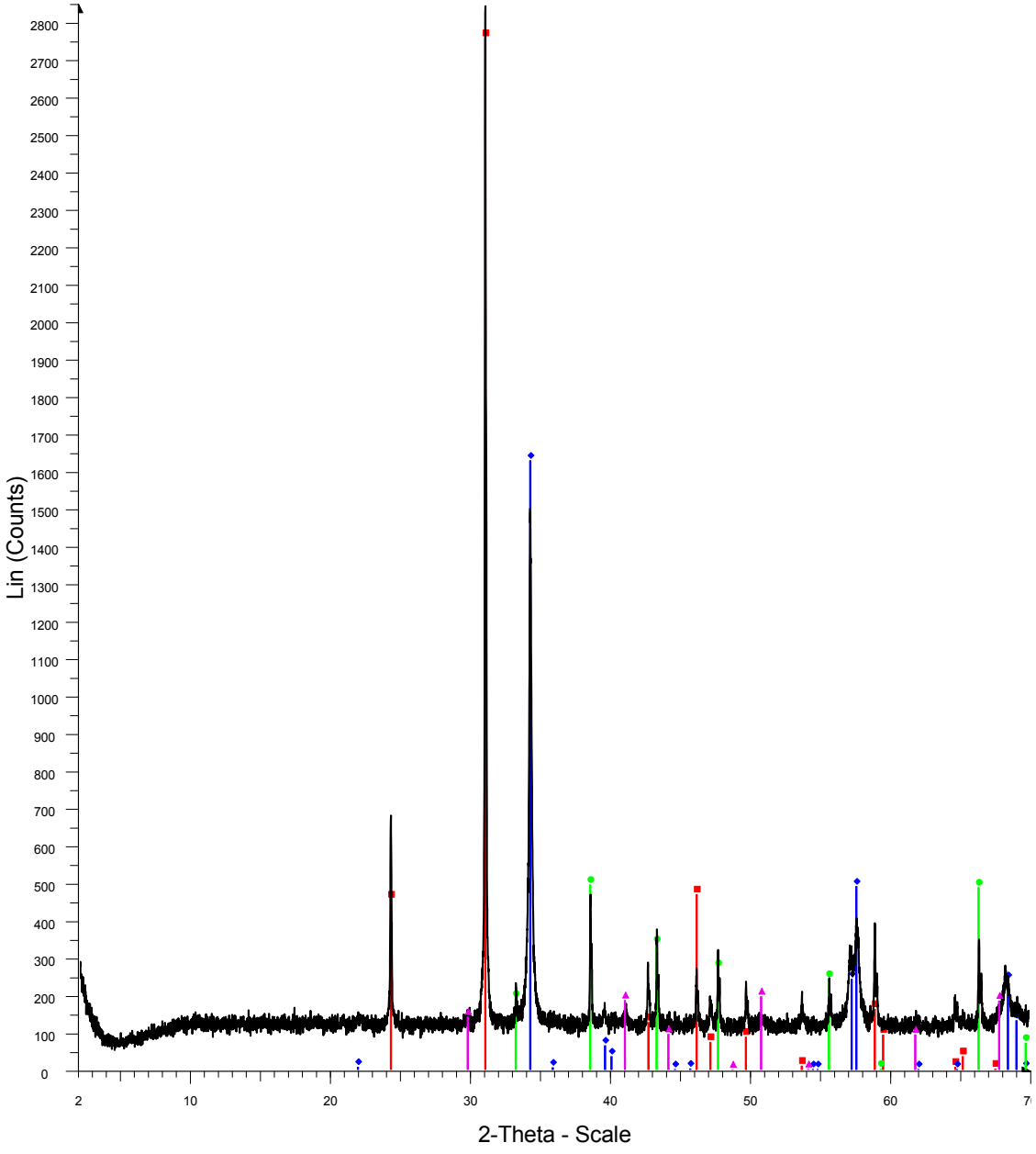

Red-Quartz
Blue-Chalcopyrite
Green-Pyrite
Pink-Corundum

23vein

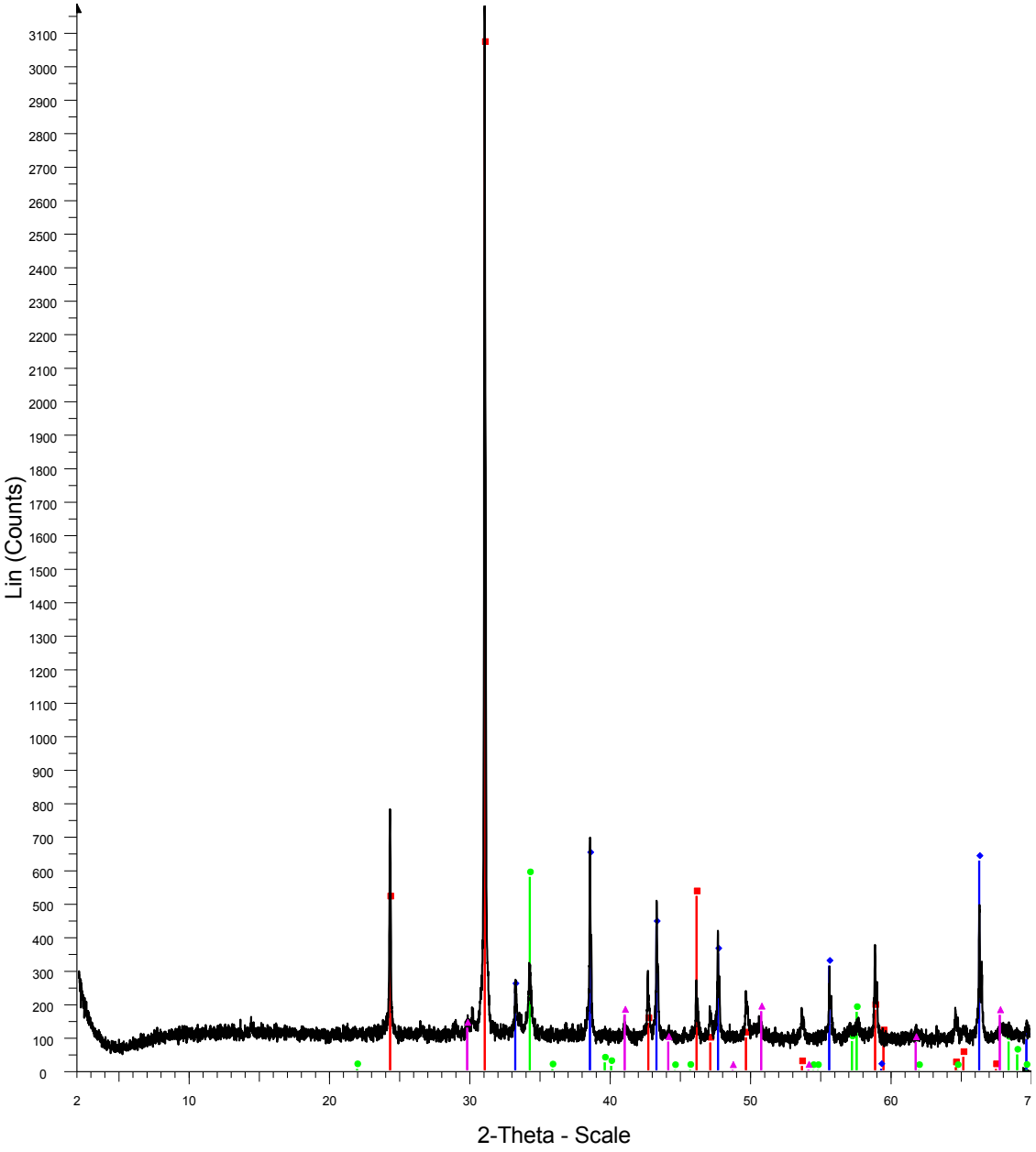

Red-Quartz
Blue-Pyrite
Green-Chalcopyrite
Pink-Corundum

33vein2

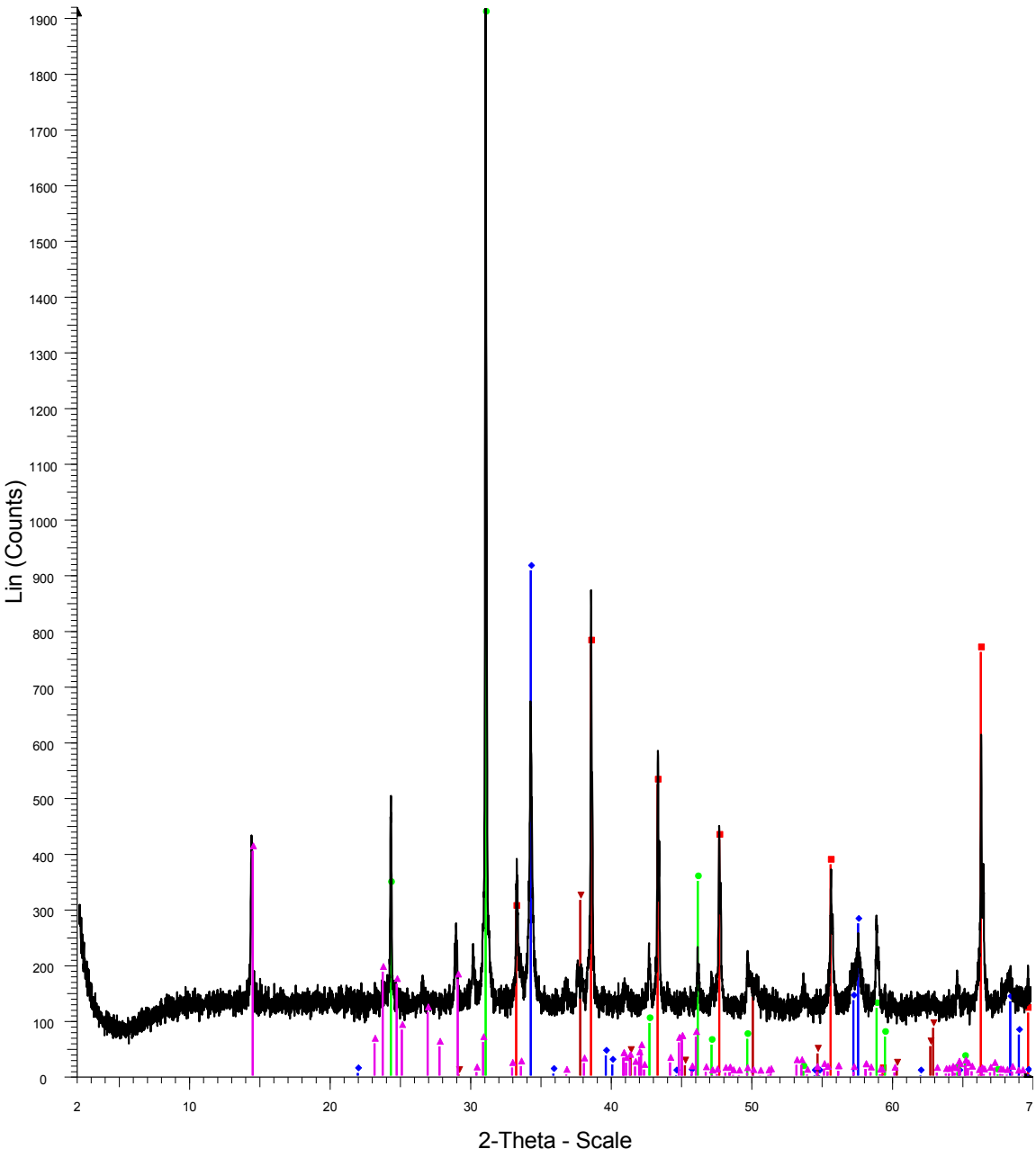

Red-Pyrite
Blue-Chalcopyrite
Green-Quartz
Pink-Kaolinite
Dark red-Magnesite

34vein

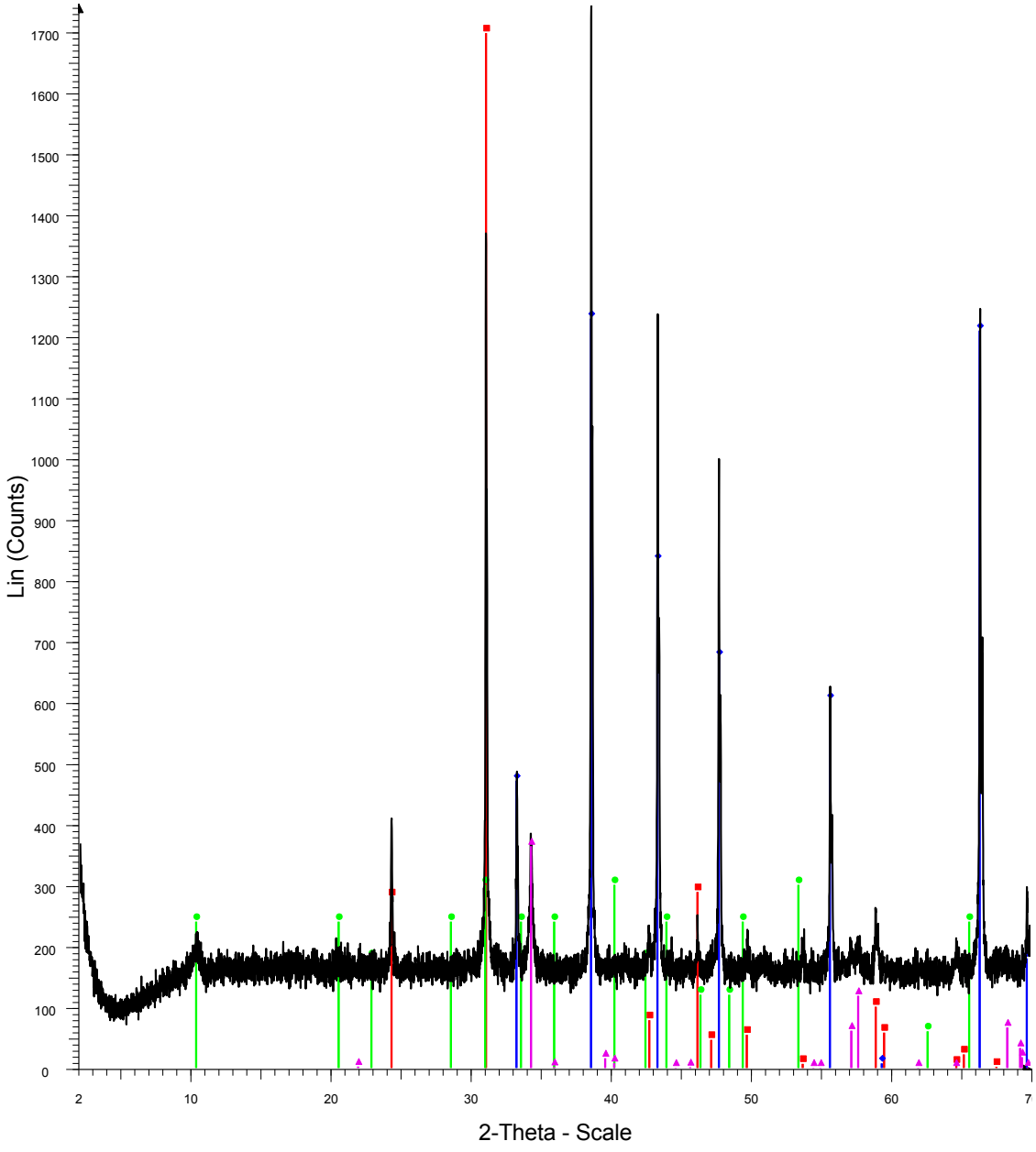

Red-Quartz
Blue-Pyrite
Green-Illite
Pink-Chalcopyrite

35

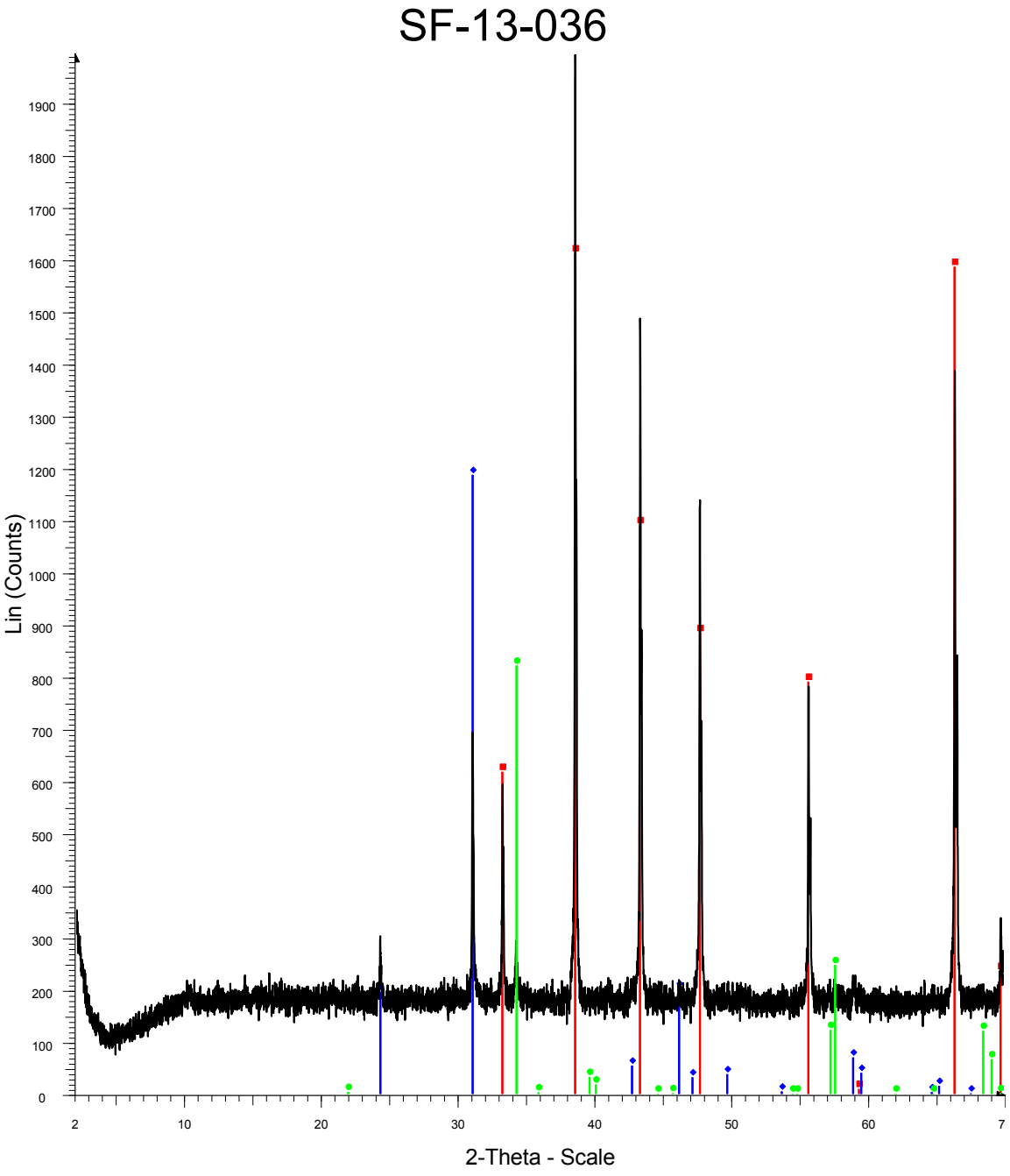

Red-Pyrite
Blue-Quartz
Green-Chalcopyrite

36

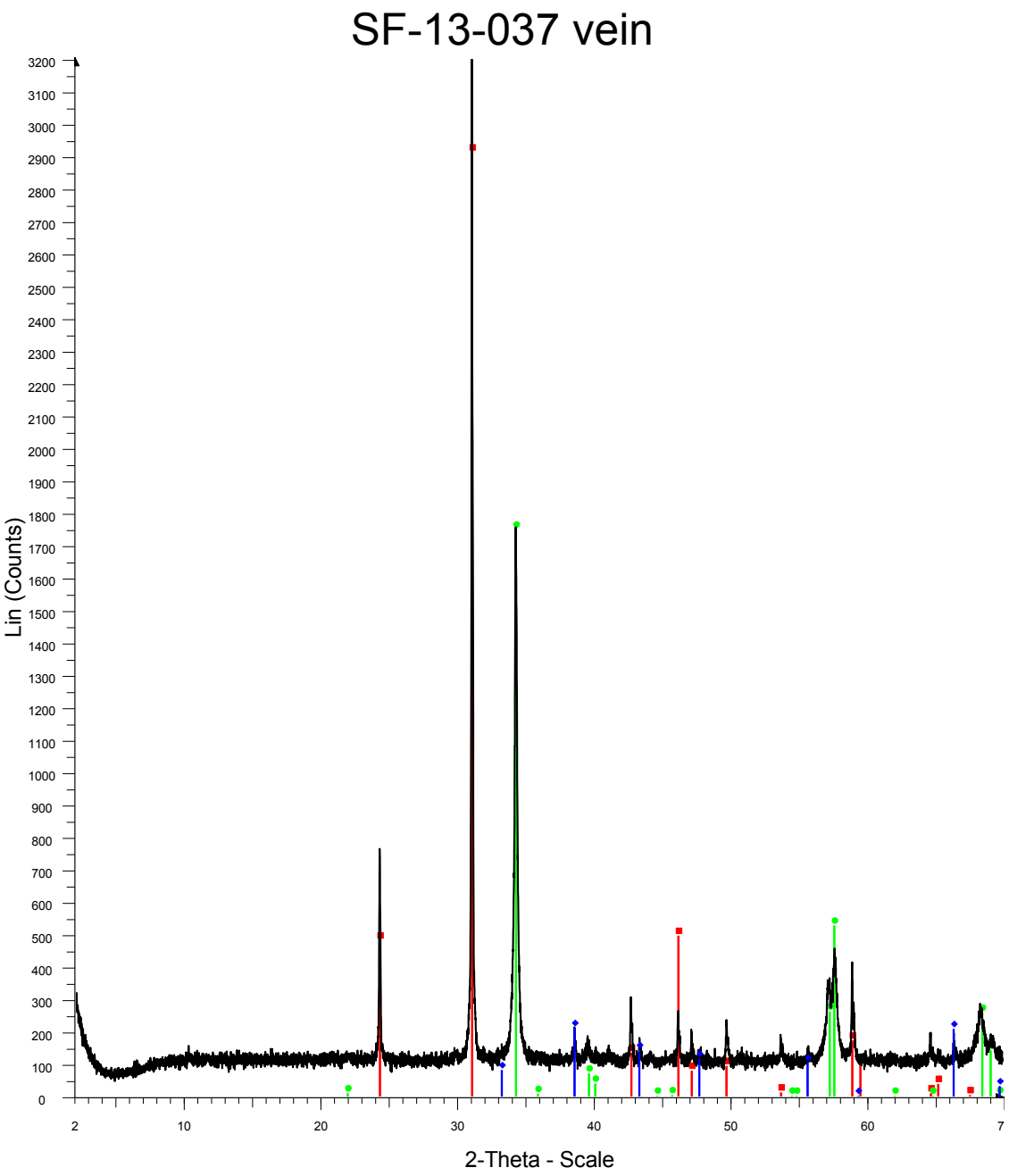

Red-Quartz
Blue-Pyrite
Green-Chalcopyrite

37vein

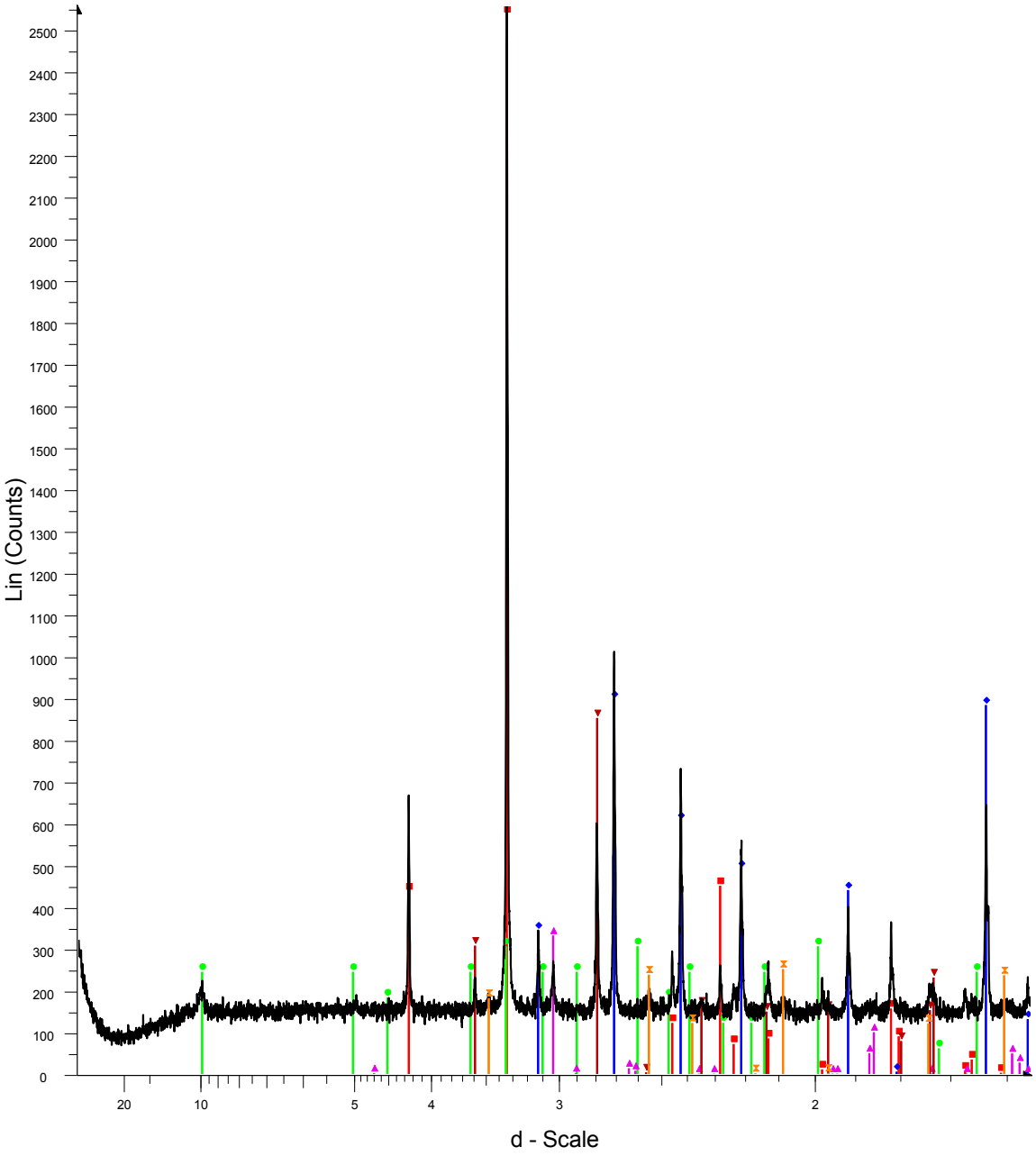

Red-Quartz
Blue-Pyrite
Green-Illite
Pink-Chalcopyrite
Dark red-Siderite
Orange-Corundum
38vein

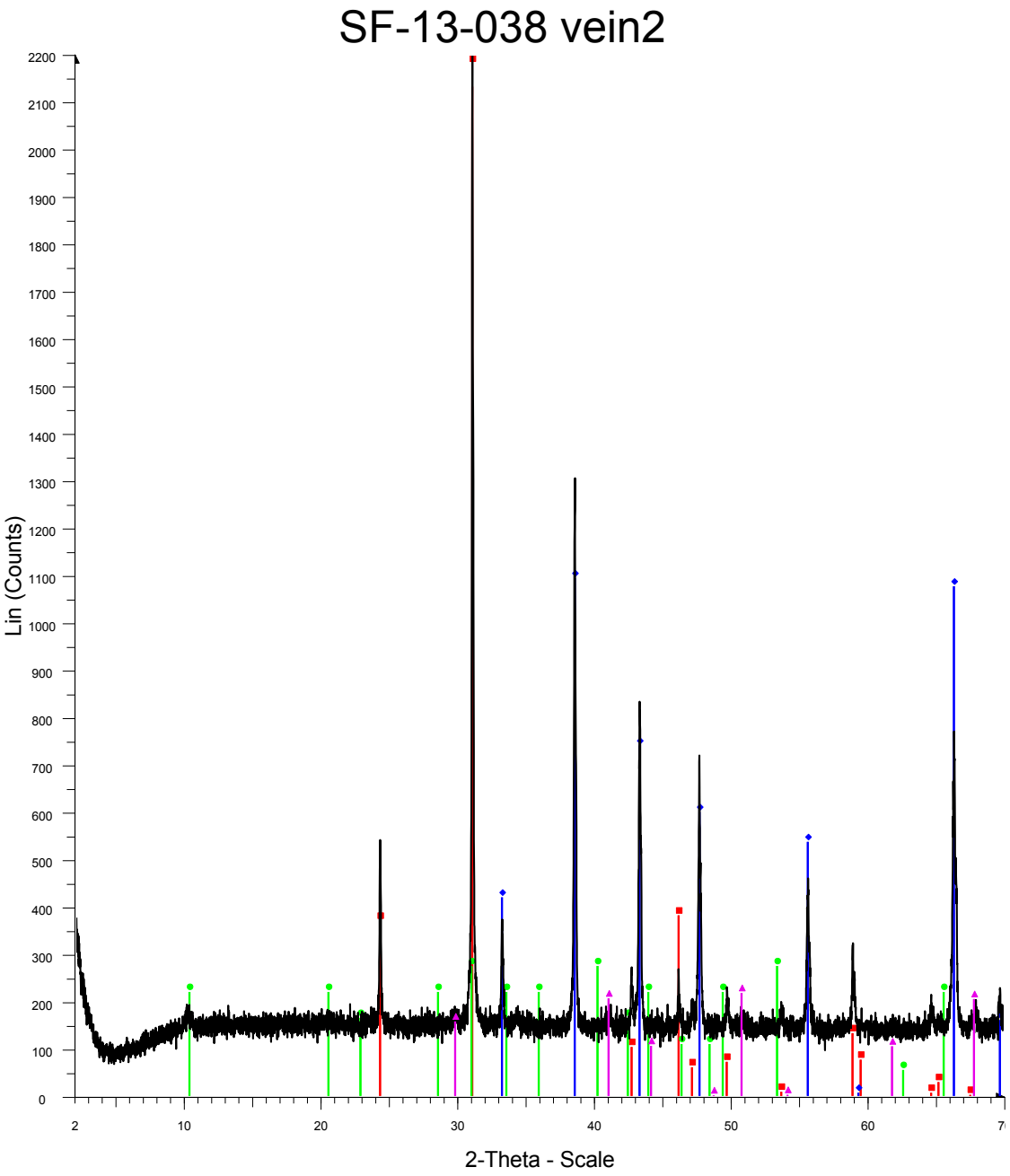

Red-Quartz
Blue-Pyrite
Green-Illite
Pink-Corundum

38vein2

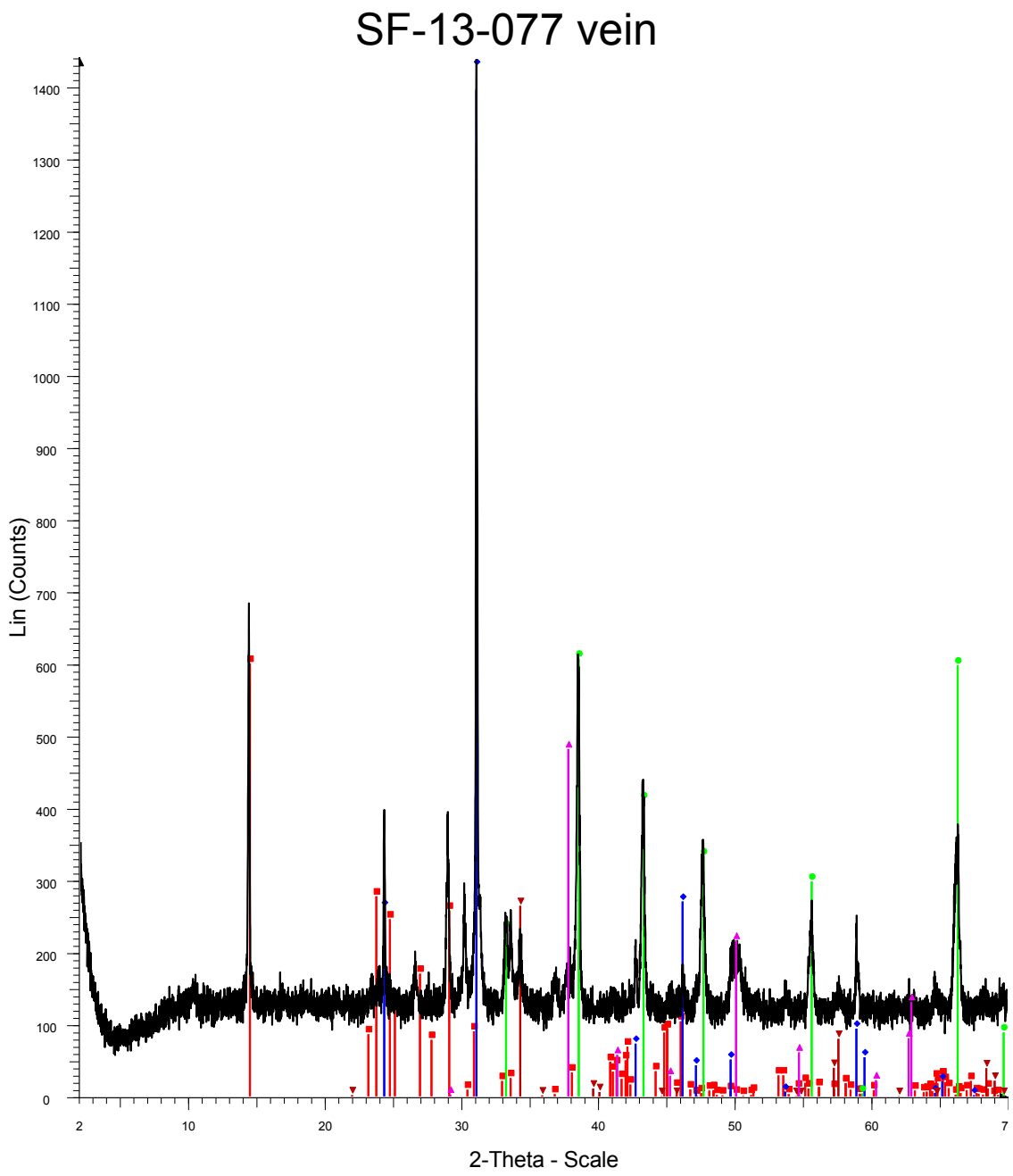

Red-Kaolinite
Blue-Quartz
Green-Pyrite
Dark red-Chalcopyrite
Pink-Magnesite

77vein

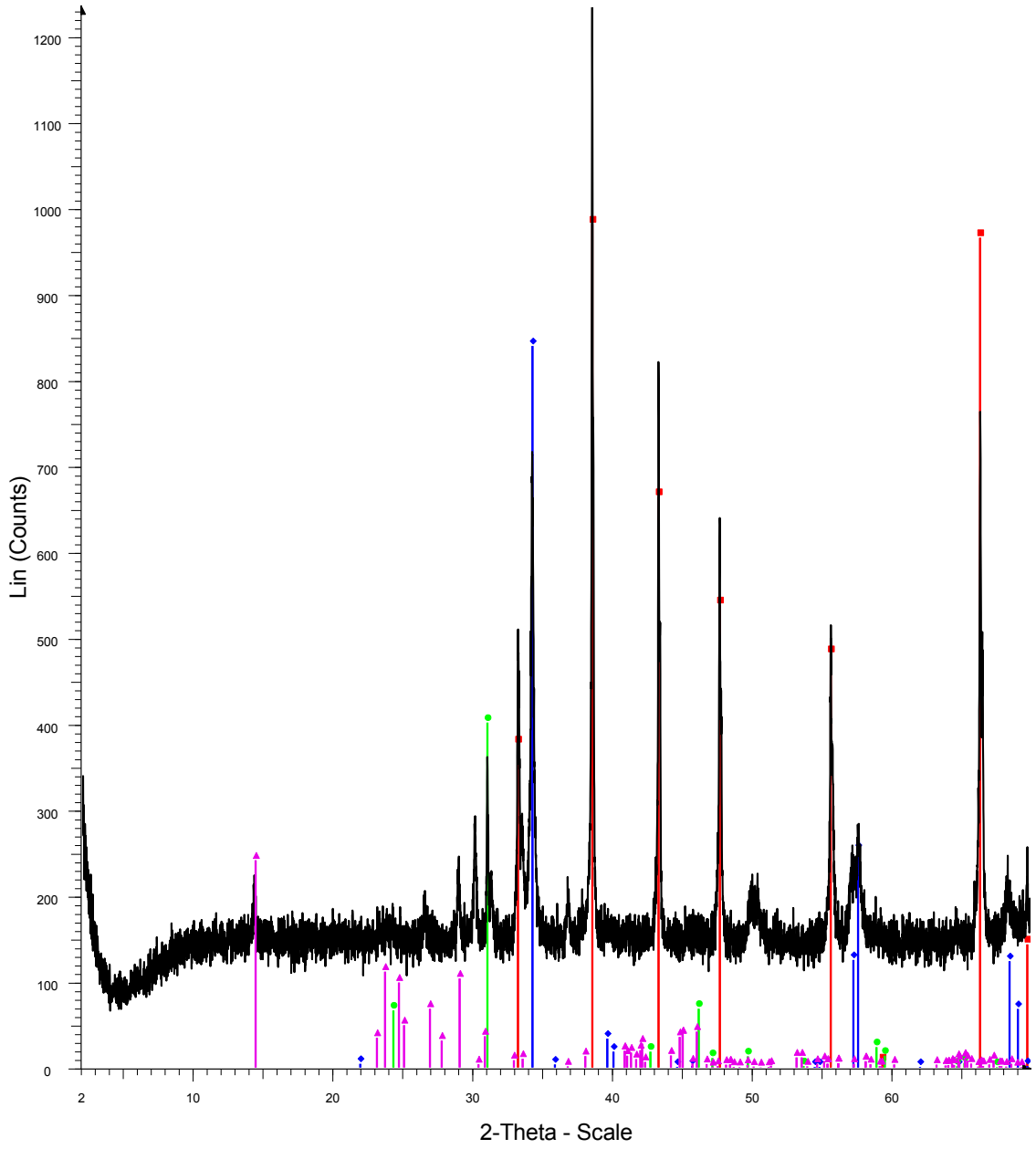

Red-Pyrite
Blue-Chalcopyrite
Green-Quartz
Pink-Kaolinite

78vein

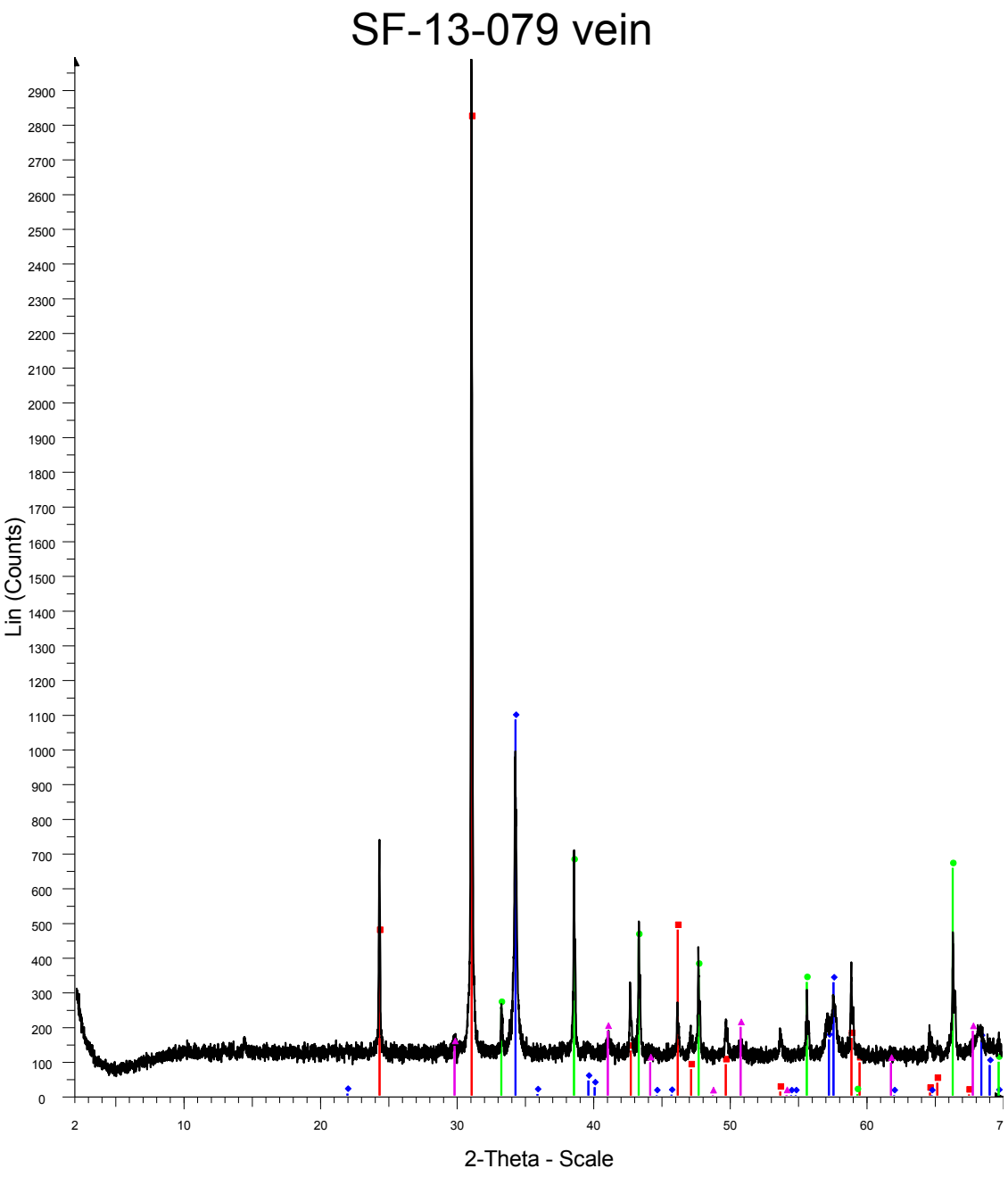

Red-Quartz
Blue-Chalcopyrite
Green-Pyrite
Pink-Corundum

79vein

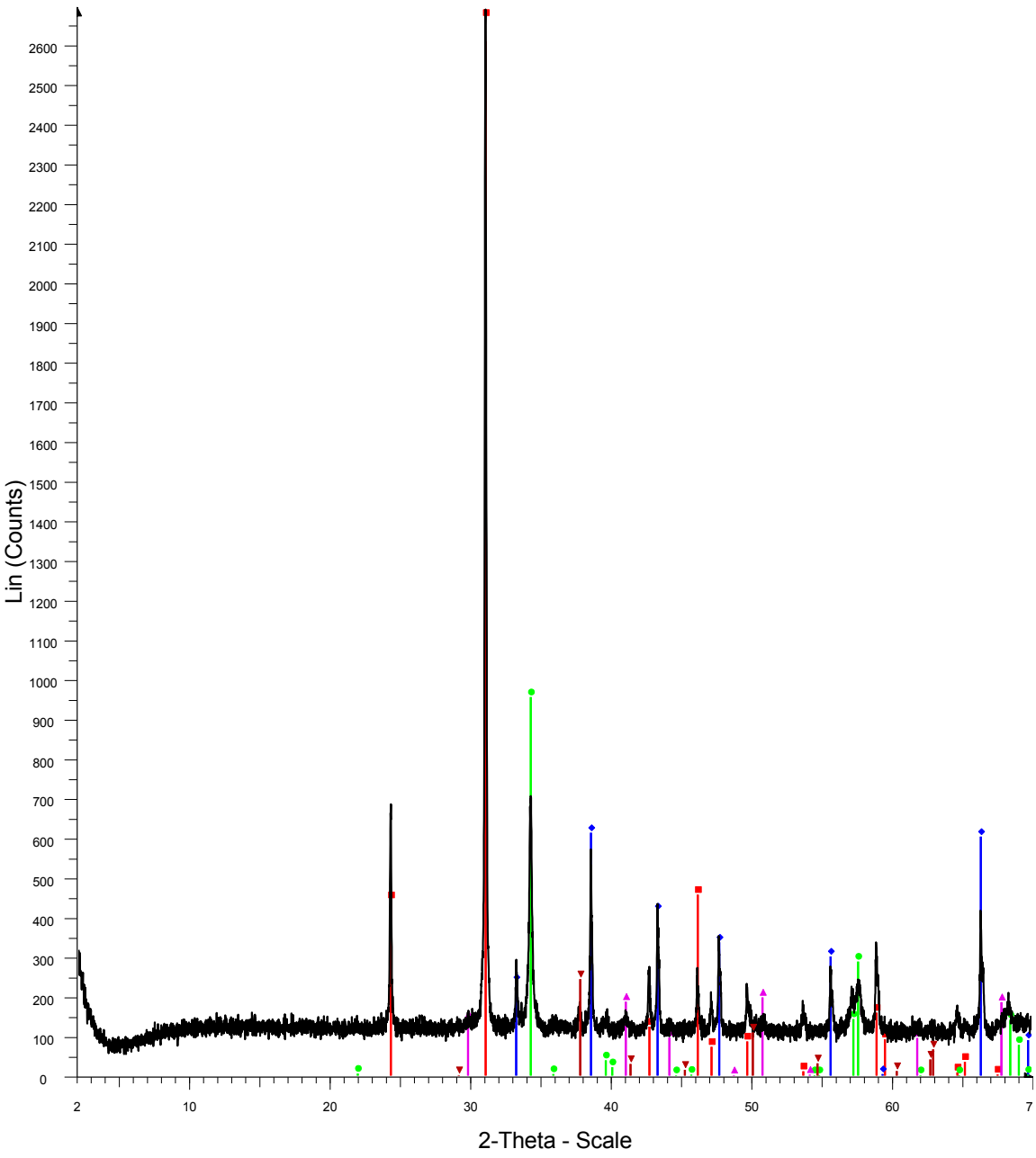

Red-Quartz
Blue-Pyrite
Green-Chalcopyrite
Pink-Corundum
Dark red-Magnesite

79vein2

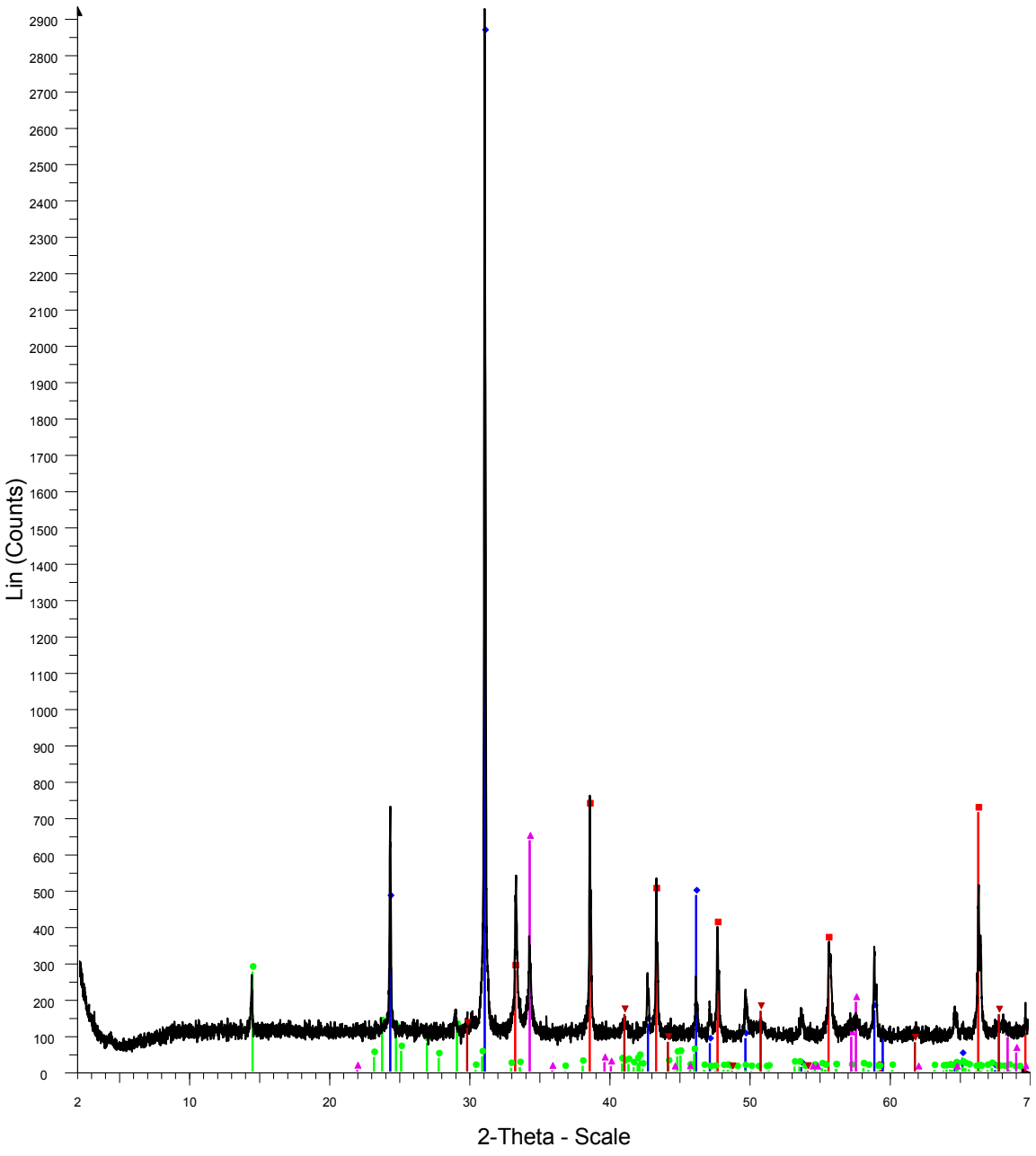

Red-Pyrite
Blue-Quartz
Green-Kaolinite
Pink-Chalcopyrite
Dark red-Corundum

80vein

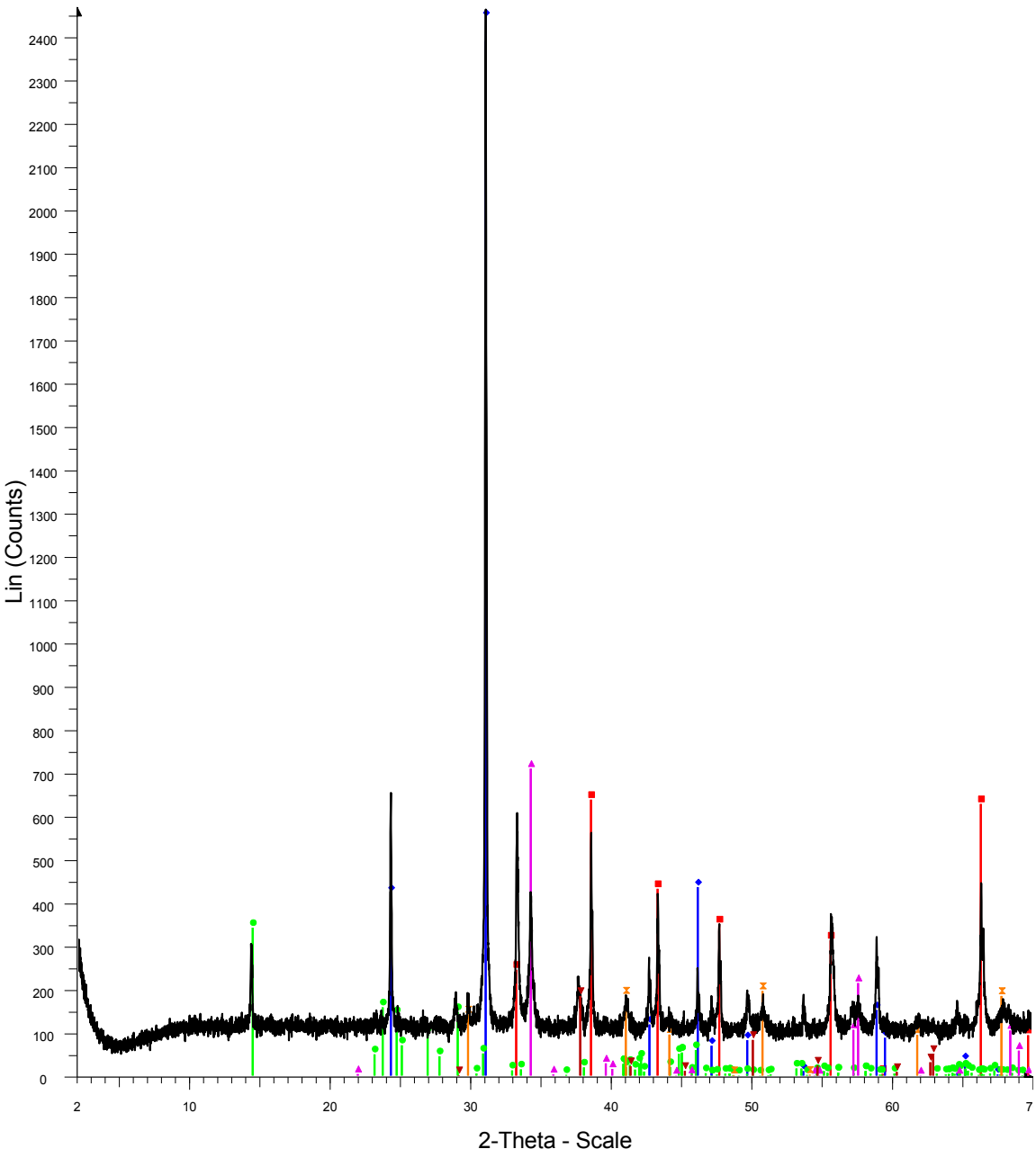

Red-Pyrite
Blue-Quartz
Green-Kaolinite
Pink-Chalcopyrite
Orange-Corundum
Dark red-Magnesite

81vein2

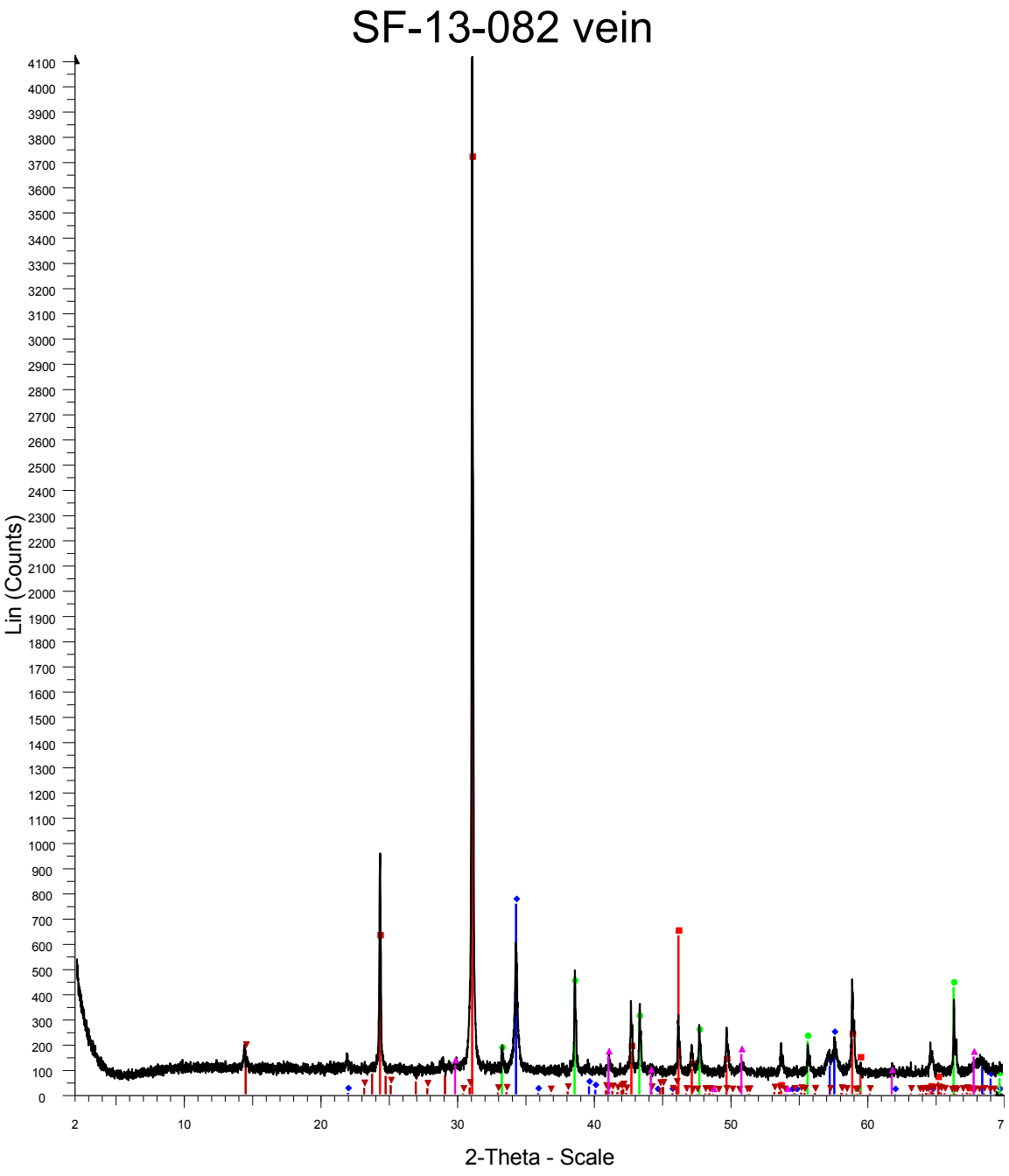

Red-Quartz
Blue-Chalcopyrite
Green-Pyrite
Dark red-Kaolinite
Pink-Corundum

82vein

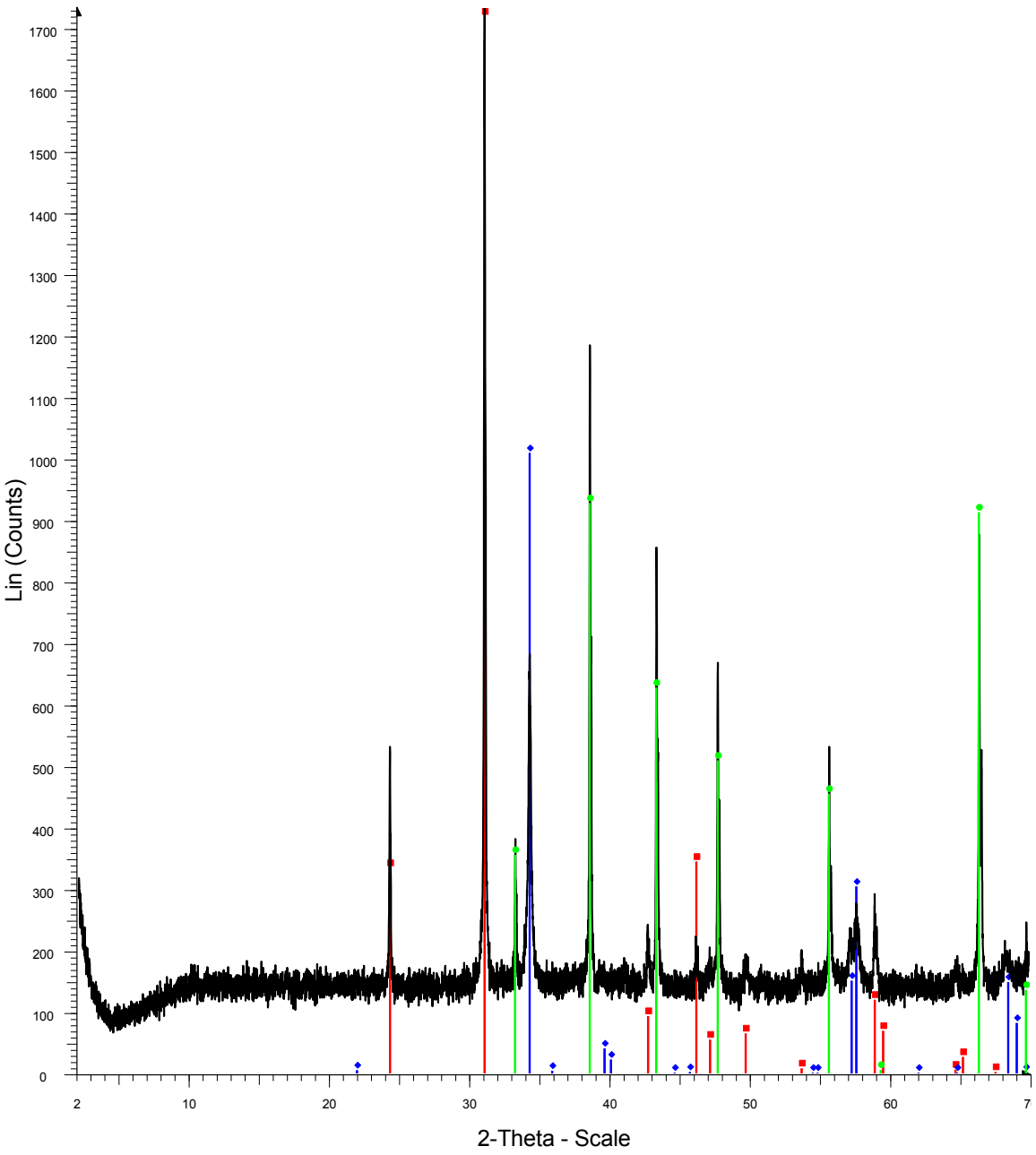

Red-Quartz
Blue-Chalcopyrite
Green-Pyrite

83vein

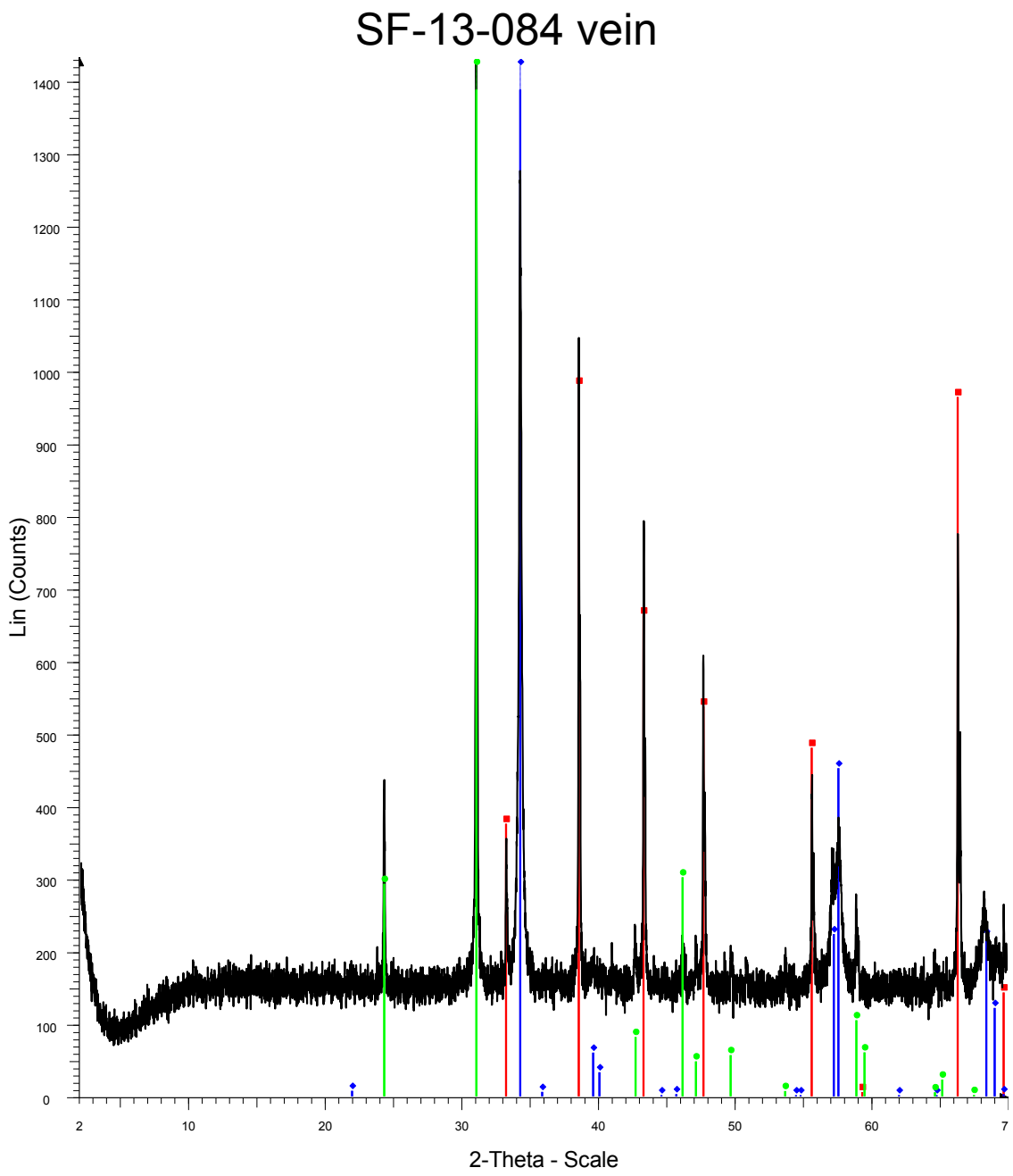

Red-Pyrite
Blue-Chalcopyrite
Green-Quartz

84vein

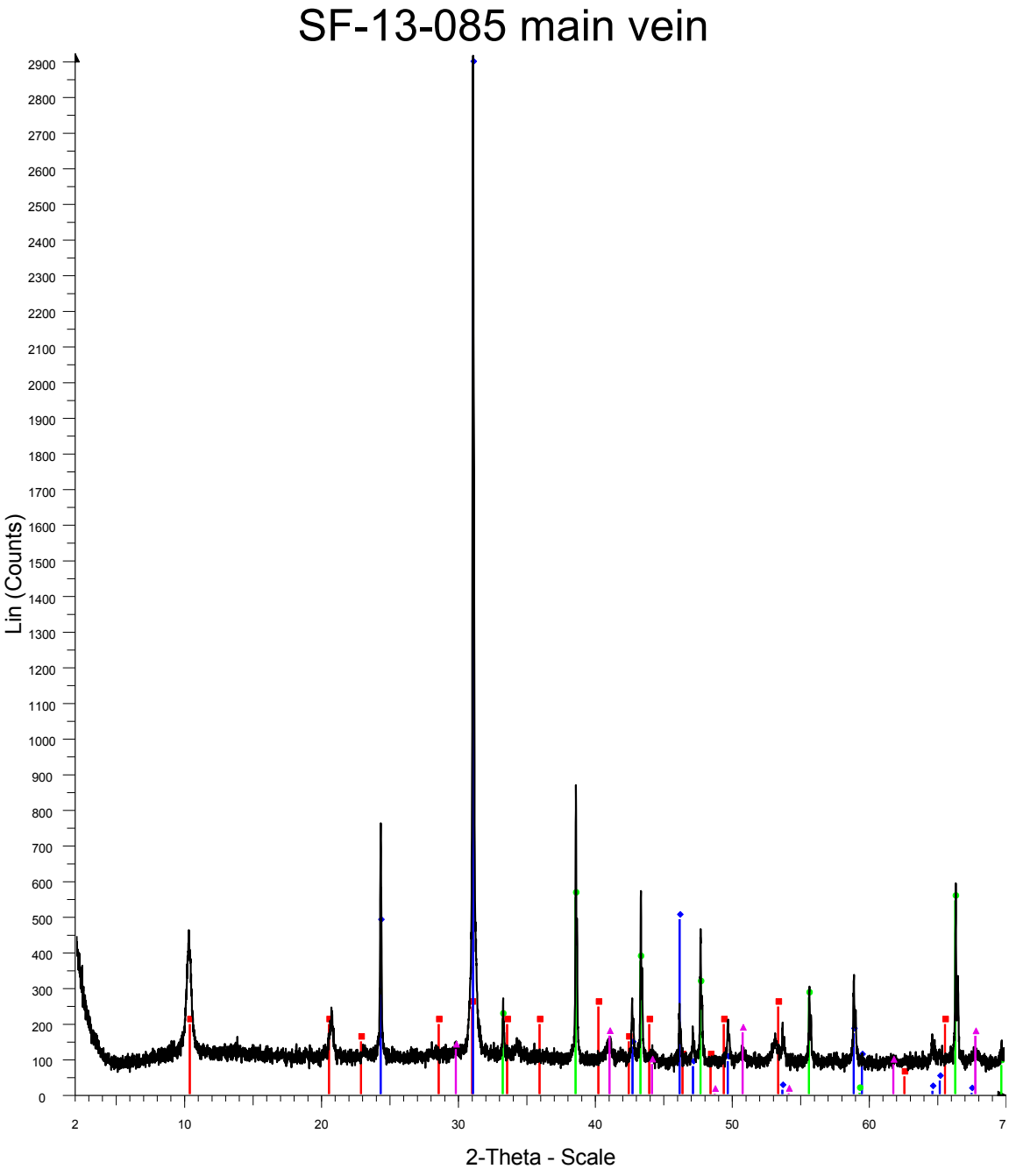

Red-Illite
Blue-Quartz
Green-Pyrite
Pink-Corundum

85mainvein

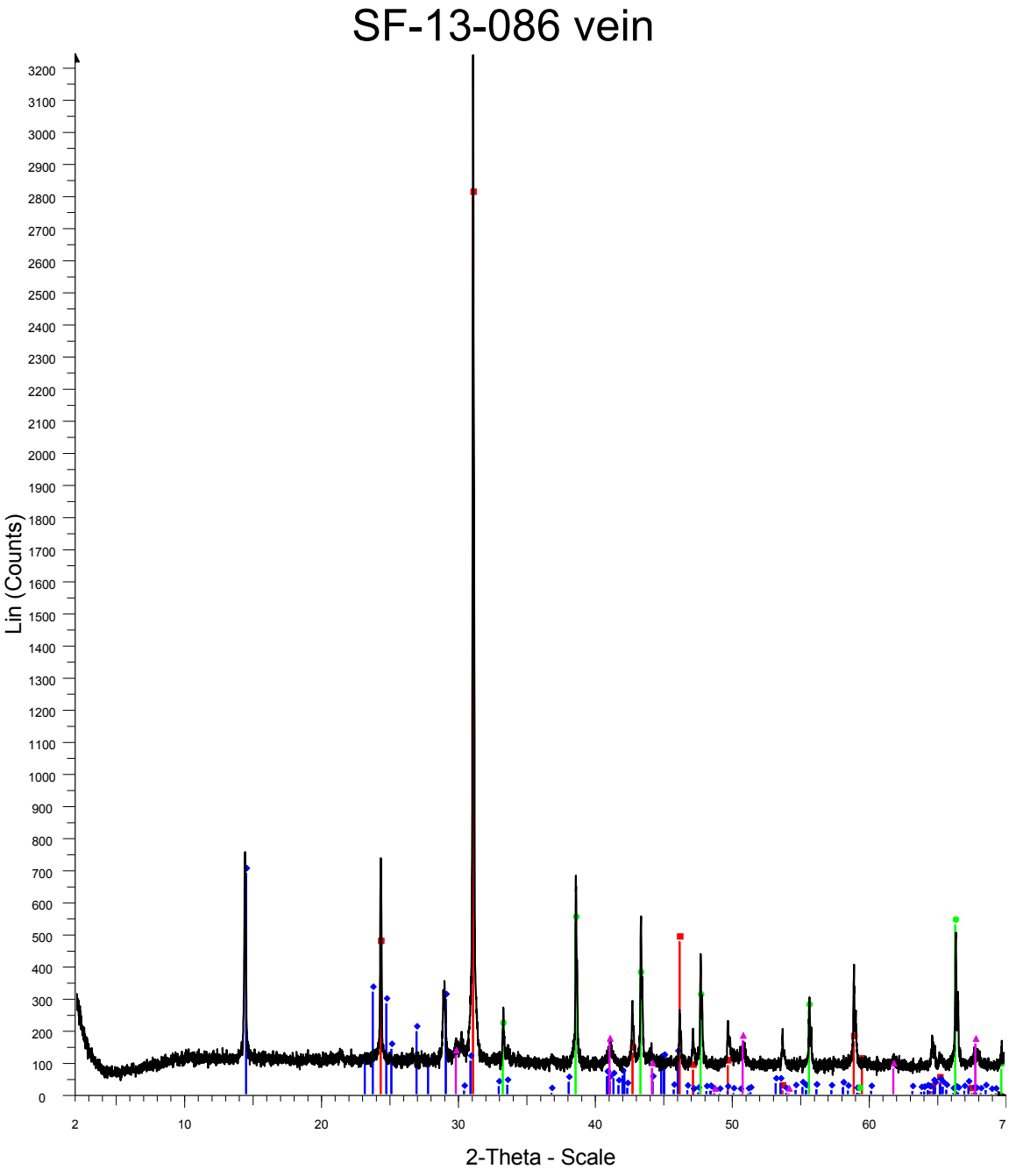

Red-Quartz
Blue-Kaolinite
Green-Pyrite
Pink-Corundum

86vein

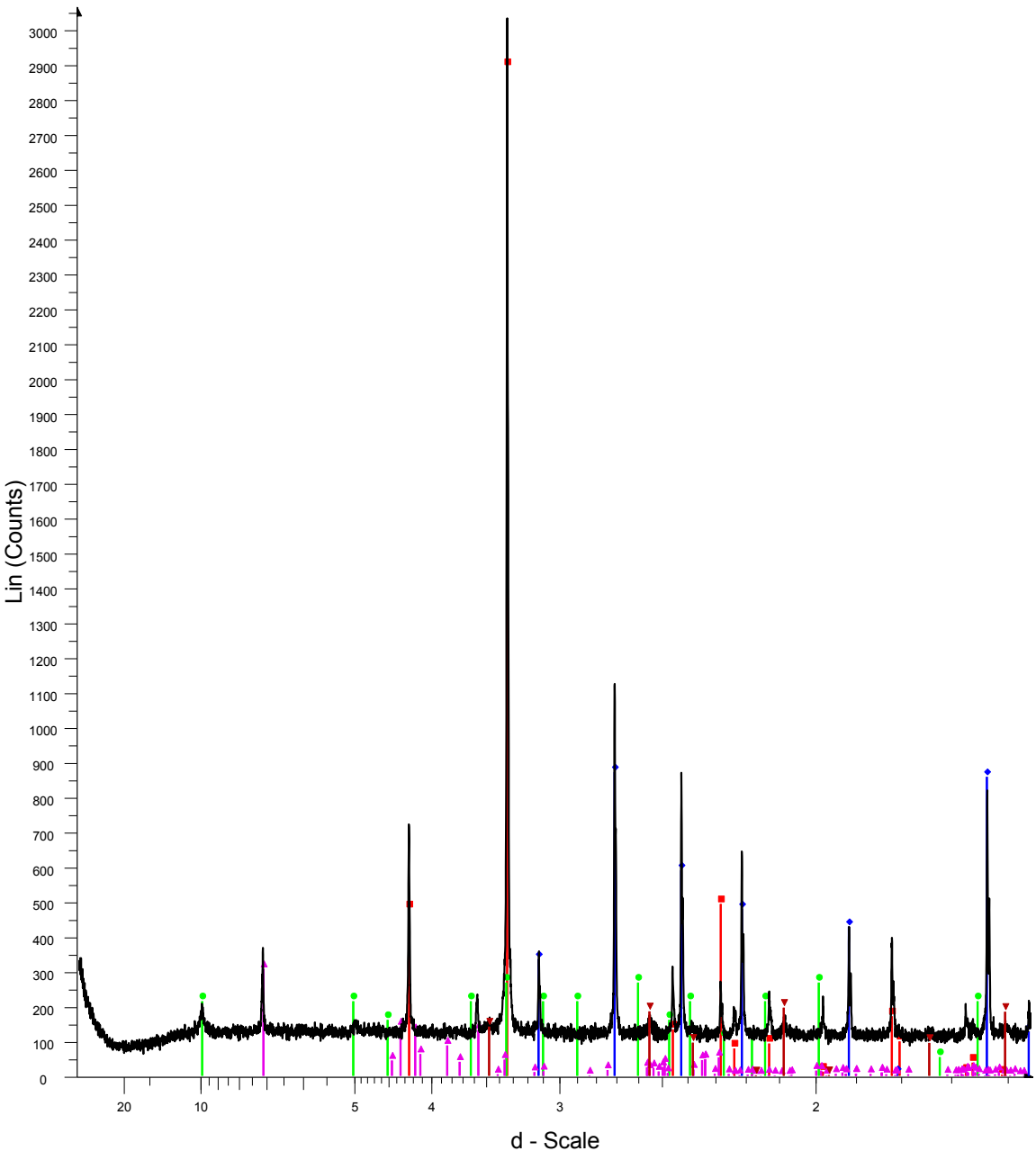

Red-Quartz
Blue-Pyrite
Green-Illite
Pink-Kaolinite
Dark red-Corundum

87vein1

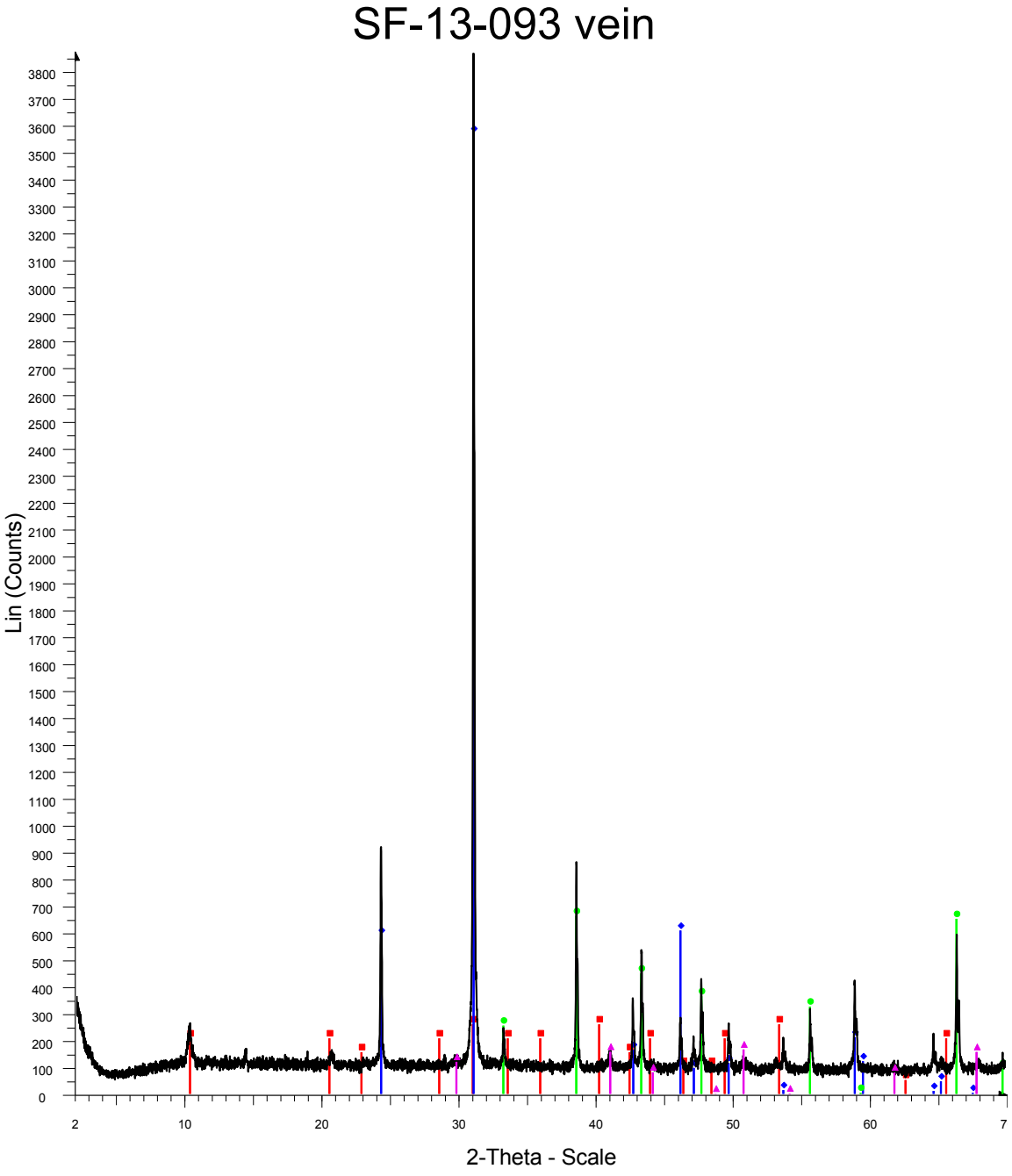

Red-Illite
Blue-Quartz
Green-Pyrite
Pink-Corundum

93vein

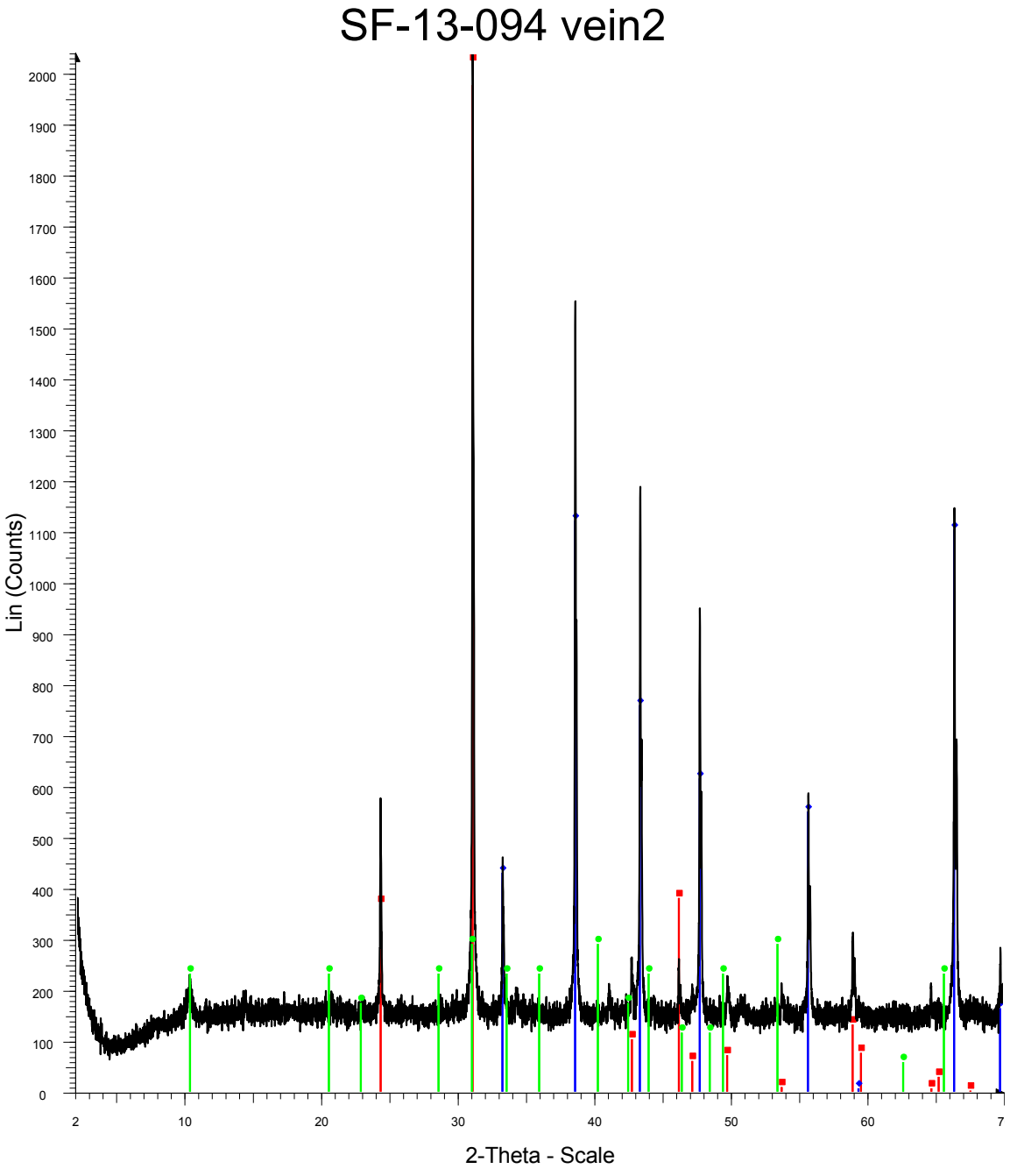

Red-Quartz
Blue-Pyrite
Green-Illite

94vein2

Middle

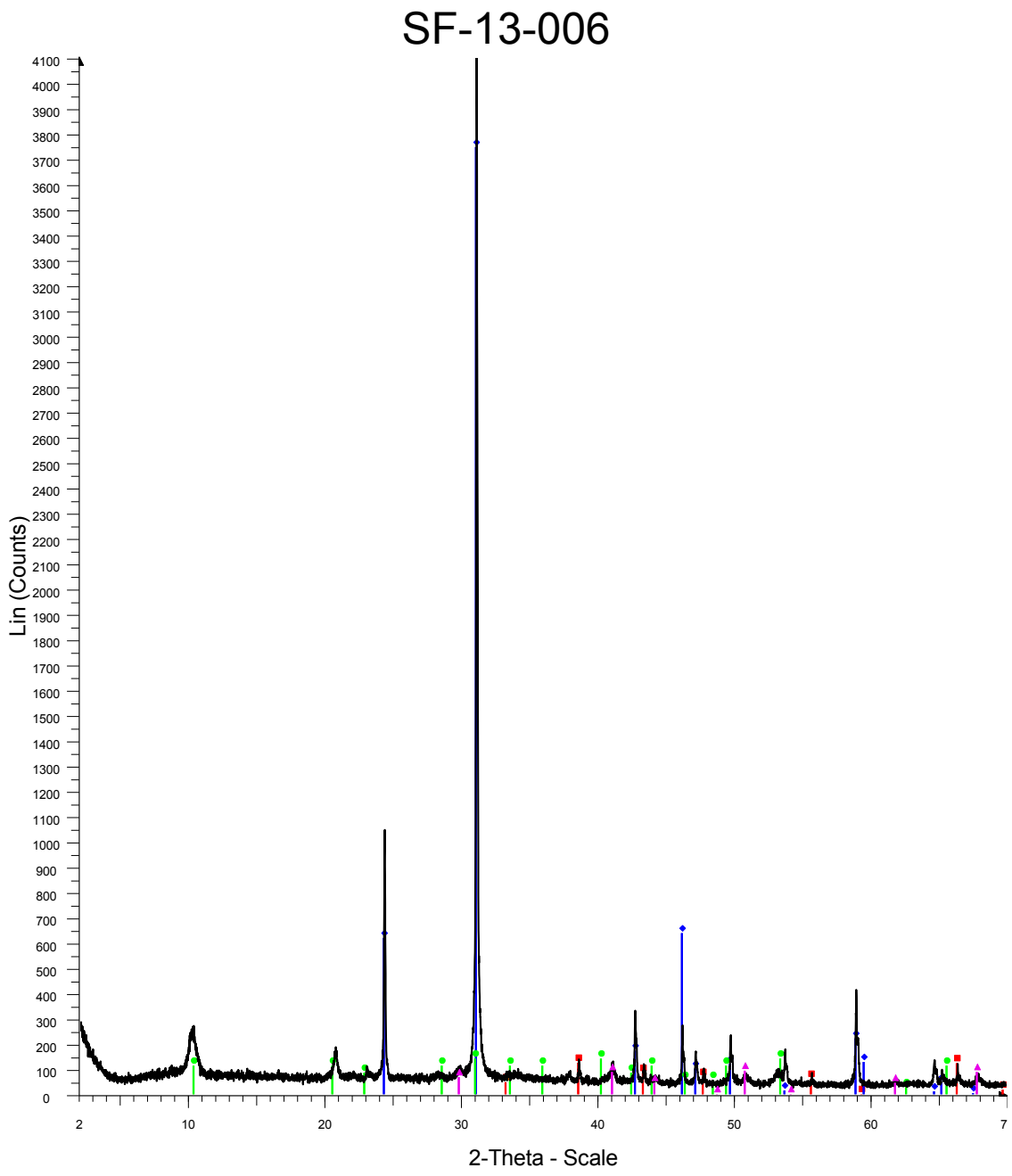

Red-Pyrite
Blue-Quartz
Green-Illite
Pink-Corundum

6

SF-13-007

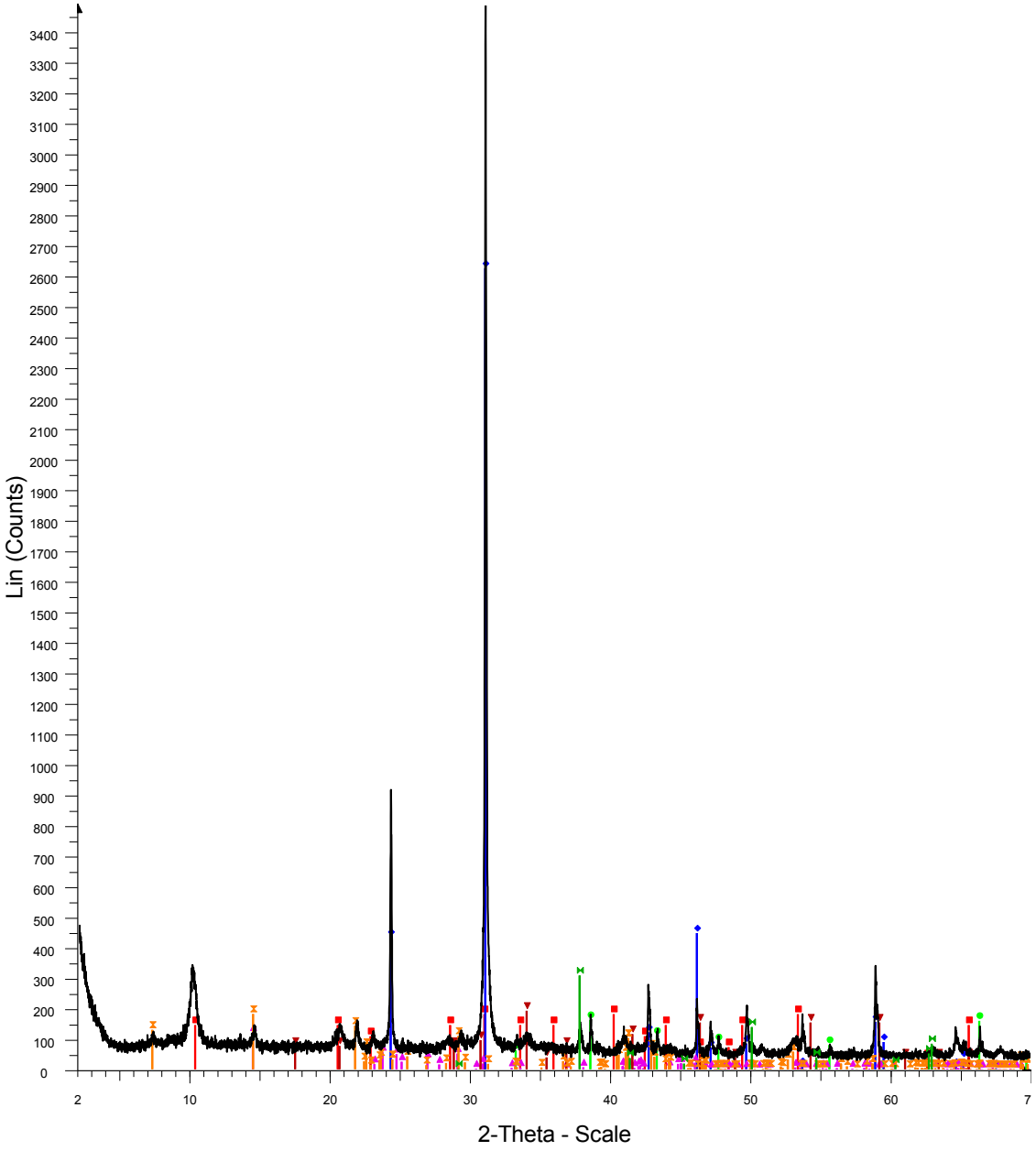

Red-Illite
Blue-Quartz
Green-Pyrite
Pink-Kaolinite
Dark red-Jarosite
Orange-Chlorite

7

SF-13-008

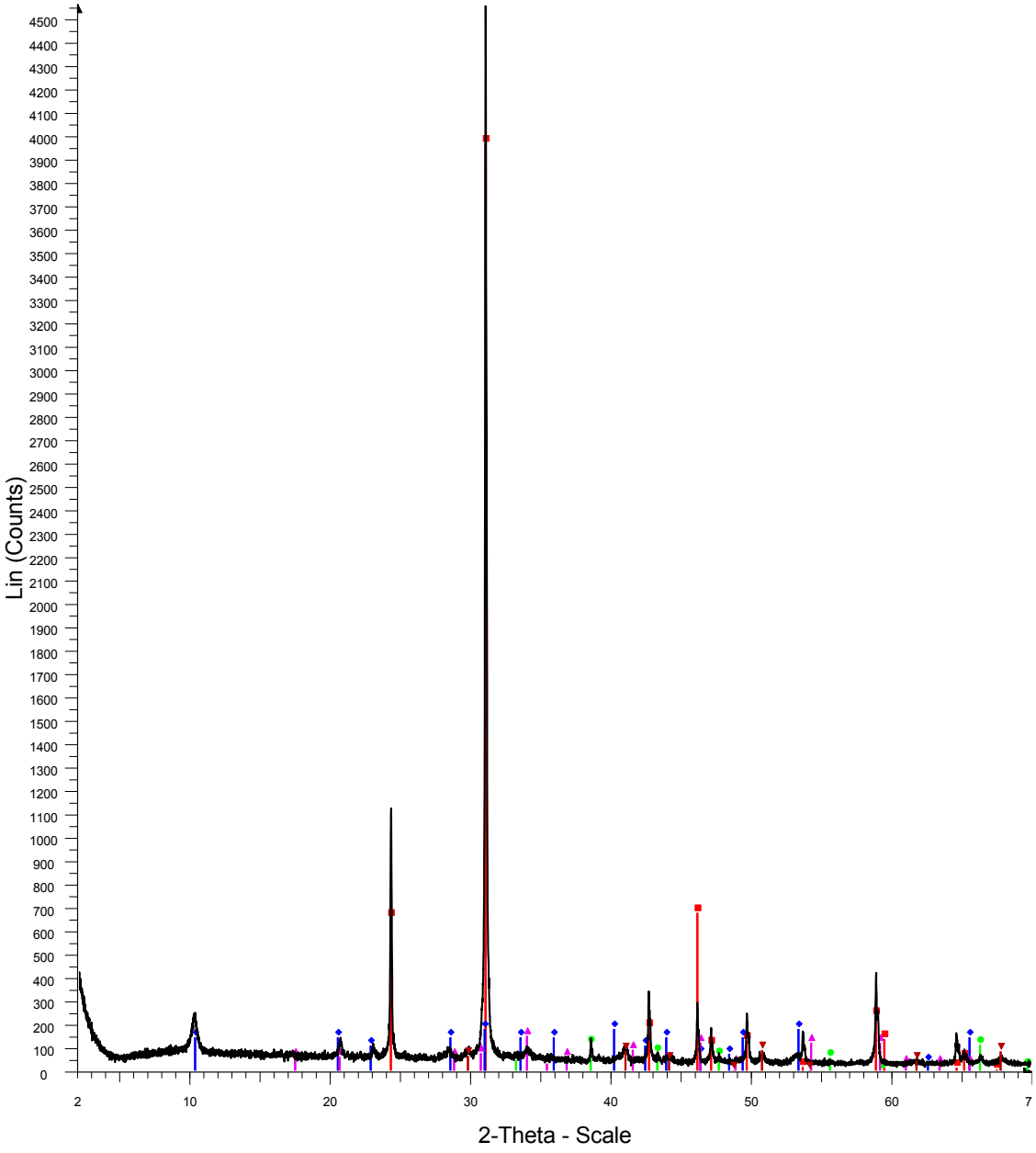

Red-Quartz
Blue-Illite
Green-Pyrite
Pink-Jarosite
Dark red-Corundum

8

SF-13-009

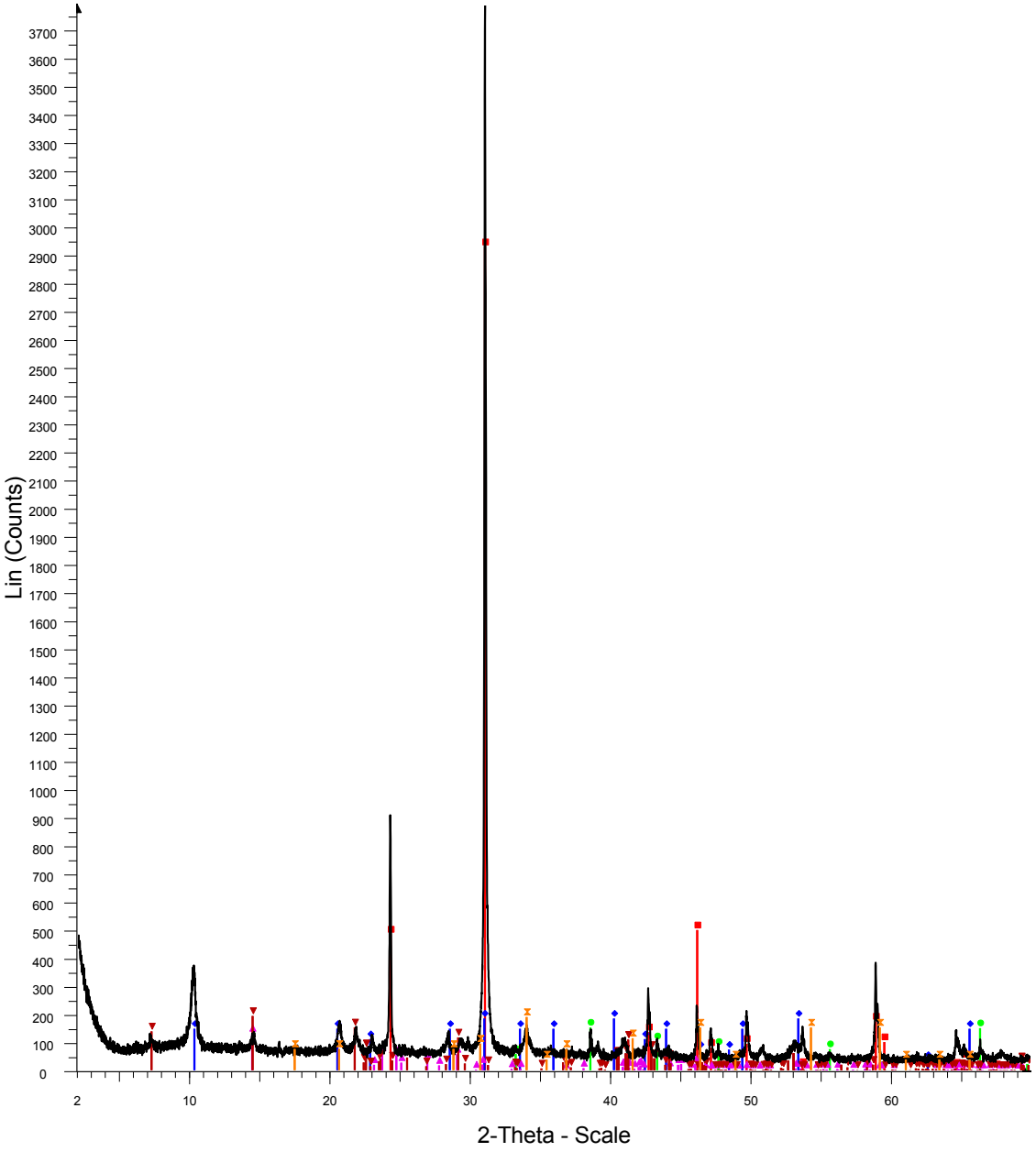

Red-Quartz
Blue-Illite
Green-Pyrite
Pink-Kaolinite
Dark red-Chlorite
Orange-Jarosite

9

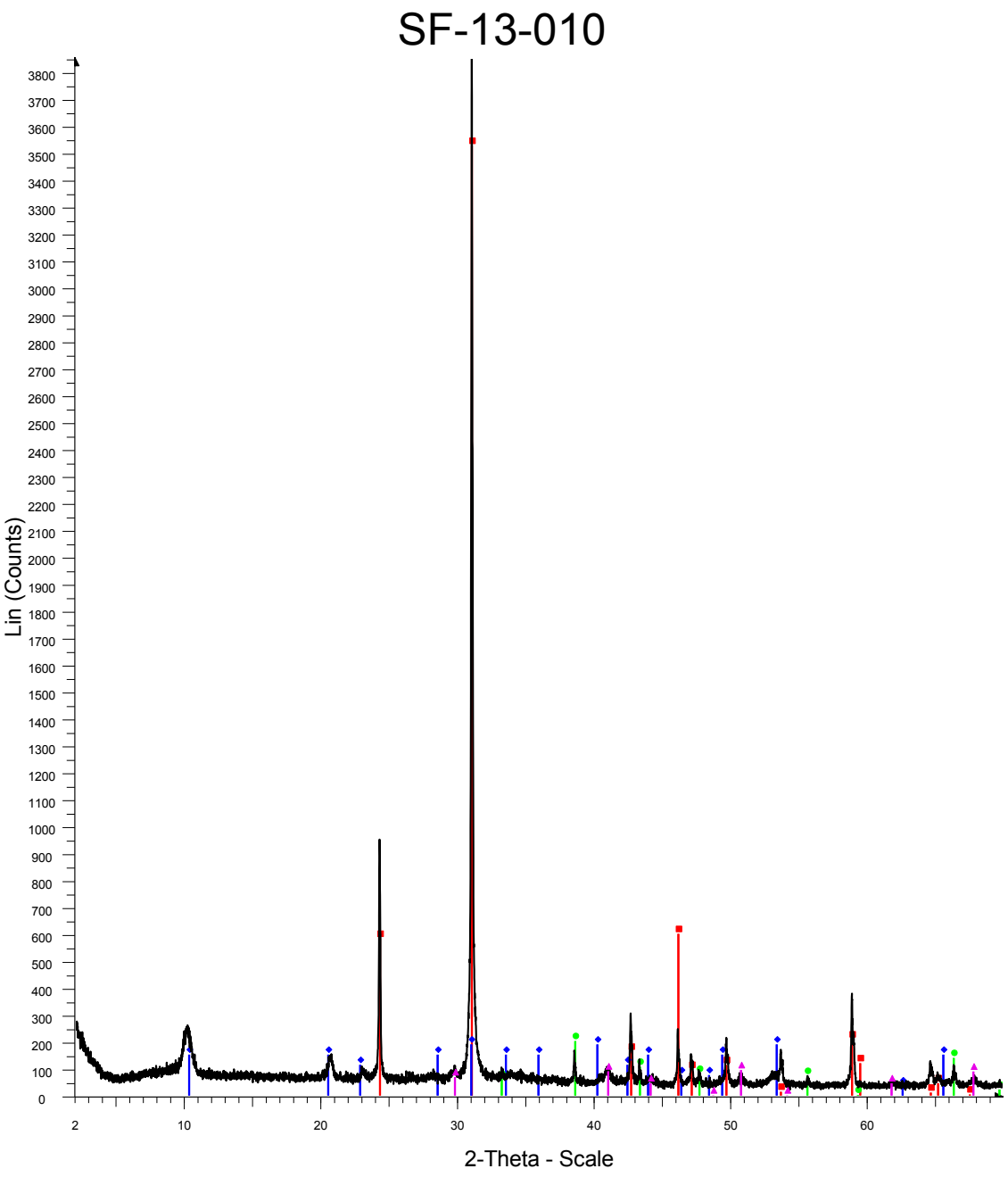

Red-Quartz
Blue-Illite
Green-Pyrite
Pink-Corundum

10

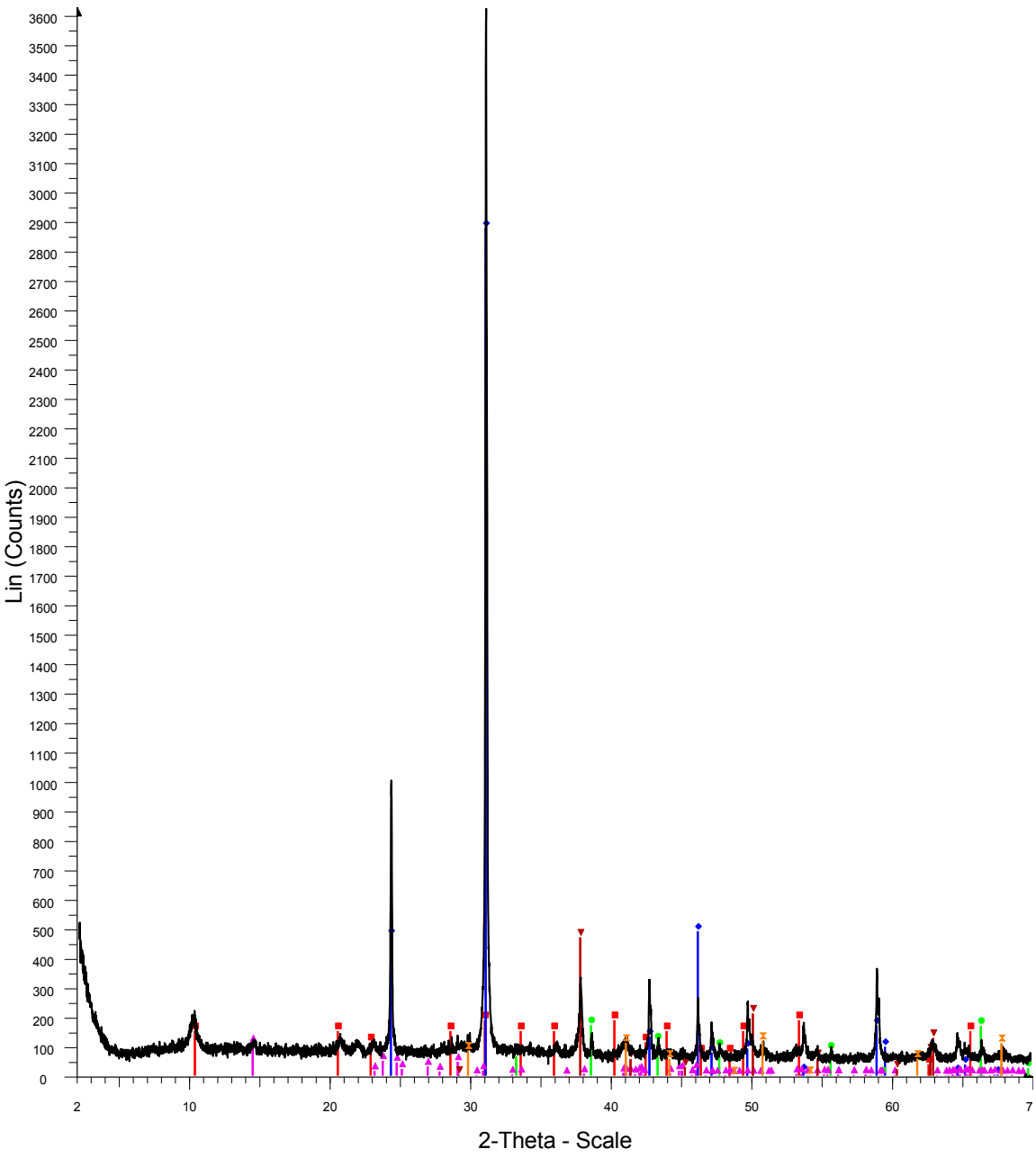

Red-Illite
Blue-Quartz
Green-Pyrite
Pink-Kaolinite
Dark red-Magnesite
Orange-Corundum
11

SF-13-027

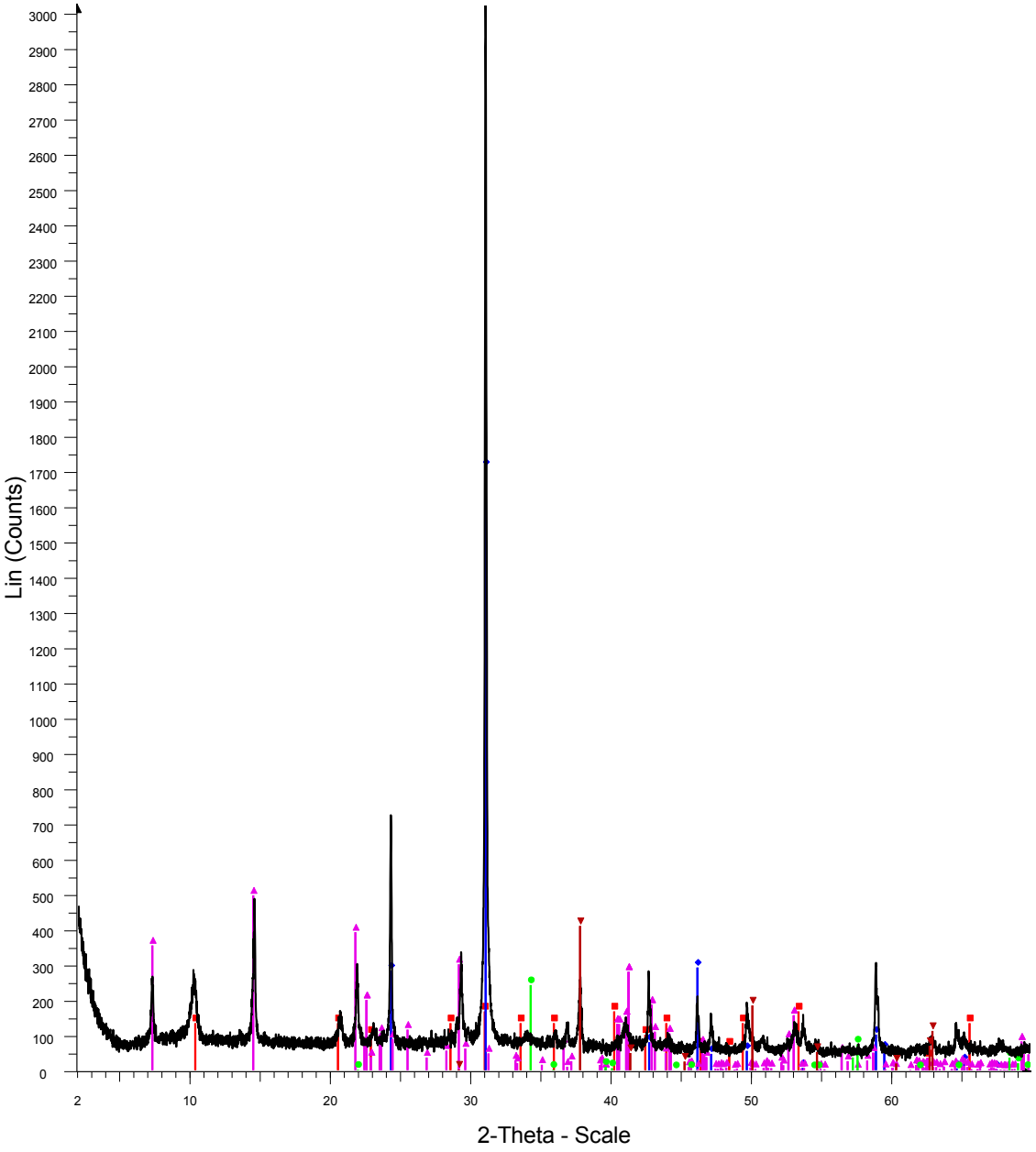

Red-Illite
Blue-Quartz
Pink-Chlorite
Green-Chalcopyrite
Dark red-Magnesite
27

SF-13-028

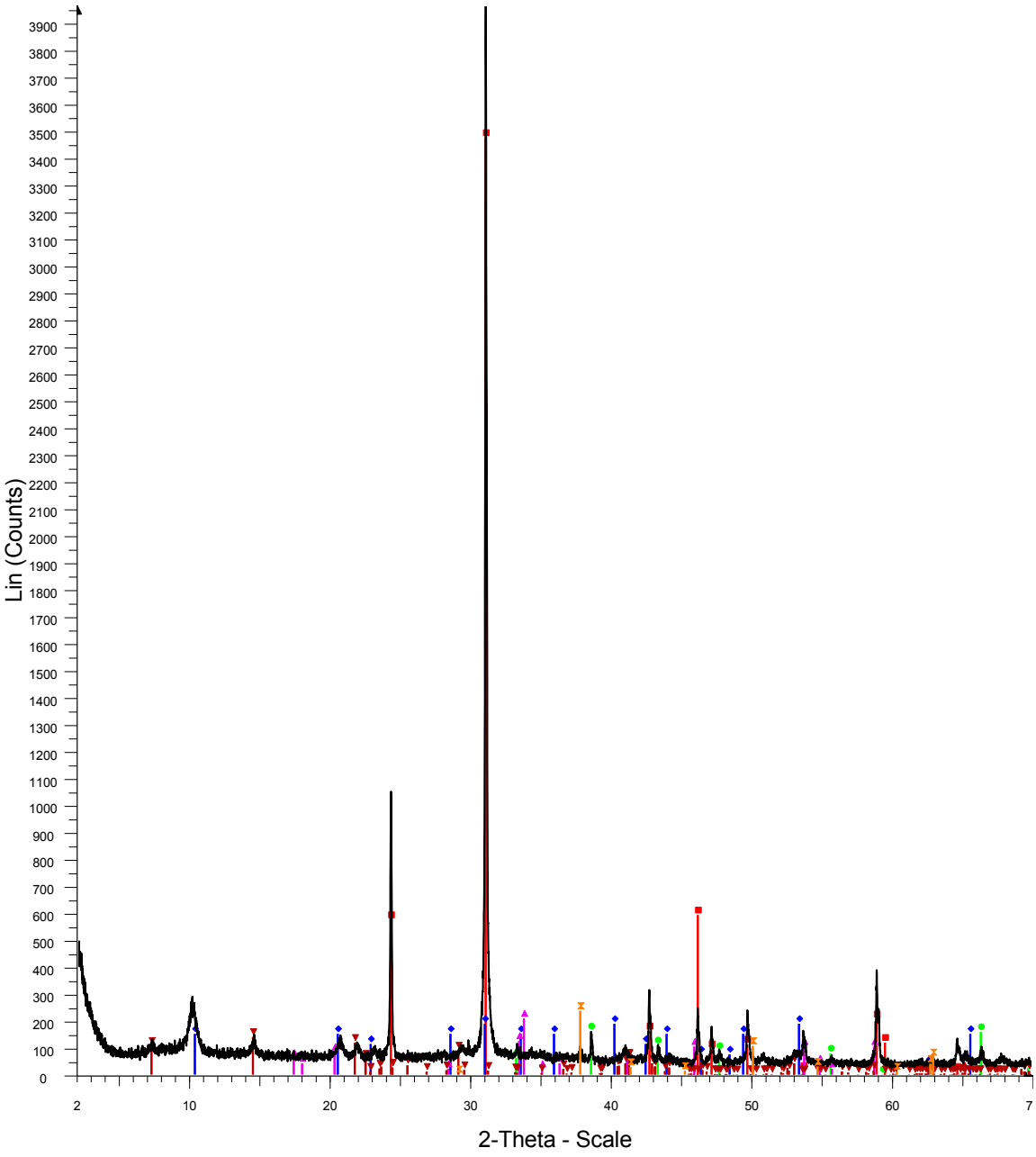

Red-Quartz
Blue-Illite
Green-Pyrite
Pink-Jarosite
Dark red-Chlorite
Orange-Magnesite
28

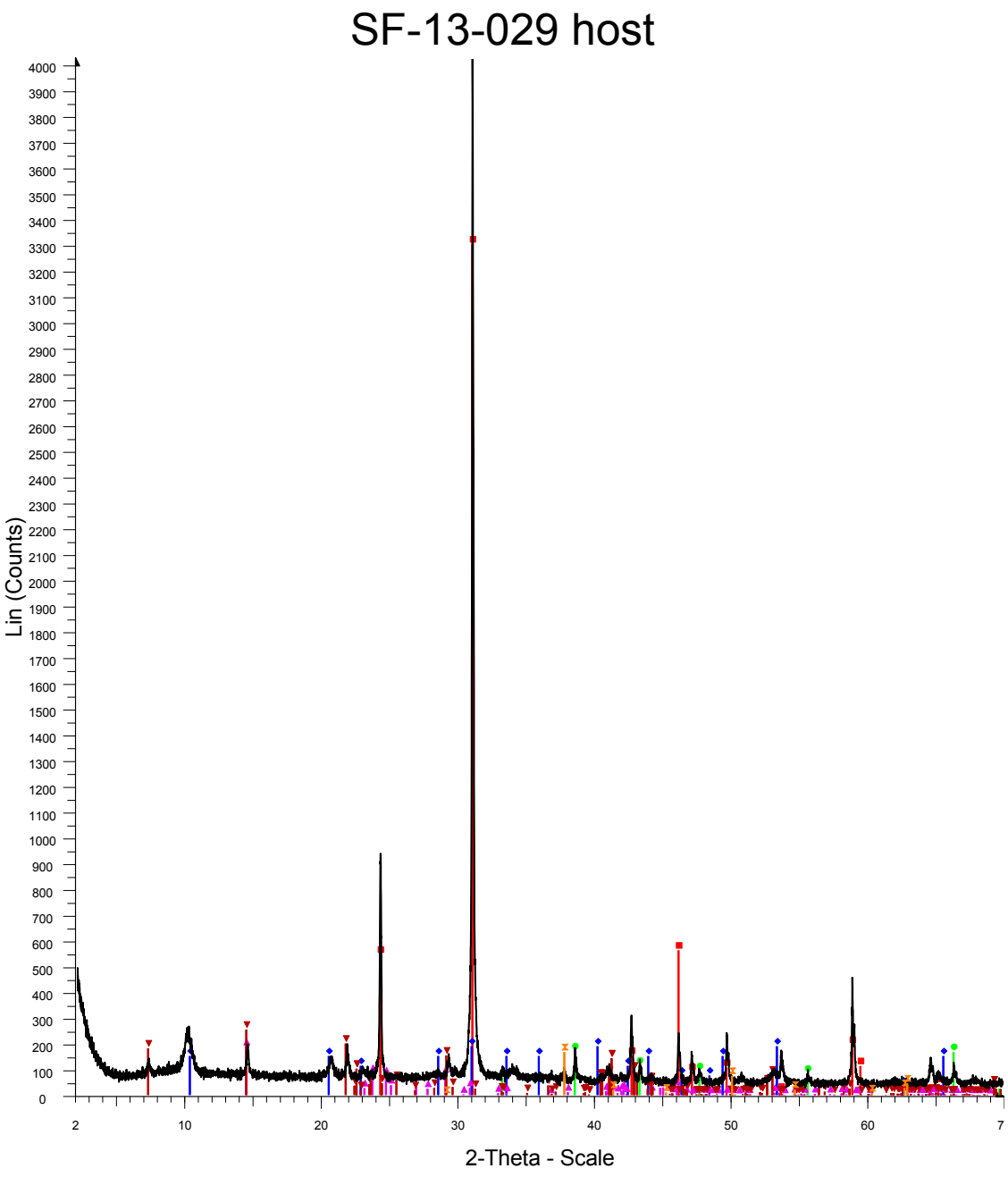

Red-Quartz
Blue-Illite
Green-Pyrite
Pink-Kaolinite
Dark red-Chlorite
Orange-Magnesite
29host

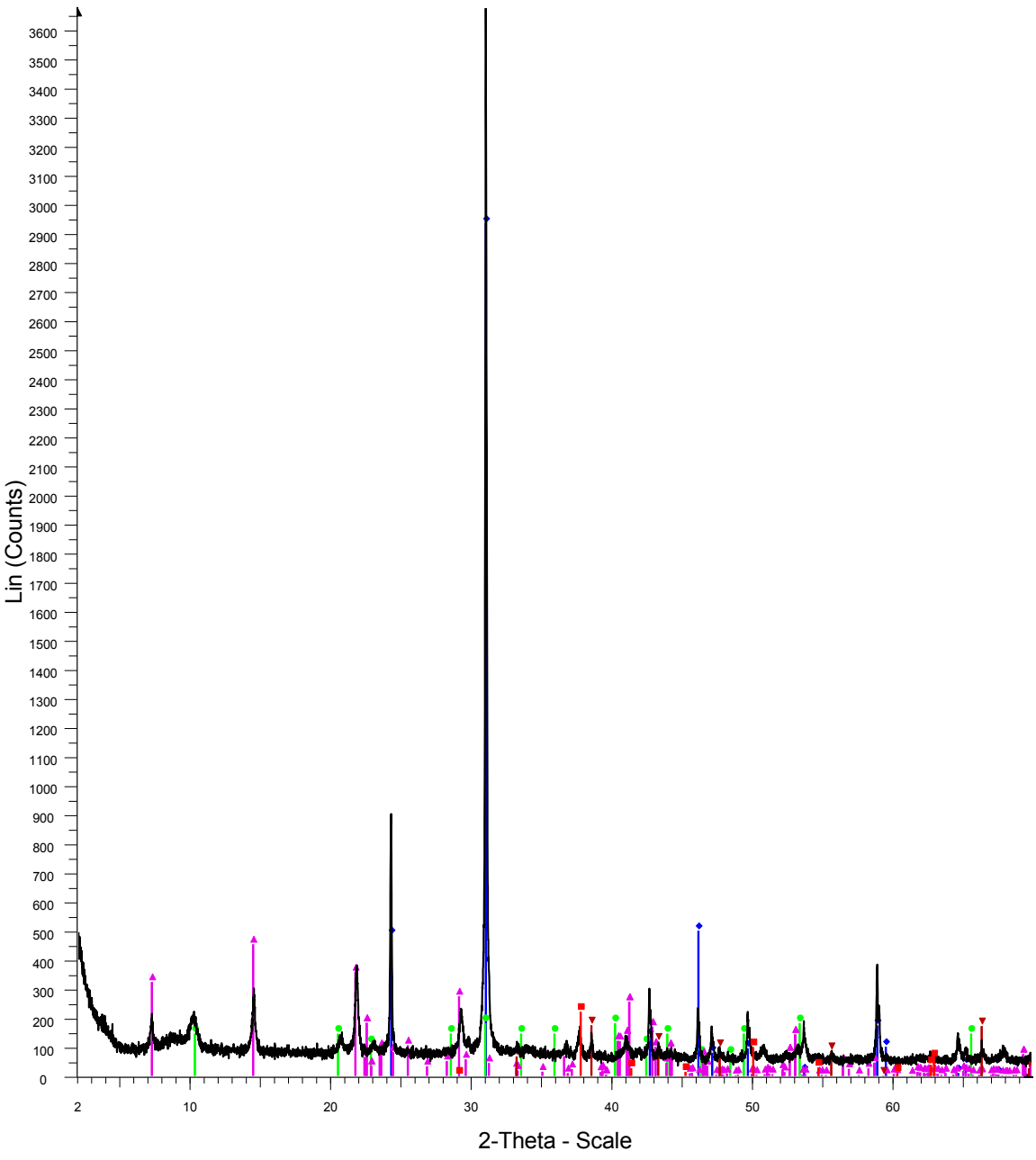

Blue-Quartz
Green-Illite
Pink-Chlorite
Dark red-Pyrite
Red-Magnesite
30host

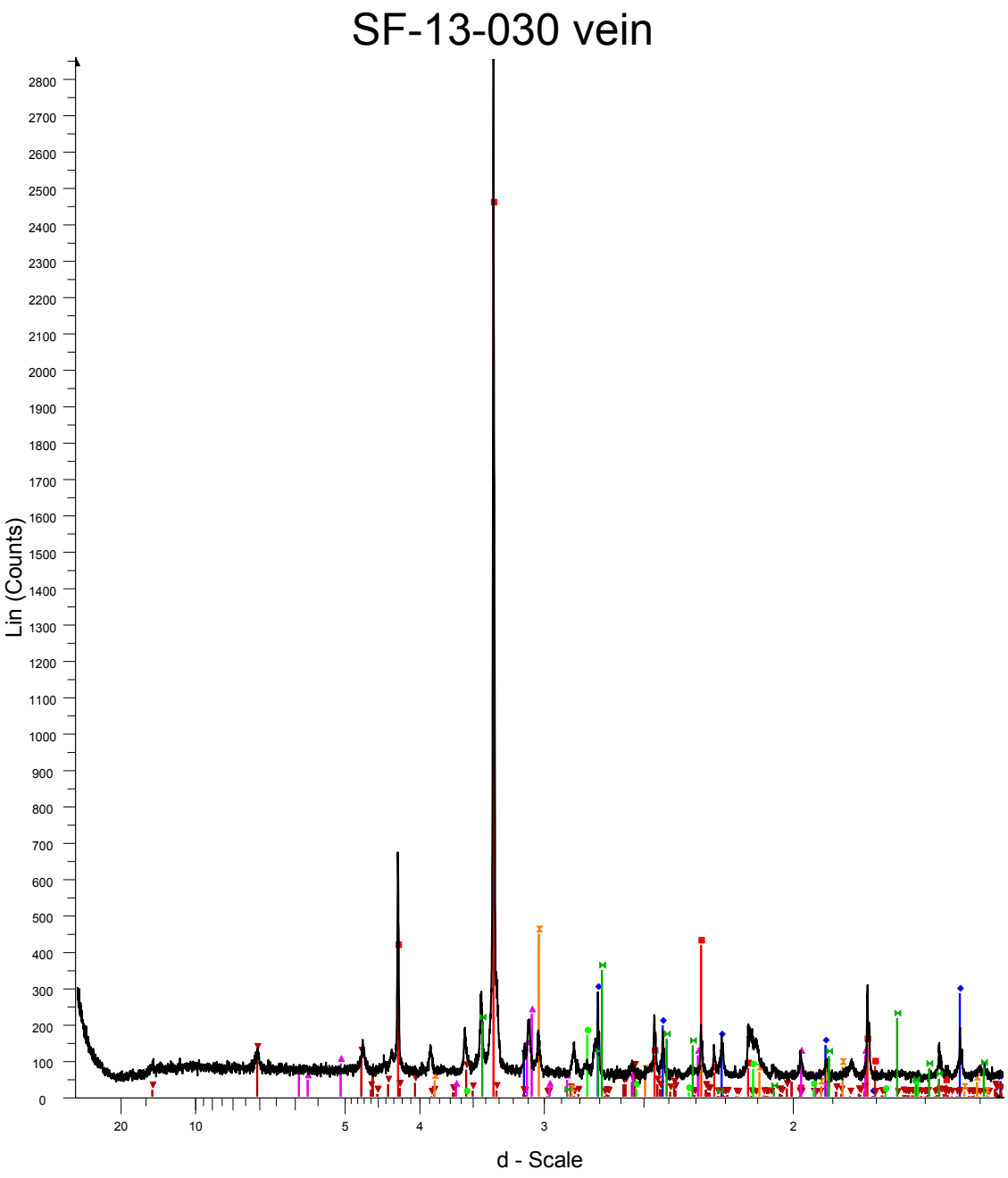

Red-Quartz
Blue-Pyrite
Dark red-Chlorite
Orange-Calcite
Pink-Jarosite
Green-Magnesite
30vein

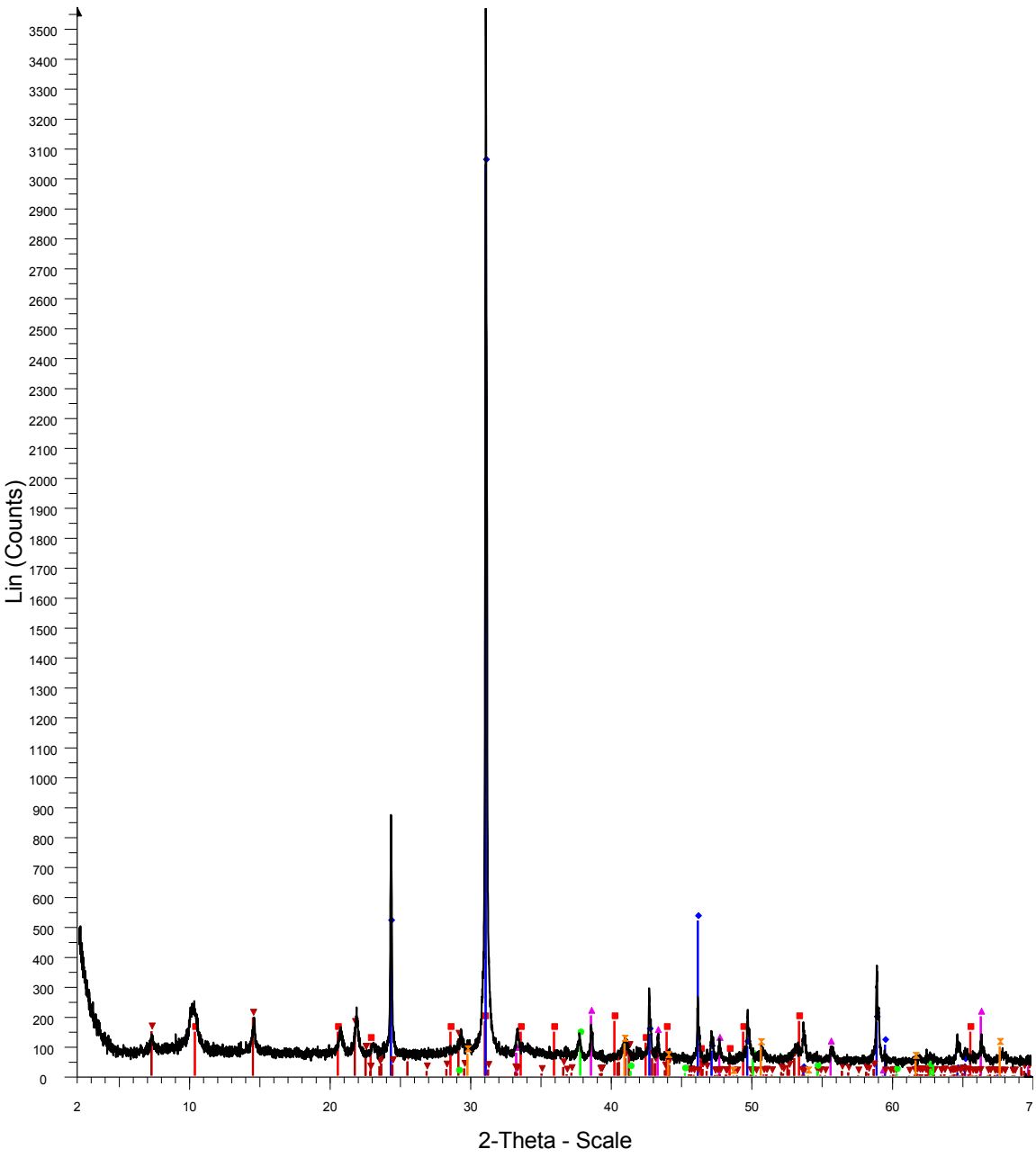

Red-Illite
Blue-Quartz
Pink-Pyrite
Dark red-Chlorite
Green-Magnesite
Orange-Corundum
31 host

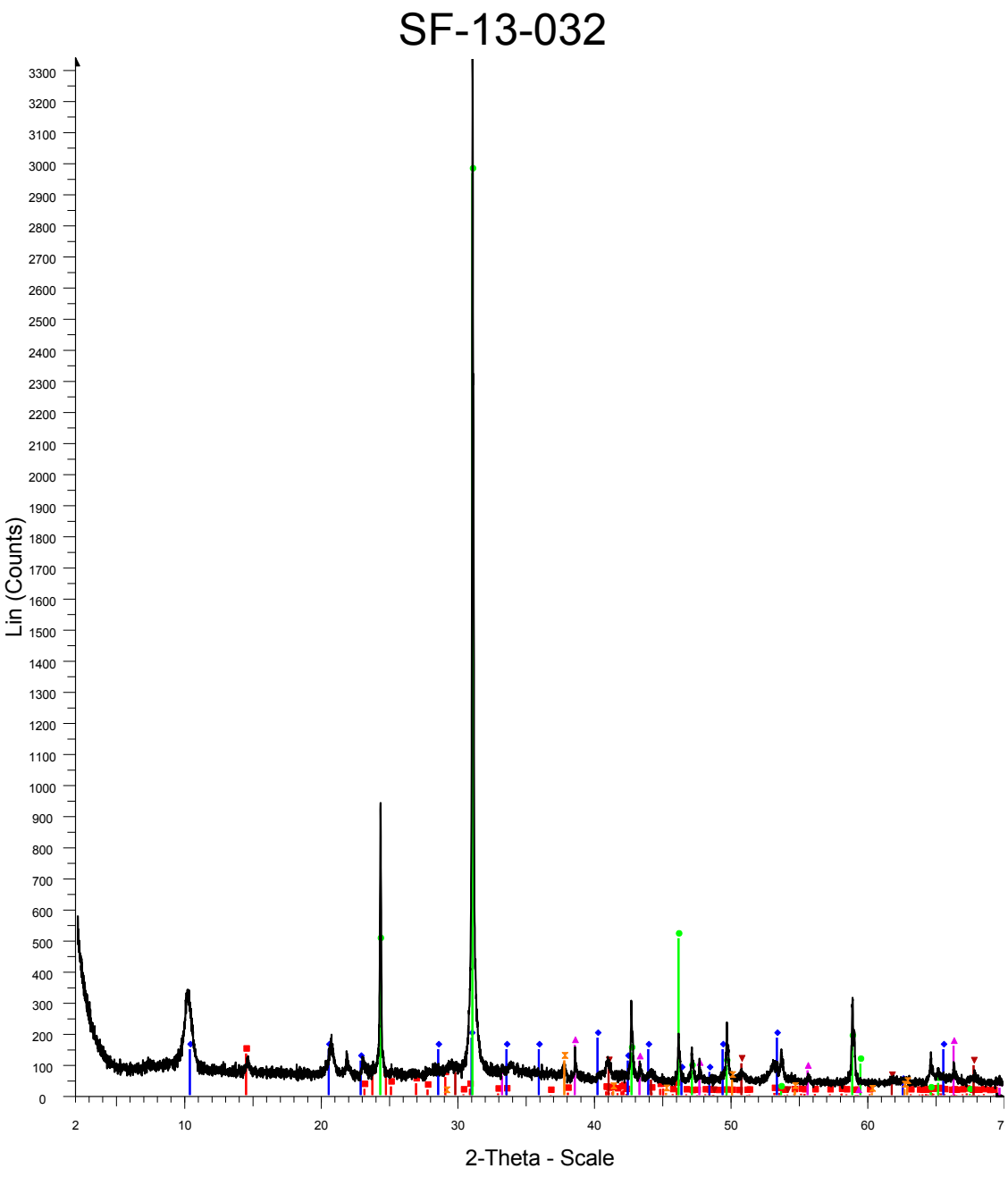

Red-Kaolinite
Blue-Illite
Green-Quartz
Pink-Pyrite
Dark red-Corundum
Orange-Magnesite
32

SF-13-047

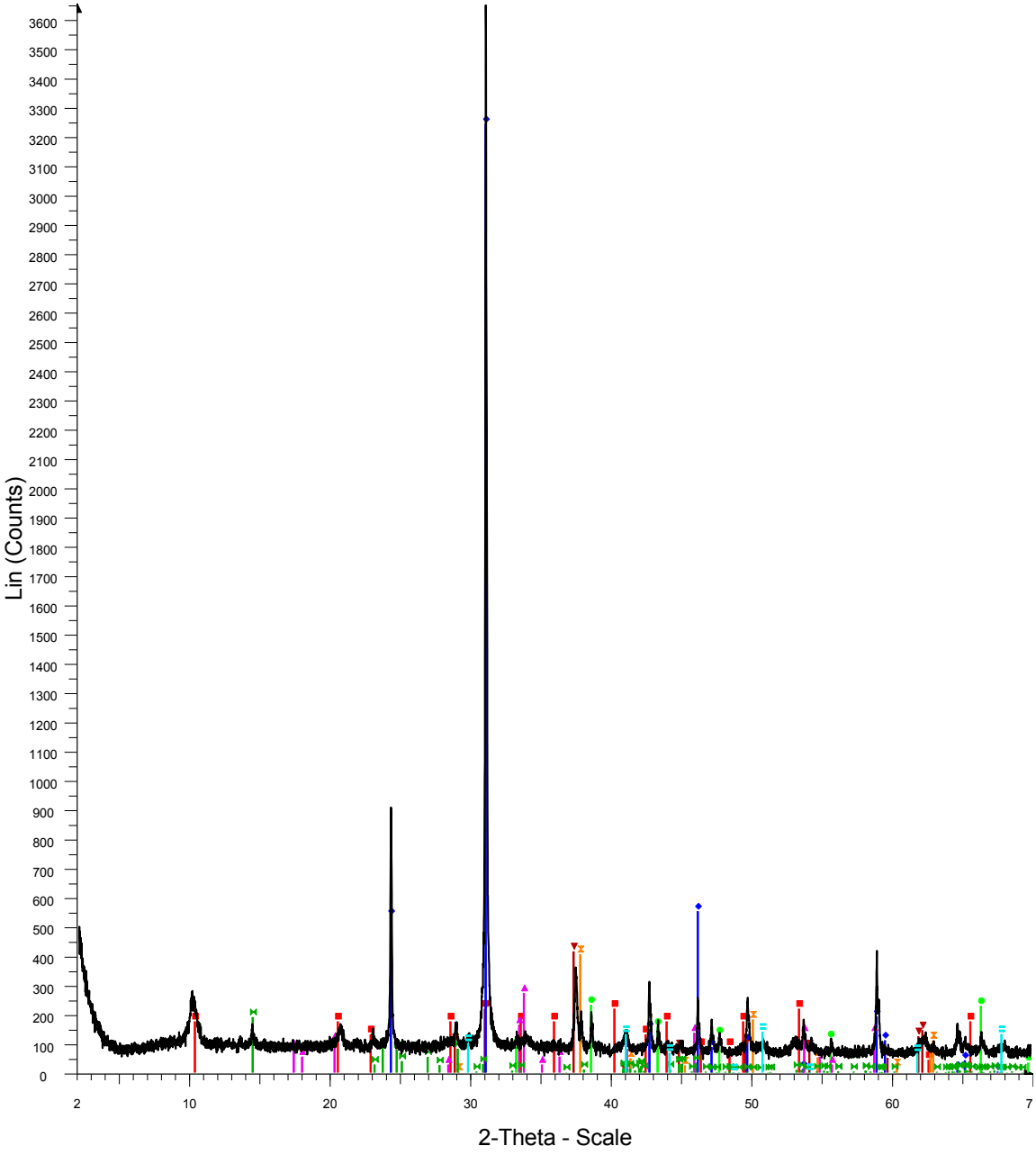

Red-Illite
Blue-Quartz
Green-Pyrite
Pink-Jarosite
Dark red-Siderite
Orange-Magnesite
Dark green-Kaolinite
Cyan-Corundum

47

SF-13-048

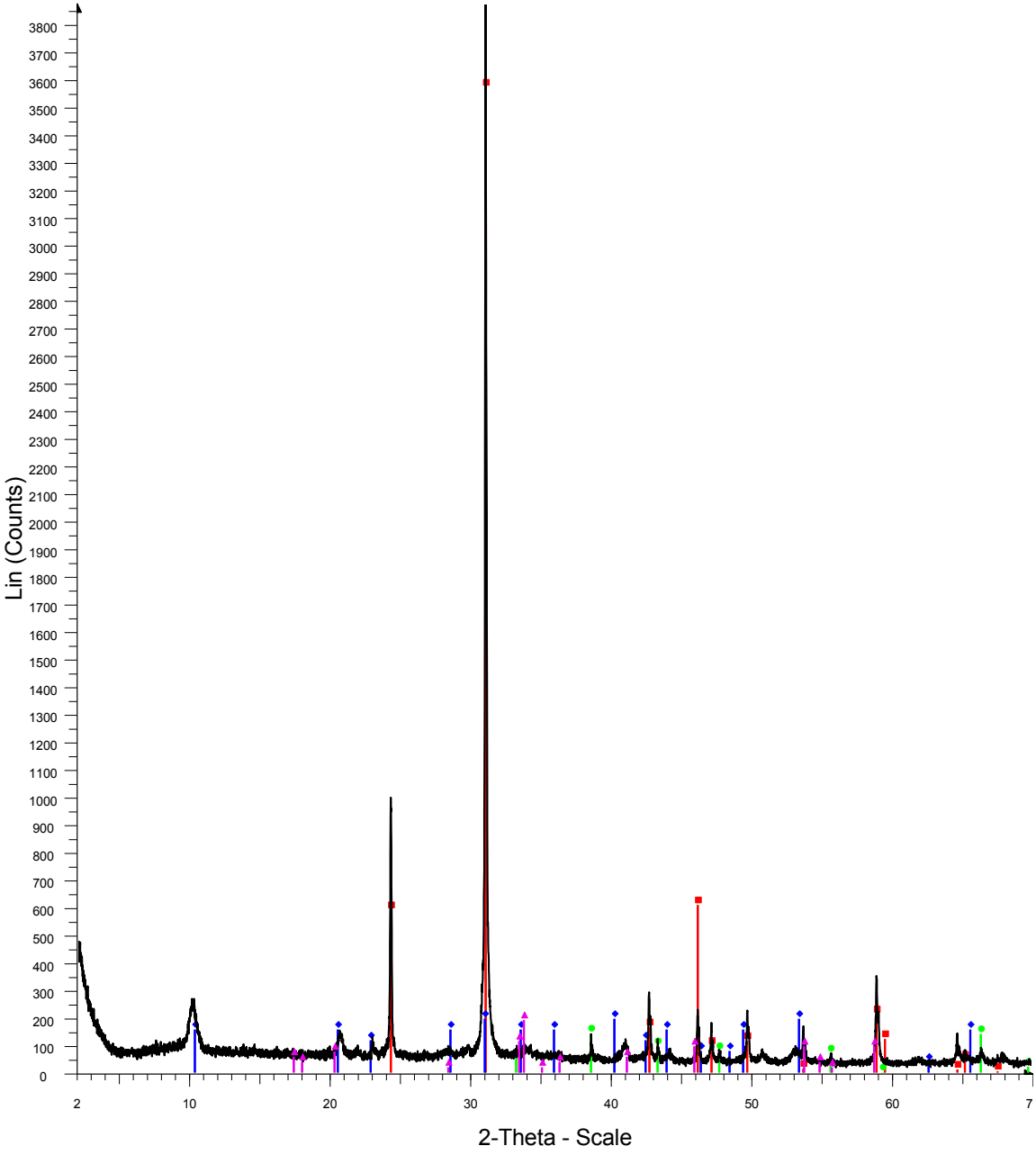

Red-Quartz
Blue-Illite
Green-Pyrite
Pink-Jarosite

48

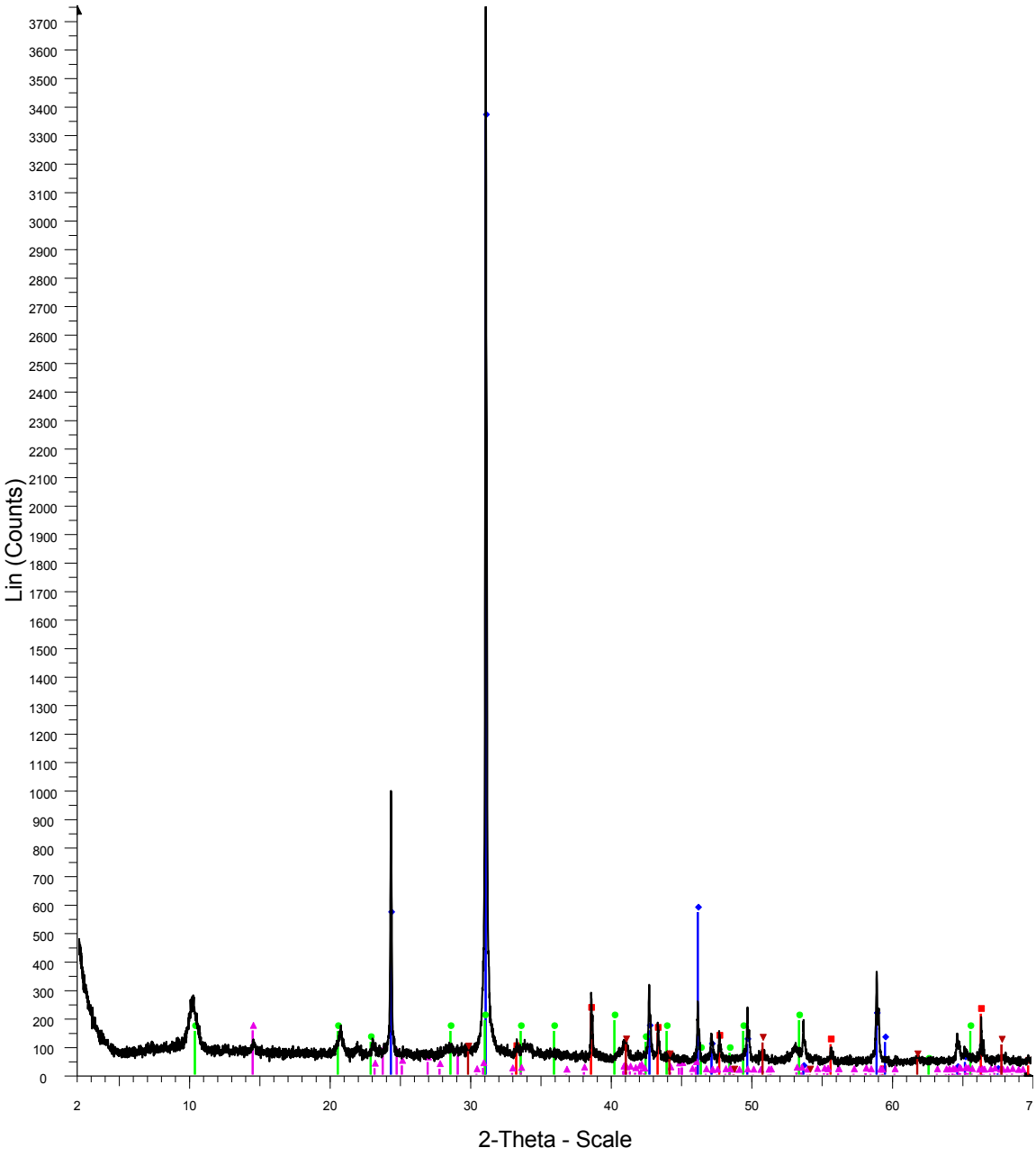

Red-Pyrite
Blue-Quartz
Green-Illite
Pink-Kaolinite
Dark red-Corundum

49

SF-13-050 host

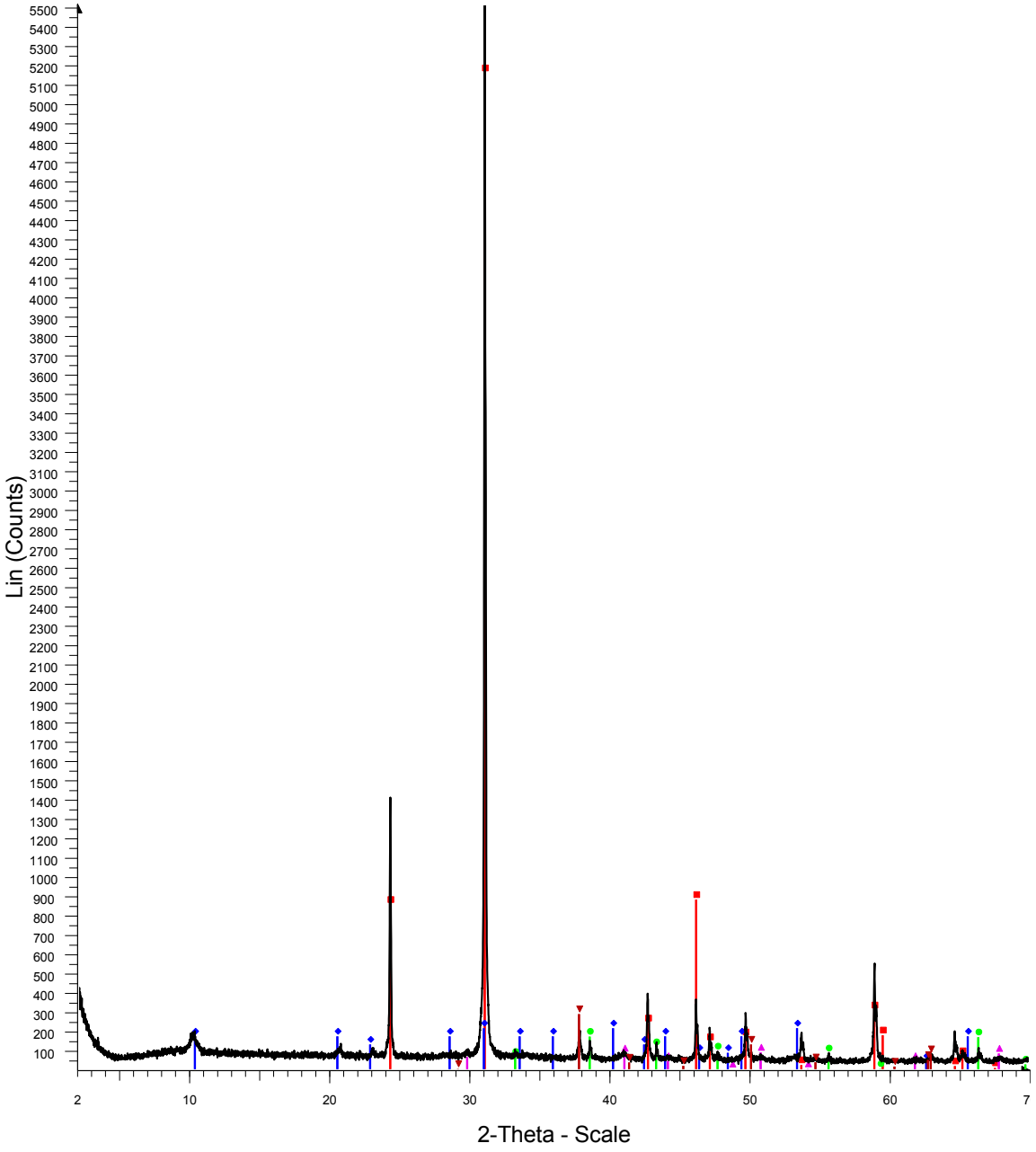

Red-Quartz
Blue-Illite
Green-Pyrite
Pink-Corundum
Dark red-Magnesite

50host

SF-13-050 vein

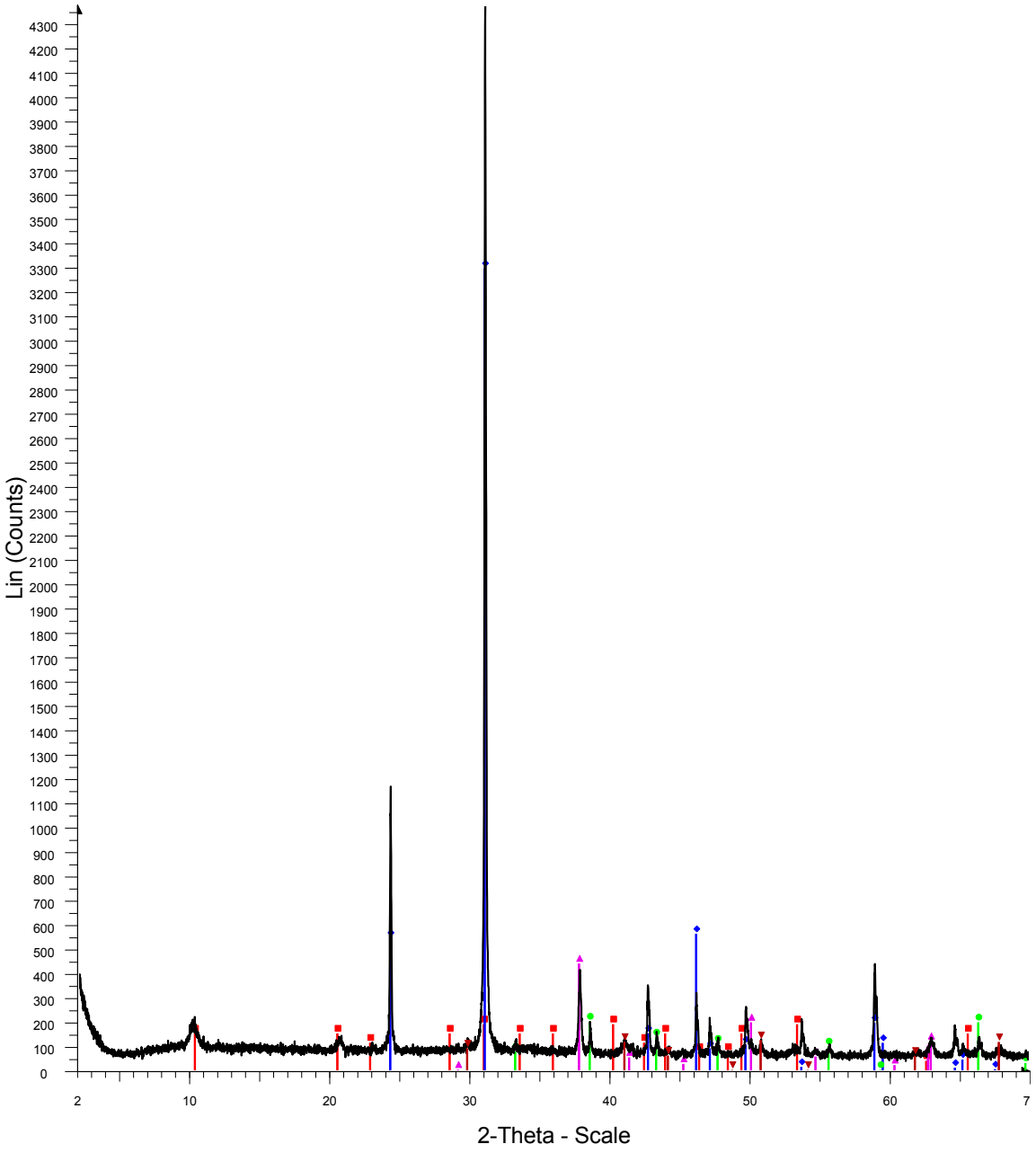

Red-Illite
Blue-Quartz
Green-Pyrite
Pink-Magnesite
Dark red-Corundum

50vein

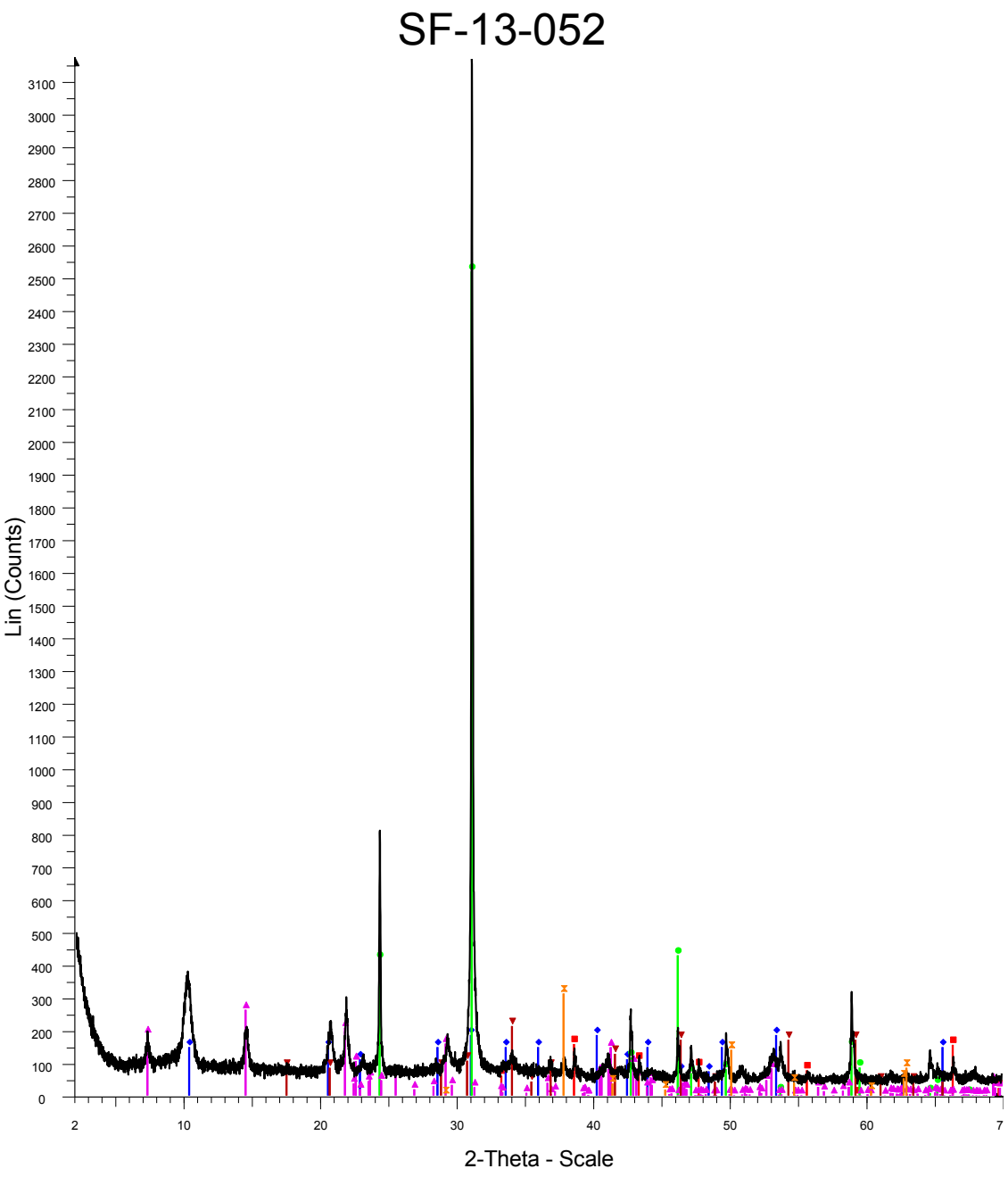

Red-Pyrite
Blue-Illite
Green-Quartz
Pink-Chlorite
Dark red-Jarosite
Orange-Magnesite

52

SF-13-053

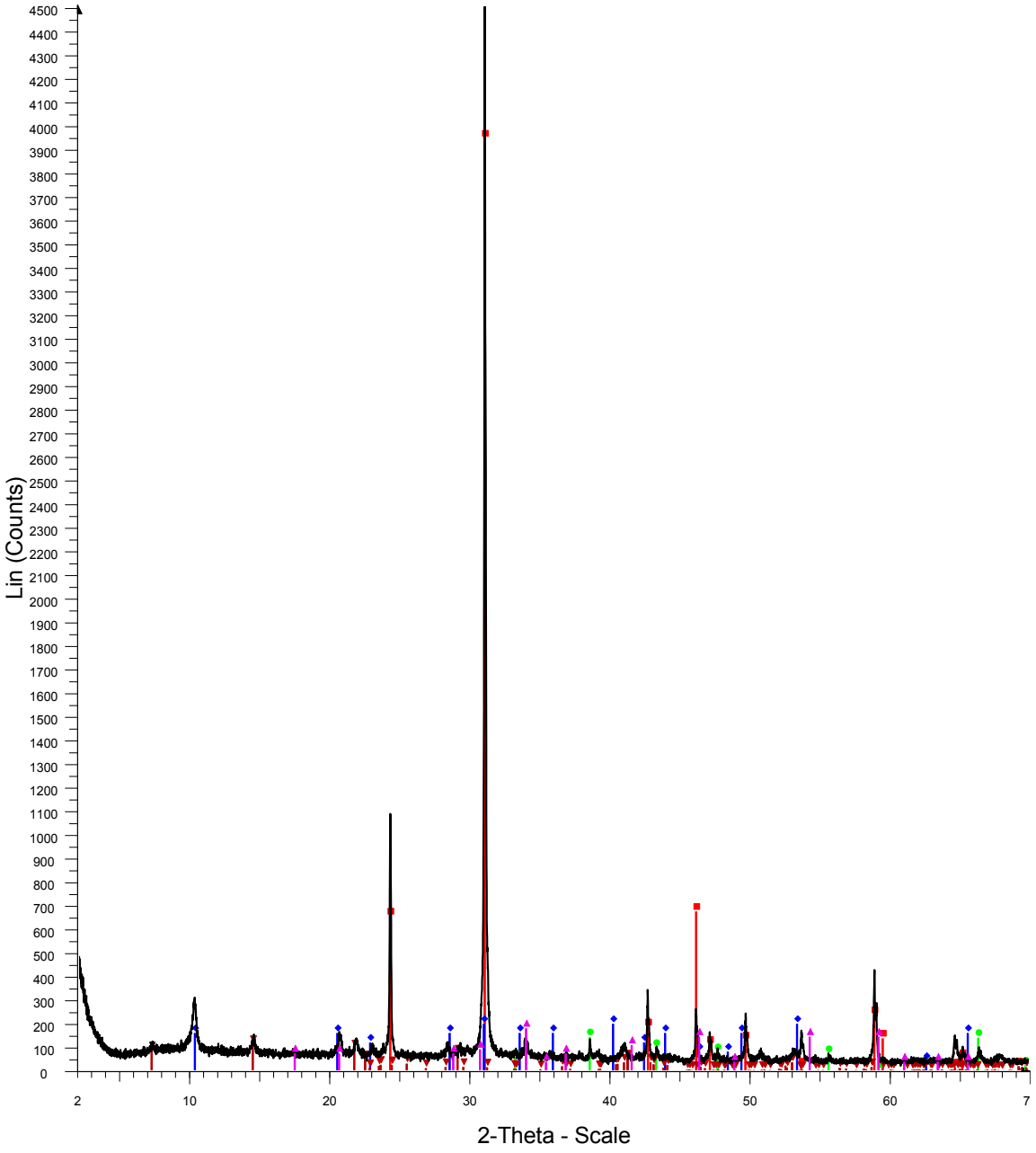

Red-Quartz
Blue-Illite
Green-Pyrite
Dark red-Chlorite
Pink-Jarosite

53

SF-13-054

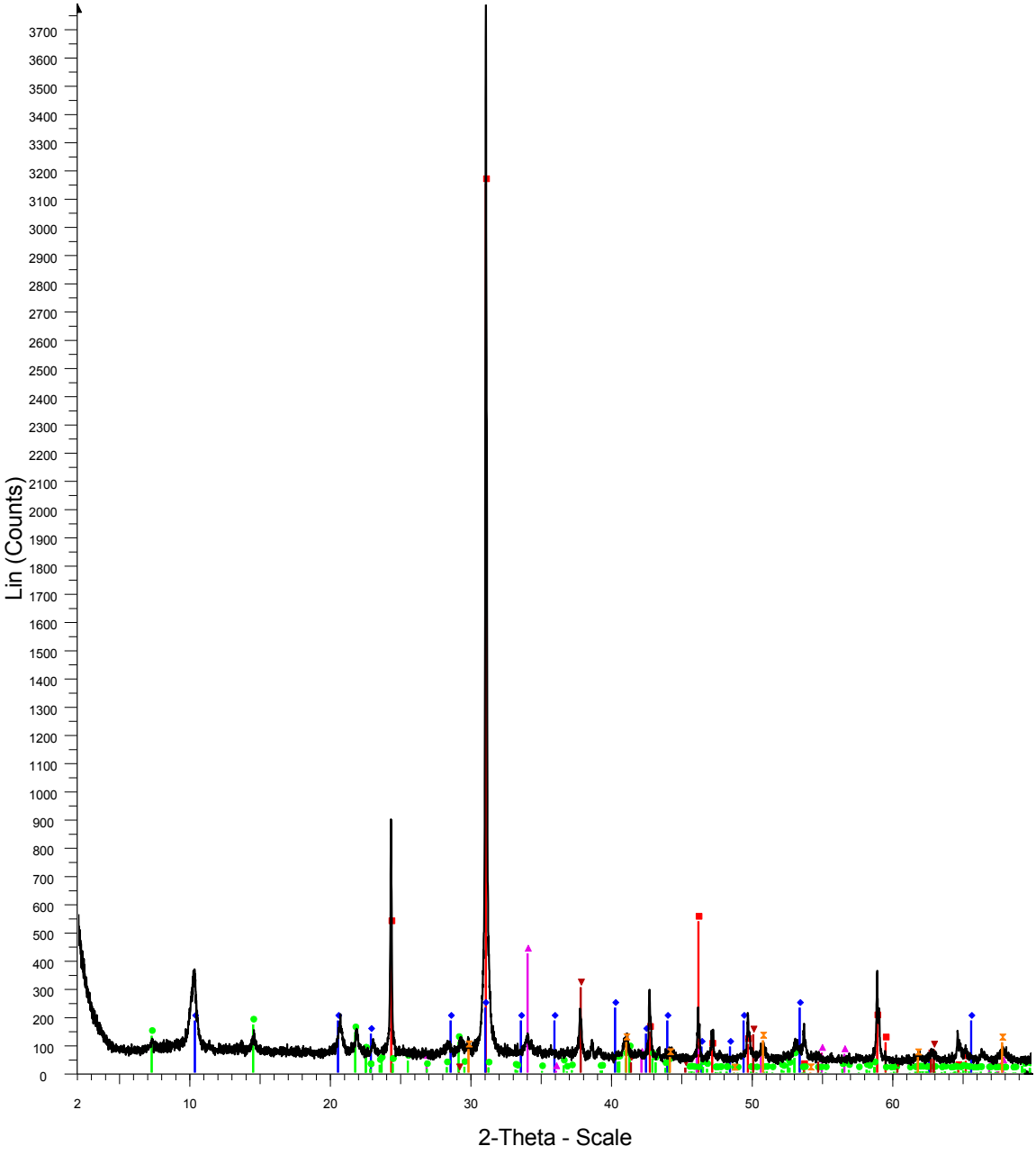

Red-Quartz
Blue-Illite
Pink-Calcite
Green-Chlorite
Dark red-Magnesite
Orange-Corundum

54

SF-13-055

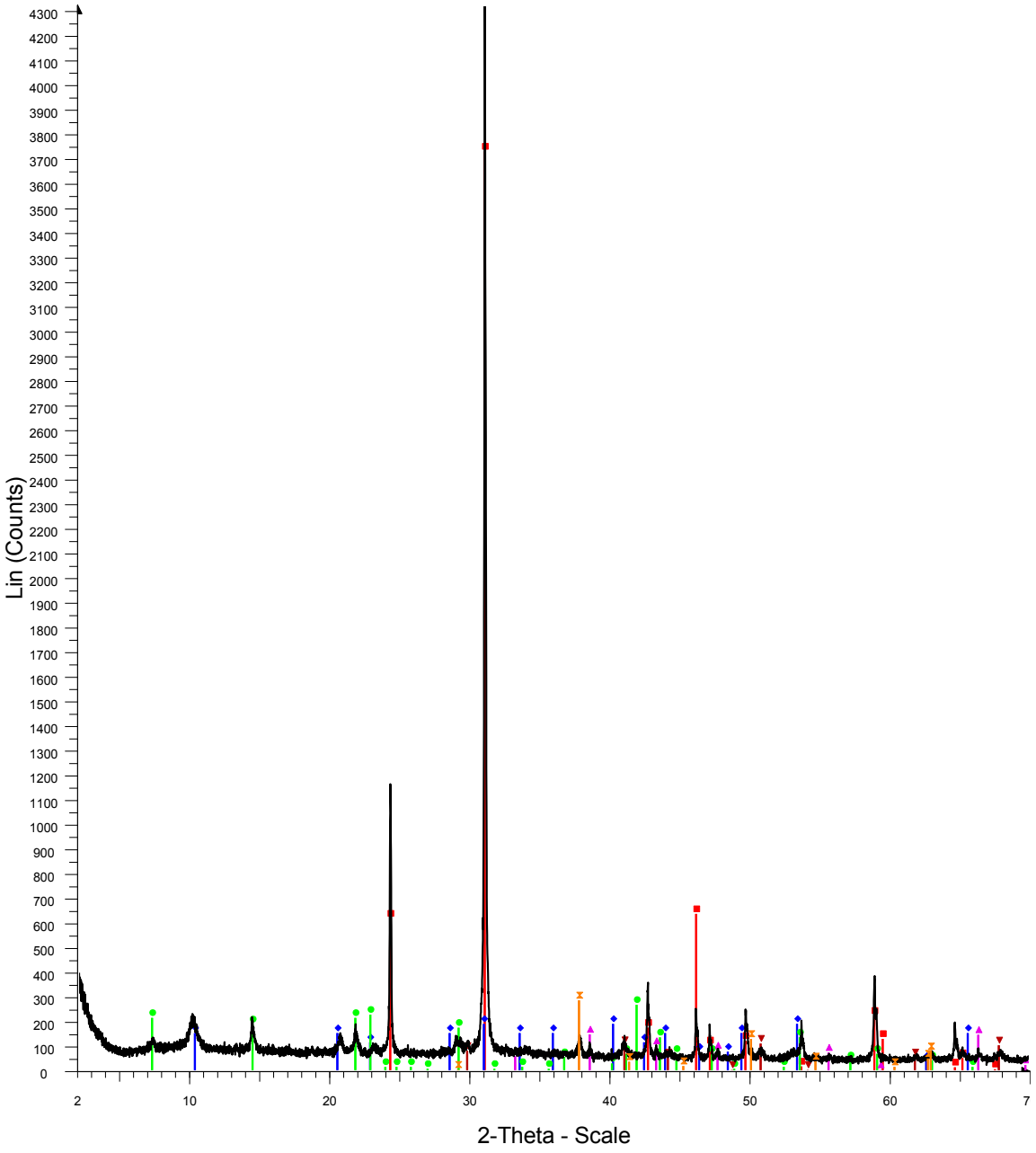

Red-Quartz
Blue-Illite
Green-Chlorite
Pink-Pyrite
Dark red-Corundum
Orange-Magnesite

55

SF-13-056

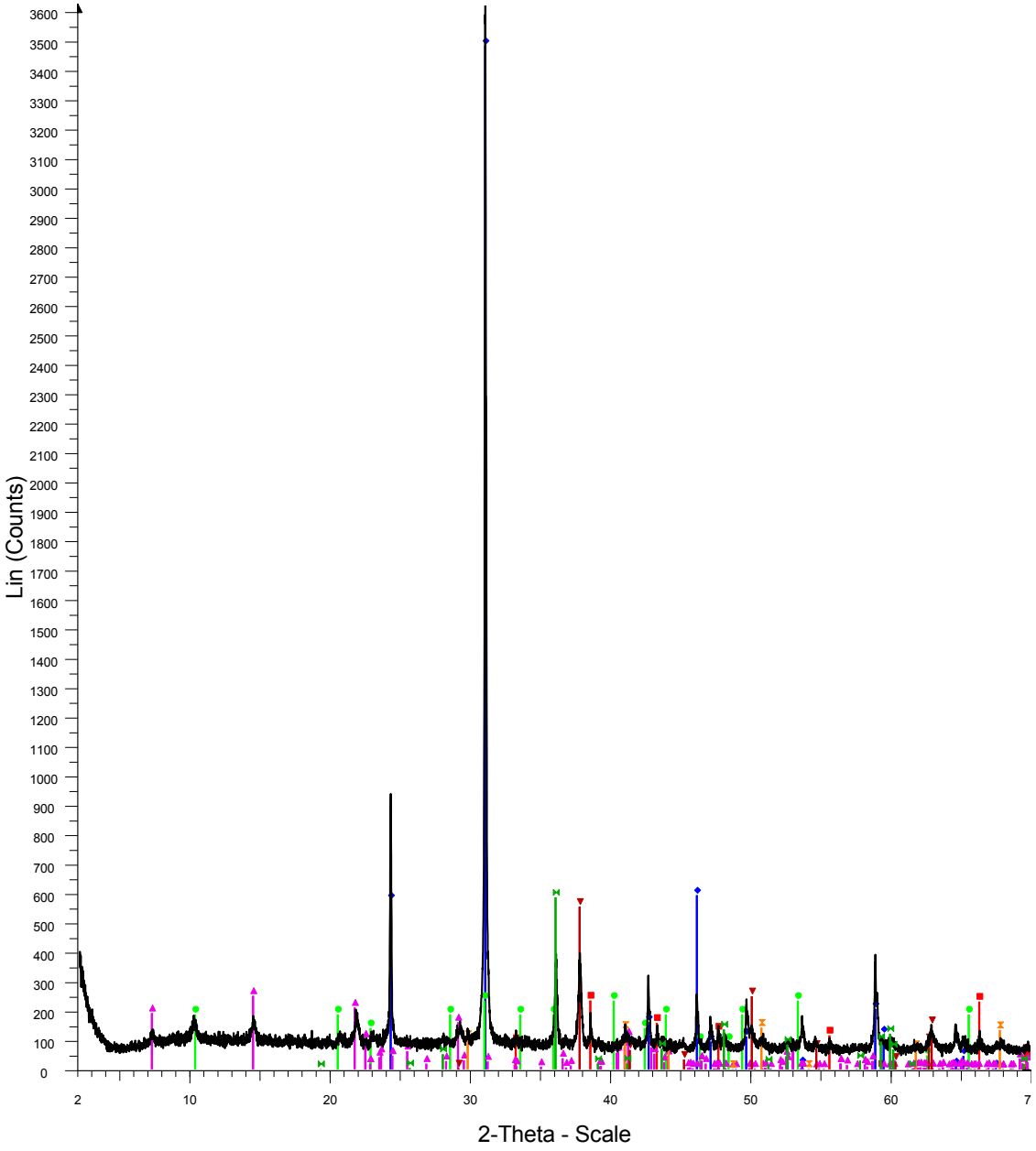

Red-Pyrite
Blue-Quartz
Green-Illite
Pink-Chlorite
Dark red-Magnesite
Orange-Corundum
Dark green-Dolomite

56

SF-13-057

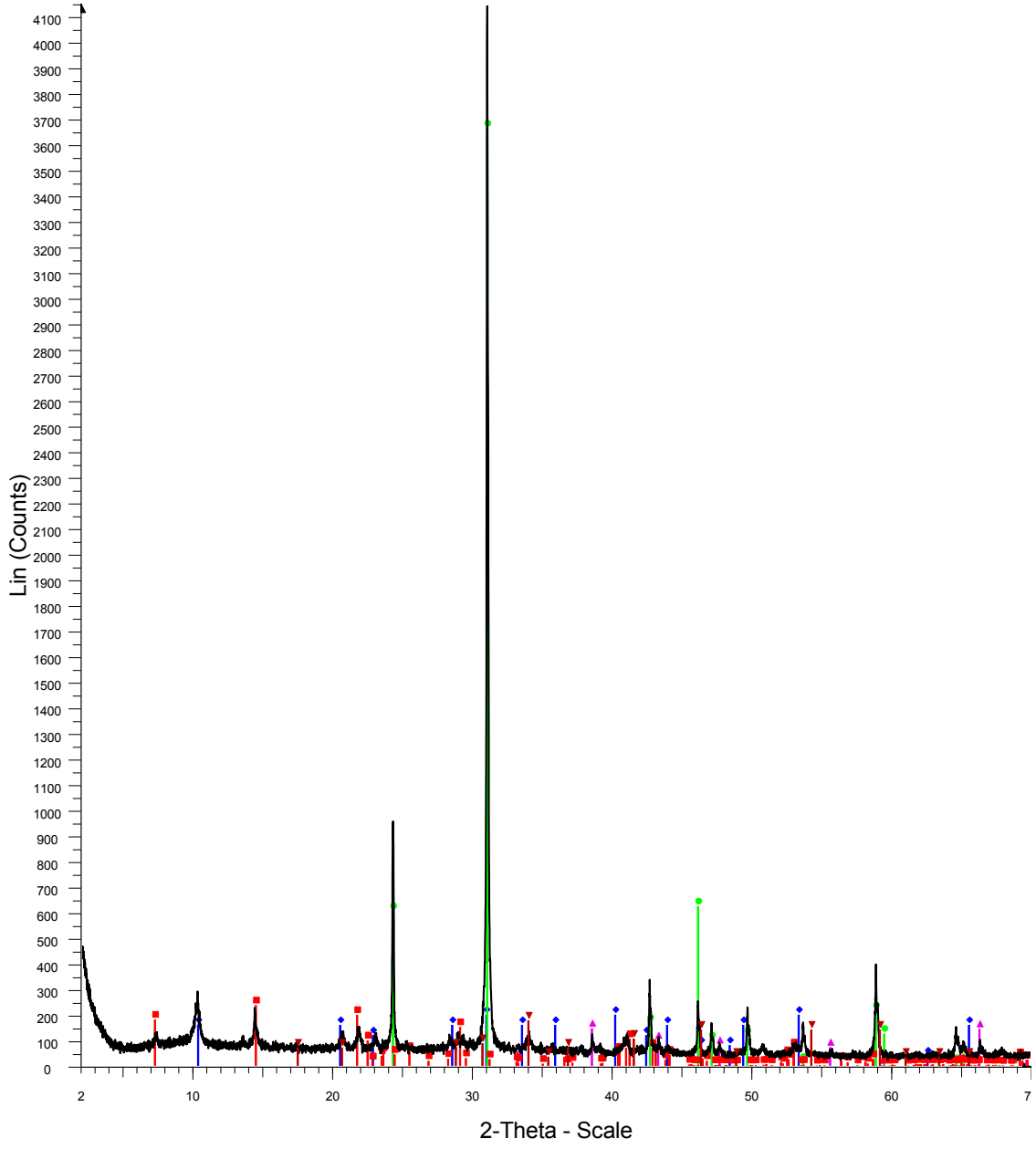

Blue-Illite
Green-Quartz
Pink-Pyrite
Red-Chlorite
Dark red-Jarosite

57

SF-13-058

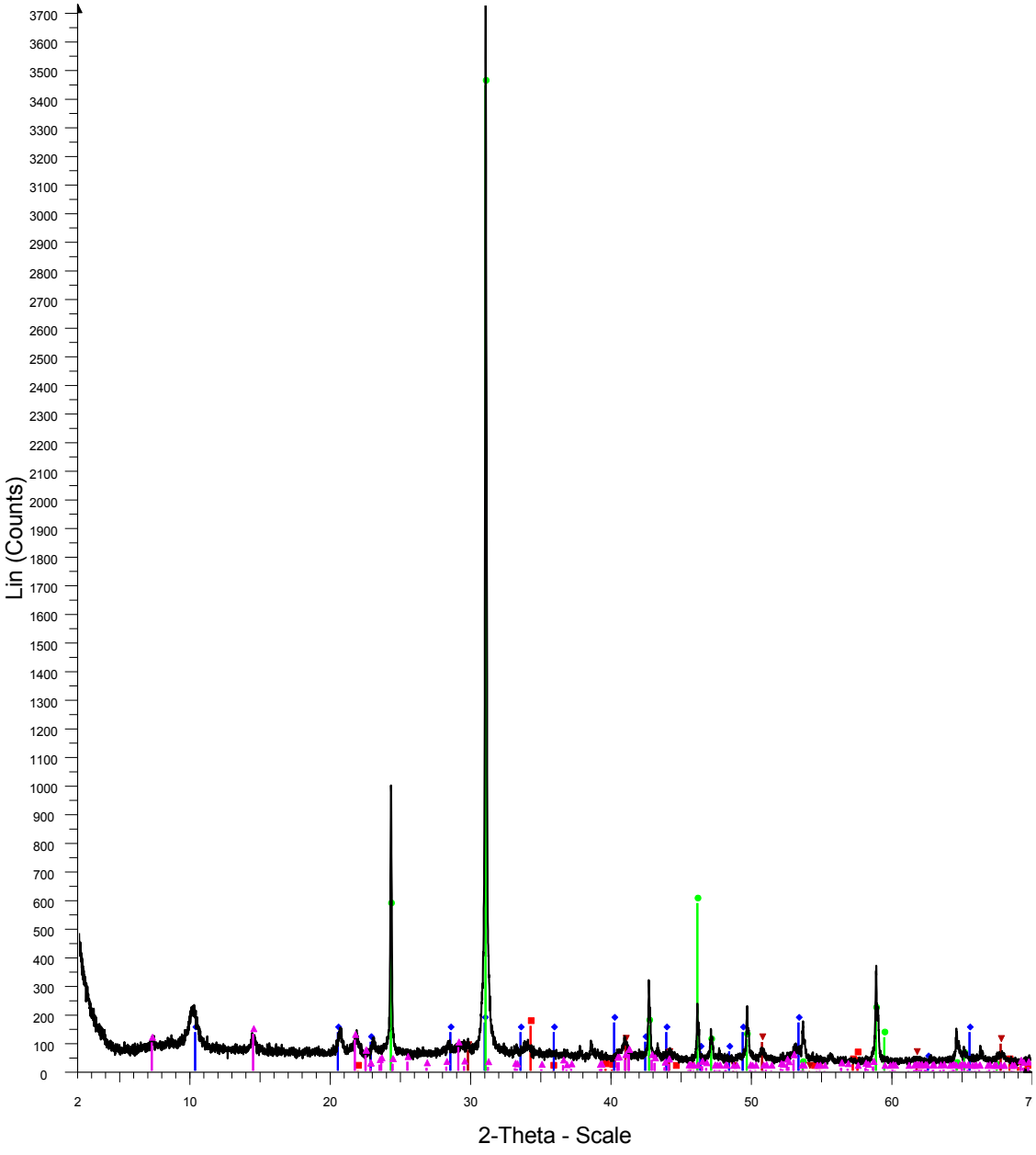

Red-Chalcopyrite
Blue-Illite
Green-Quartz
Dark red-Corundum
Pink-Chlorite

58

SF-13-059

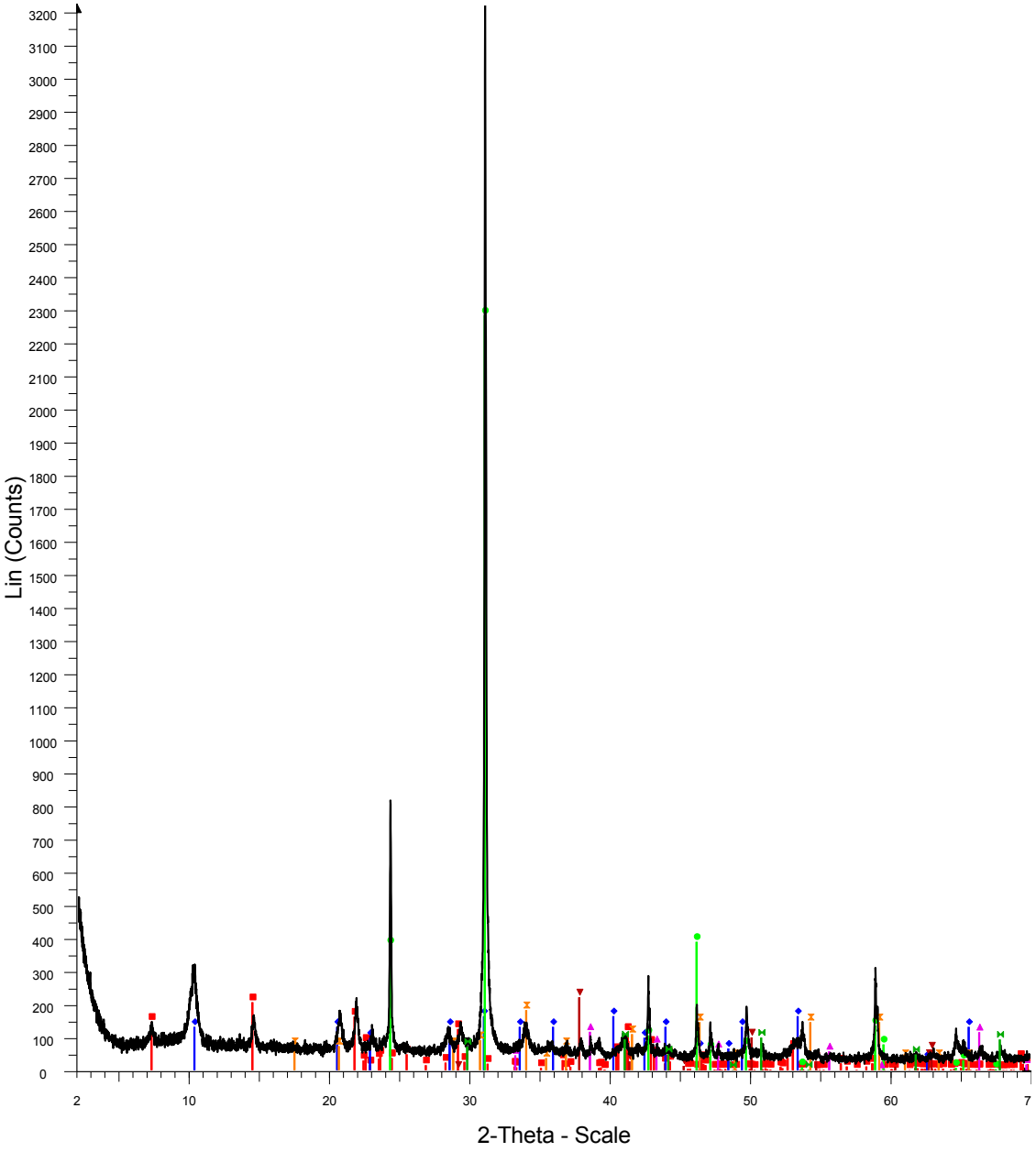

Red-Chlorite
Blue-Illite
Green-Quartz
Pink-Pyrite
Dark red-Magnesite
Orange-Jarosite
Dark green-Corundum
59

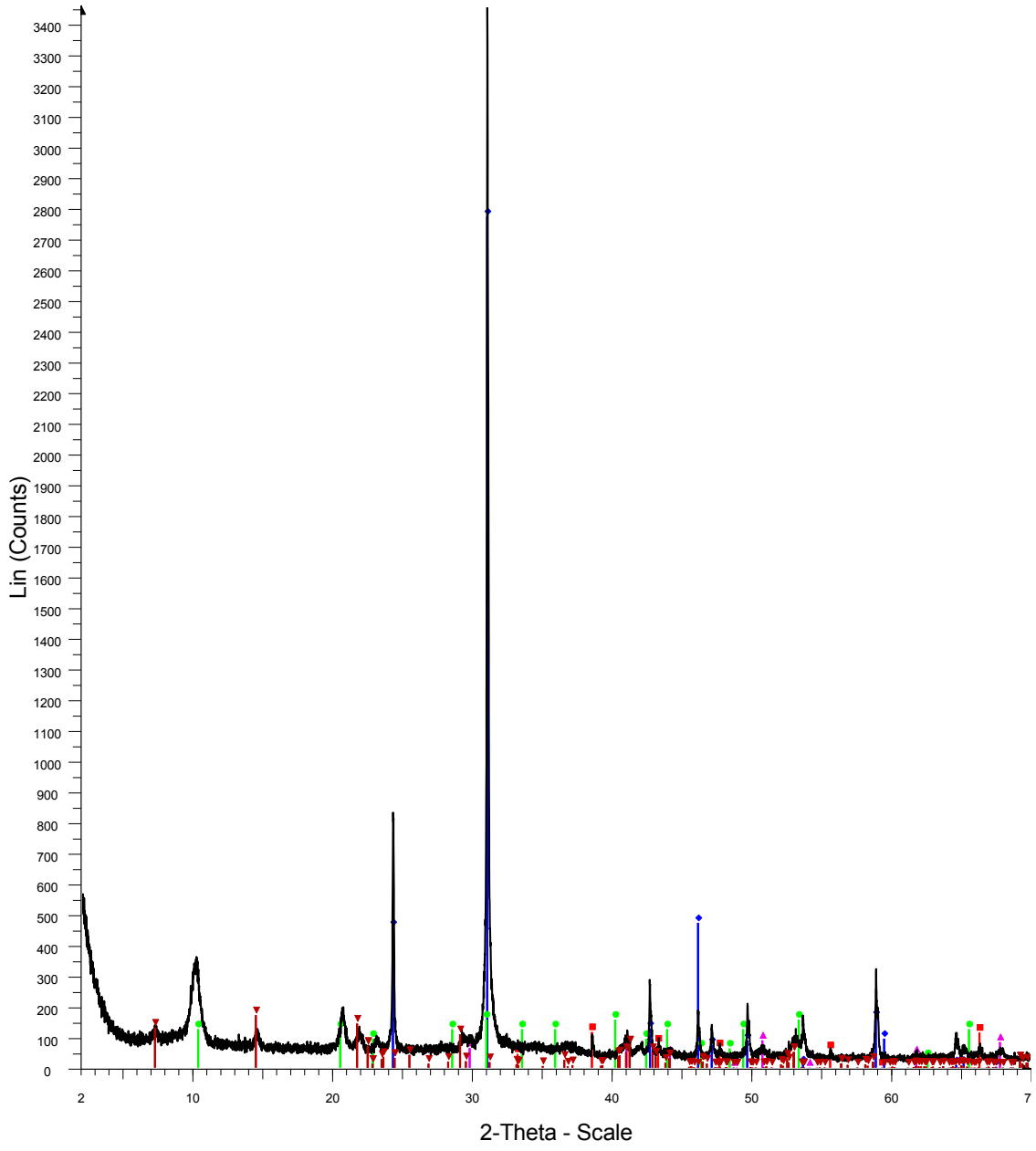

Red-Pyrite
Blue-Quartz
Green-Illite
Pink-Corundum
Dark red-Chlorite

60

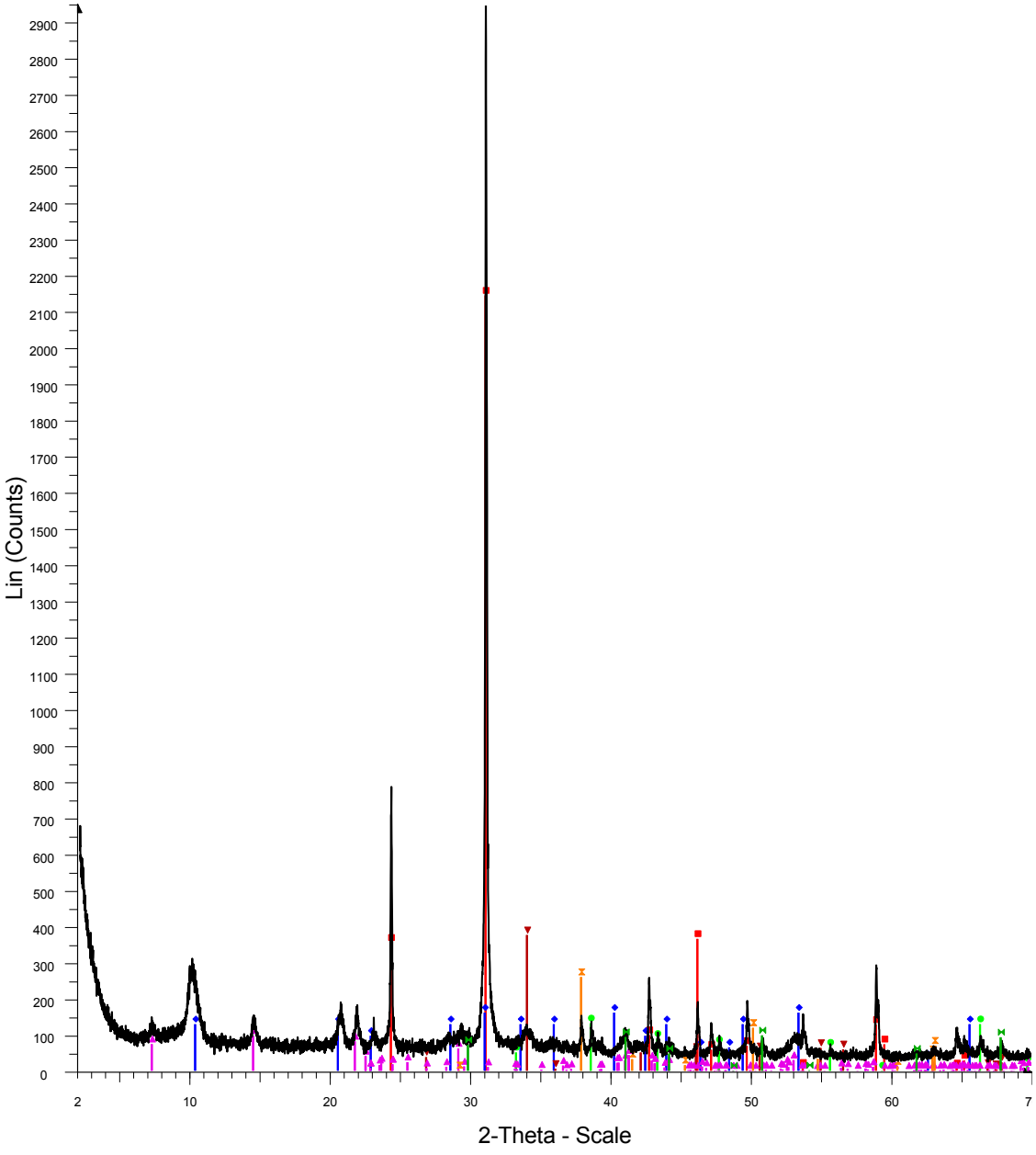

Red-Quartz
Blue-Illite
Green-Pyrite
Dark red-Calcite
Pink-Chlorite
Orange-Magnesite
Dark green-Corundum
61

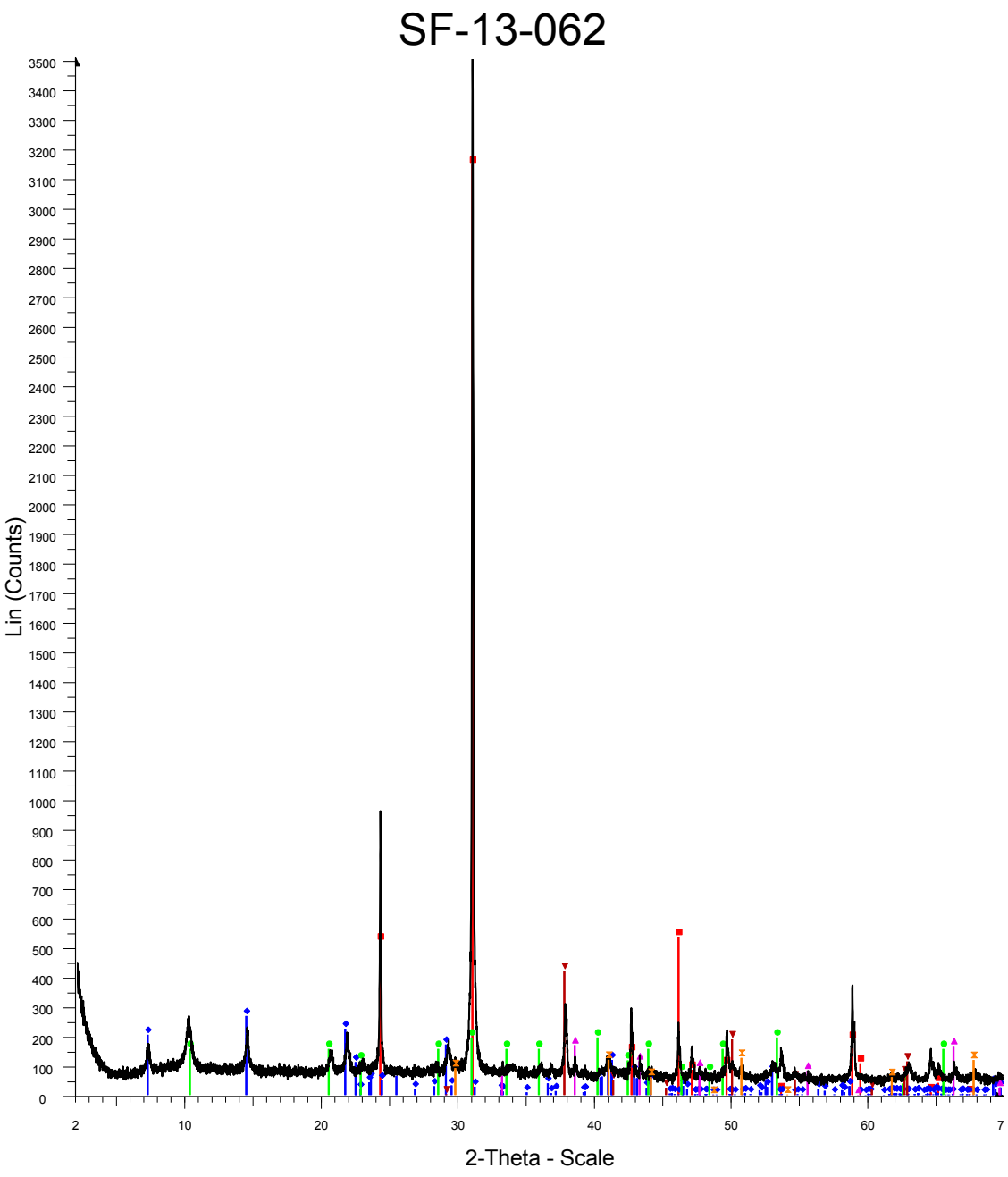

Red-Quartz
Blue-Chlorite
Green-Illite
Pink-Pyrite
Dark red-Magnesite
Orange-Corundum
62

SF-13-063

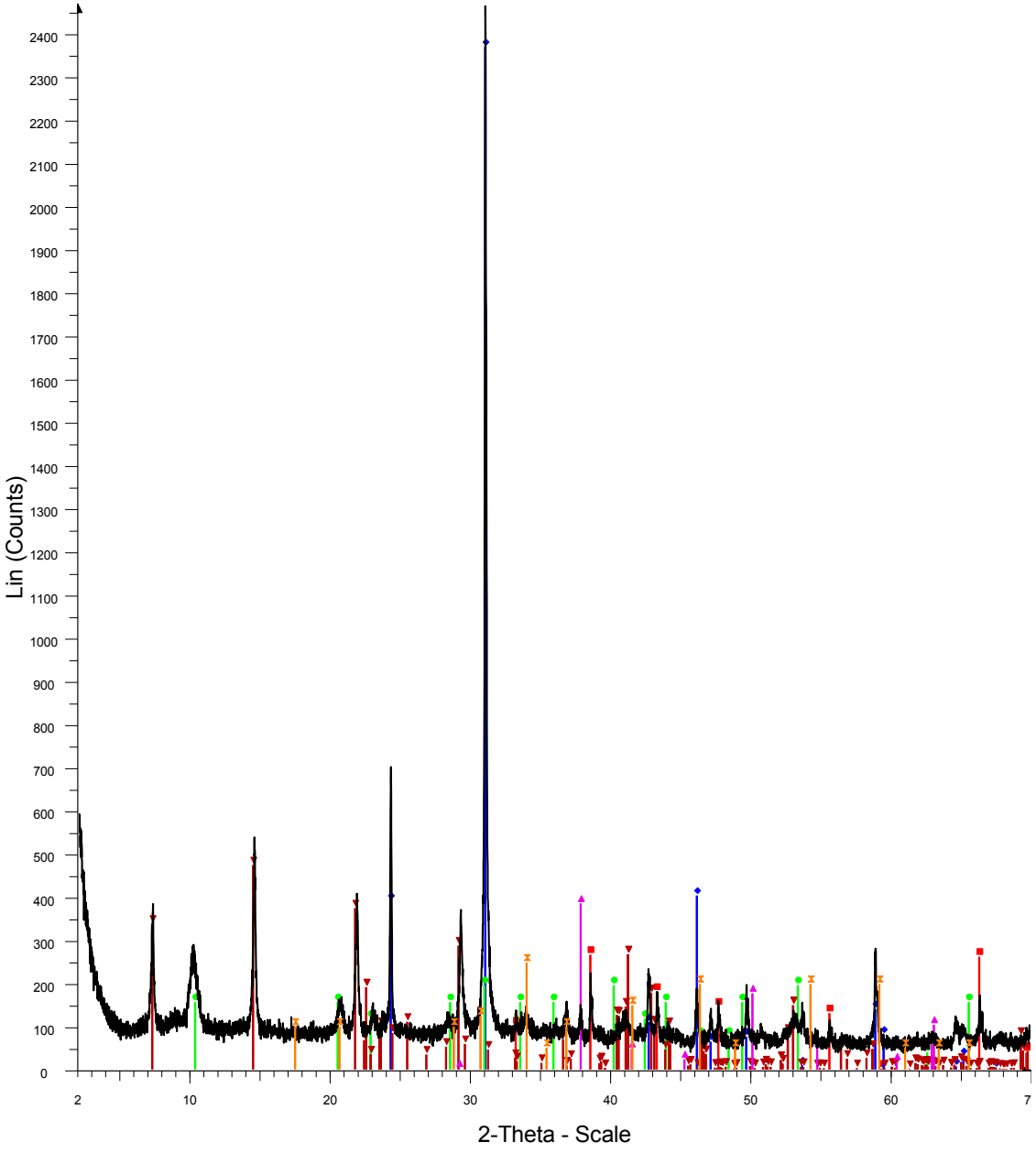

Red-Pyrite
Blue-Quartz
Green-Illite
Dark red-Chlorite
Pink-Magnesite
Orange-Jarosite
63

SF-13-064

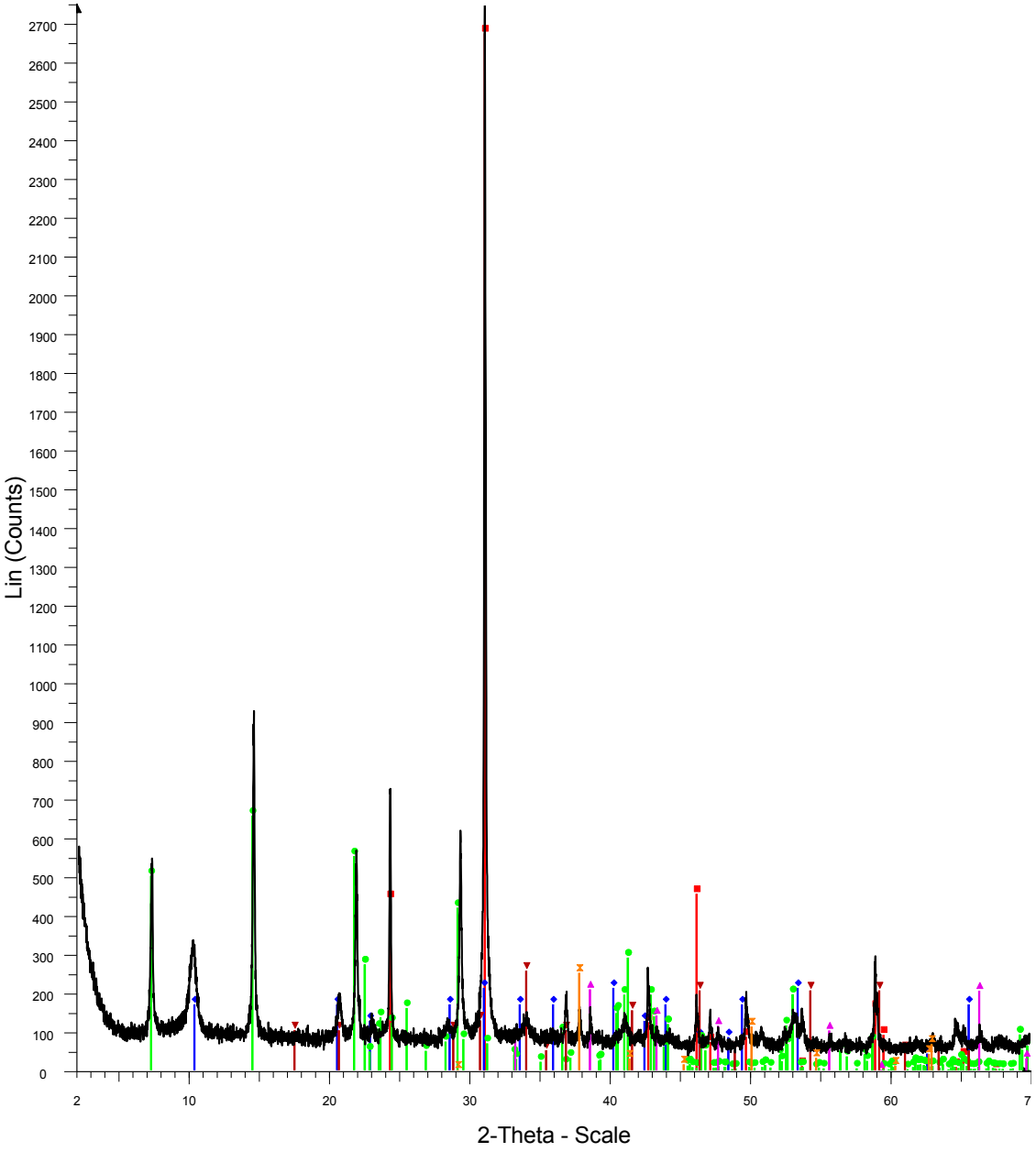

Red-Quartz
Blue-Illite
Green-Chlorite
Pink-Pyrite
Dark red-Jarosite
Orange-Magnesite
64

SF-13-065

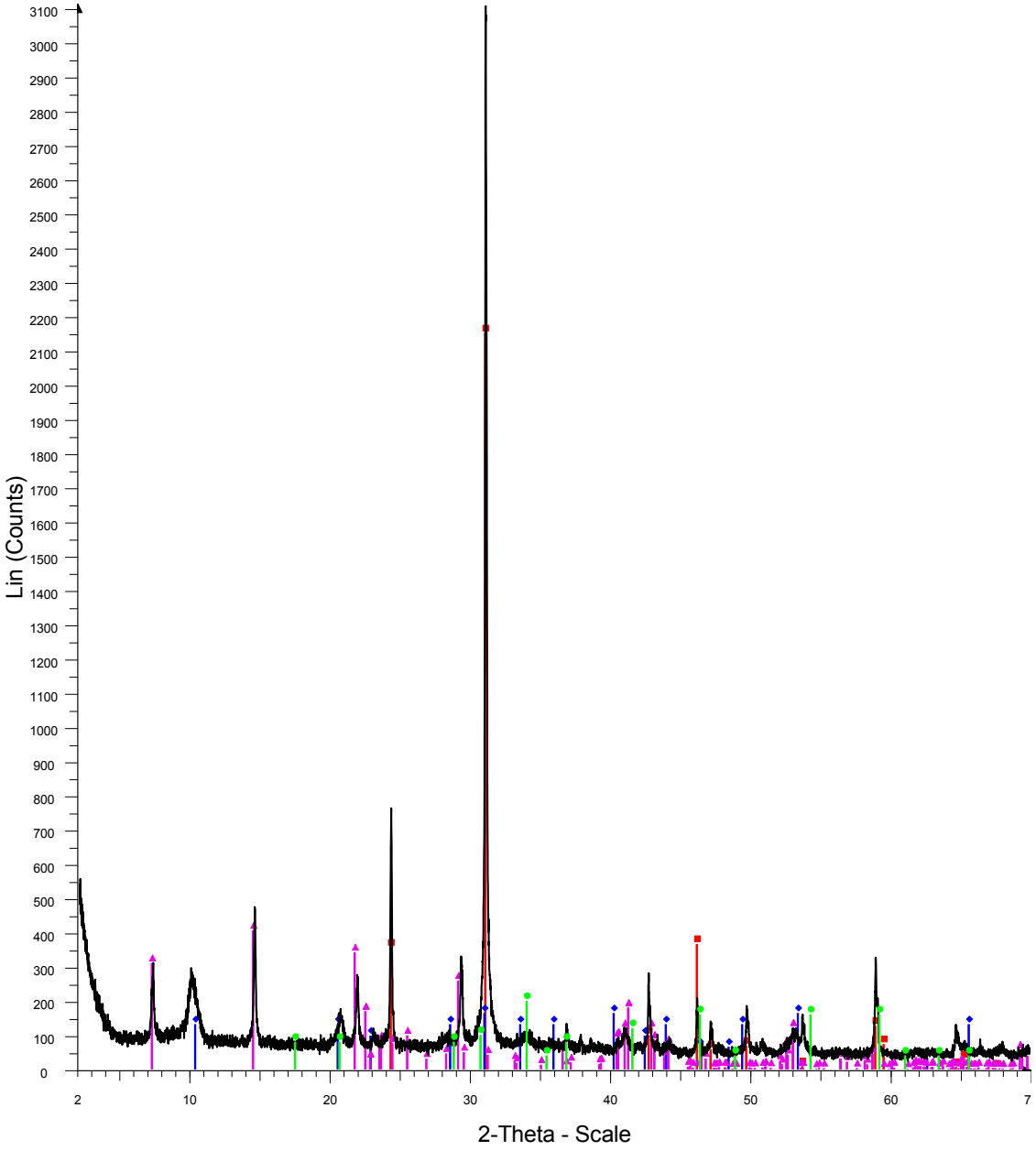

Red-Quartz
Blue-Illite
Pink-Chlorite
Green-Jarosite
65

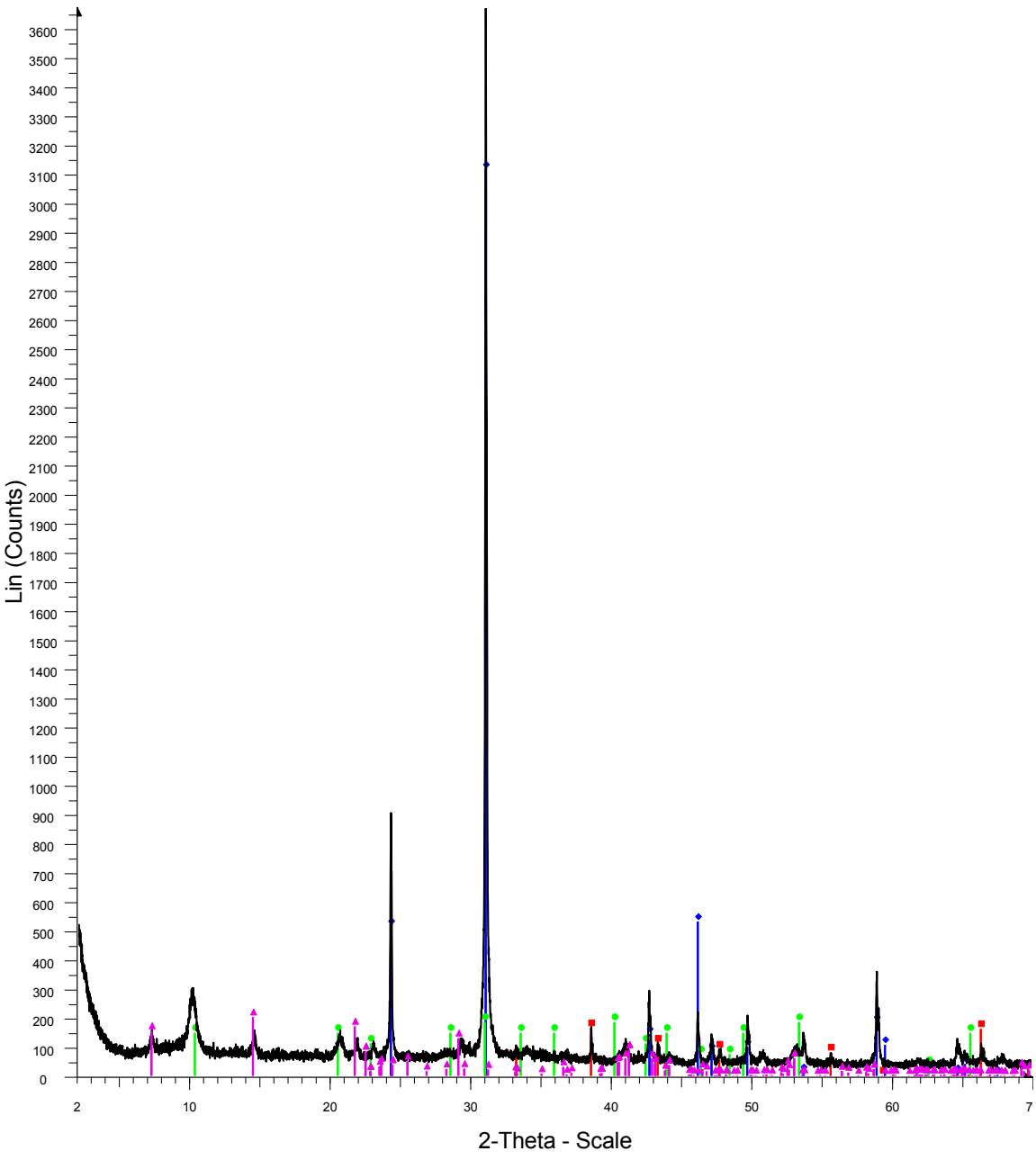

Red-Pyrite
Blue-Quartz
Green-Illite
Pink-Chlorite
66host

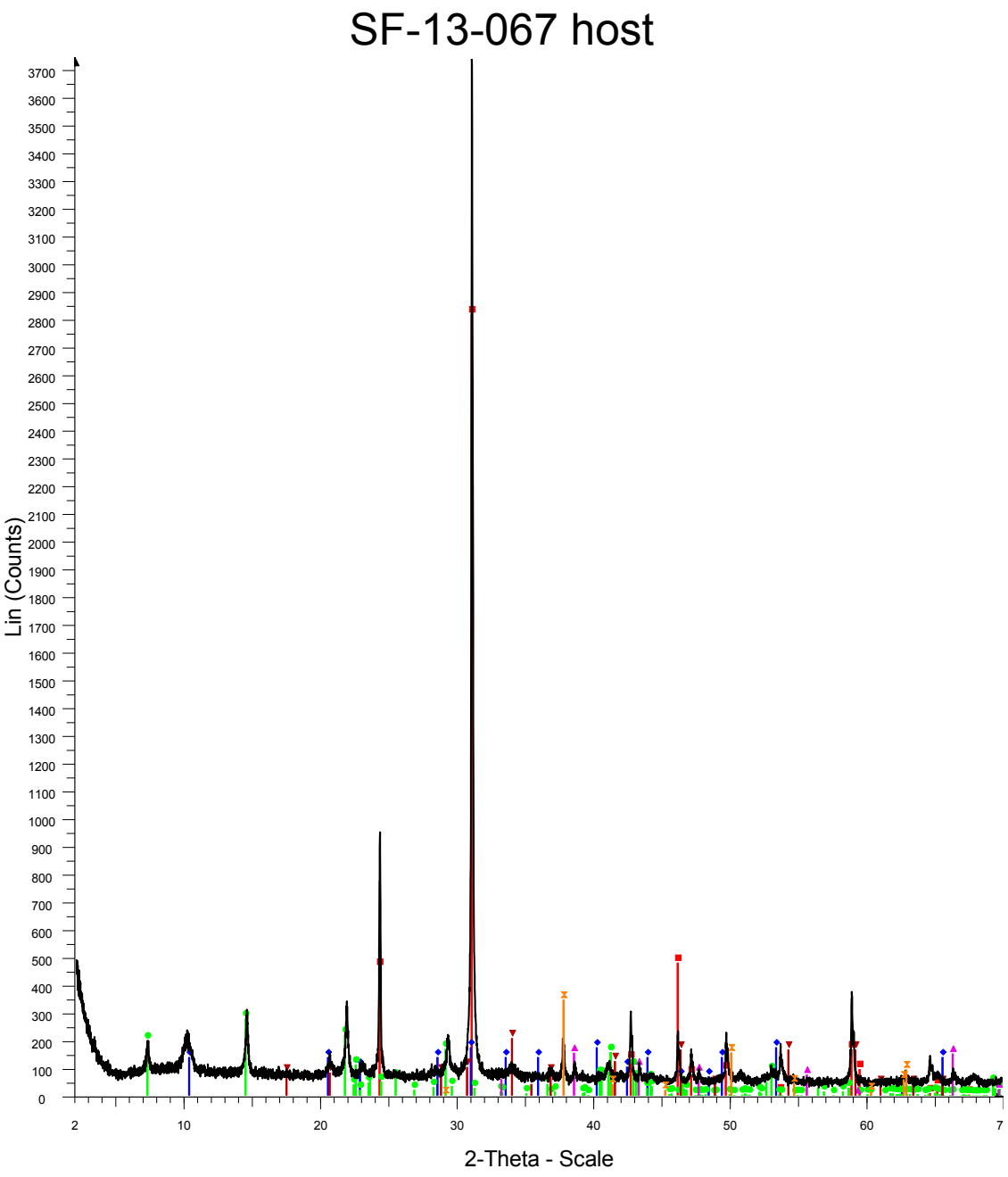

Red-Quartz
Blue-Illite
Green-Chlorite
Pink-Pyrite
Dark red-Jarosite
Orange-Magnesite
67host

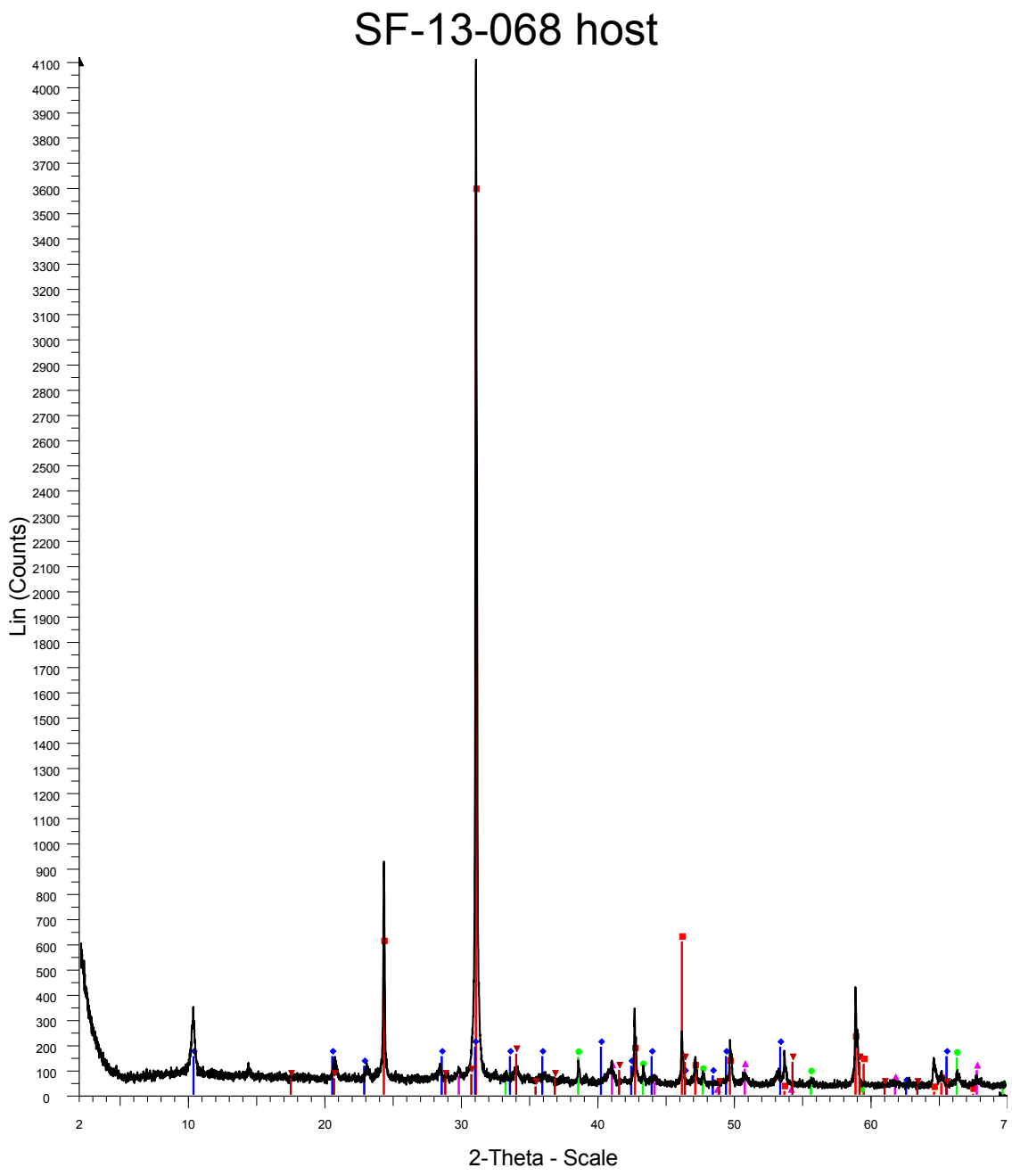

Red-Quartz
Blue-Illite
Green-Pyrite
Pink-Corundum
Dark red-Jarosite
68host

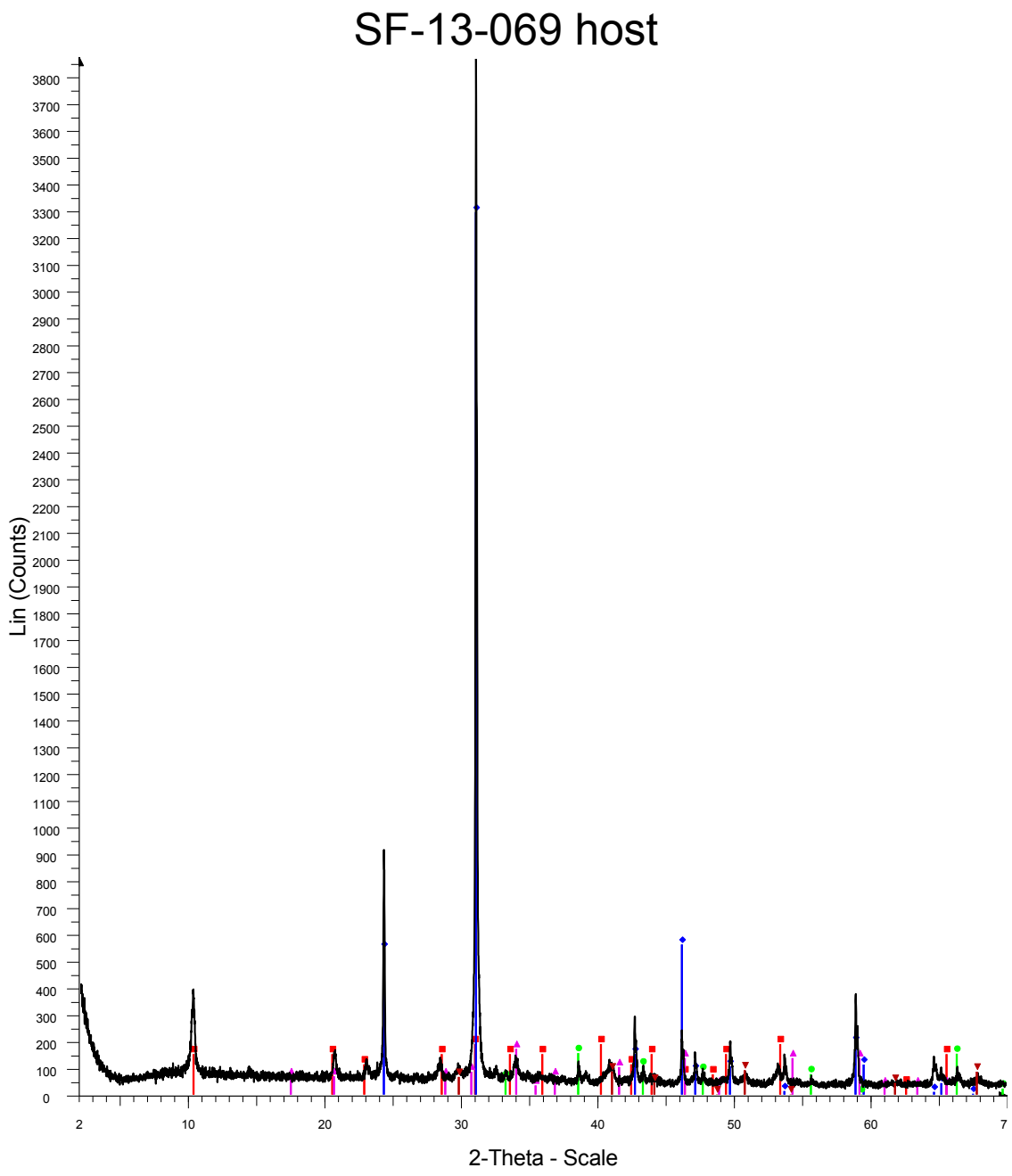

Red-Illite
Blue-Quartz
Green-Pyrite
Pink-Jarosite
Dark red-Corundum
69host

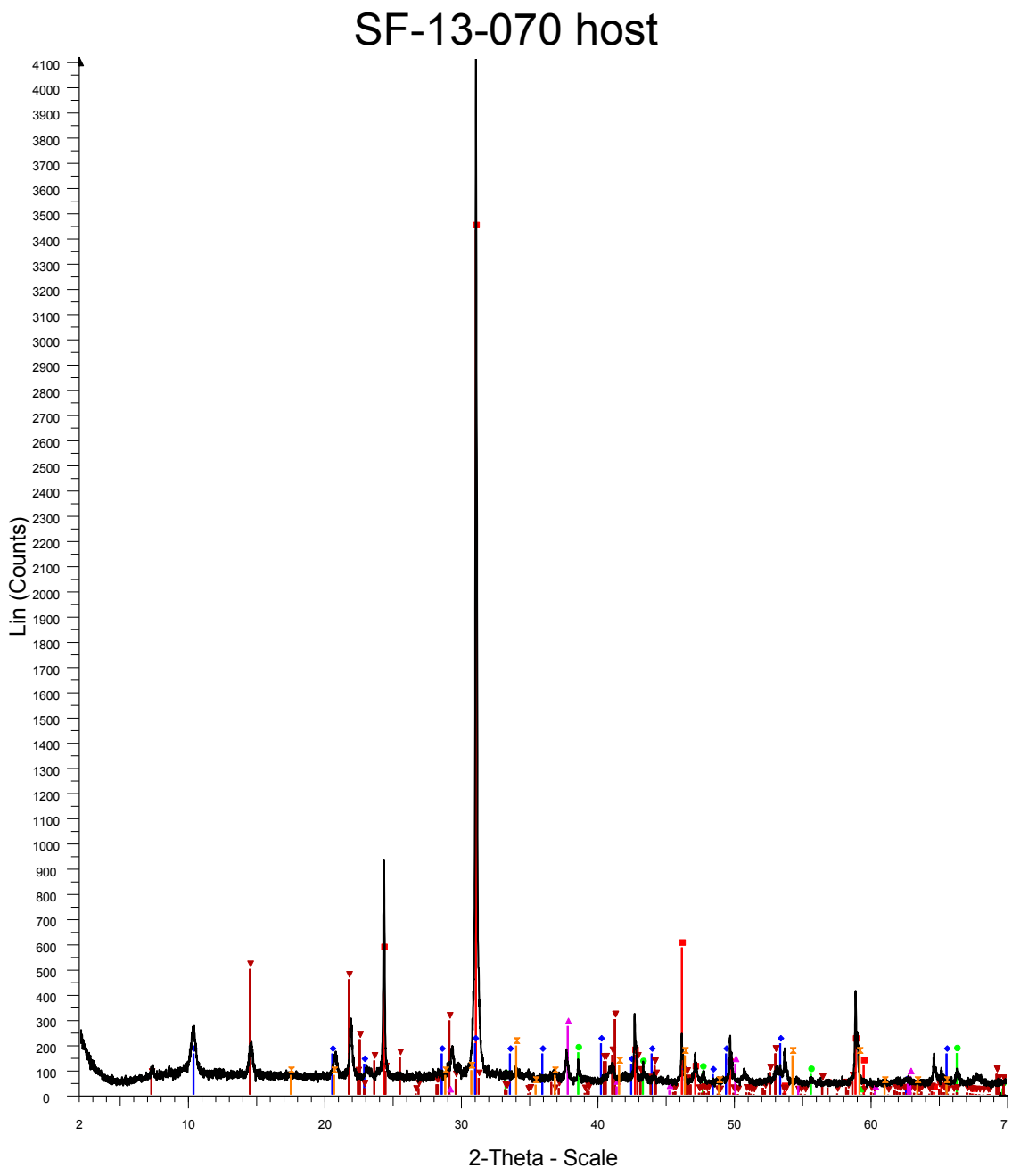

Red-Quartz
Blue-Illite
Green-Pyrite
Dark red-Chlorite
Pink-Magnesite
Orange-Jarosite
70host

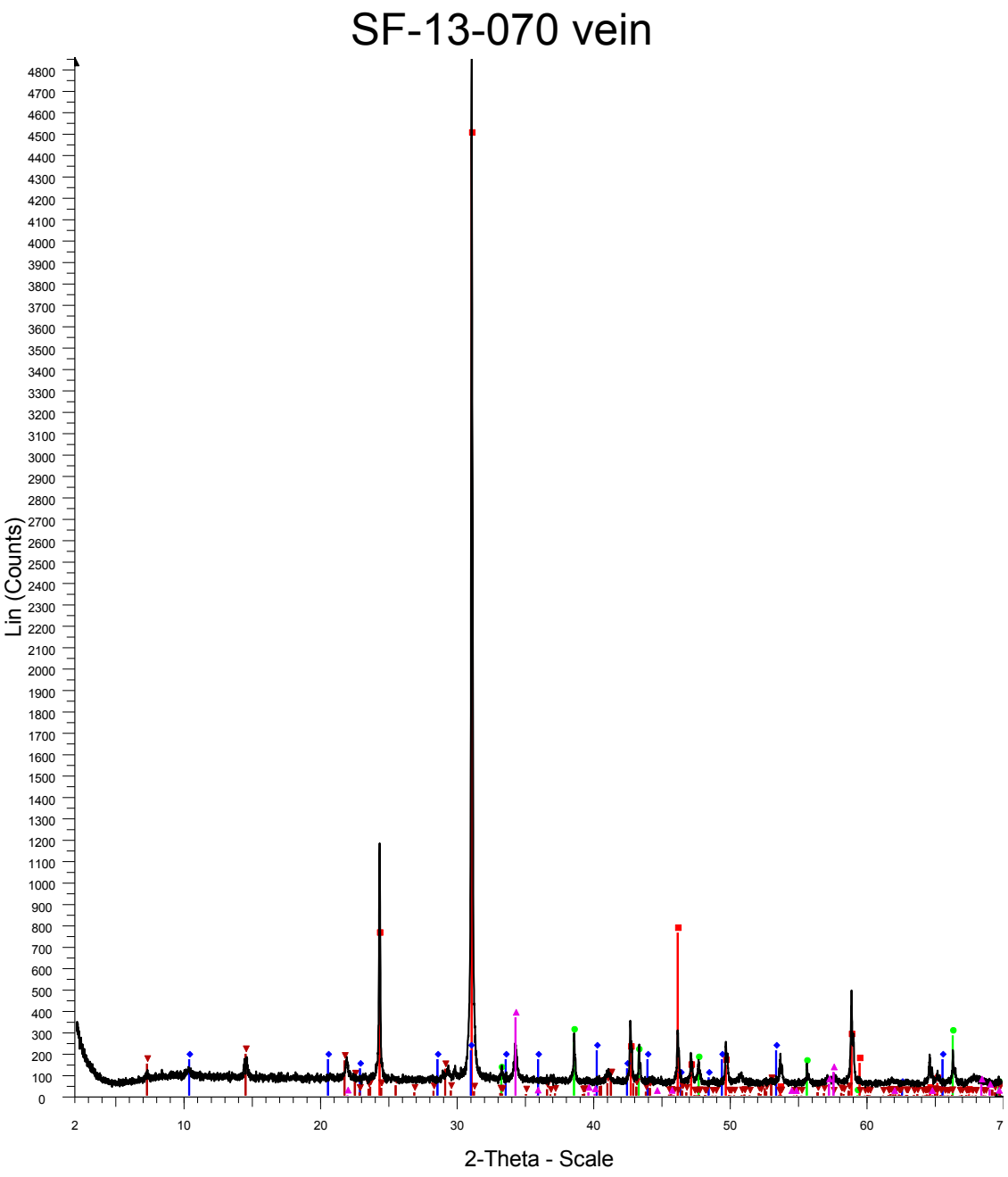

Red-Quartz
Blue-Illite
Green-Pyrite
Dark red-Chlorite
Pink-Chalcopyrite
70vein

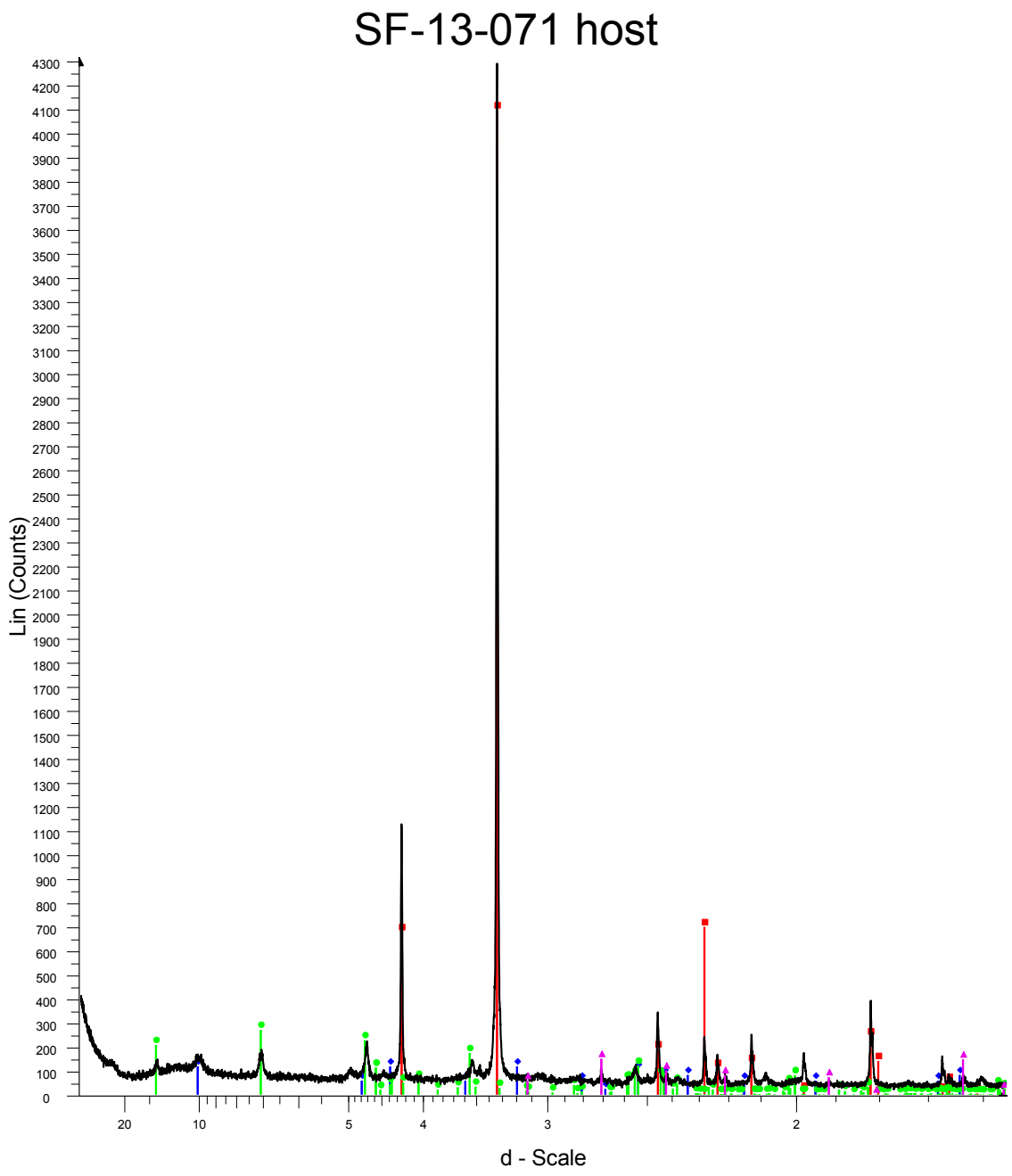

Red-Quartz
Blue-Illite
Green-Chlorite
Pink-Pyrite
71host

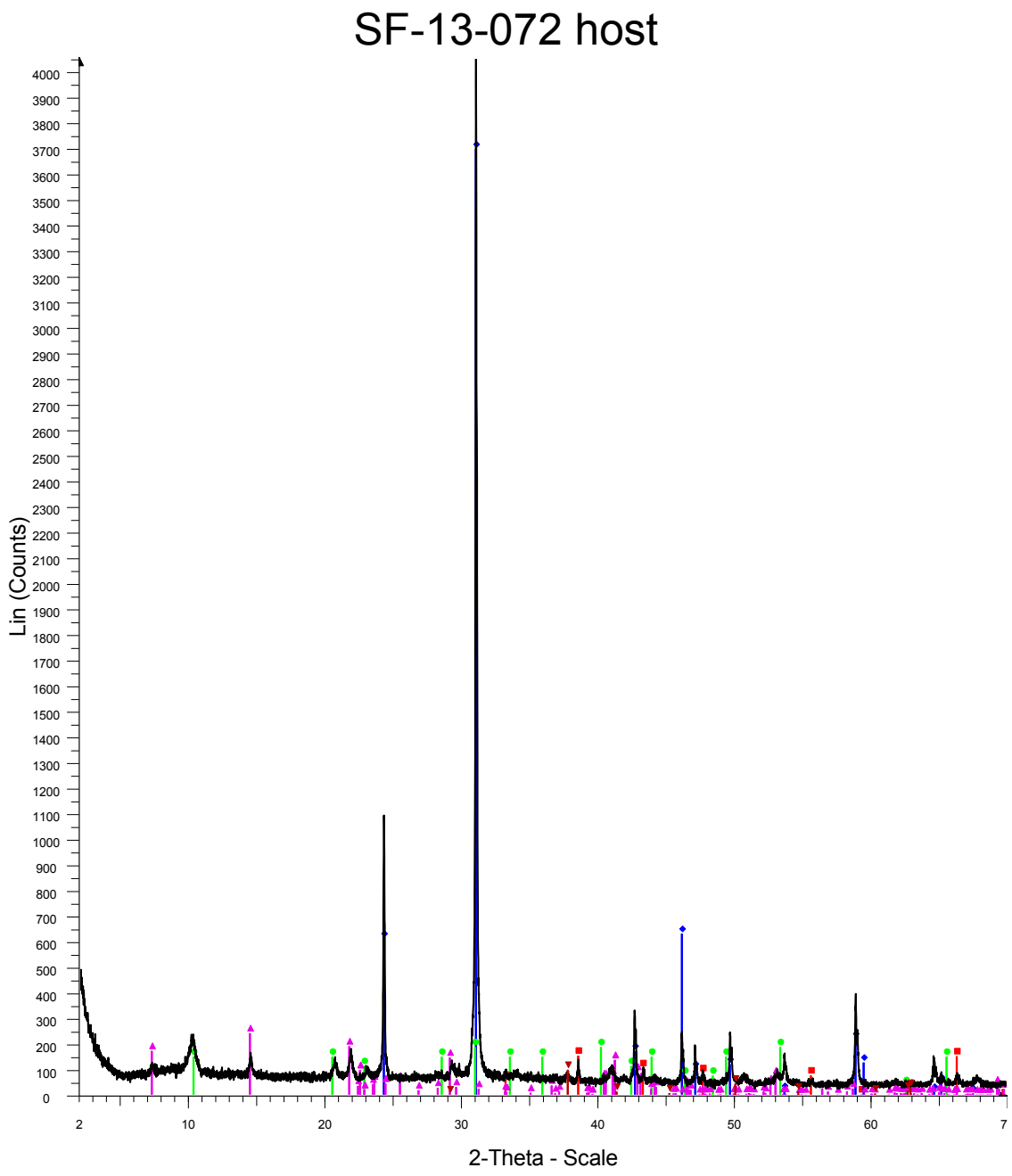

Red-Pyrite
Blue-Quartz
Green-Illite
Pink-Chlorite
Dark red-Magnesite
72host

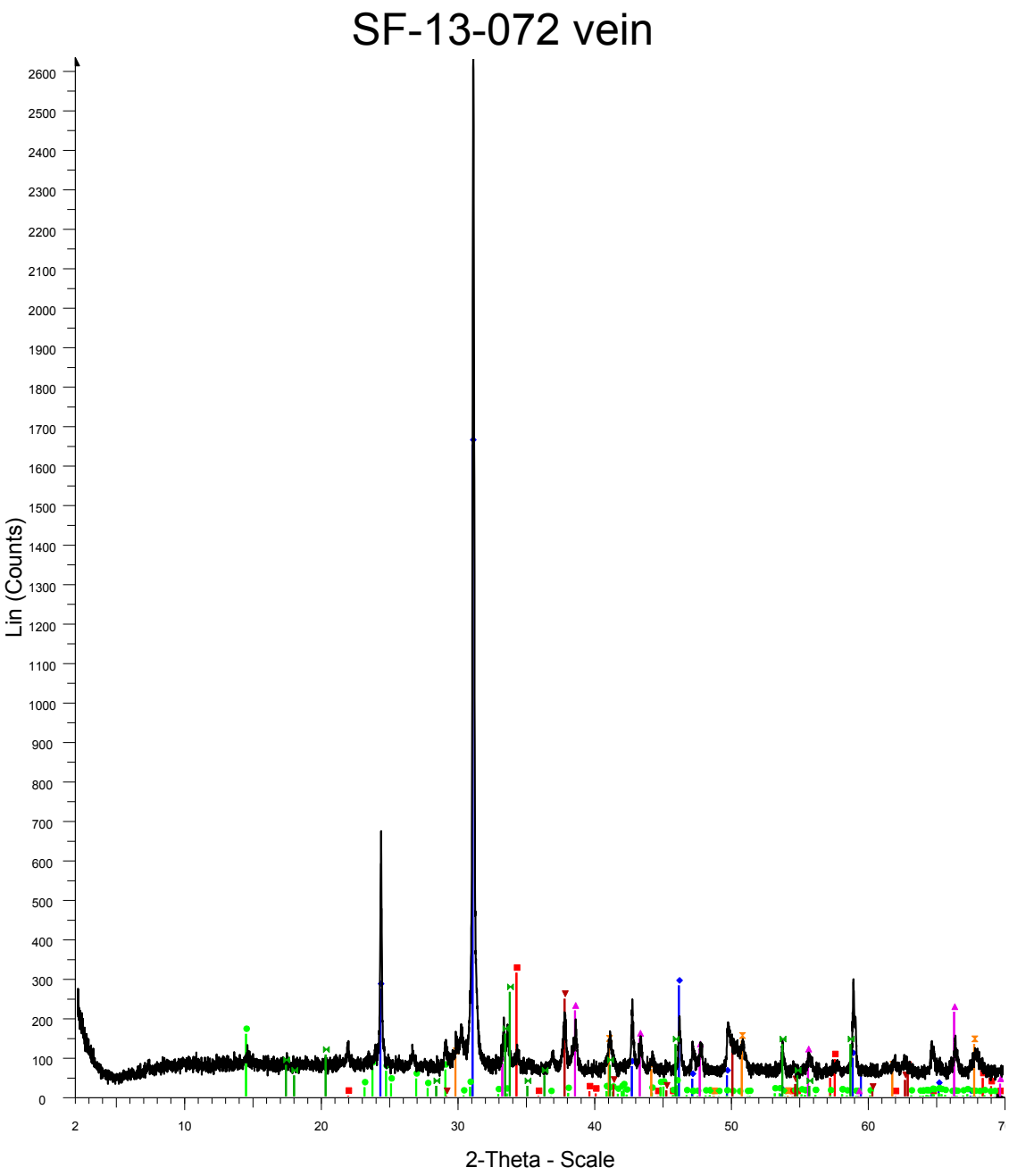

Red-Chalcopyrite
Blue-Quartz
Green-Kaolinite
Pink-Pyrite
Dark red-Magnesite
Orange-Corundum
Dark green-Jarosite
72vein

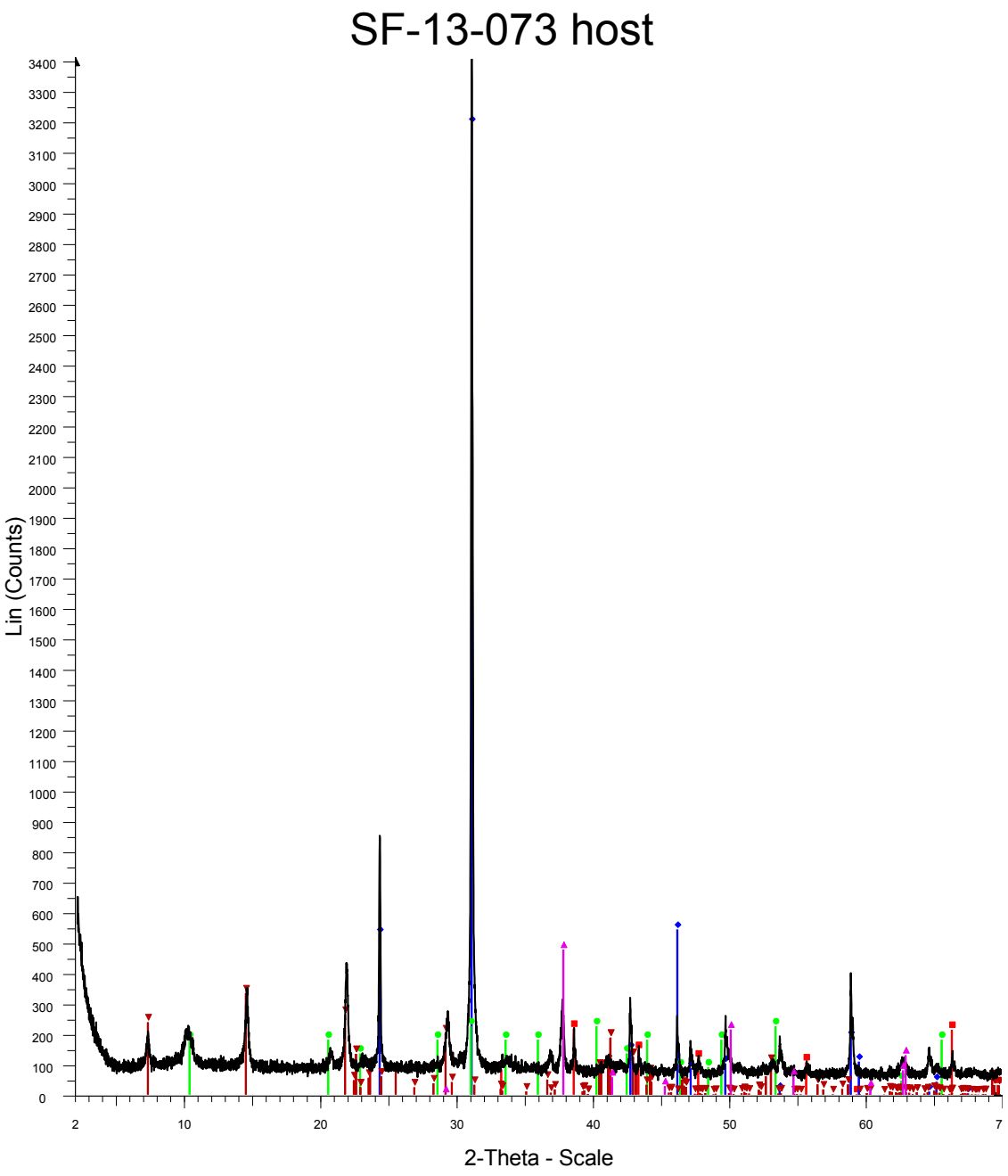

Red-Pyrite
Blue-Quartz
Green-Illite
Dark red-Chlorite
Pink-Magnesite
73host

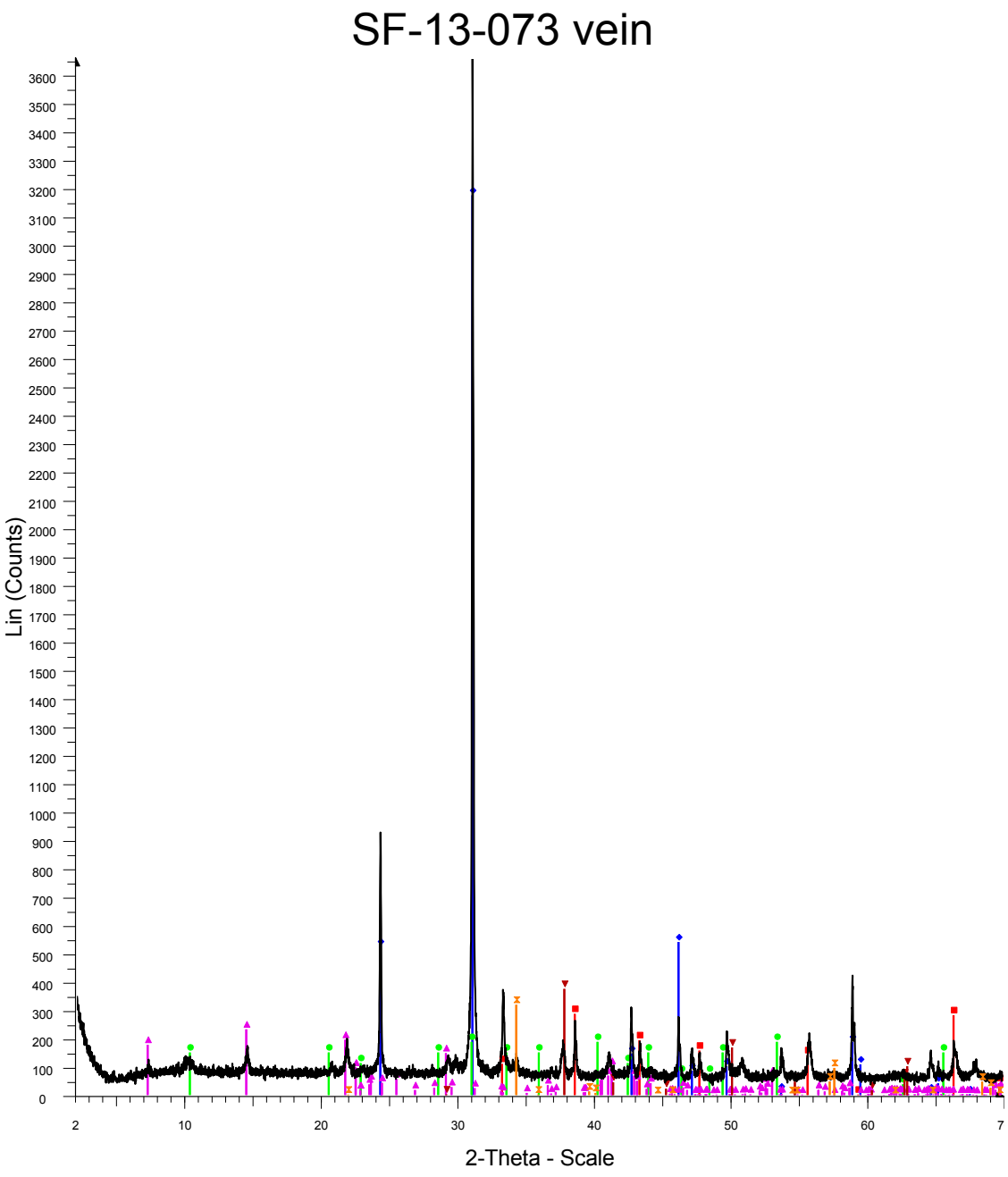

Red-Pyrite
Blue-Quartz
Green-Illite
Pink-Chlorite
Dark red-Magnesite
Orange-Chalcopyrite

73vein

SF-13-074 host

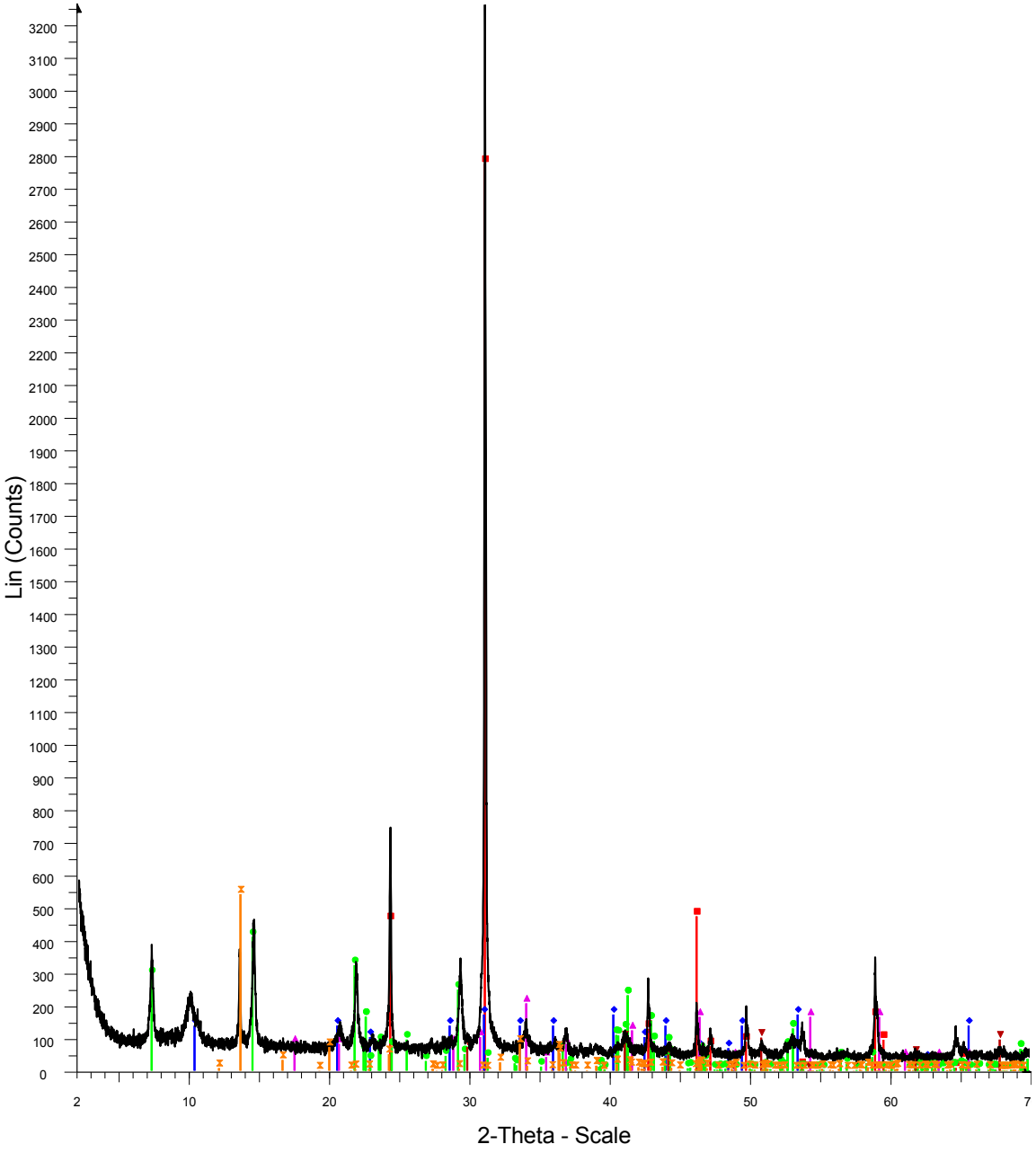

Red-Quartz
Blue-Illite
Green-Chlorite
Pink-Jarosite
Dark red-Corundum
Orange-Gypsum

74host

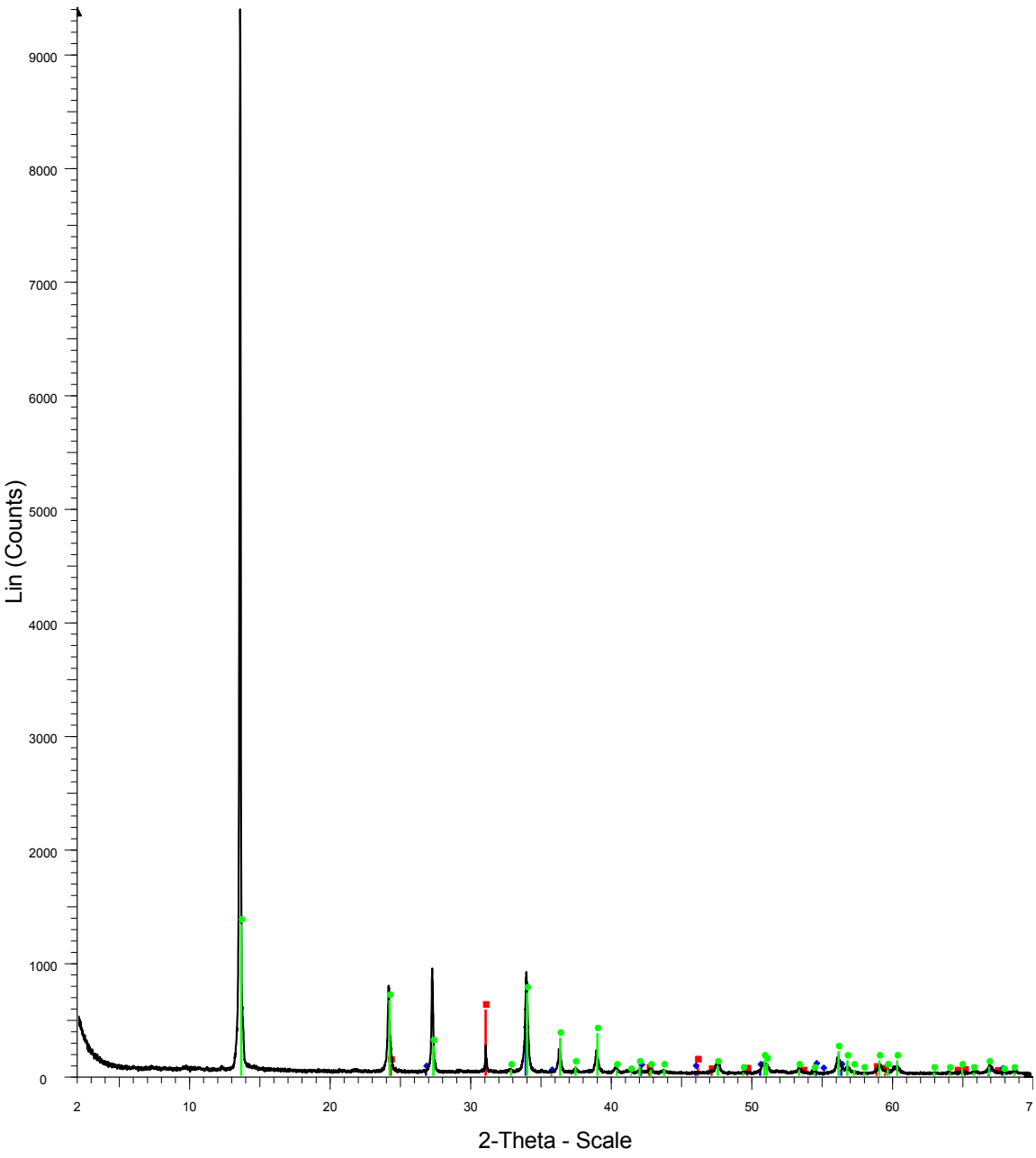

Red-Quartz
Blue-Calcite
Green-Gypsum

74vein

SF-13-075

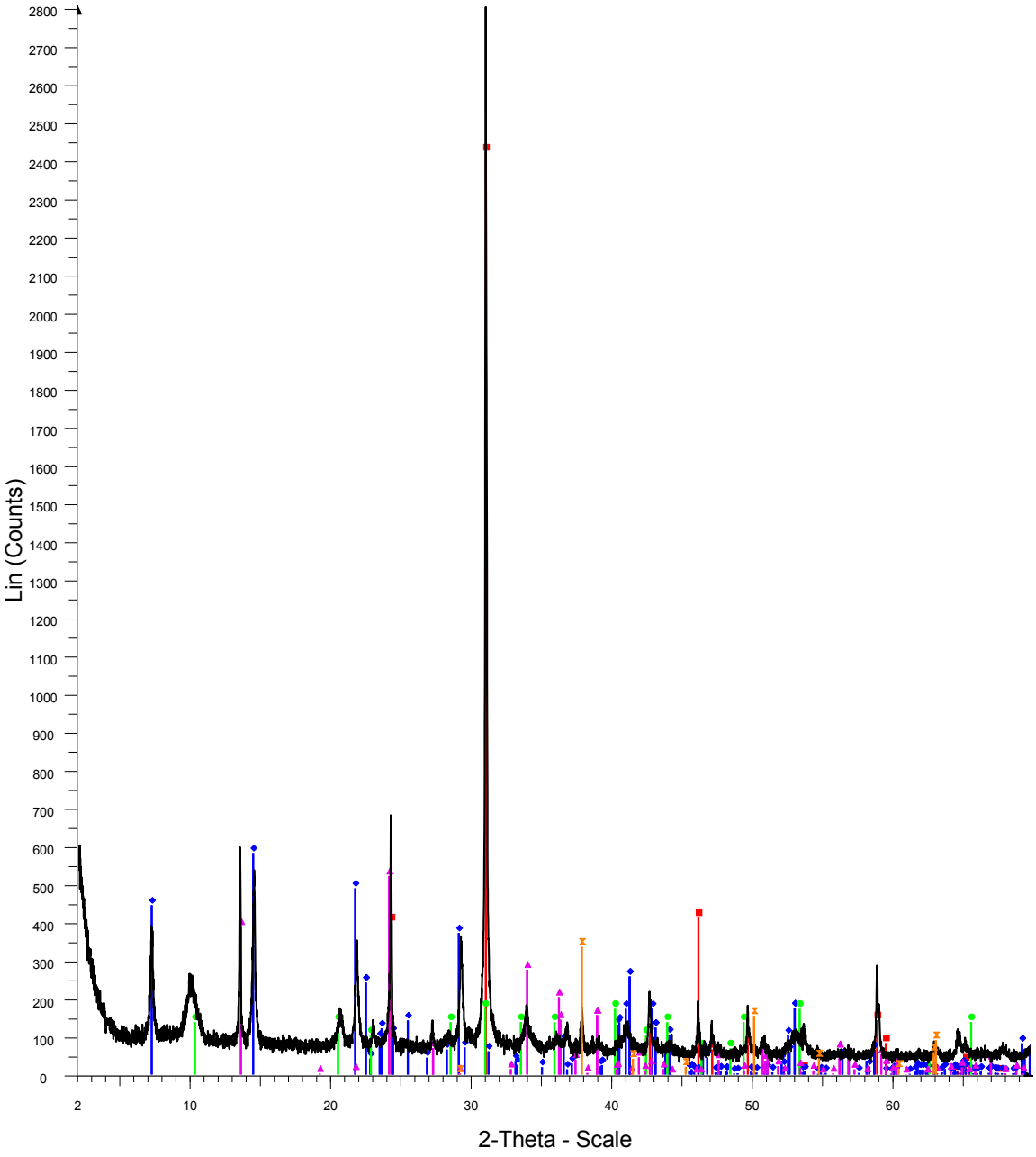

Red-Quartz
Blue-Chlorite
Green-Illite
Pink-Gypsum
Orange-Magnesite

75

SF-13-076

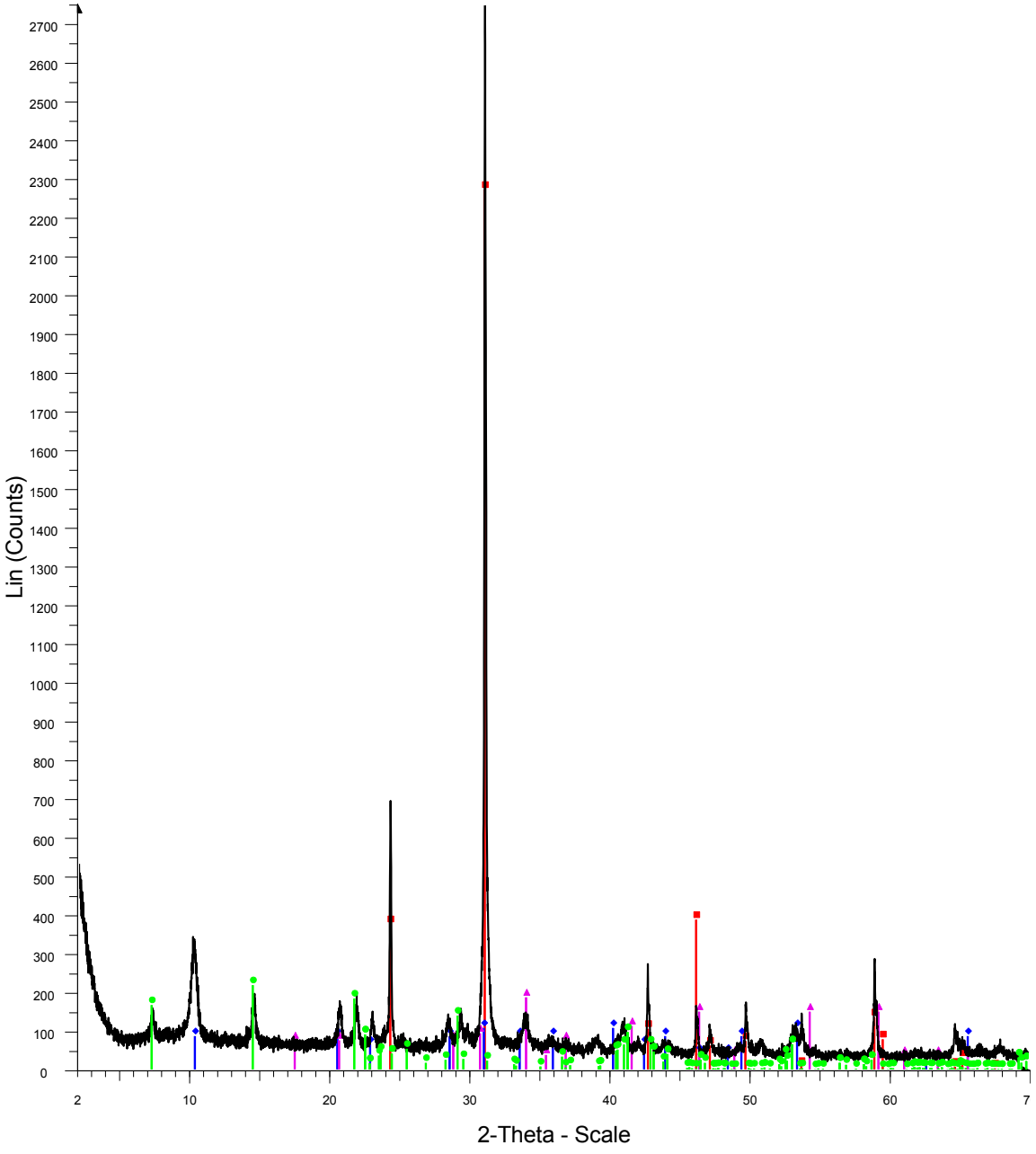

Red-Quartz
Blue-Illite
Pink-Jarosite
Green-Chlorite

76

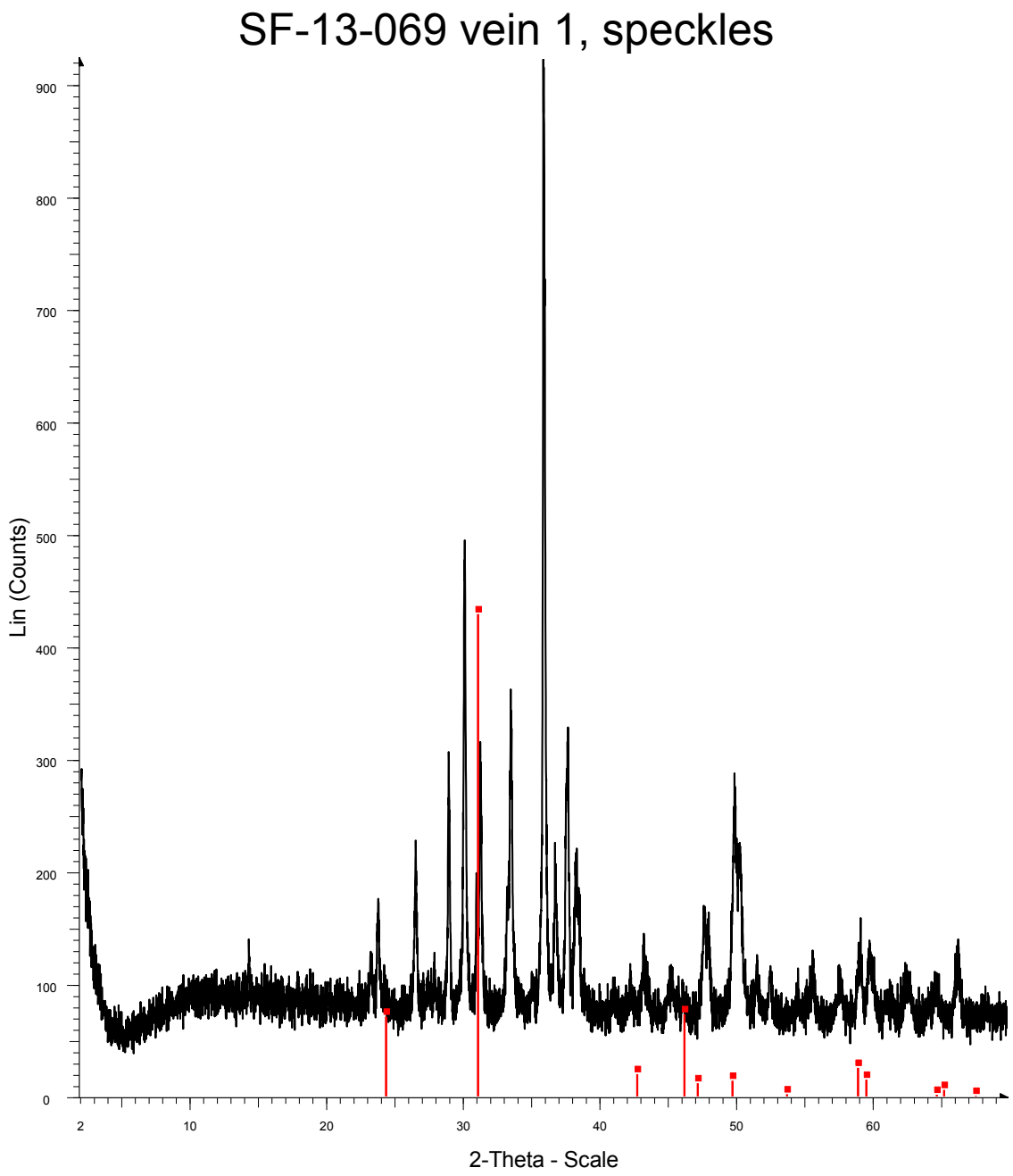

Red-Quartz

69vein

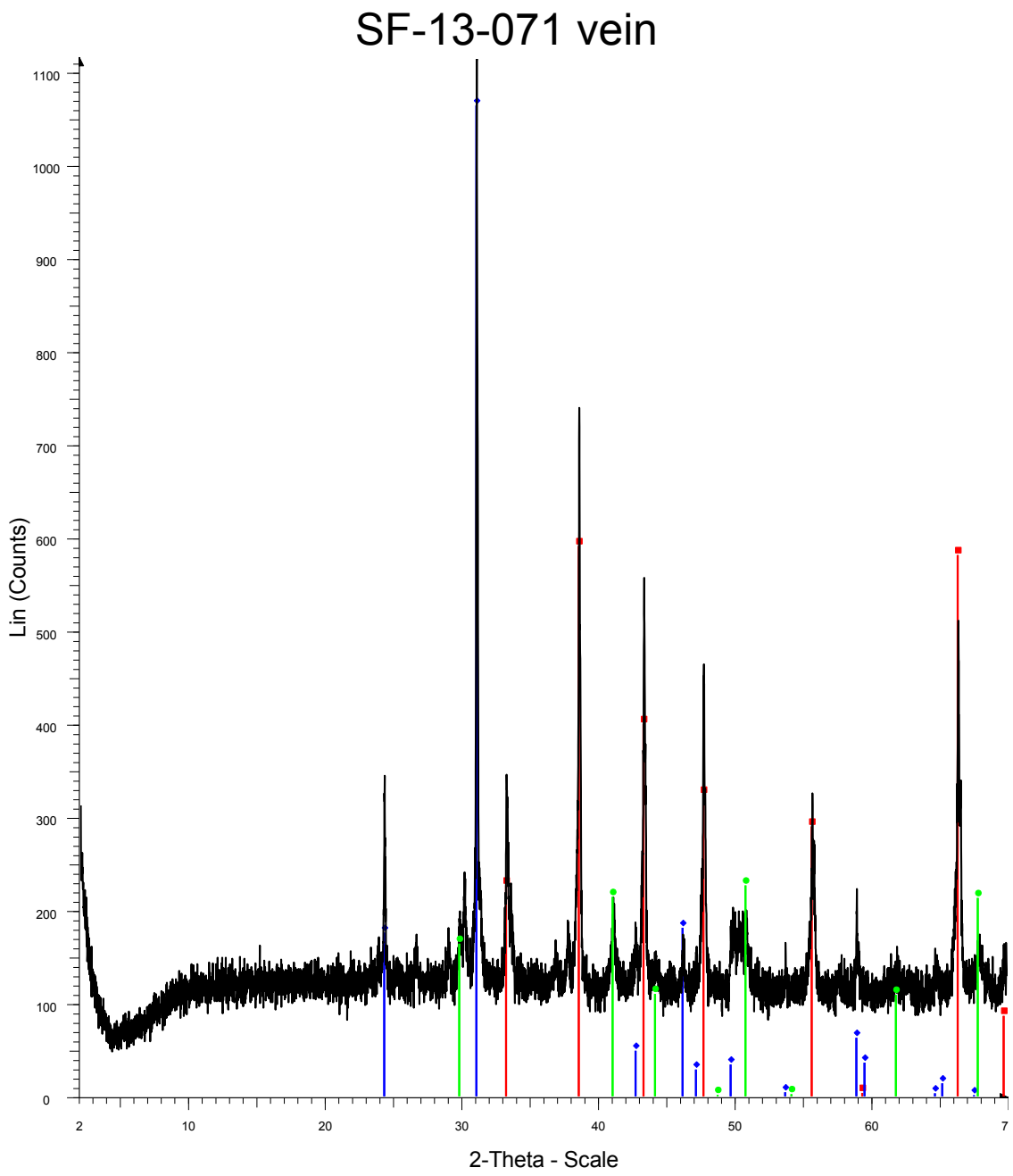

Red-Pyrite
Blue-Quartz
Green-Corundum

71vein

Deep

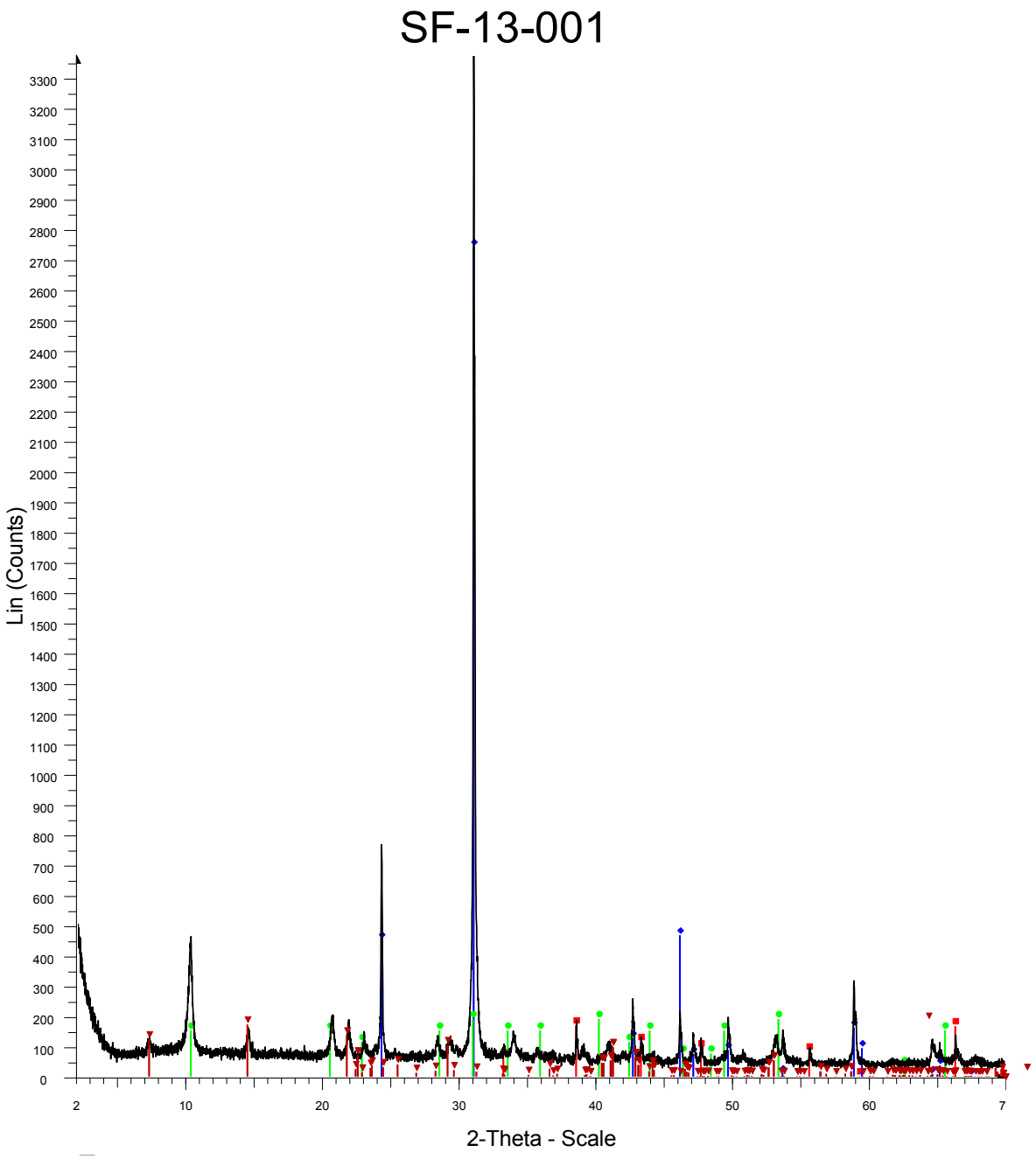

Red-Pyrite
Blue-Quartz
Green-Illite
Dark red-Chlorite

1

SF-13-002

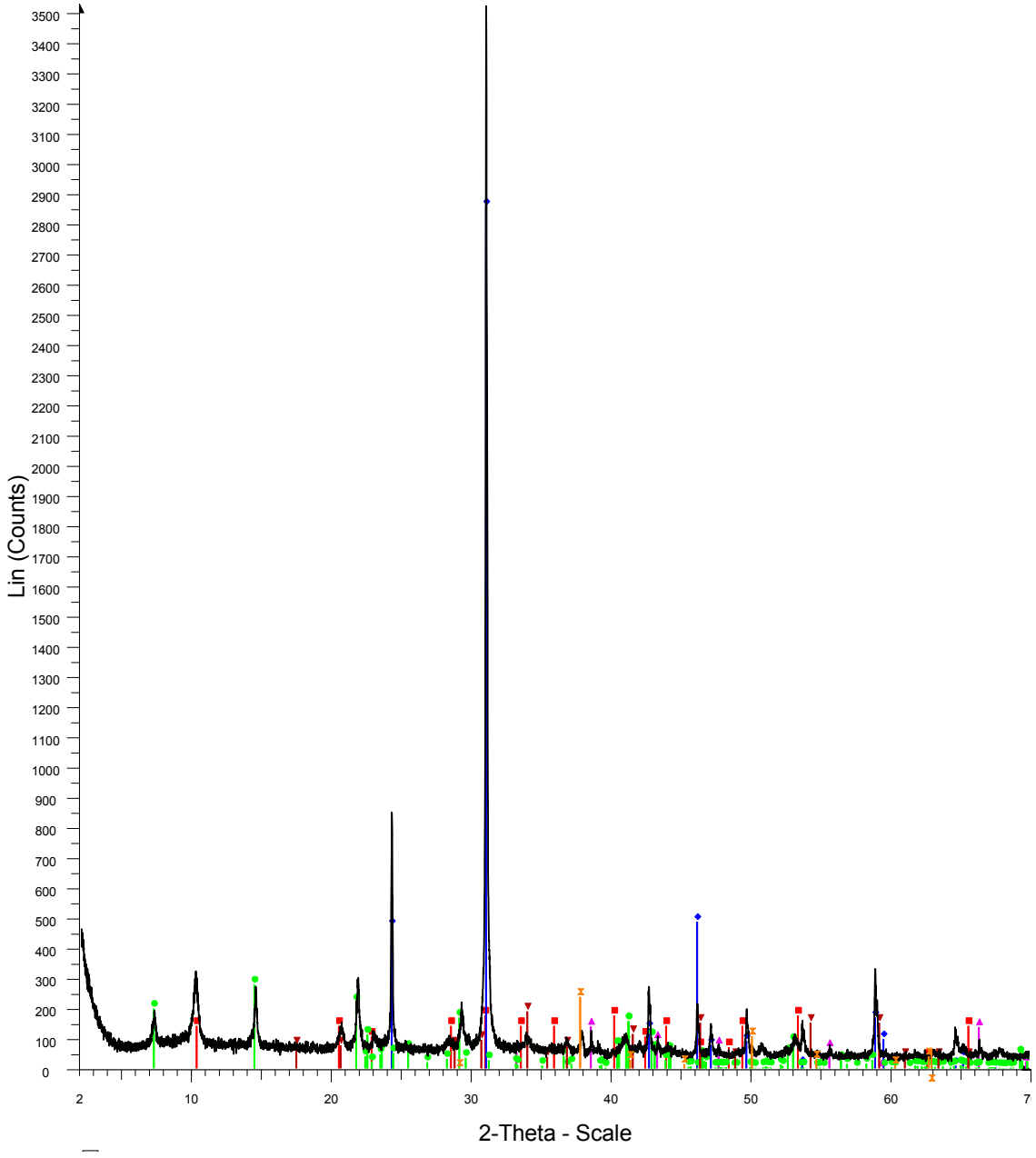

Red-Illite
Blue-Quartz
Pink-Pyrite
Green-Chlorite
Dark red-Jarosite
Orange-Magnesite

2

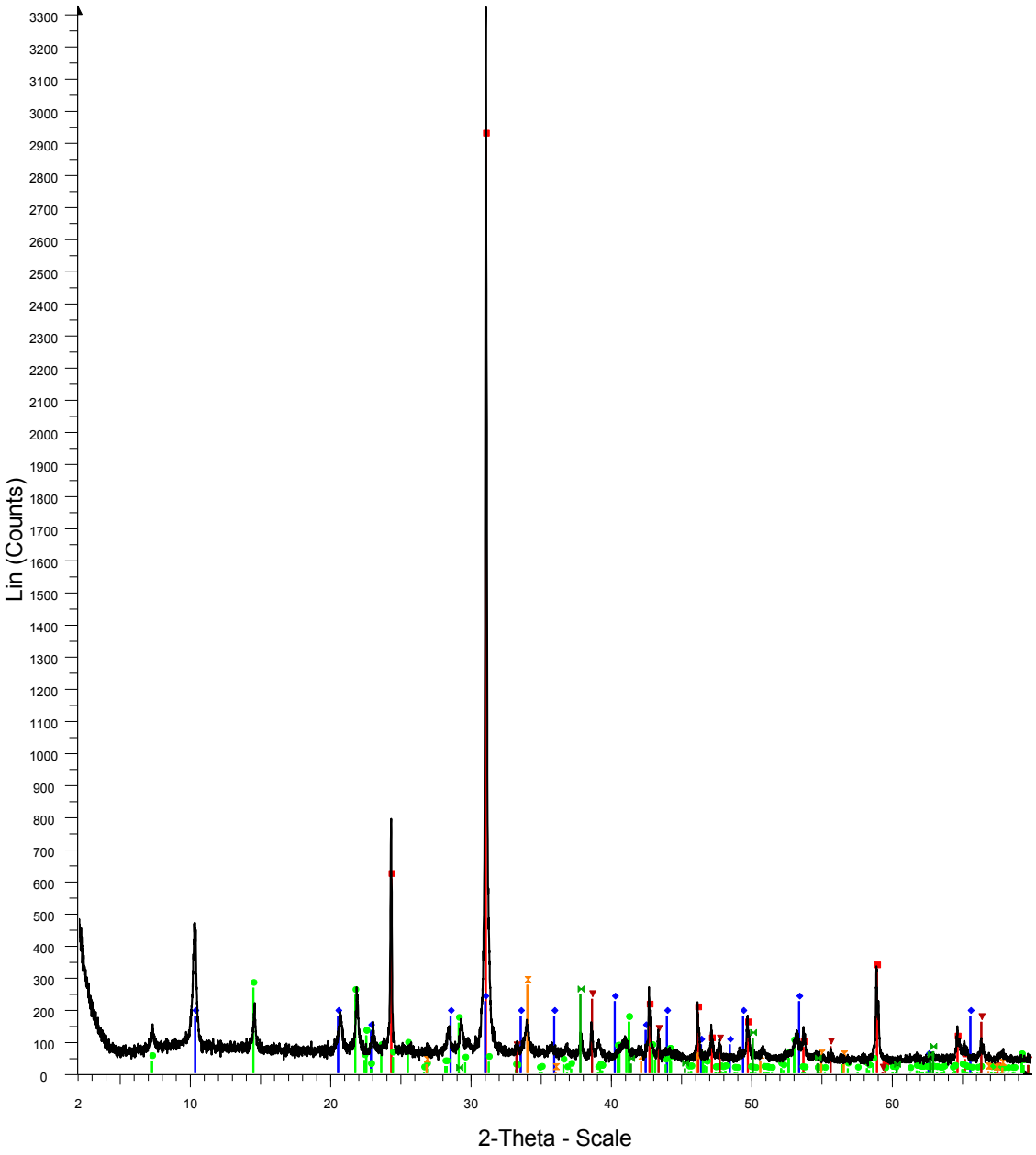

Red-Quartz
Blue-Illite
Green-Chlorite
Dark red-Pyrite
Orange-Calcite
3

SF-13-004

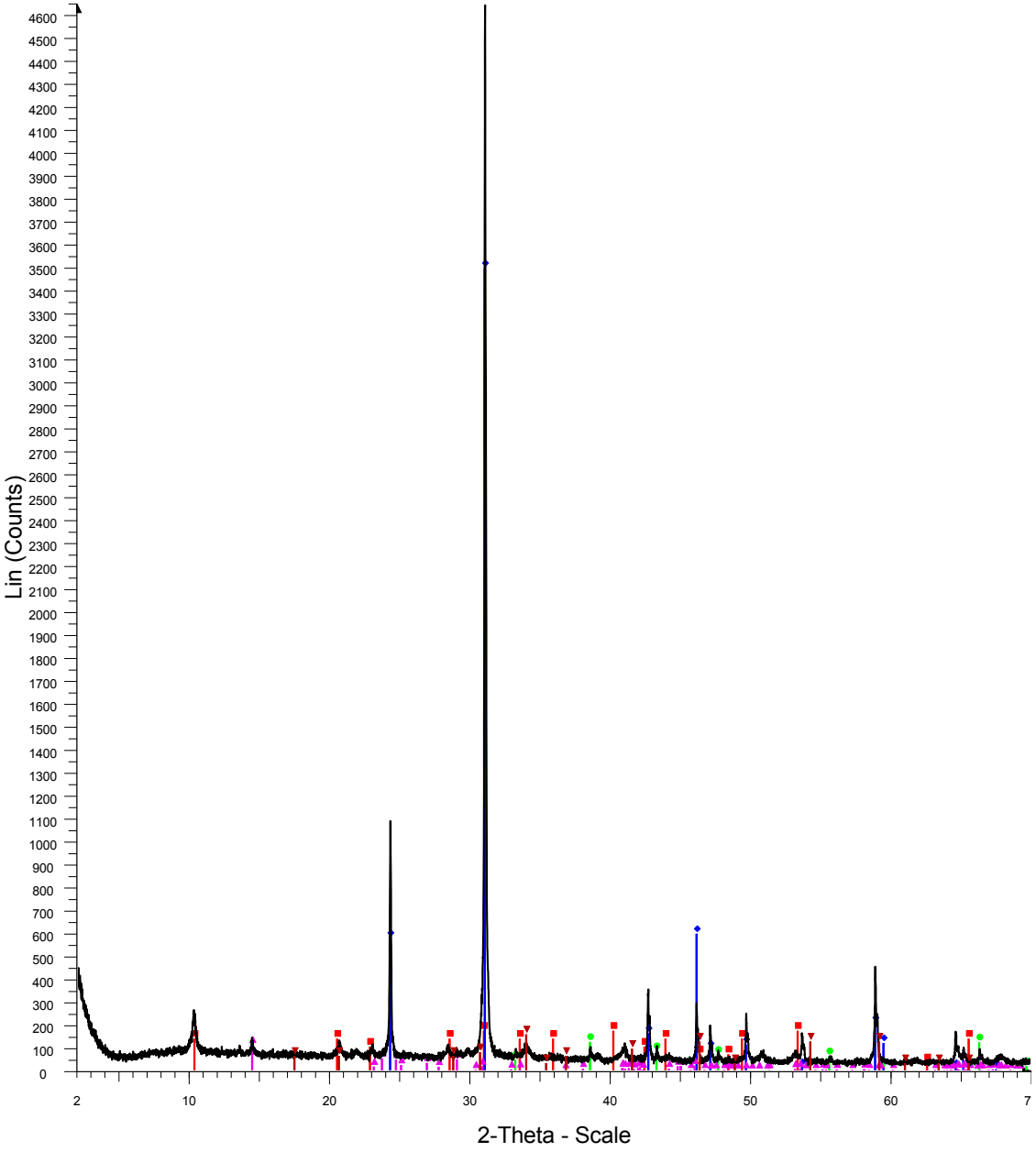

Red-Illite
Blue-Quartz
Green-Pyrite
Pink- Kaolinite
Dark red-Jarosite
4

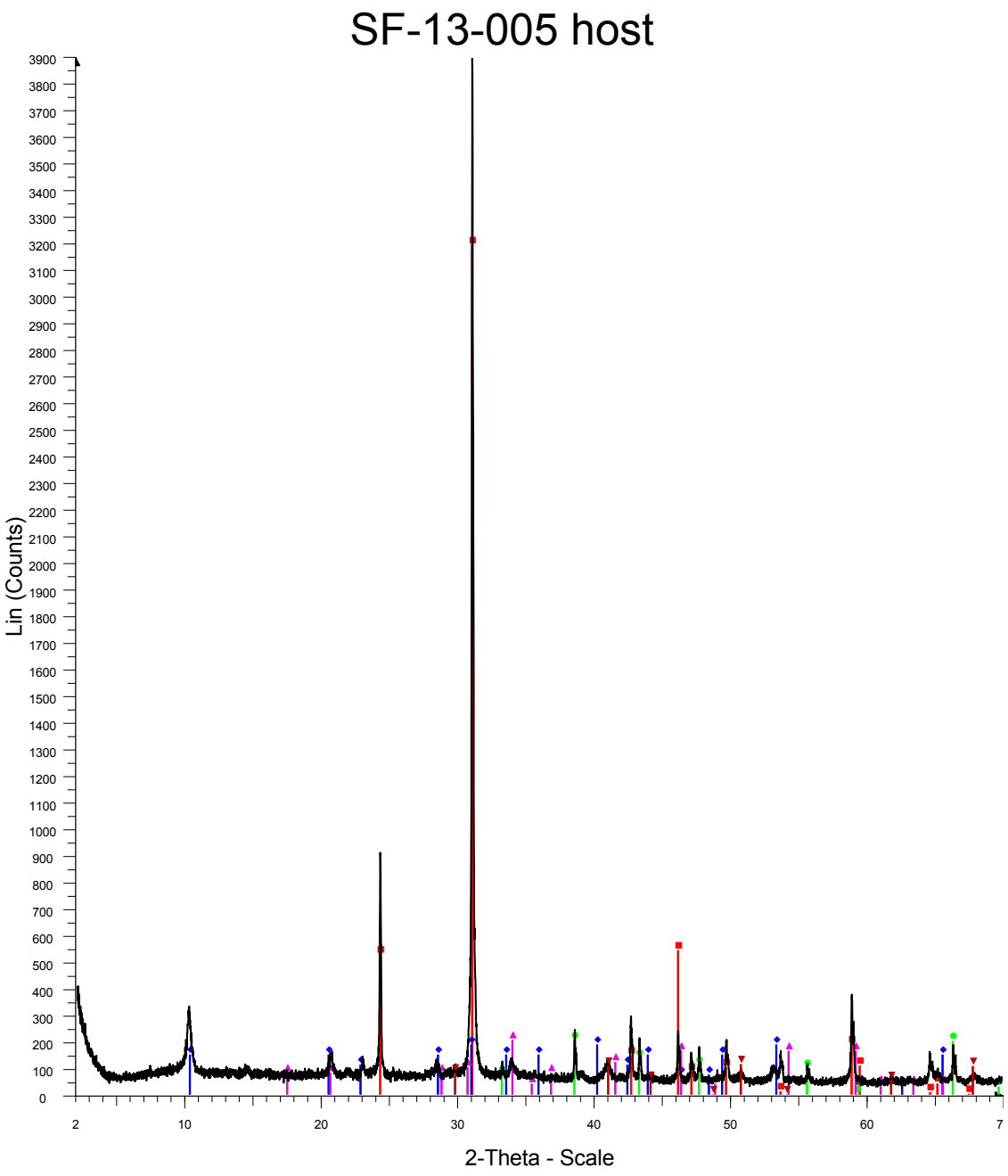

Red-Quartz
Blue-Illite
Green-Pyrite
Pink- Jarosite
Dark red-Corundum
5host

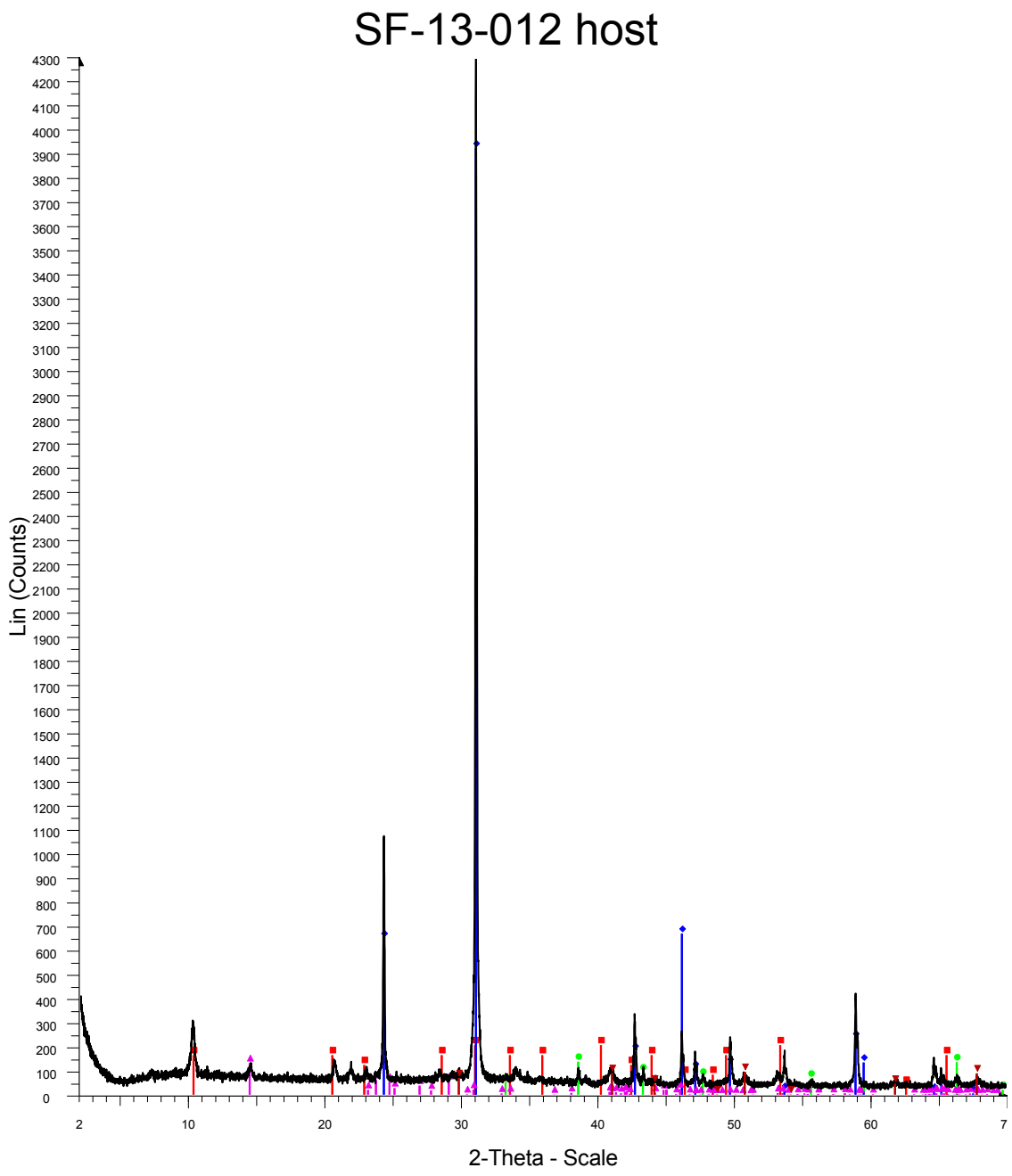

Red-Illite
Blue-Quartz
Green-Pyrite
Pink-Kaolinite
Dark red-Corundum

12host

SF-13-014 host

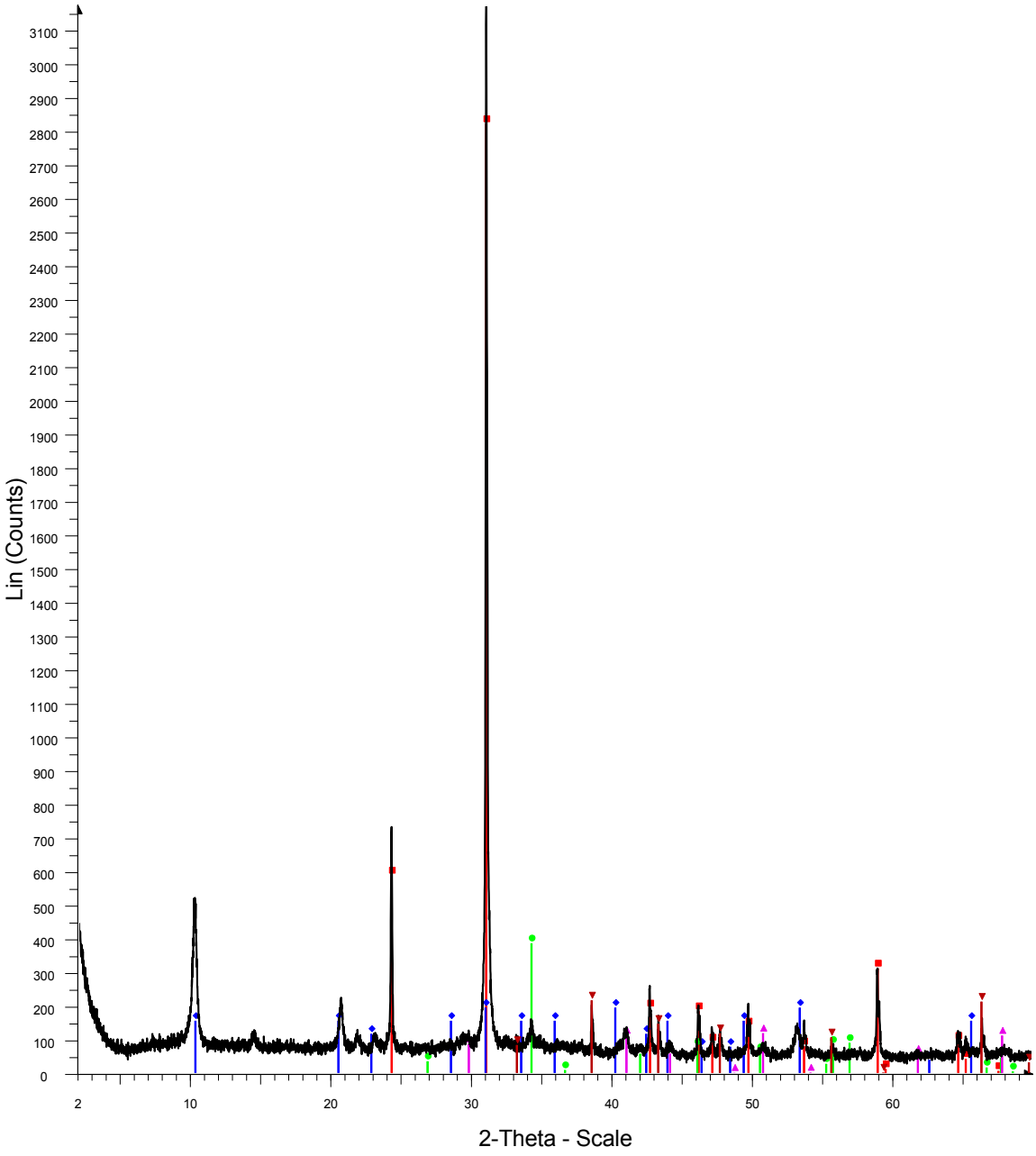

Red-Quartz
Blue-Illite
Green-Calcite
Pink-Corundum
Dark red-Pyrite

14host

SF-13-015

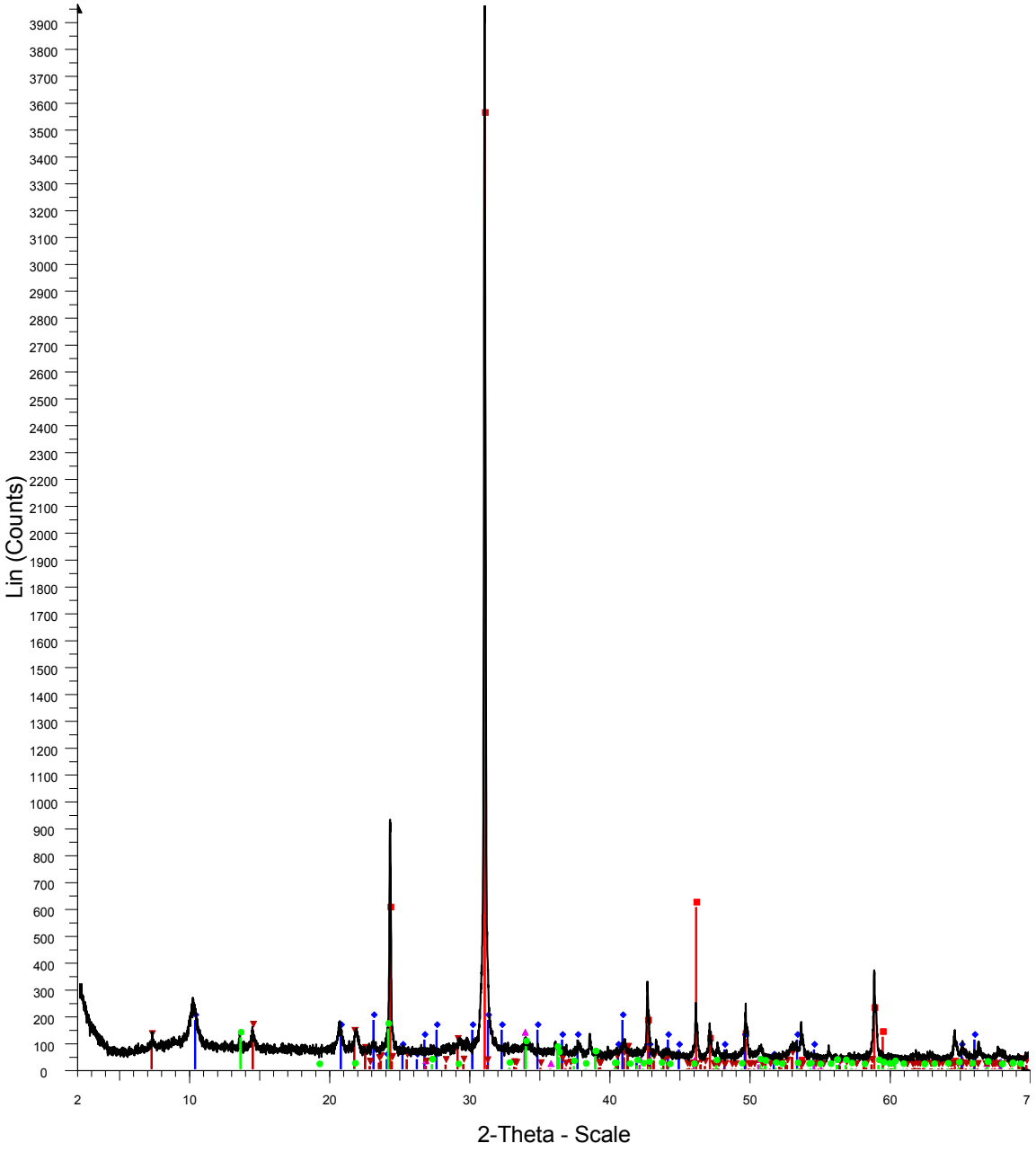

Red-Quartz
Blue-Illite
Pink-Calcite
Dark red-Chlorite
Green-Gypsum

15

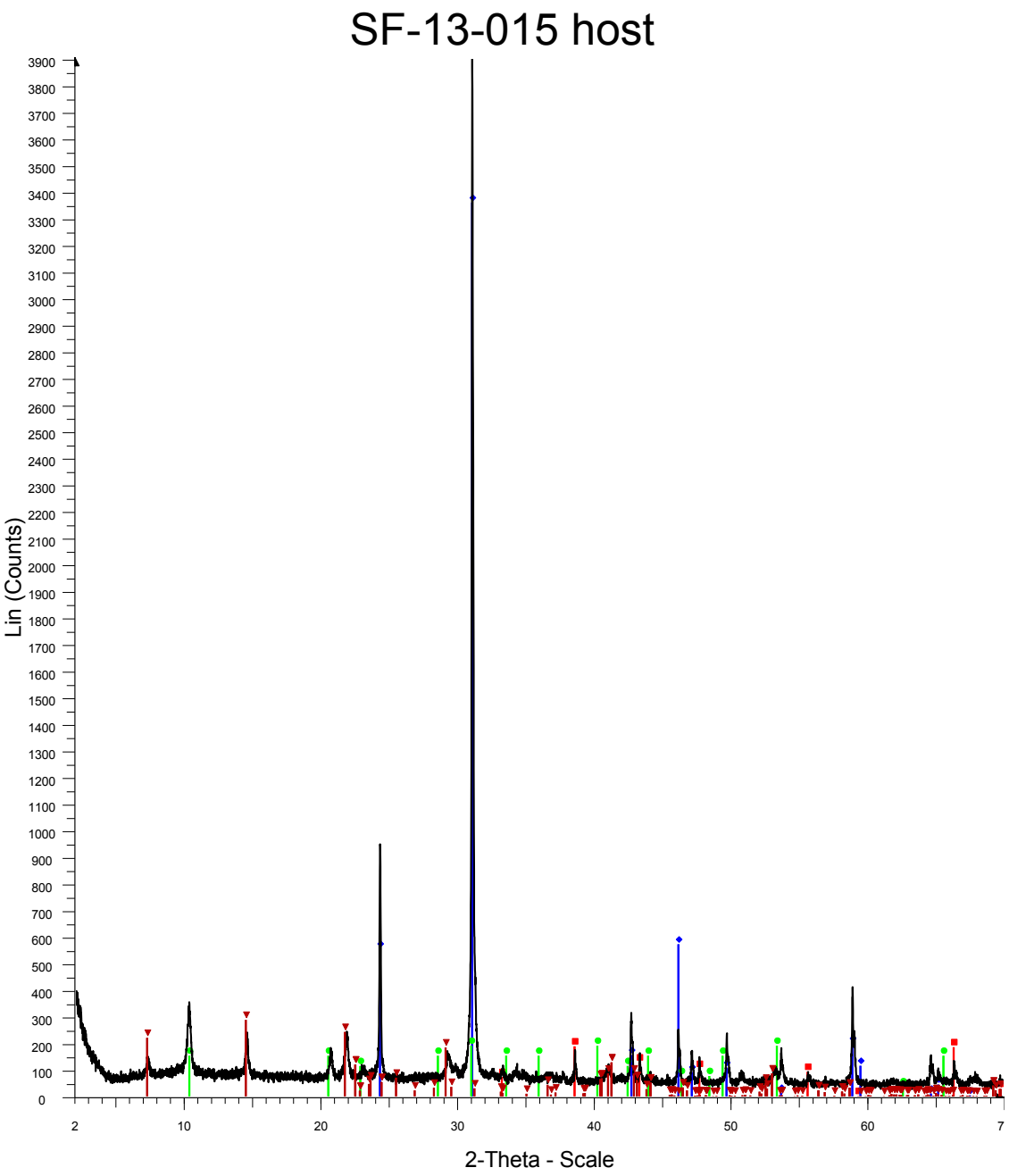

Red-Pyrite
Blue-Quartz
Green-Illite
Dark red-Chlorite

15host

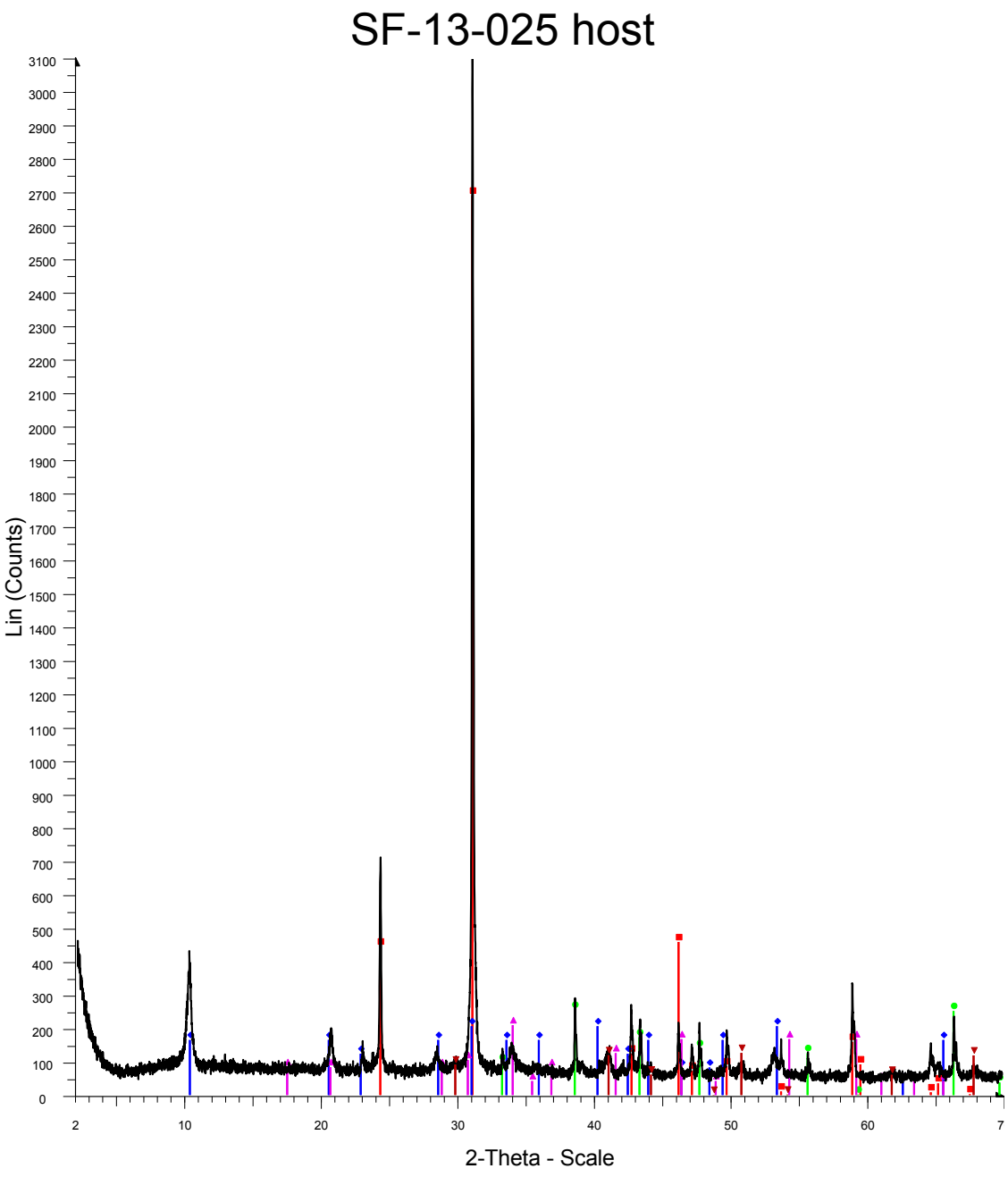

Red-Quartz
Blue-Illite
Green-Pyrite
Pink- Jarosite
Dark red-Corundum
25host

SF-13-026

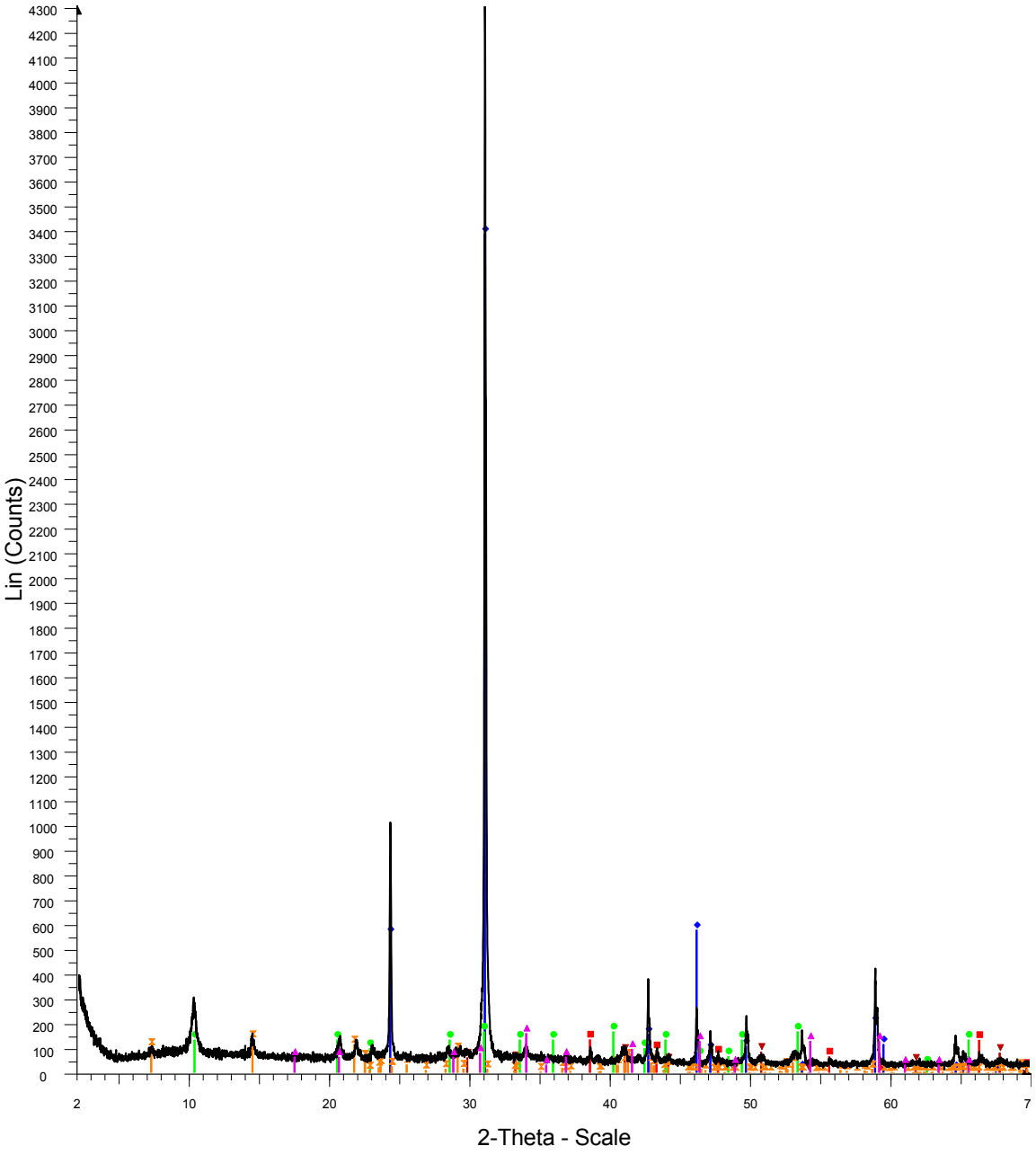

Red-Pyrite
Blue-Quartz
Green-Illite
Dark red-Corundum
Orange-Chlorite
Pink- Jarosite

26

SF-13-039.4 host

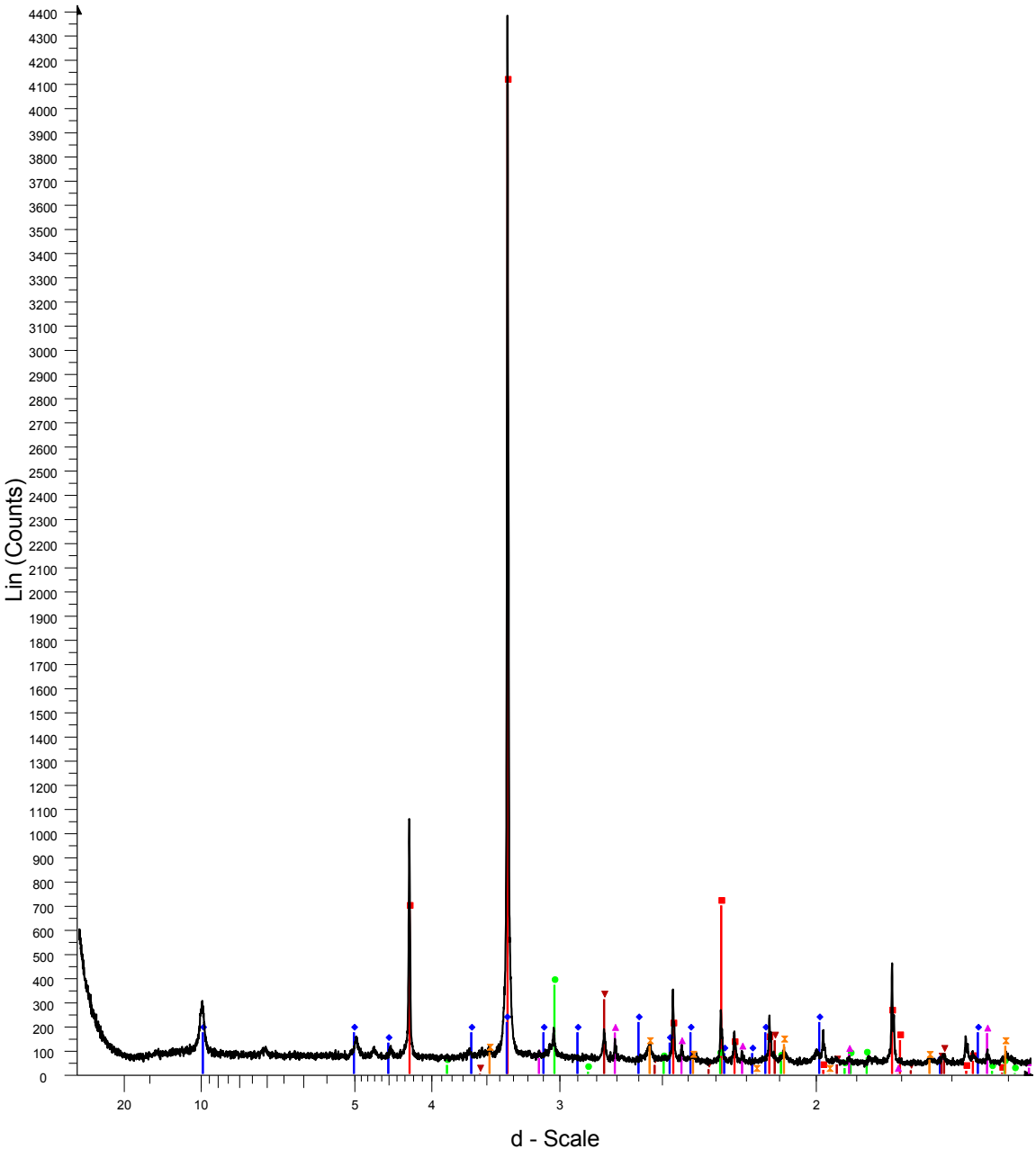

Red-Quartz
Blue-Illite
Green-Calcite
Pink-Pyrite
Dark red-Magnesite
Orange-Corundum

0394host

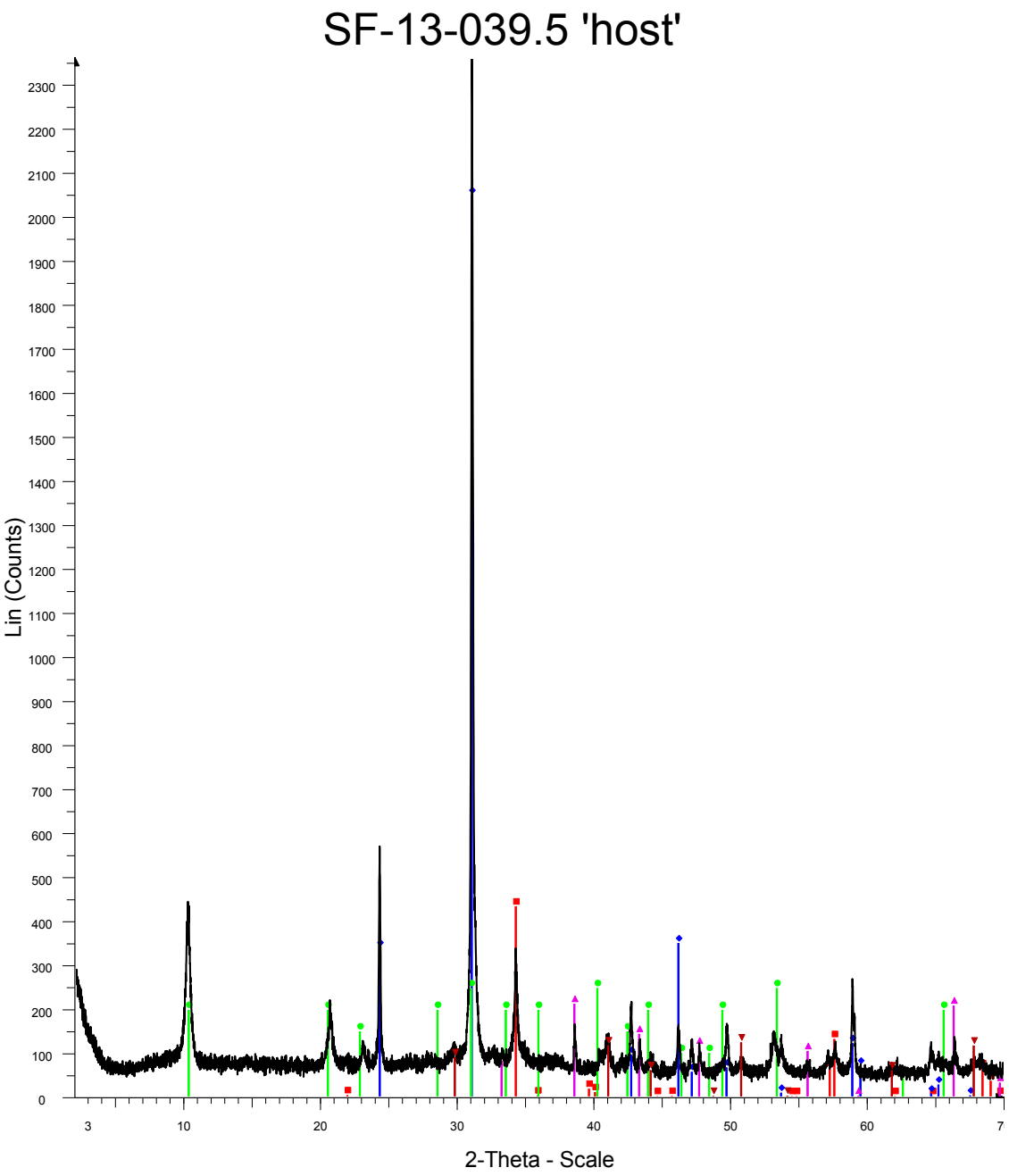

Red-Chalcopyrite
Blue-Quartz
Green-Illite
Pink-Pyrite
Dark red-Corundum

0395host

SF-13-040

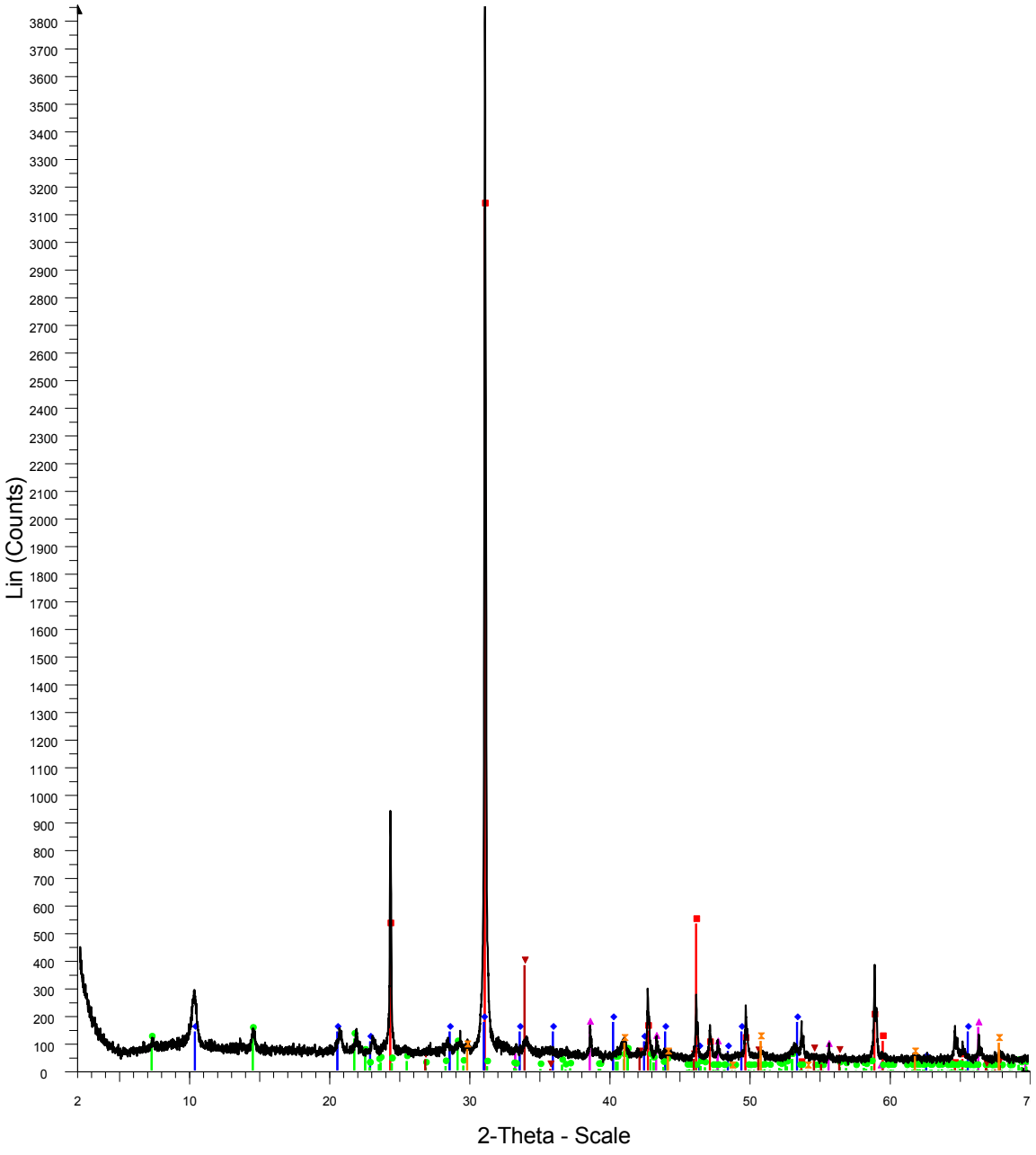

Red-Quartz
Blue-Illite
Pink- Pyrite
Green-Chlorite
Dark red-Calcite
Orange-Corundum
40

SF-13-041

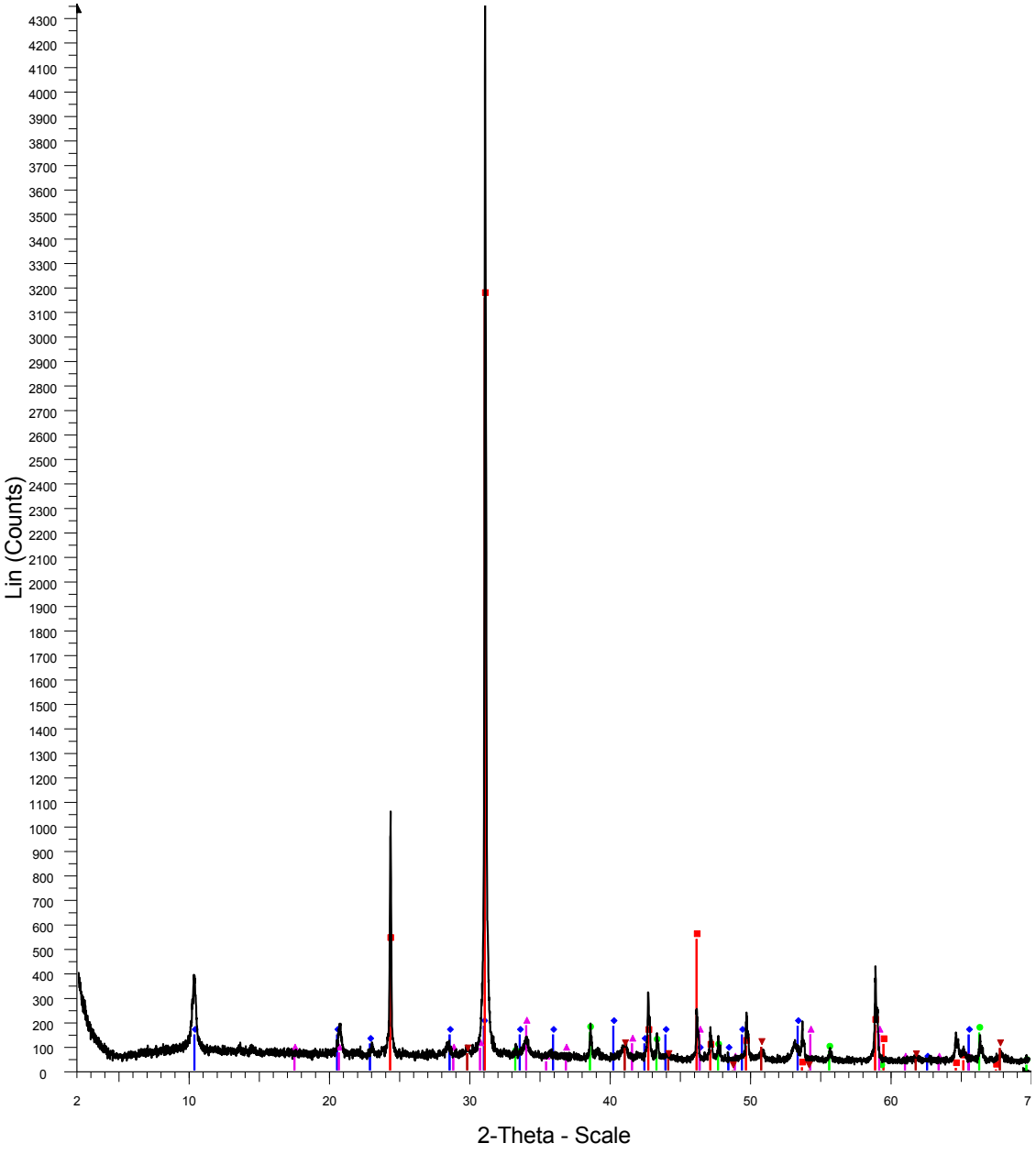

Blue-Illite
Red-Quartz
Green-Pyrite
Pink- Jarosite
Dark red-Corundum
41

SF-13-042

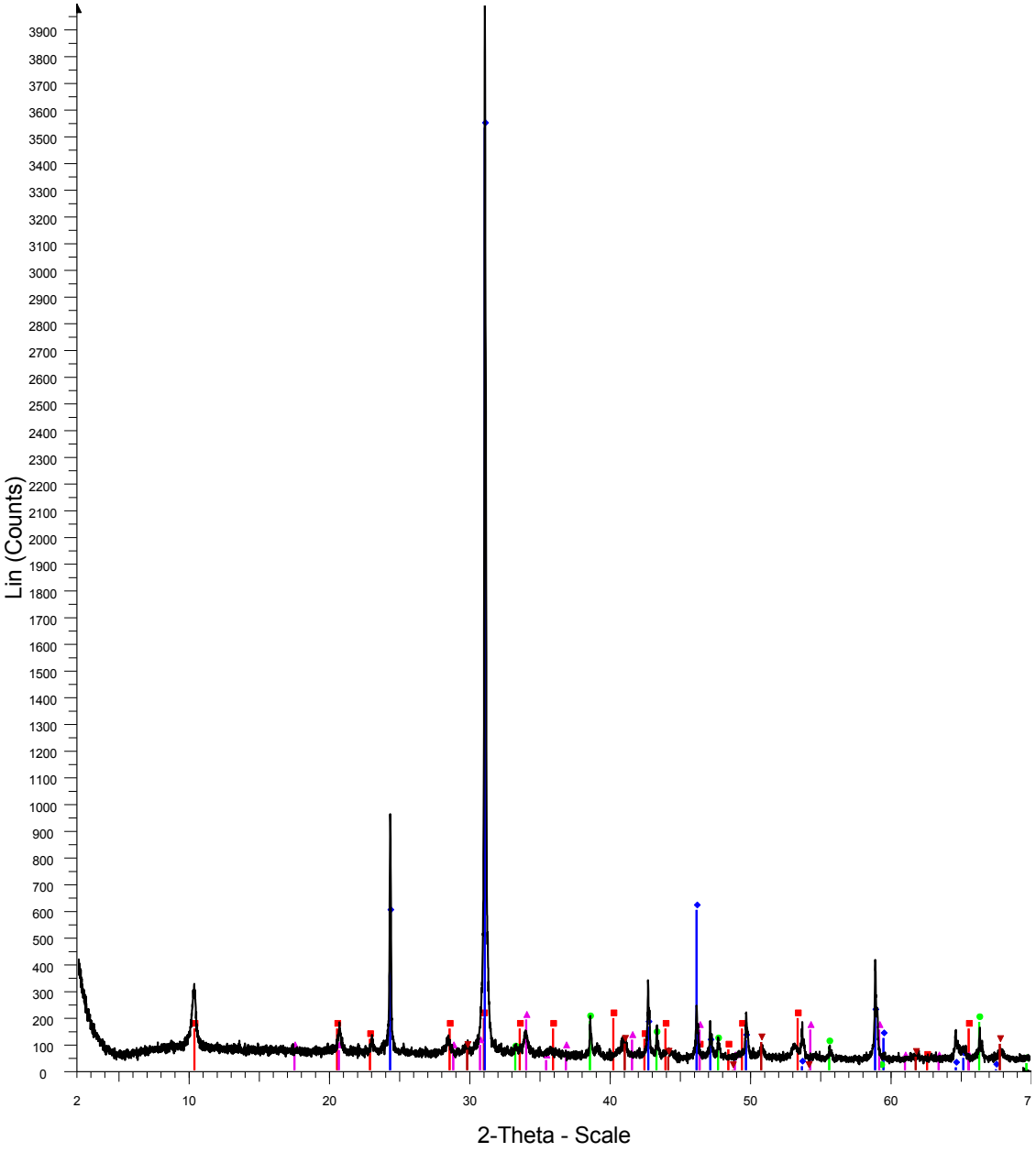

Red-Illite
Blue-Quartz
Green-Pyrite
Pink- Jarosite
Dark red-Corundum
42

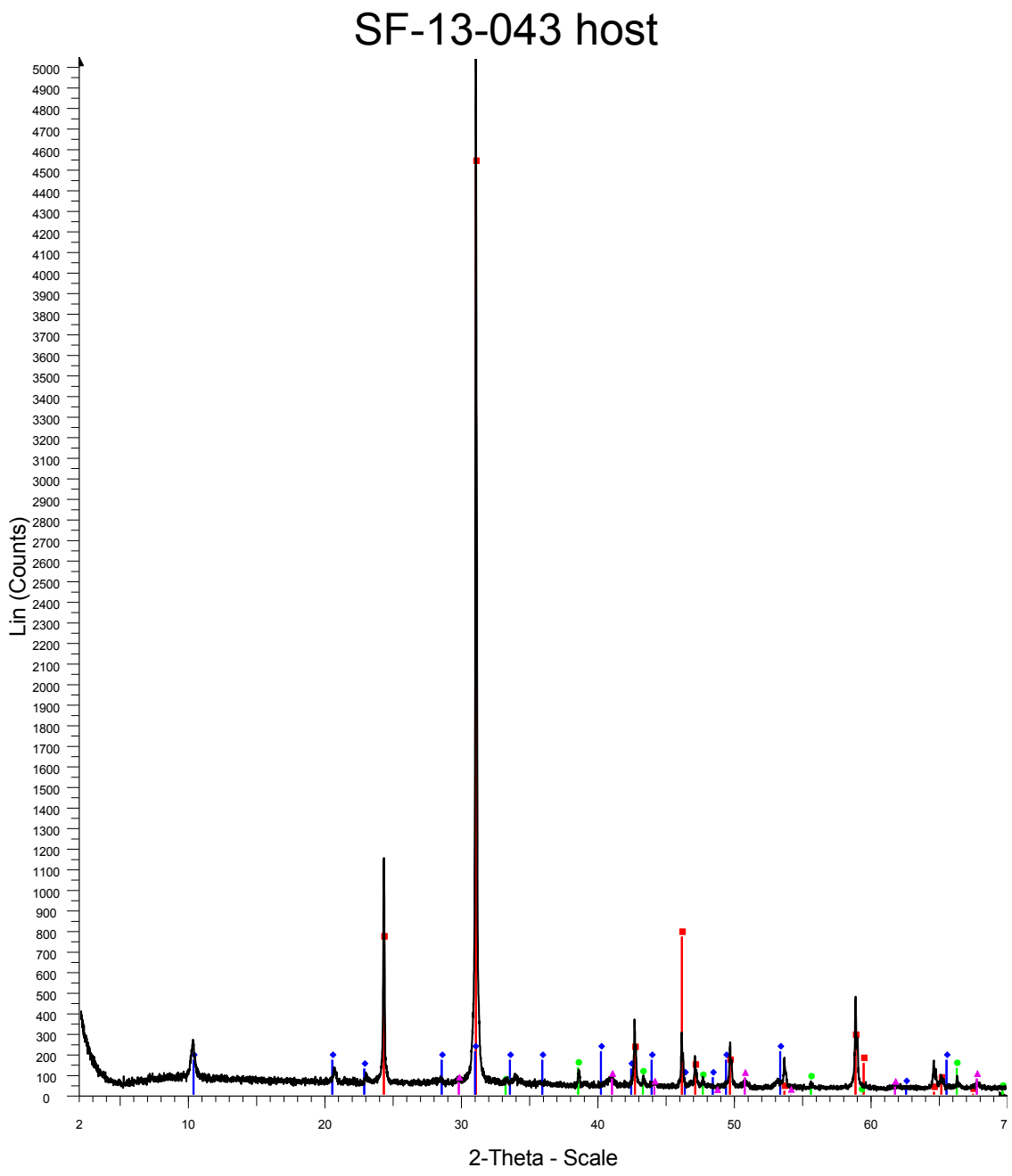

Red-Quartz
Blue-Illite
Green-Pyrite
Pink- Corundum
43host

SF-13-044

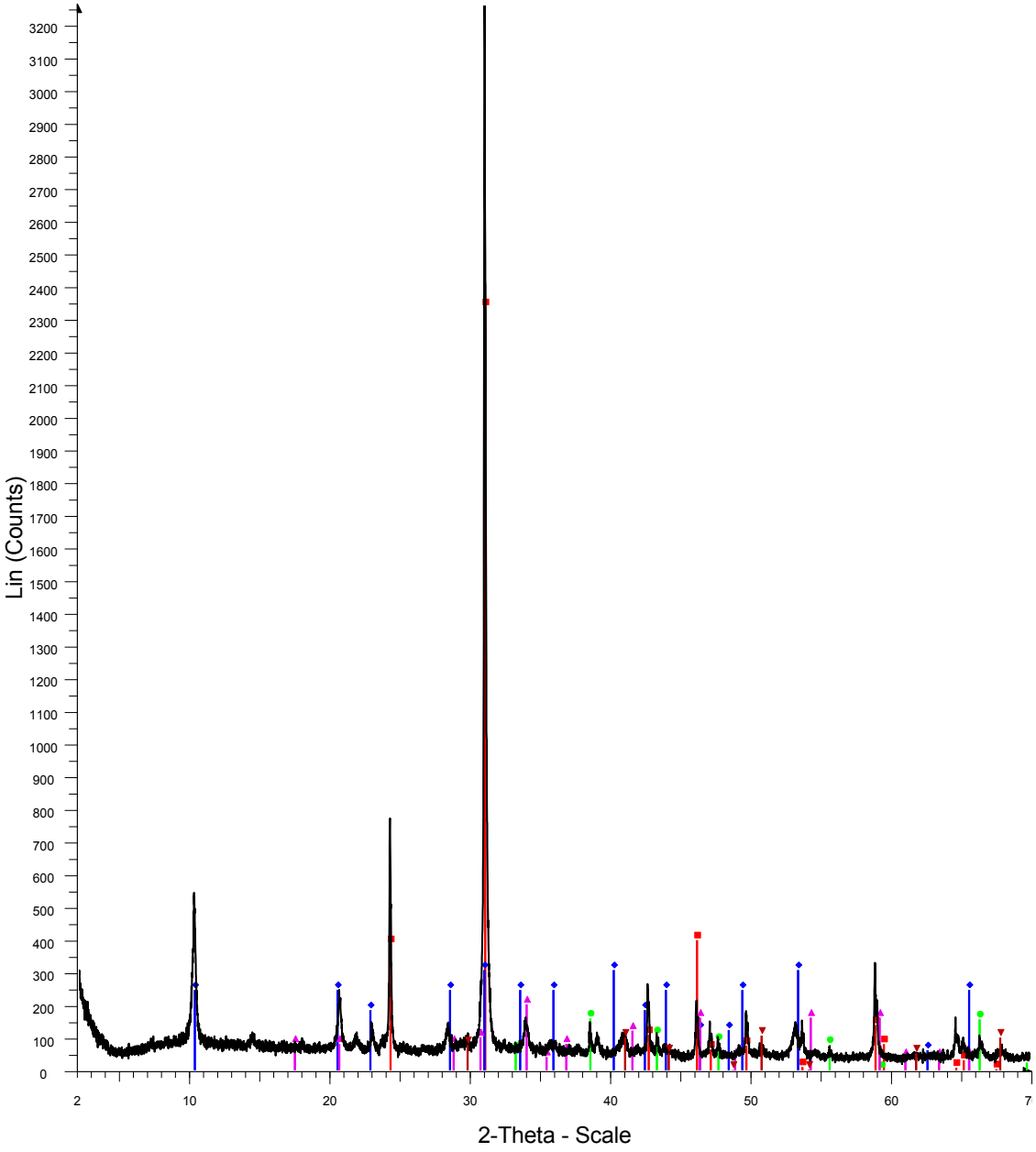

Red-Quartz
Blue-Illite
Green-Pyrite
Pink- Jarosite
Dark red-Corundum
44

SF-13-045

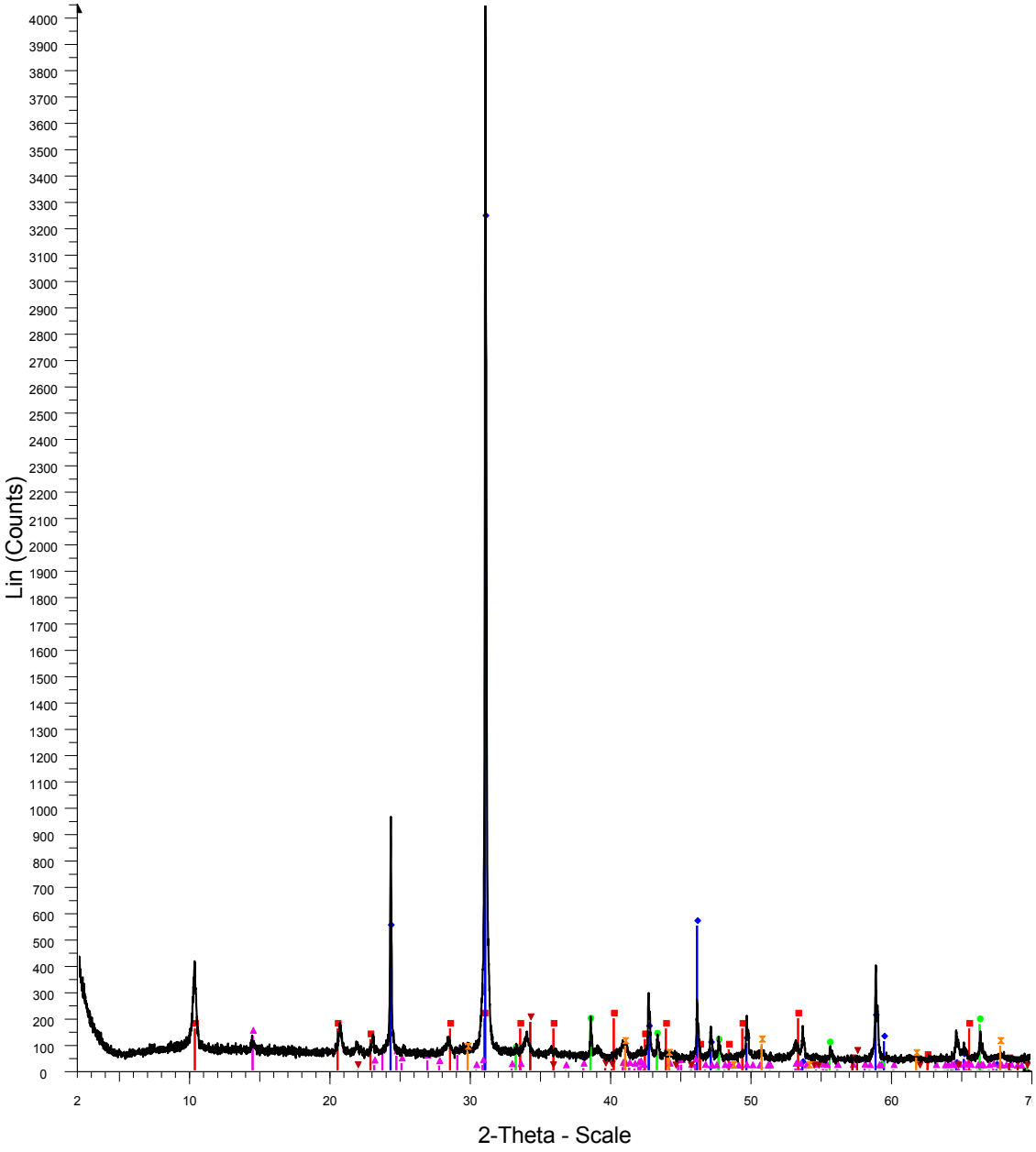

Red-Illite
Blue-Quartz
Green-Pyrite
Pink- Kaolinite
Dark red-Chalcopyrite
Orange-Corundum
45

SF-13-046 host

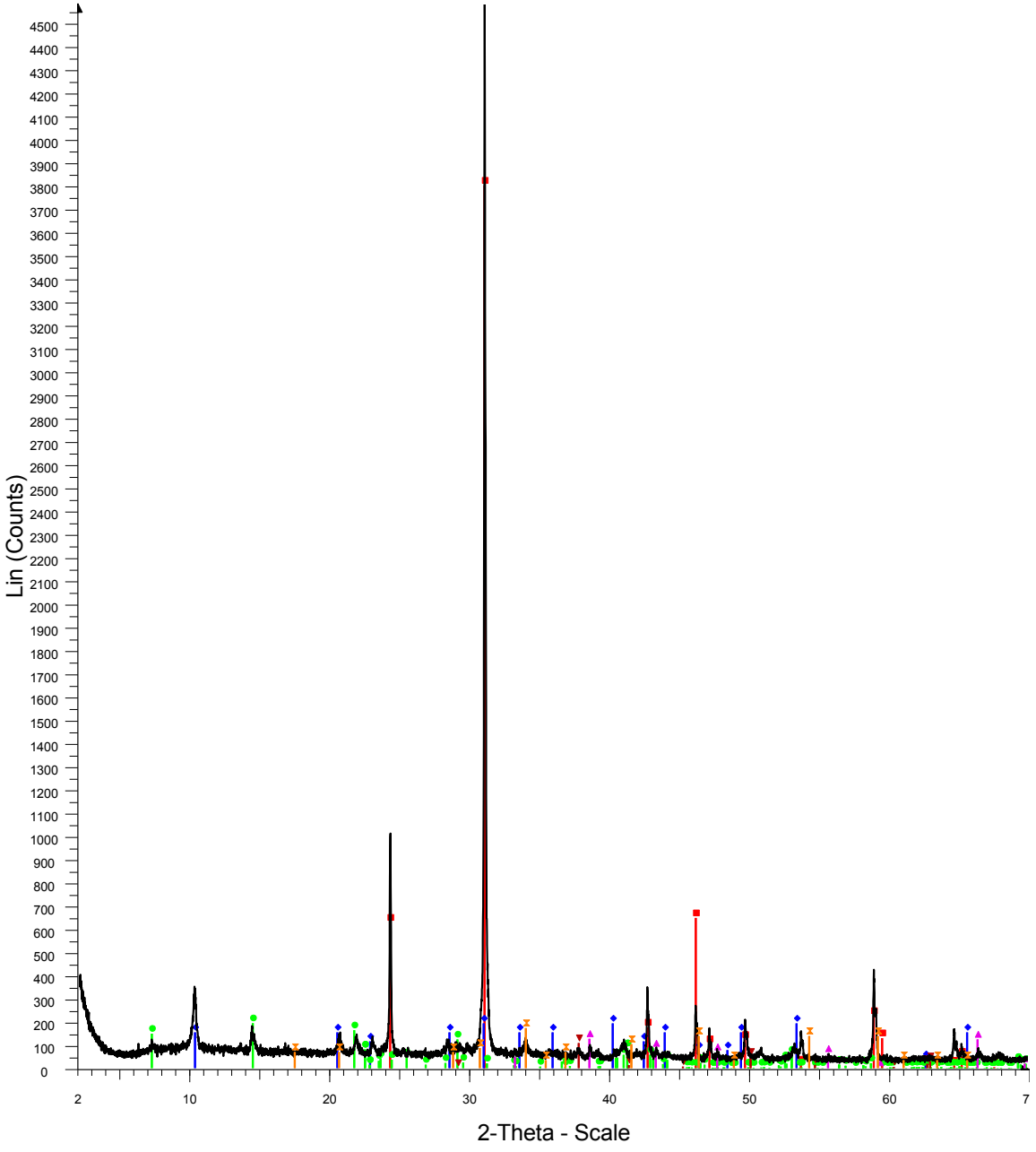

Red-Quartz
Blue-Illite
Green-Chlorite
Pink- Pyrite
Dark red-Magnesite
Orange-Jarosite
46host

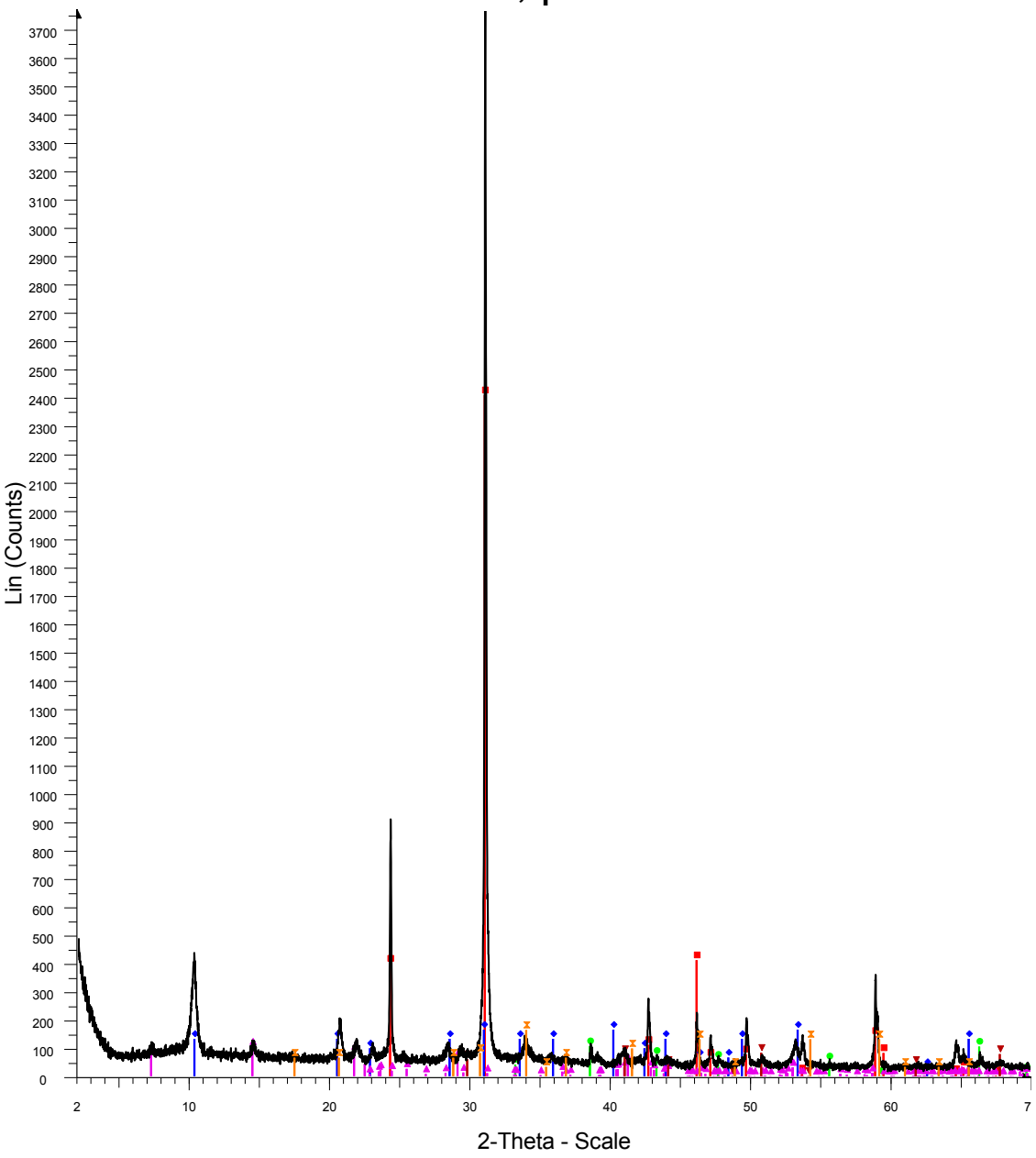

Red-Quartz
Blue-Illite
Green-Pyrite
Pink-Chlorite
Dark red-Corundum
Orange-Jarosite

88host

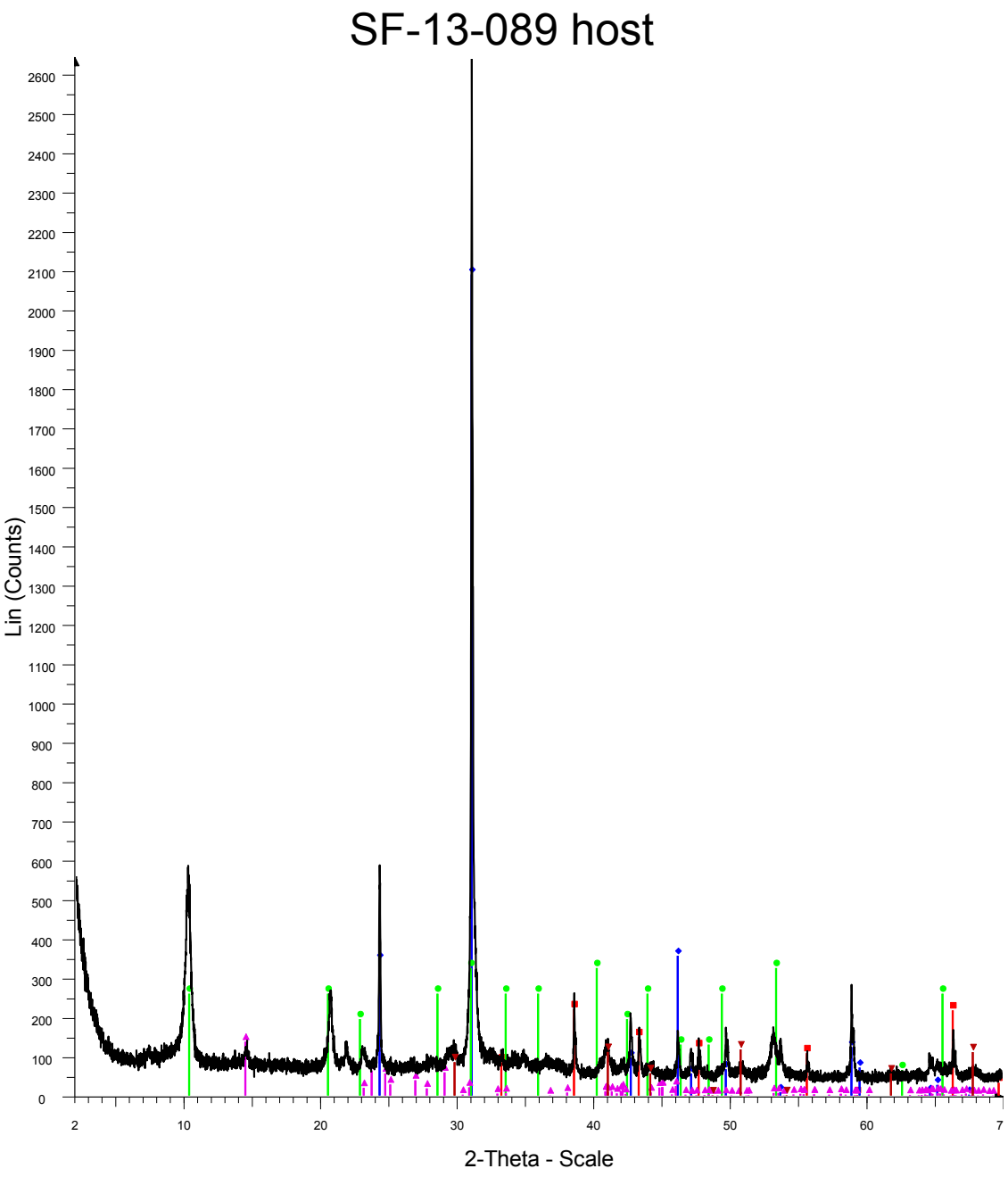

Red-Pyrite
Blue-Quartz
Green-Illite
Pink-Kaolinite
Dark red-Corundum

89host

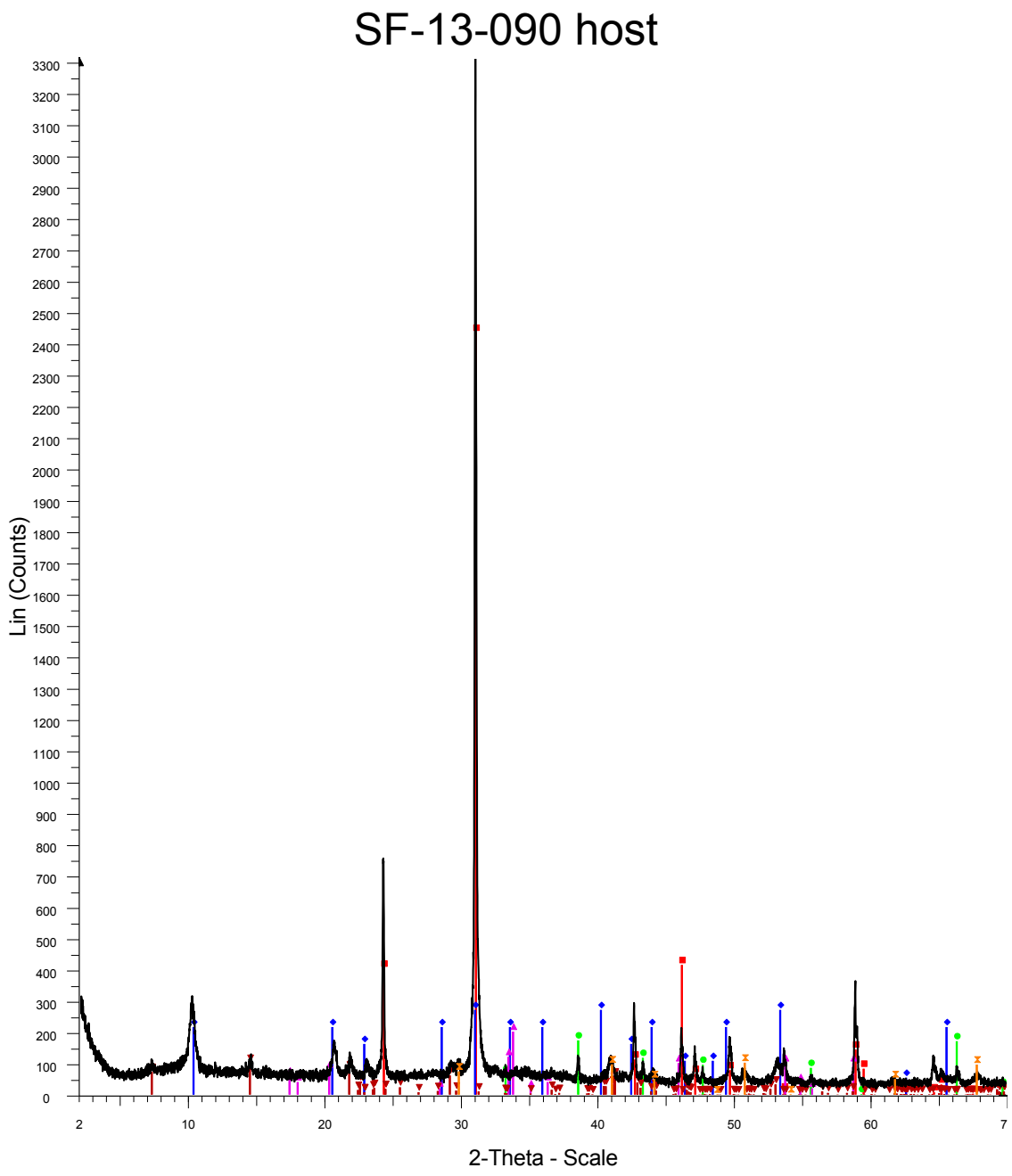

Red-Quartz
Blue-Illite
Green-Pyrite
Pink-Jarosite
Dark red-Chlorite
Orange-Corundum

90host

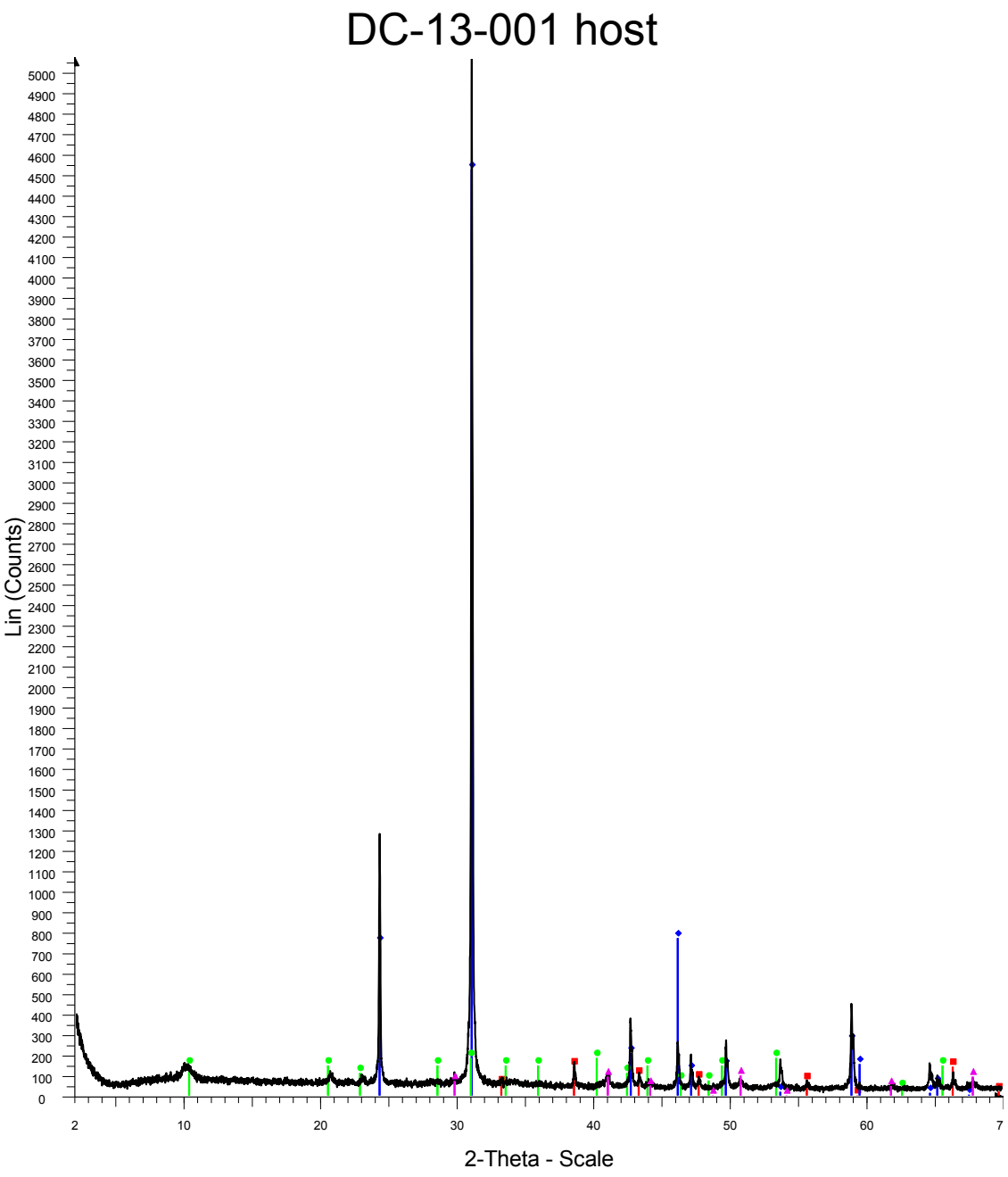

Red-Pyrite
Blue-Quartz
Green-Illite
Pink- Corundum
Dc1host

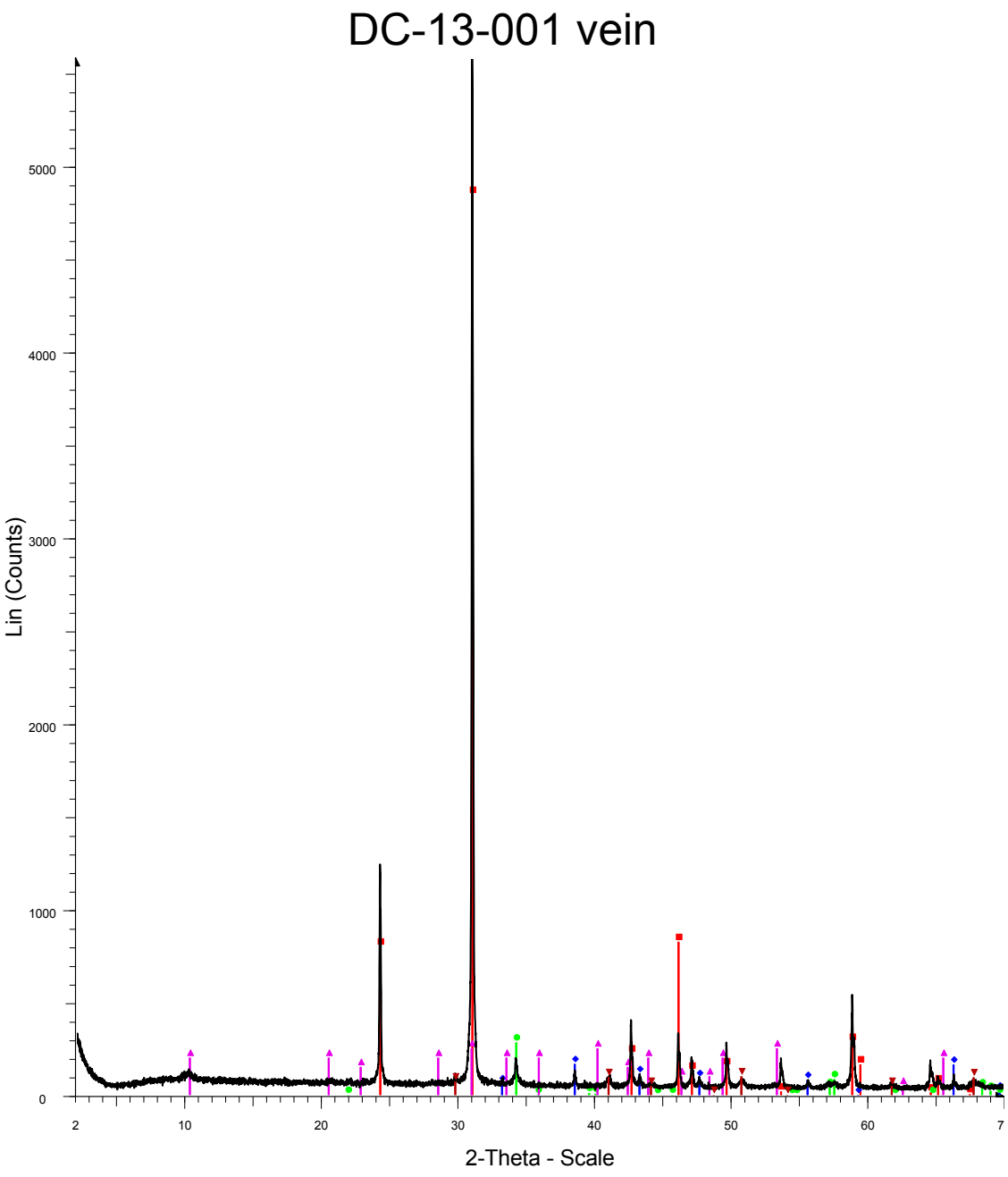

Red-Quartz
Blue-Pyrite
Green-Chalcopyrite
Pink- Illite
Dark red-Corundum
Dc1vein

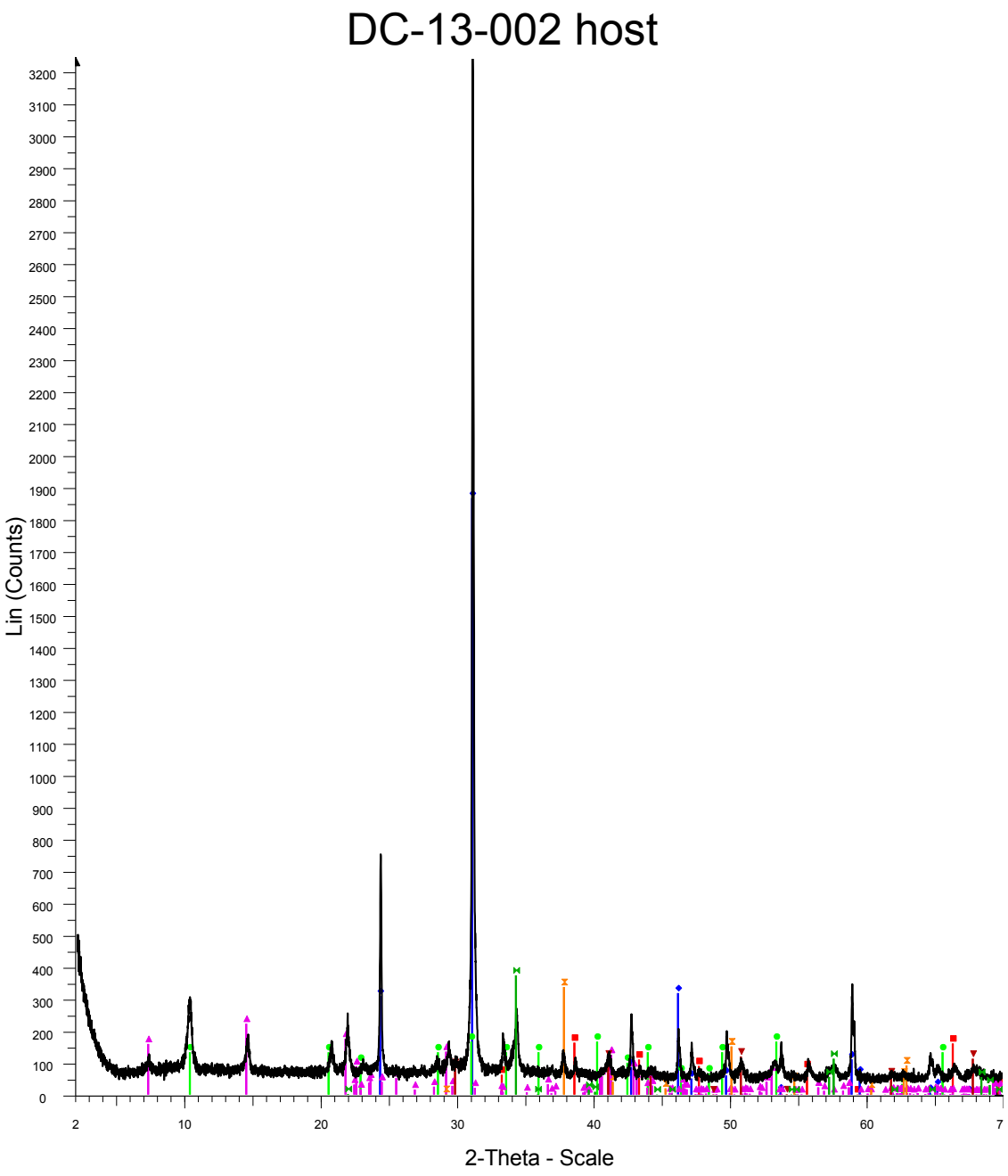

Red-Pyrite
Blue-Quartz
Green-Illite
Pink-Chlorite
Dark red-Corundum
Orange-Magnesite
Dark green-Chalcopyrite
Dc2host

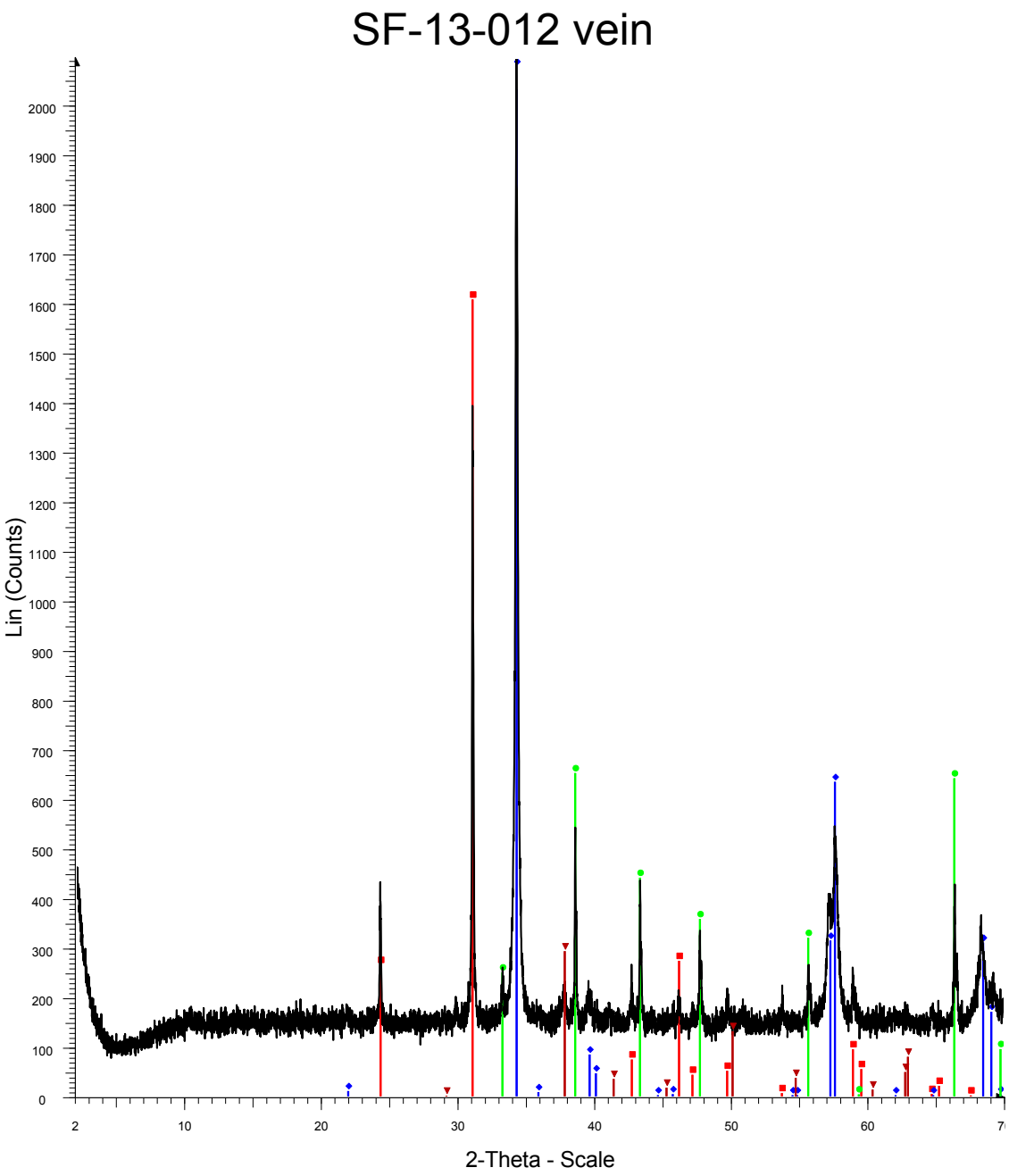

Red-Quartz
Blue-Chalcopyrite
Green-Pyrite
Dark red-Magnesite
12vein

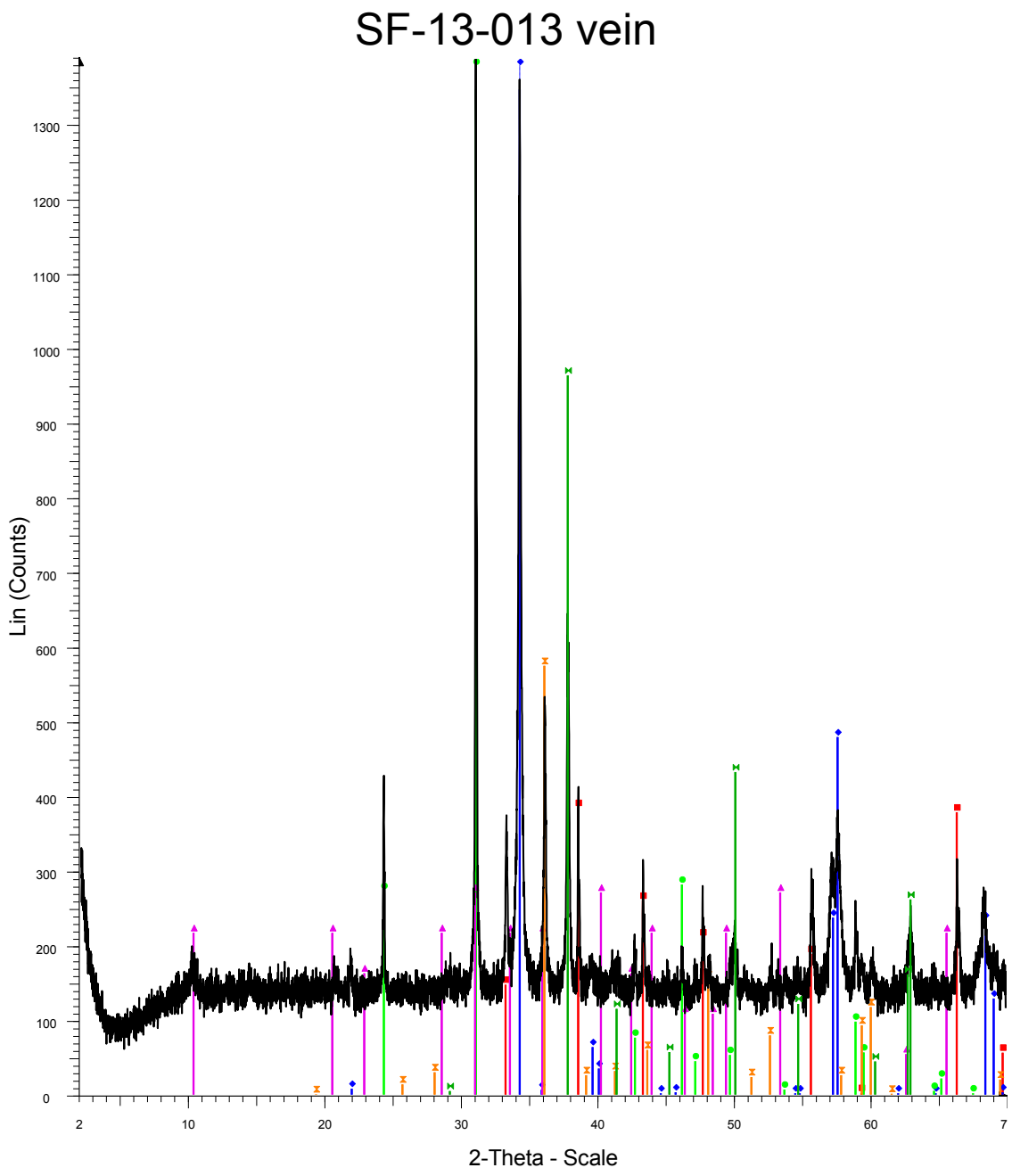

Red-Pyrite
Blue-Chalcopyrite
Green-Quartz
Pink-Illite
Orange-Dolomite
Dark green-Magnesite
13vein

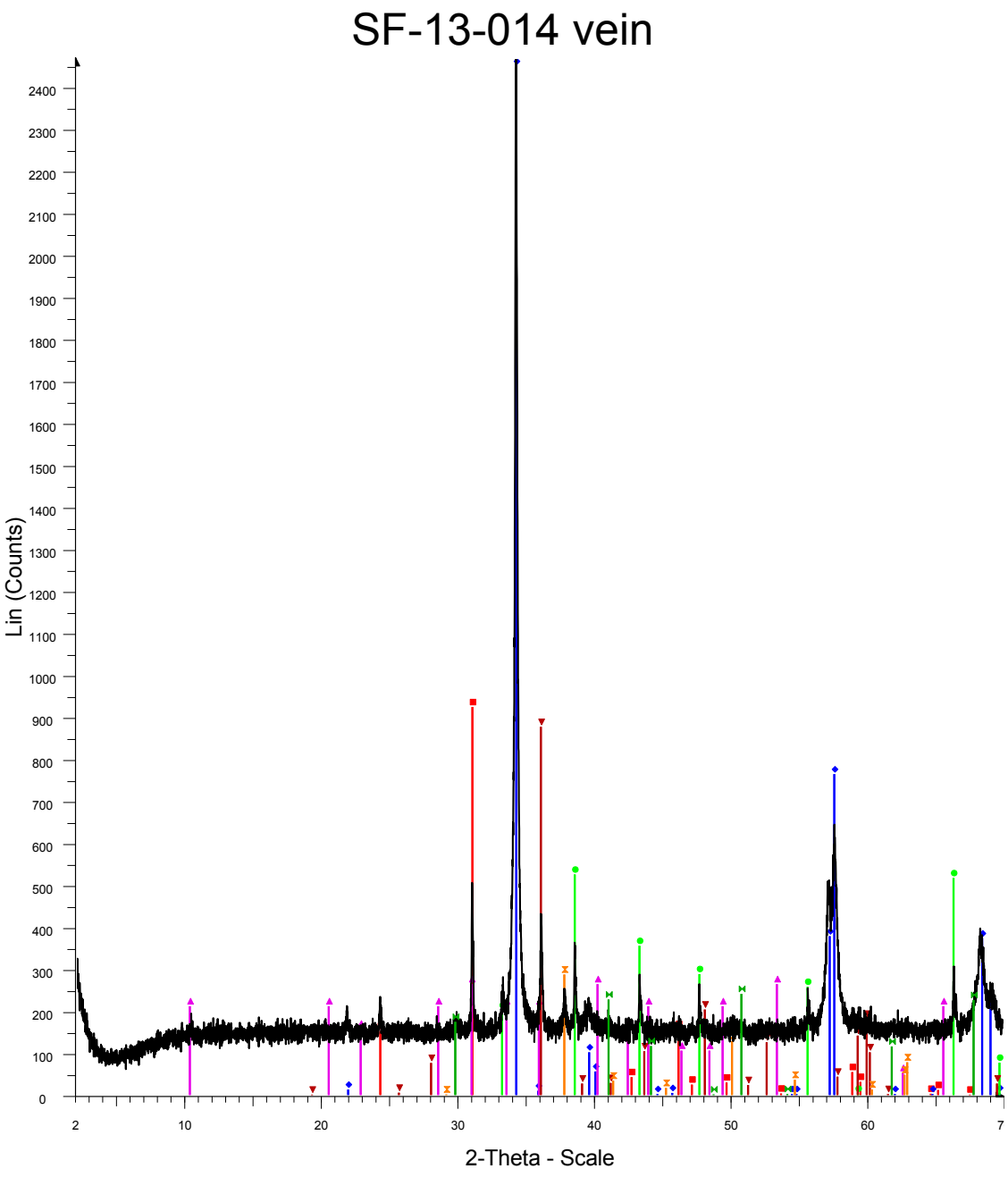

Red-Quartz
Blue-Chalcopyrite
Green-Pyrite
Pink-Illite
Dark red-Dolomite
Orange-Magnesite
Dark green-Corundum
14vein

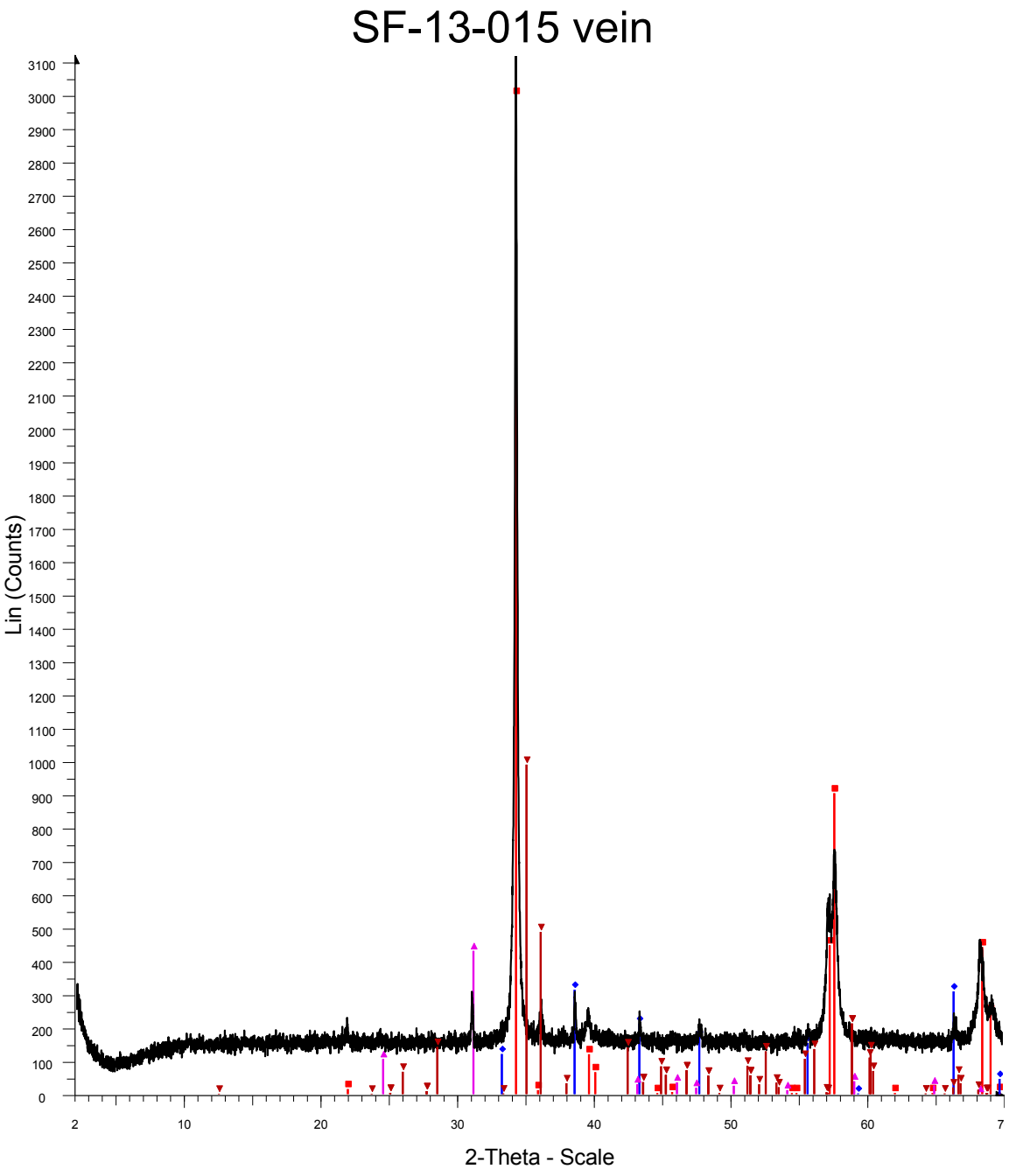

Red-Chalcopyrite
Blue-Pyrite
Pink-Quartz
Dark red-Calcite
15vein

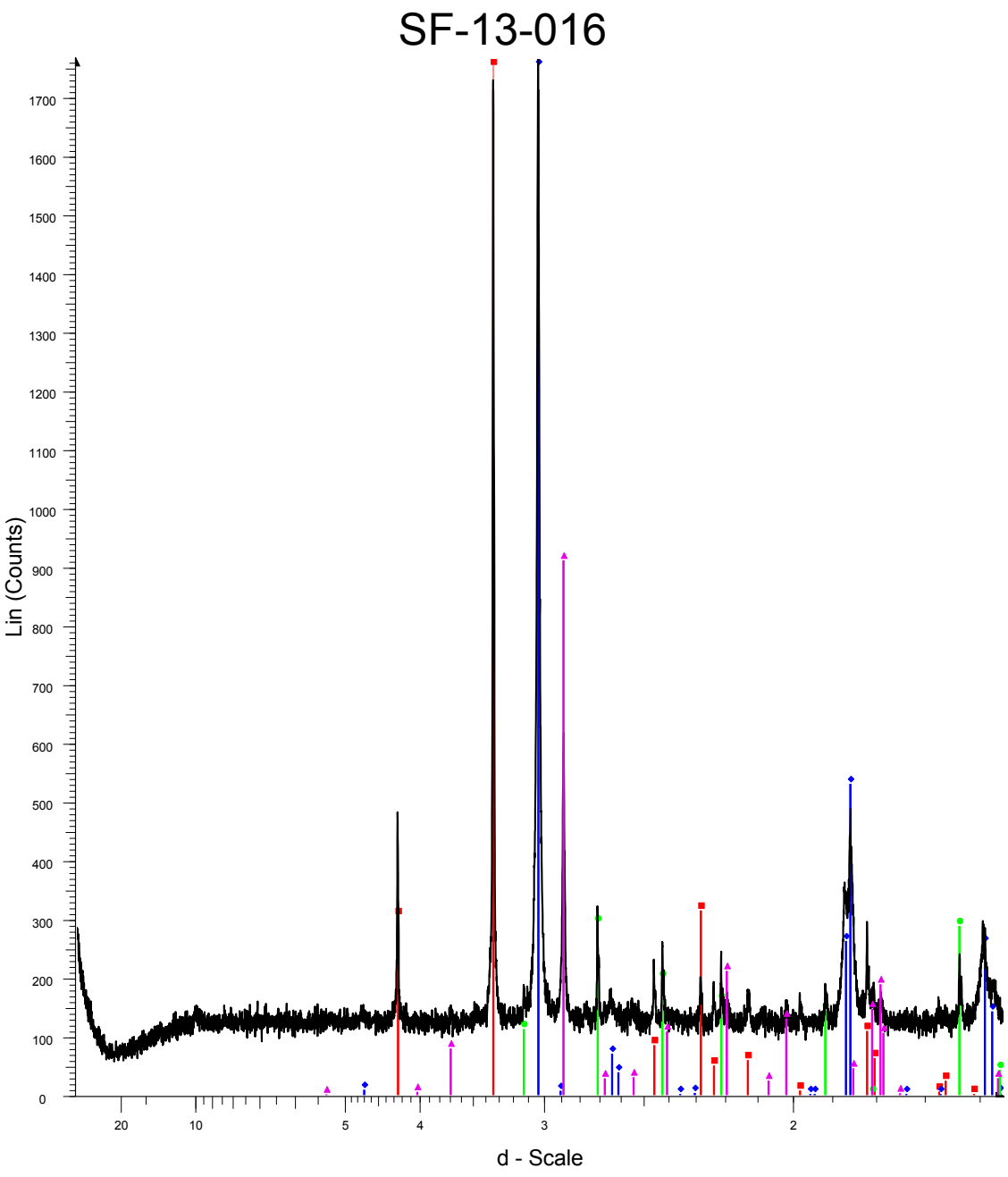

Red-Quartz
Blue-Chalcopyrite
Green-Pyrite
Pink-Dolomite
16

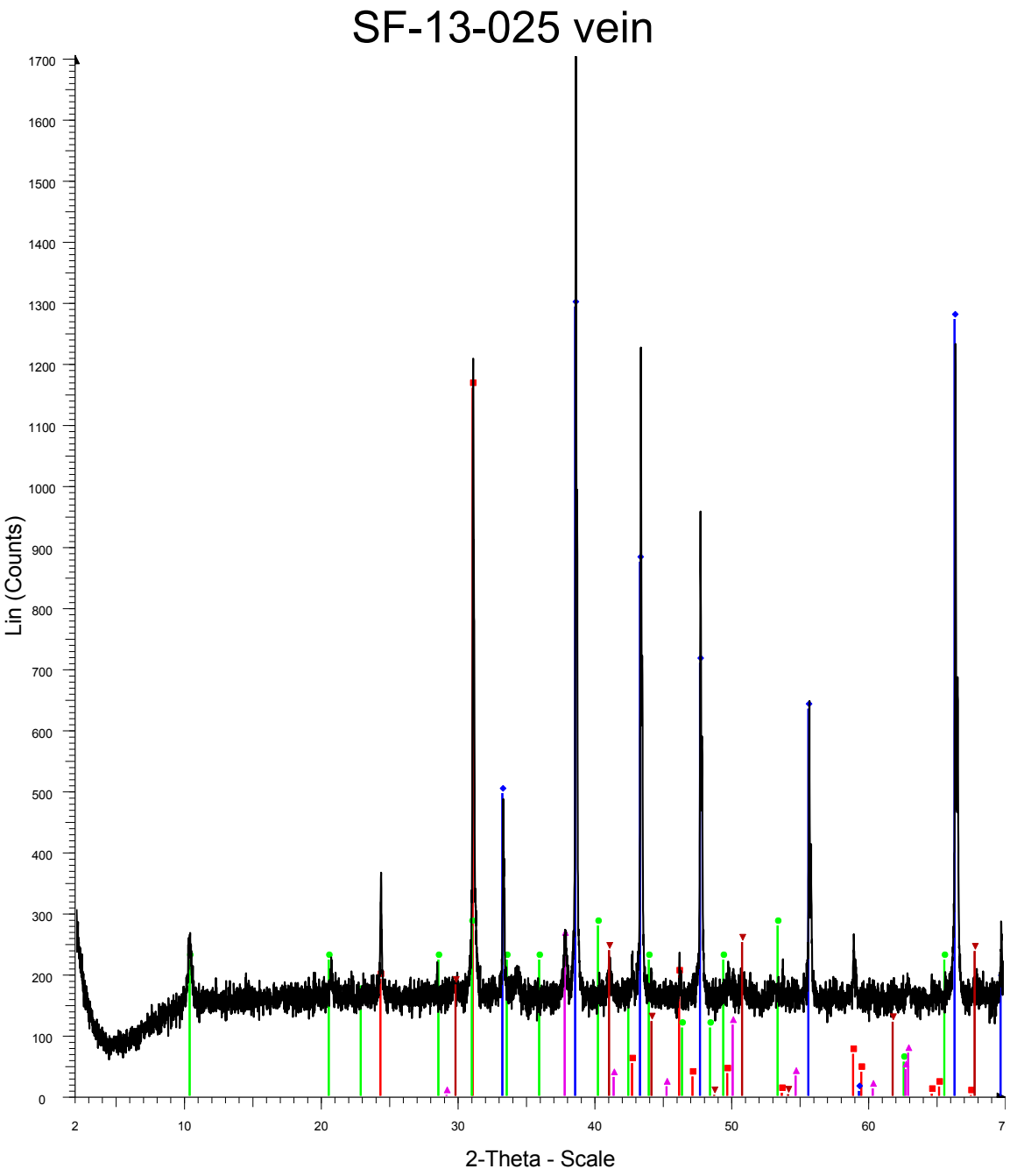

Red-Quartz
Blue-Pyrite
Green-Illite
Pink-Magnesite
Dark red-Corundum
25vein

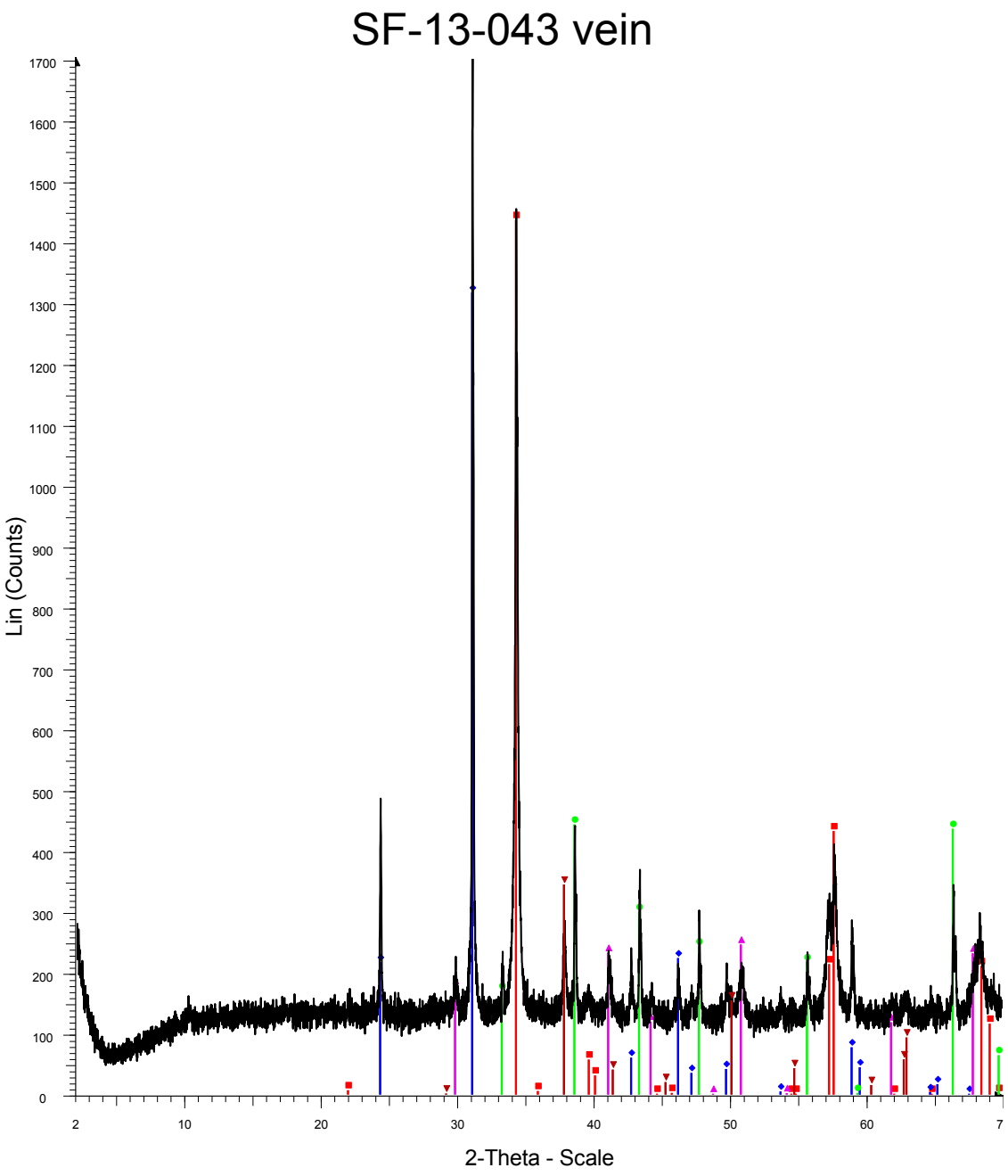

Red-Chalcopyrite
Blue-Quartz
Green-Pyrite
Pink-Corundum
Dark red-Magnesite
43vein

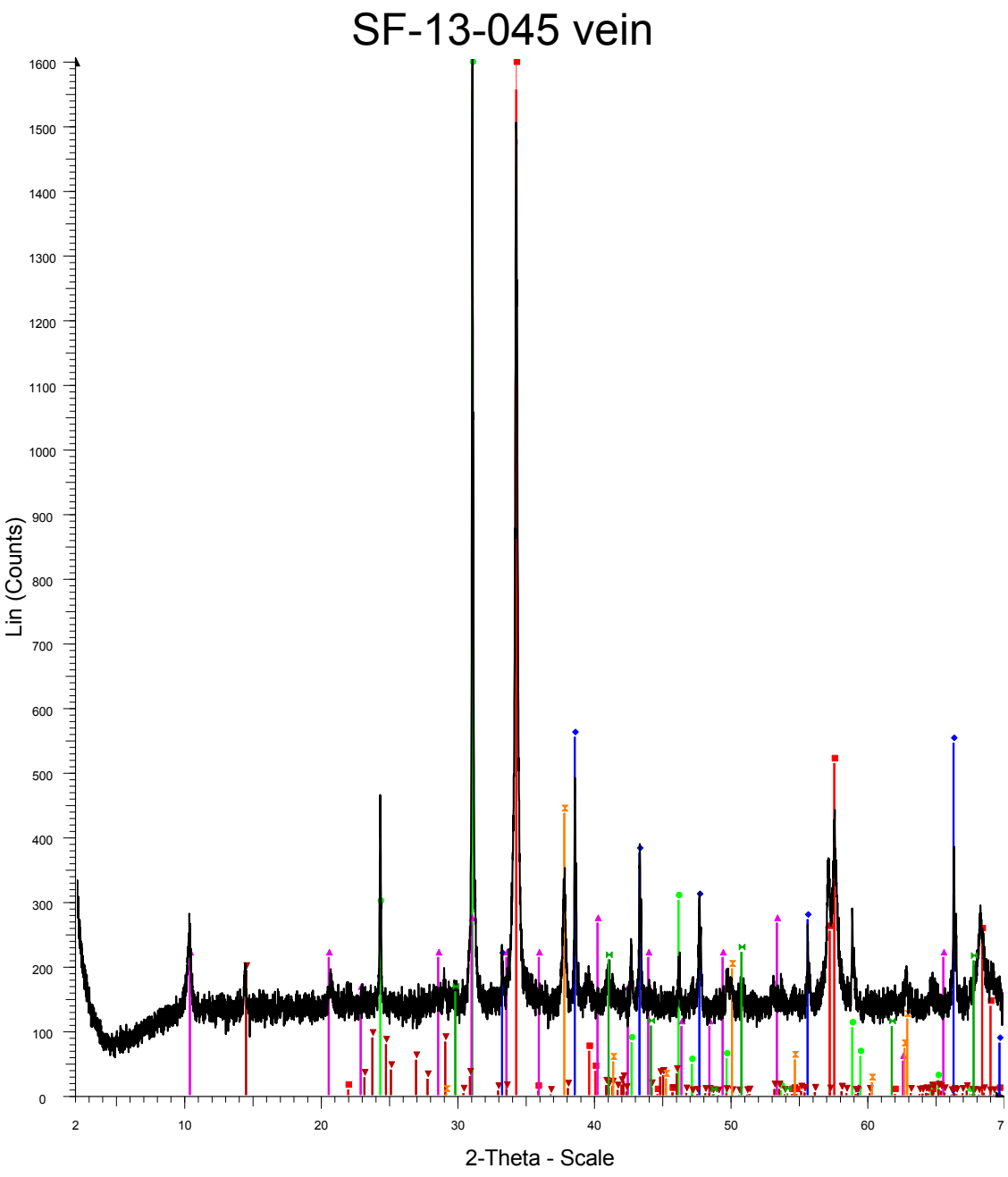

Red-Chalcopyrite
Blue-Pyrite
Green-Quartz
Pink-Illite
Dark red-Kaolinite
Orange-Magnesite
Dark green-Corundum
45vein

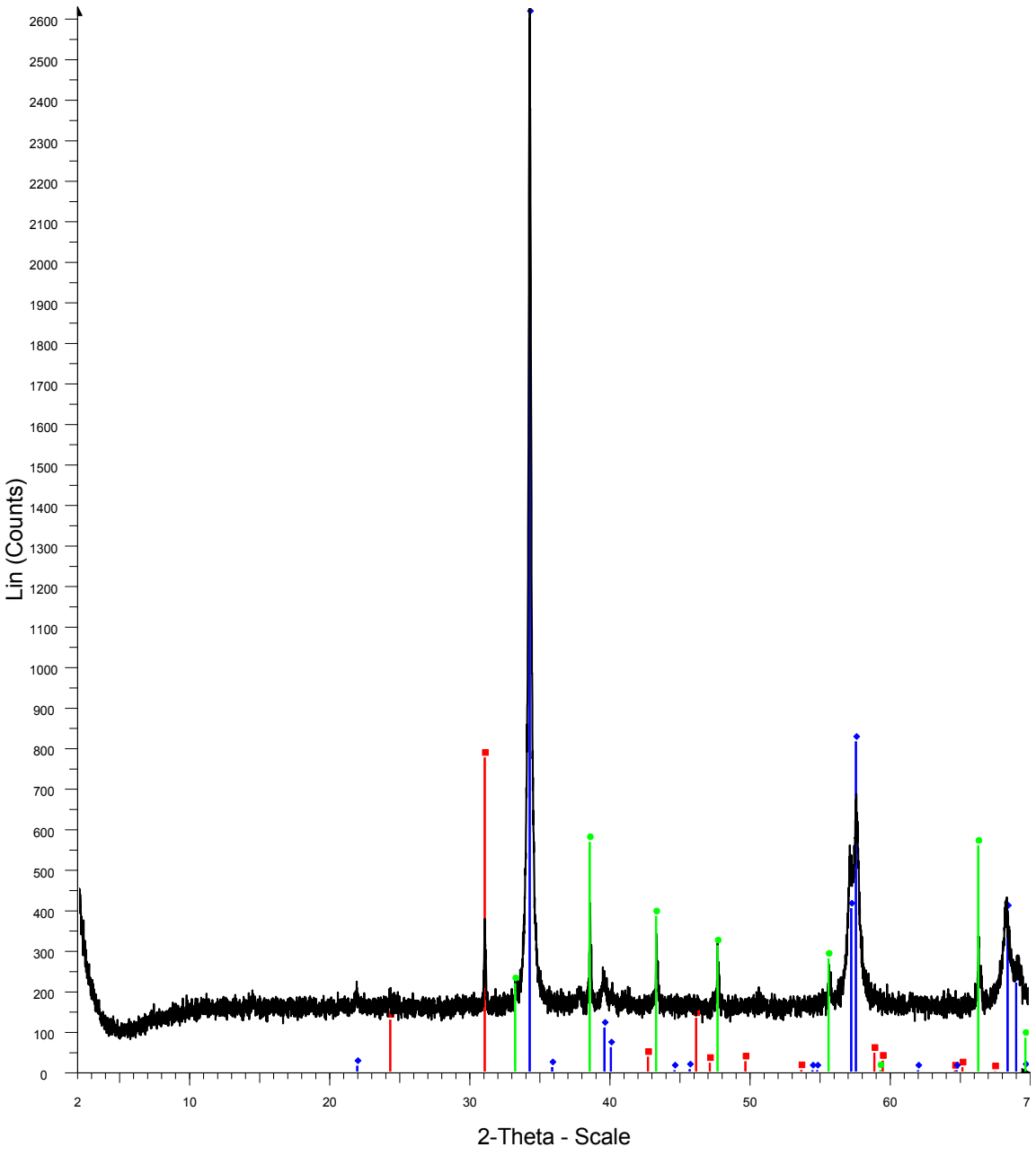

Red-Quartz
Blue-Chalcopyrite
Green-Pyrite
88vein

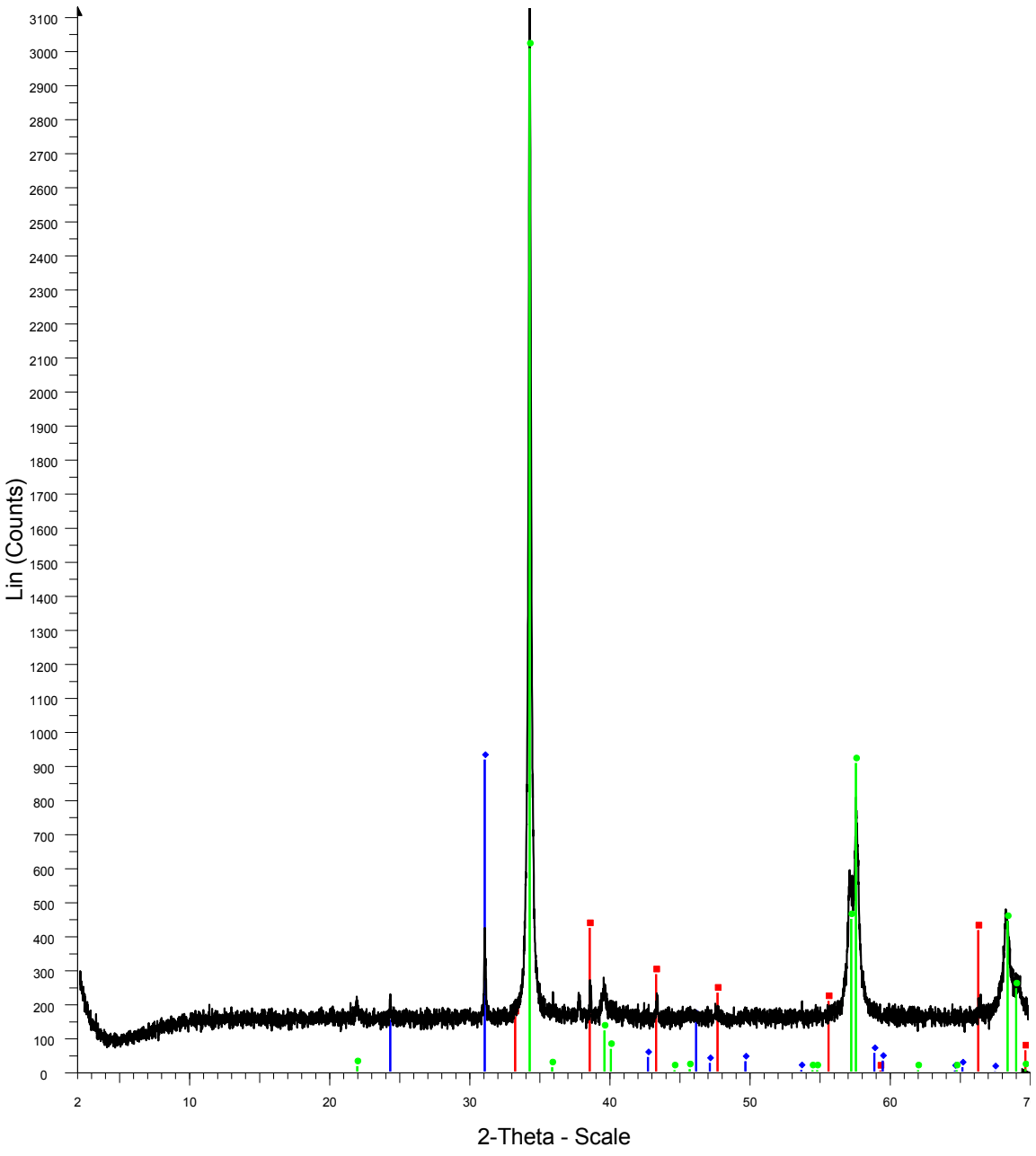

Red-Pyrite
Blue-Quartz
Green-Chalcopyrite
89vein

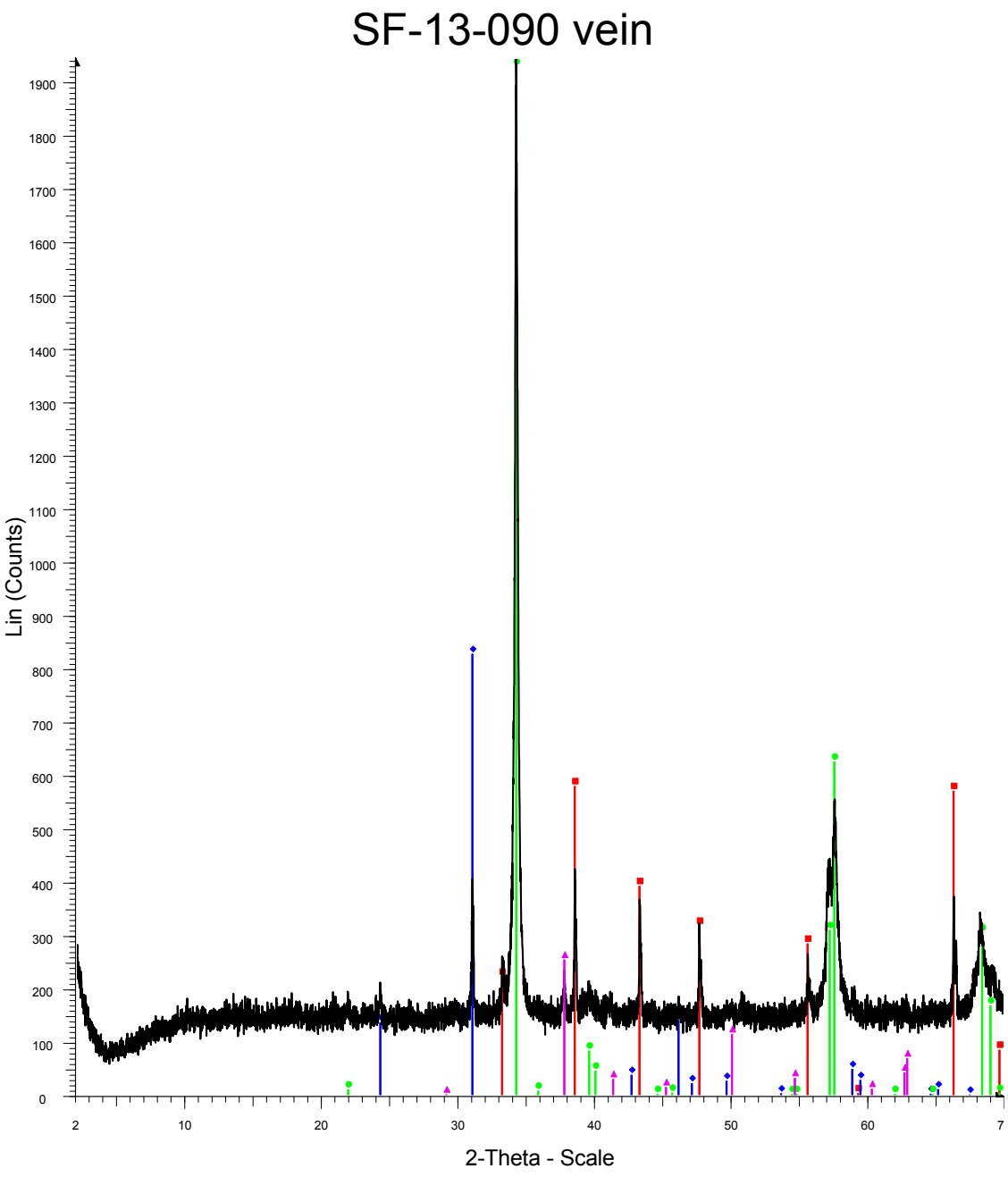

Red-Pyrite
Blue-Quartz
Green-Chalcopyrite
Pink-Magnesite
90vein

SF-13-039.1

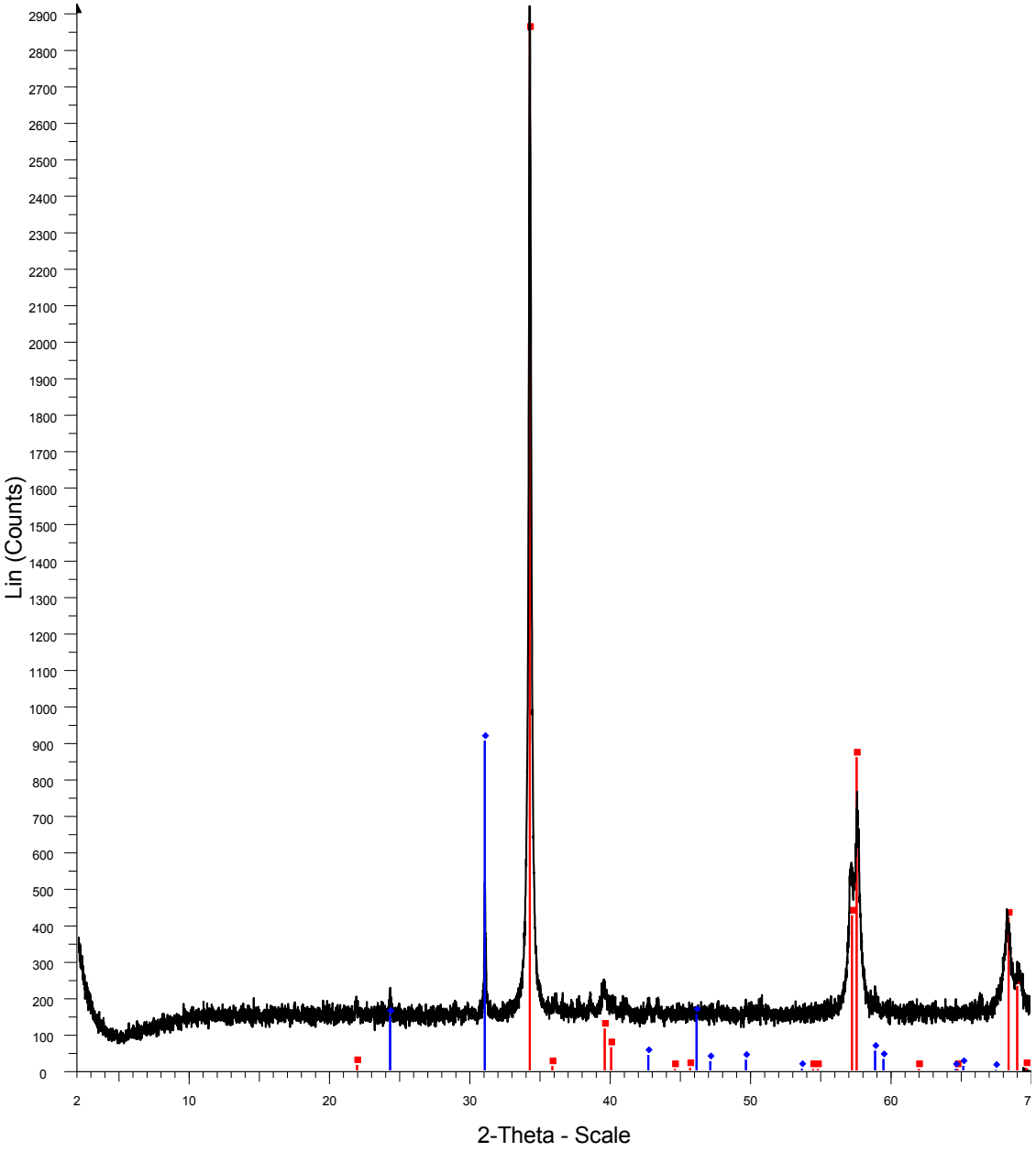

Red-Chalcopyrite
Blue-Quartz
0391

SF-13-039.2

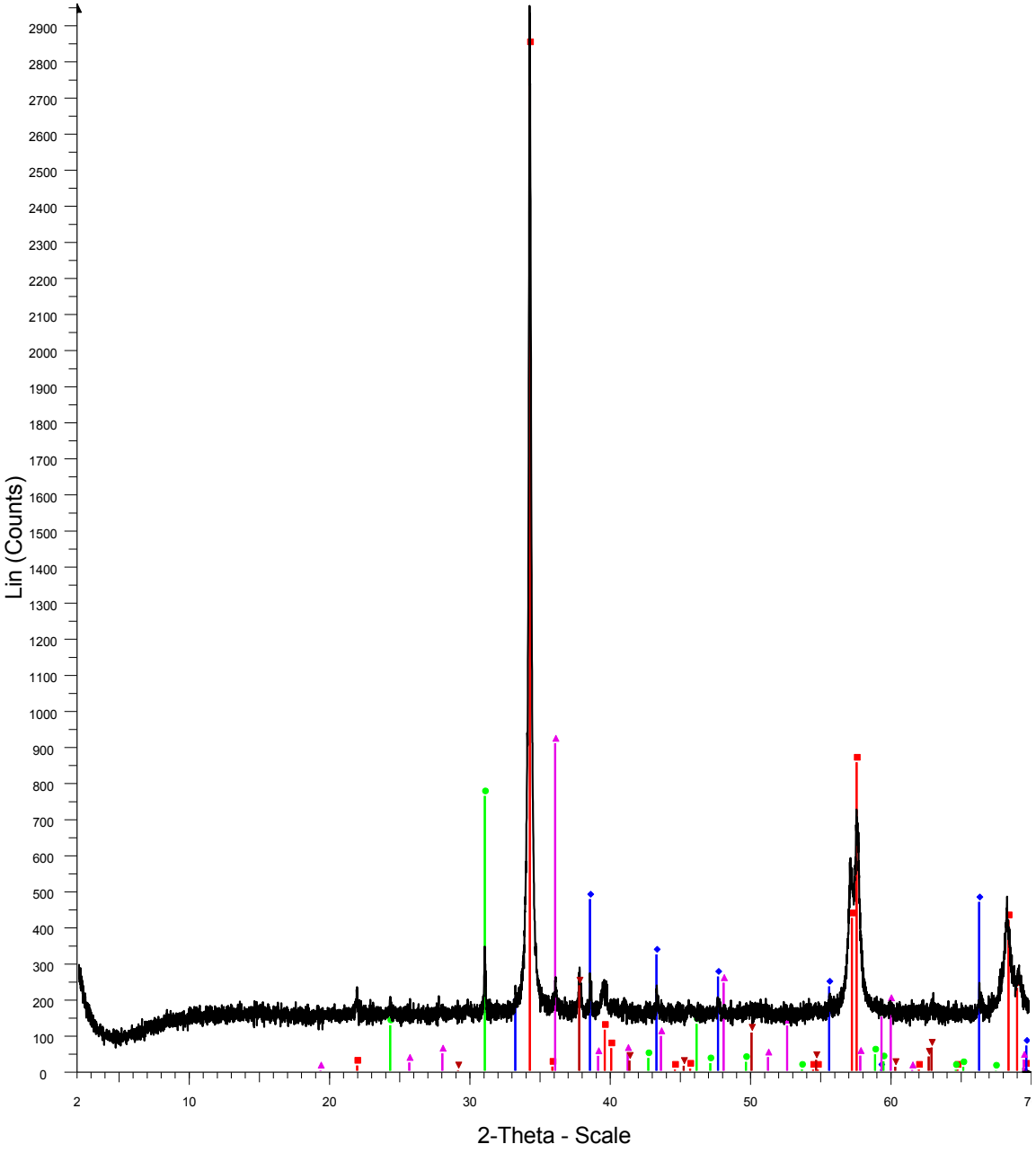

Red-Chalcopyrite
Blue-Pyrite
Green-Quartz
Pink-Dolomite
Dark red-Magnesite

0392

SF-13-039.3

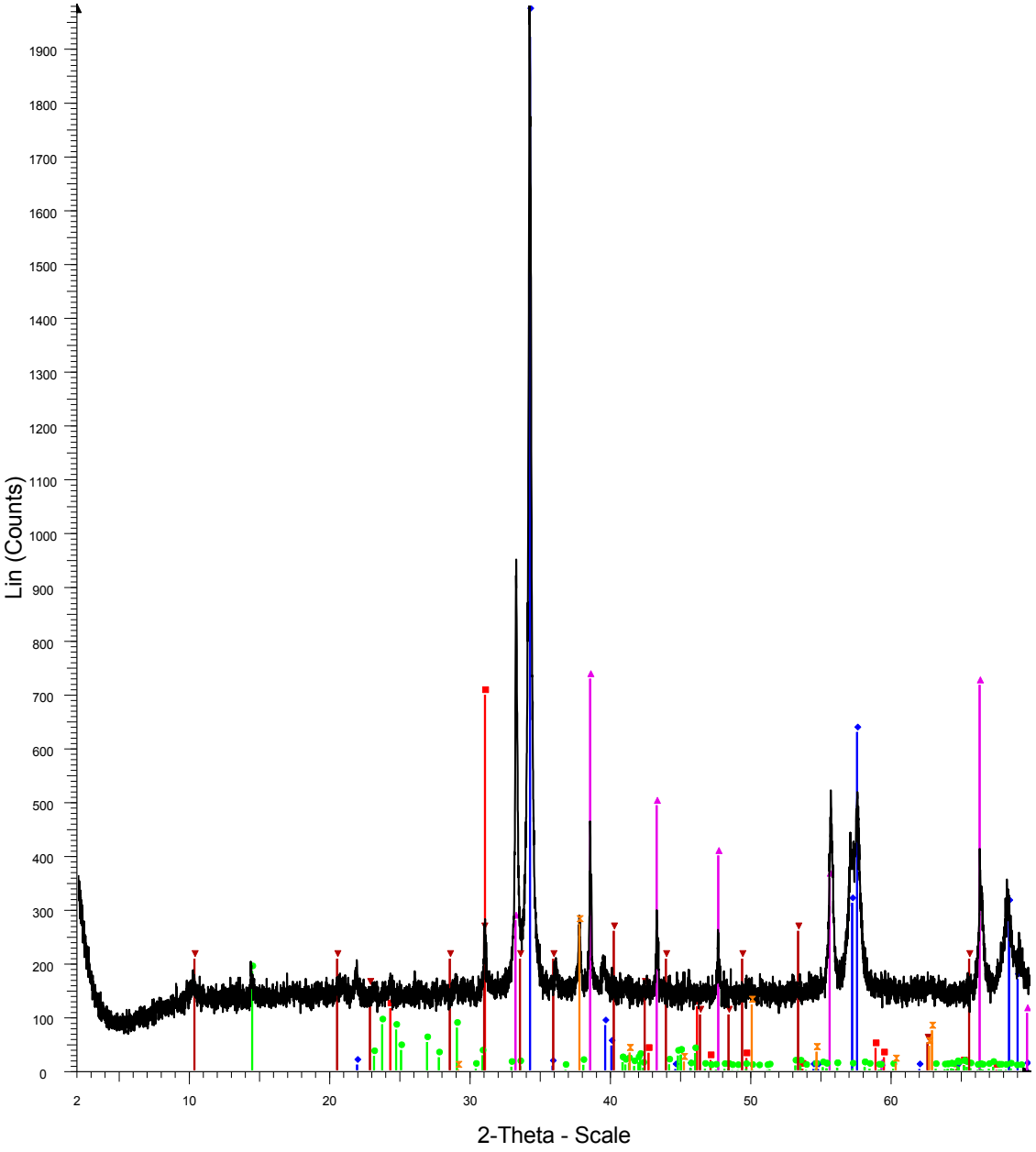

Red-Quartz
Blue-Chalcopyrite
Pink-Pyrite
Green-Kaolinite
Dark red-Illite
Orange-Magnesite

0393

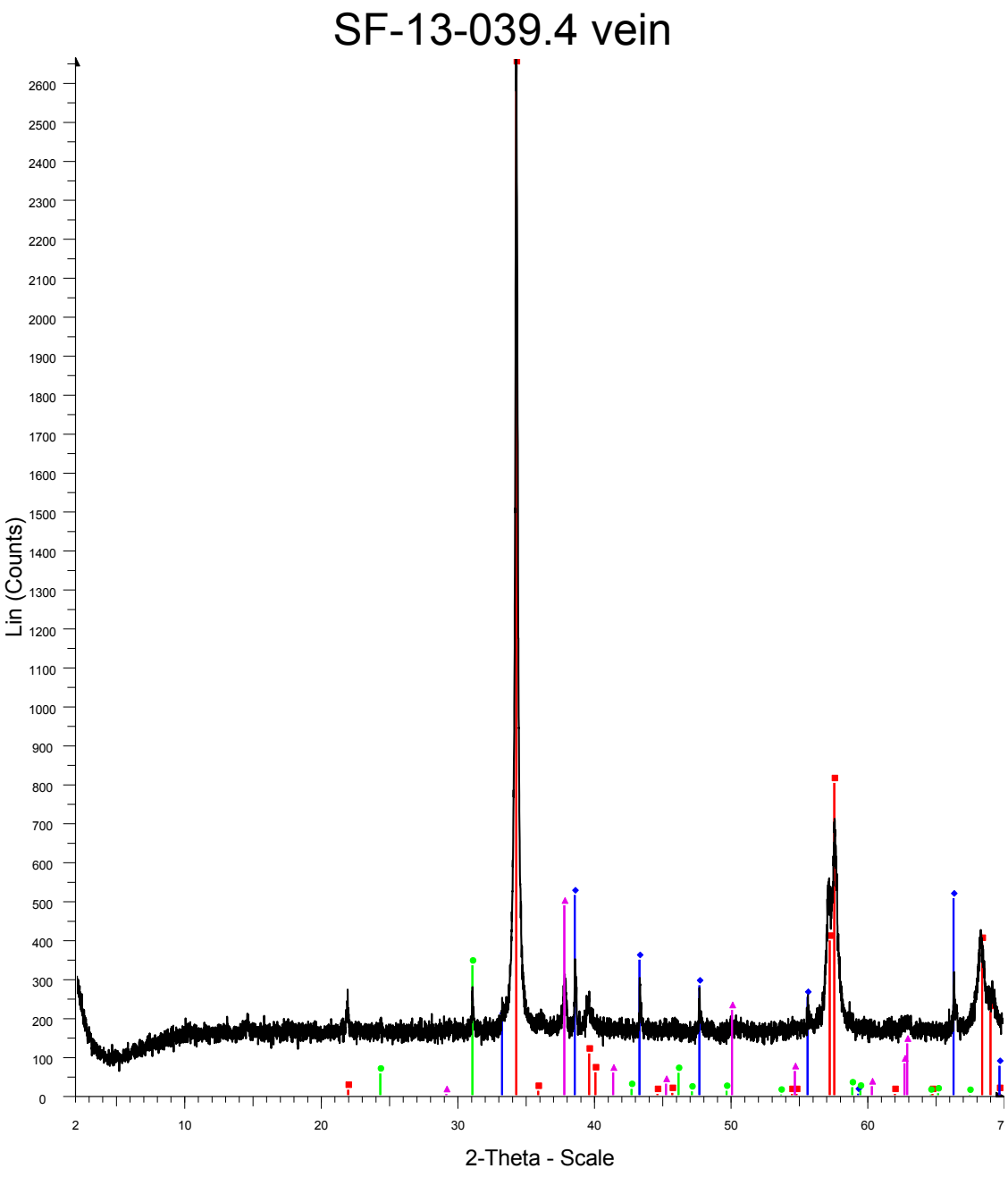

Red-Chalcopyrite
Blue-Pyrite
Green-Quartz
Pink-Magnesite

0394vein

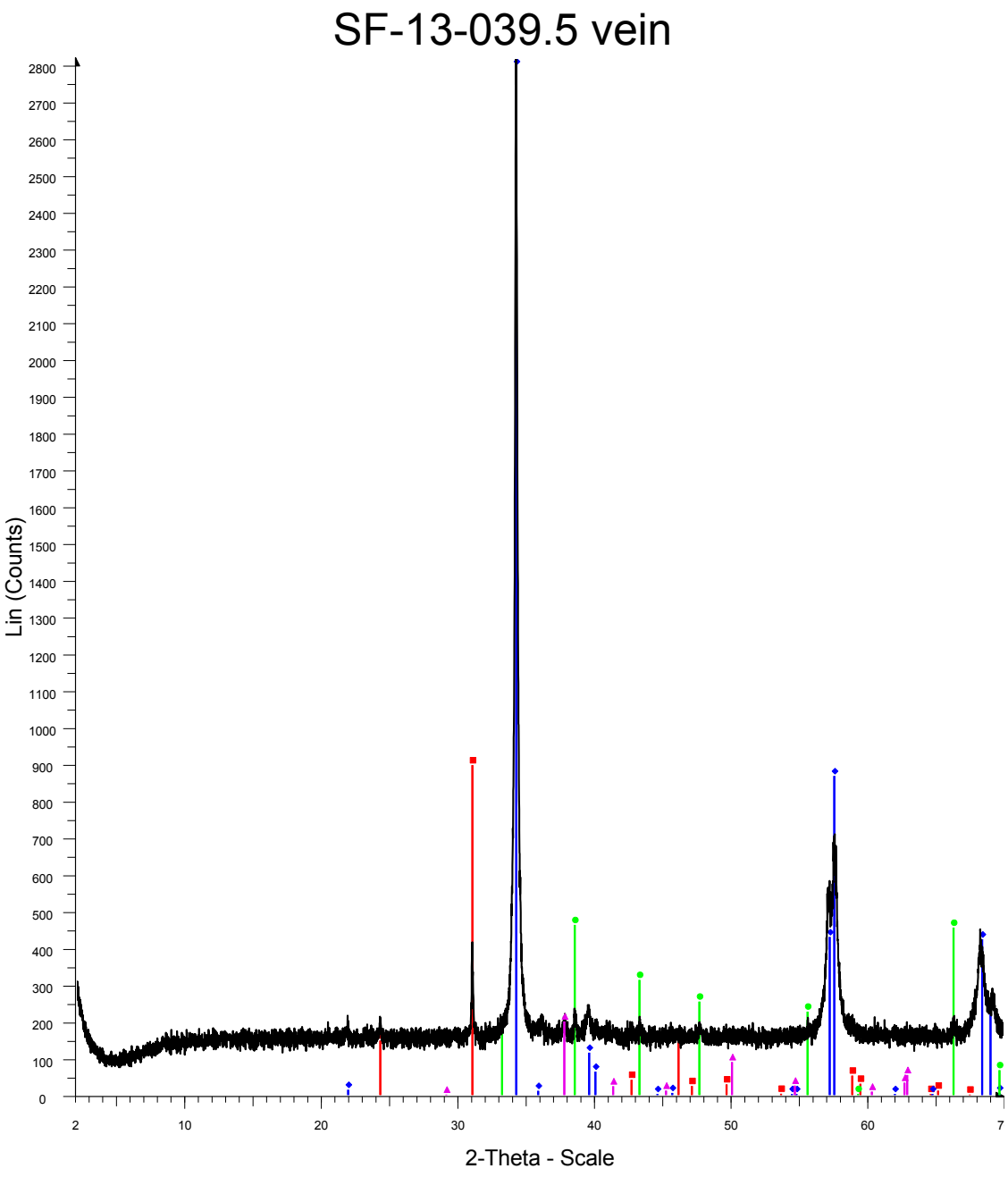

Red-Quartz
Blue-Chalcopyrite
Green-Pyrite
Pink-Magnesite

0395vein

SF-13-039.6

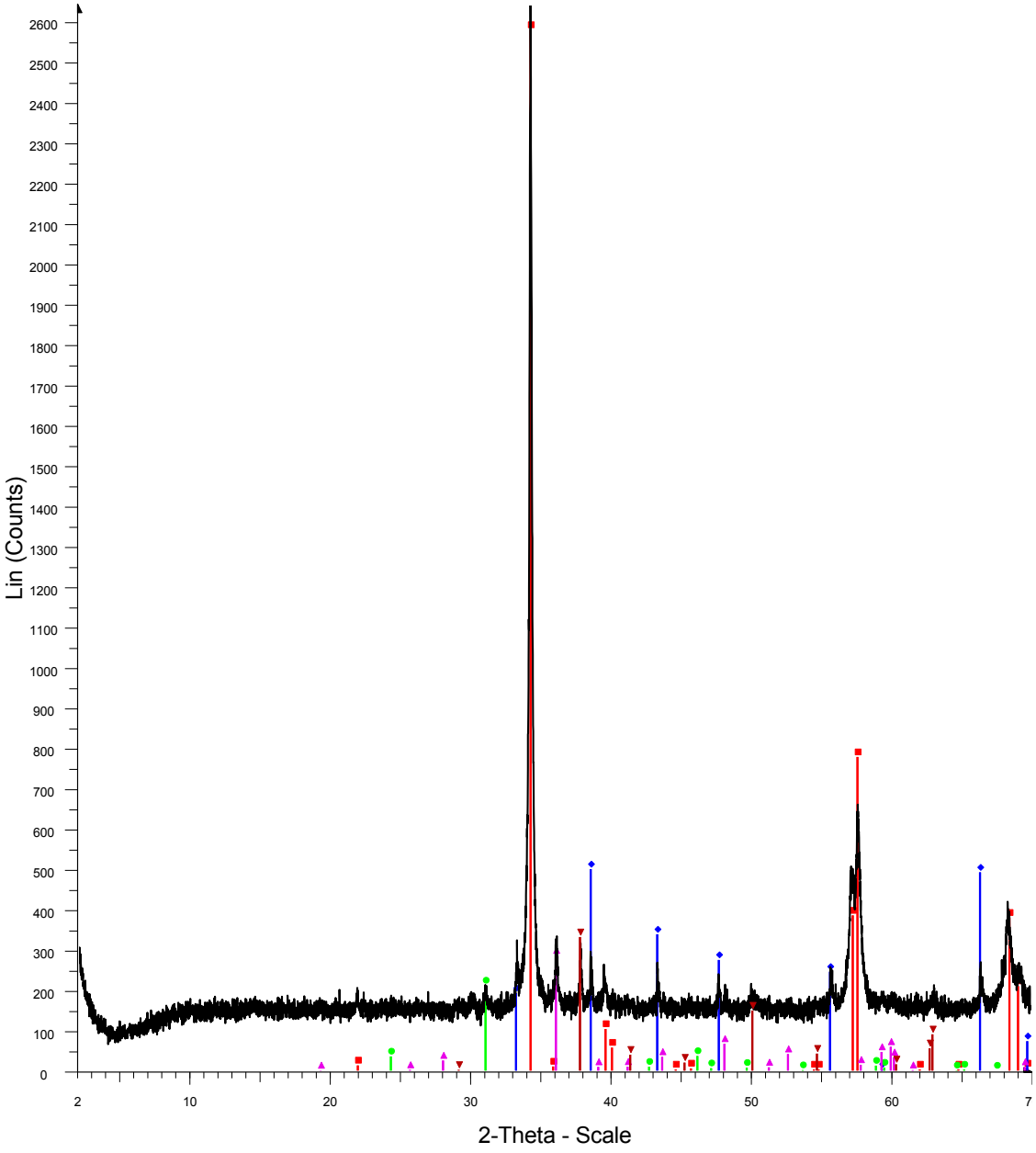

Red-Chalcopyrite
Blue-Pyrite
Green-Quartz
Pink-Dolomite
Dark red-Magnesite

0396

SF-13-039.7

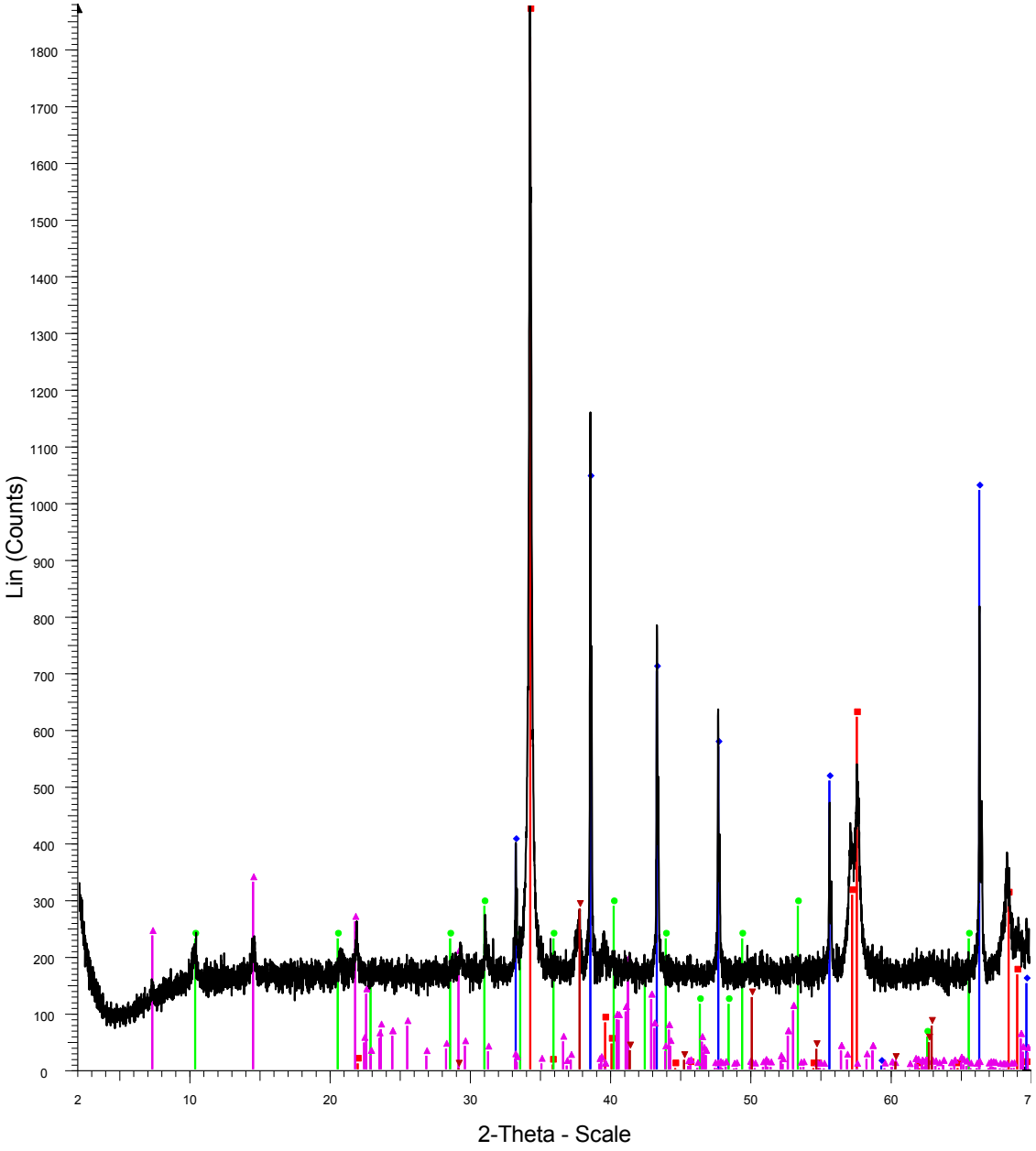

Red-Chalcopyrite
Blue-Pyrite
Green-Illite
Pink-Chlorite
Dark red-Magnesite

0397

SF-13-039.8

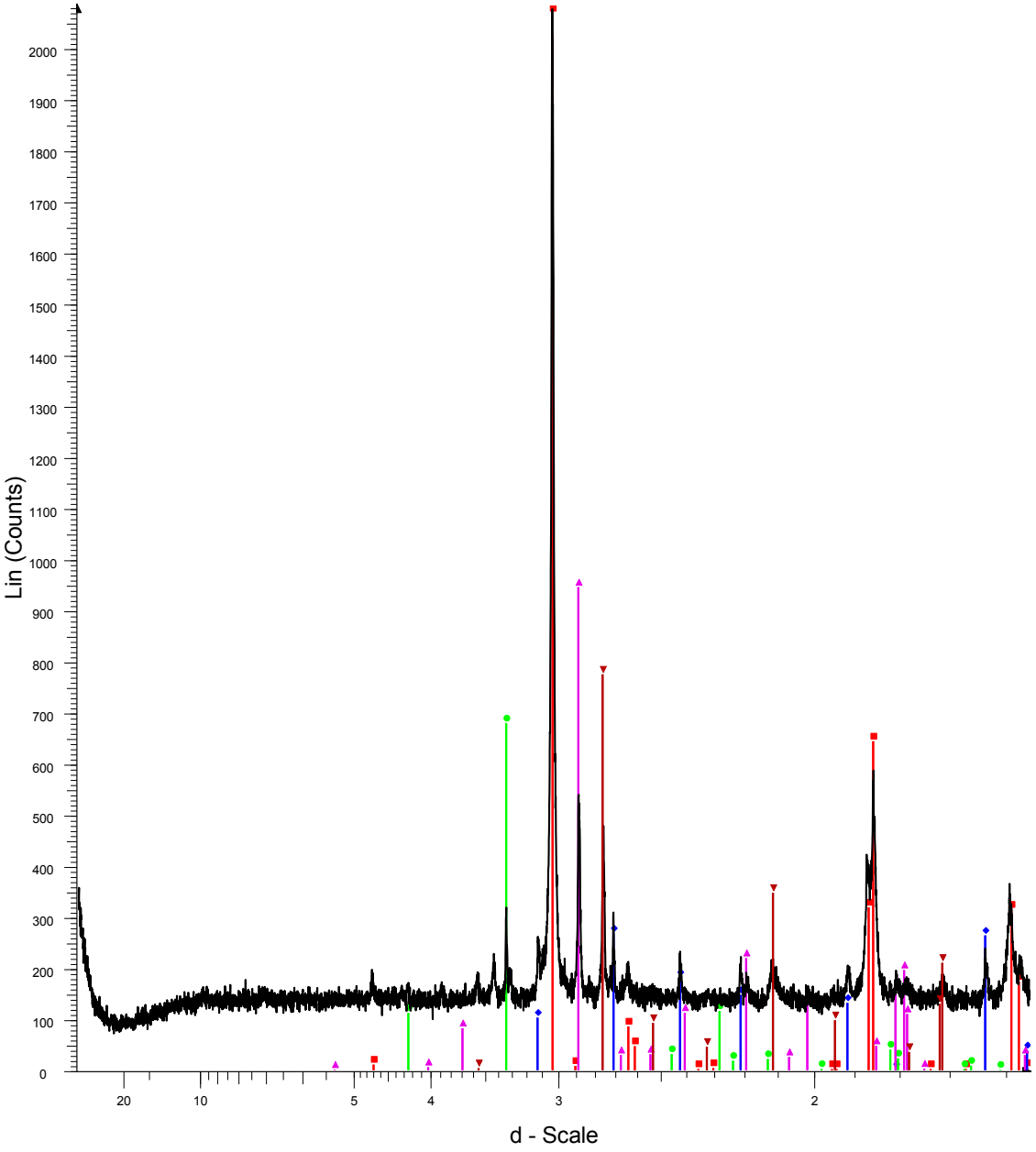

Red-Chalcopyrite
Blue-Pyrite
Green-Quartz
Pink-Dolomite
Dark red-Magnesite

0398

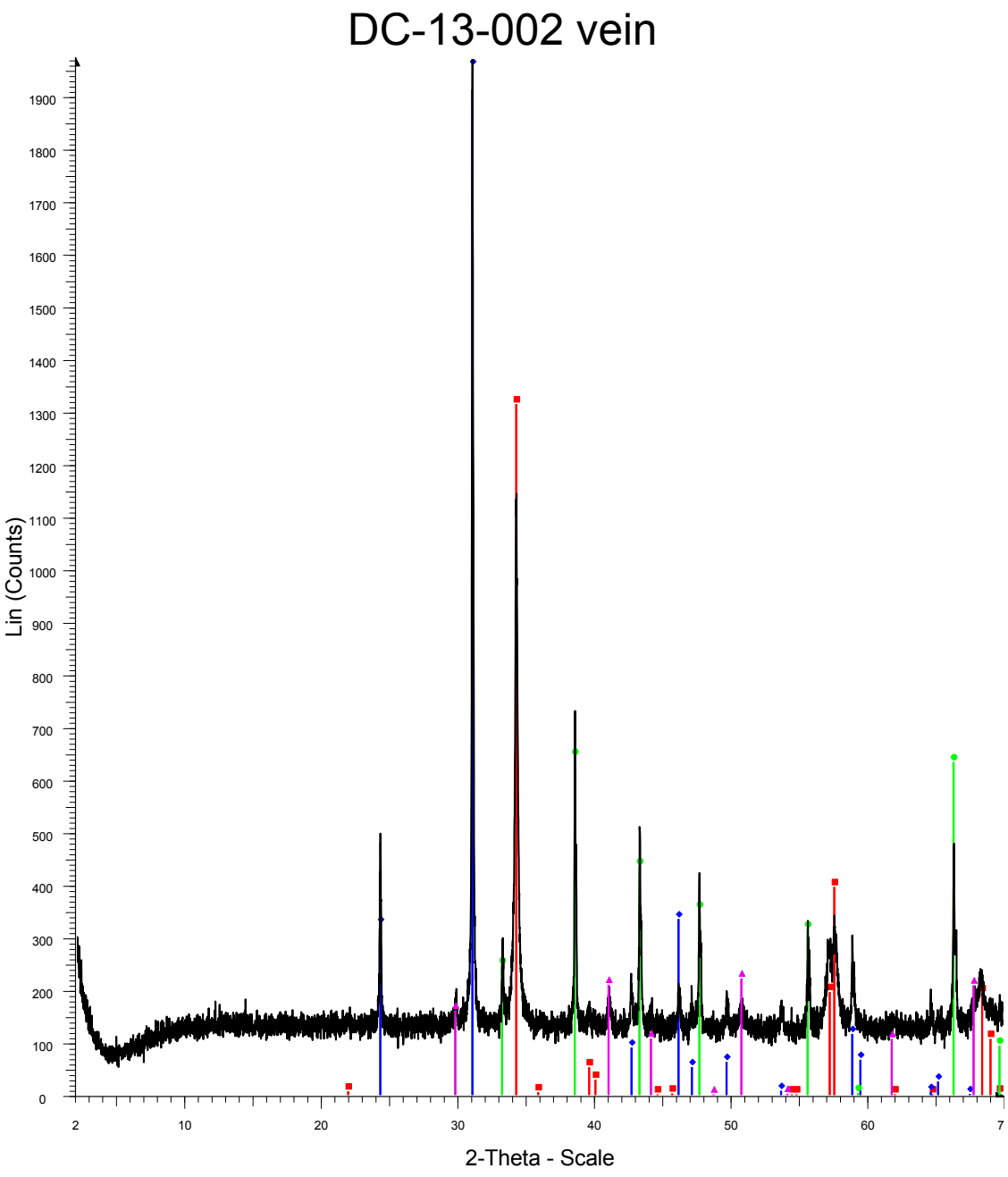

Red-Chalcopyrite
Blue-Quartz
Green-Pyrite
Pink-Corundum

Dc2veinteeny

DC-13-003

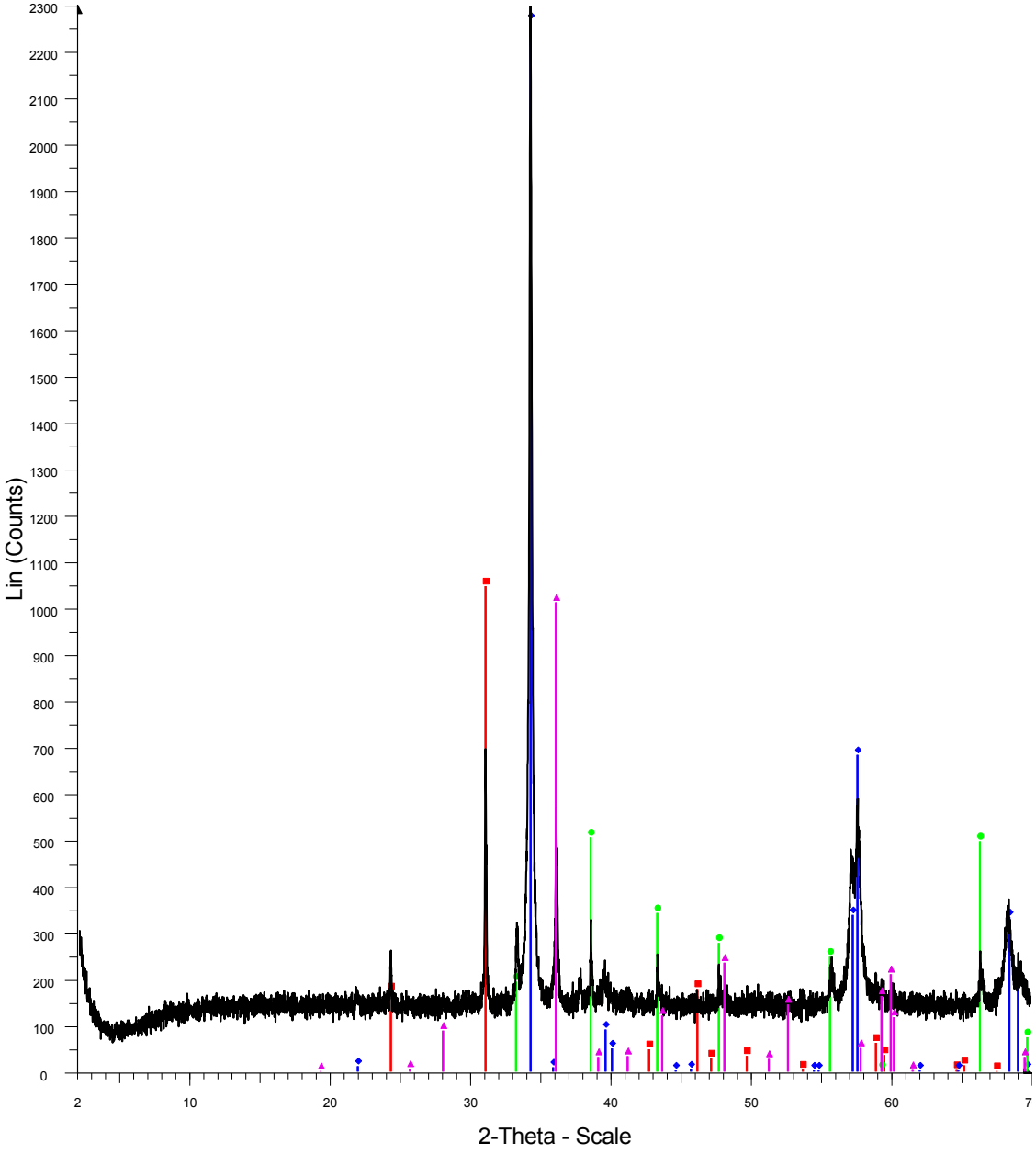

Red-Quartz
Blue-Chalcopyrite
Green-Pyrite
Pink-Dolomite

Dc3

DC-13-004

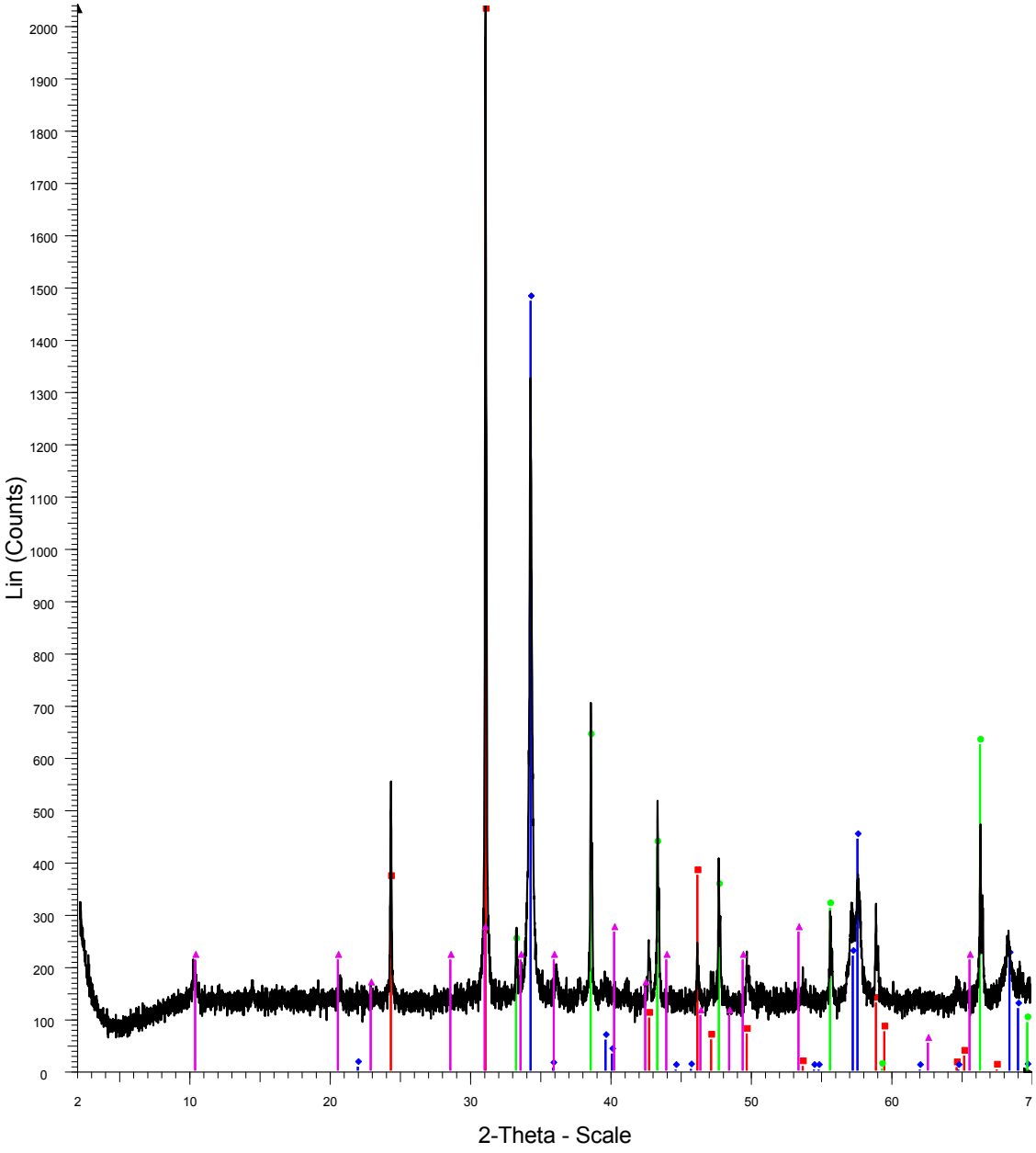

Red-Quartz
Blue-Chalcopyrite
Green-Pyrite
Pink-Illite

Dc4

APPENDIX B

Drill hole sample pictures, displaying the sample as well as the drill locations for the stable isotope work. They are ordered numerically, split into silicate and sulfide sections.

Silicates

Scale bar is in cm, broken into mm. Black arrows point to quartz locations, yellow arrows point to illite locations.

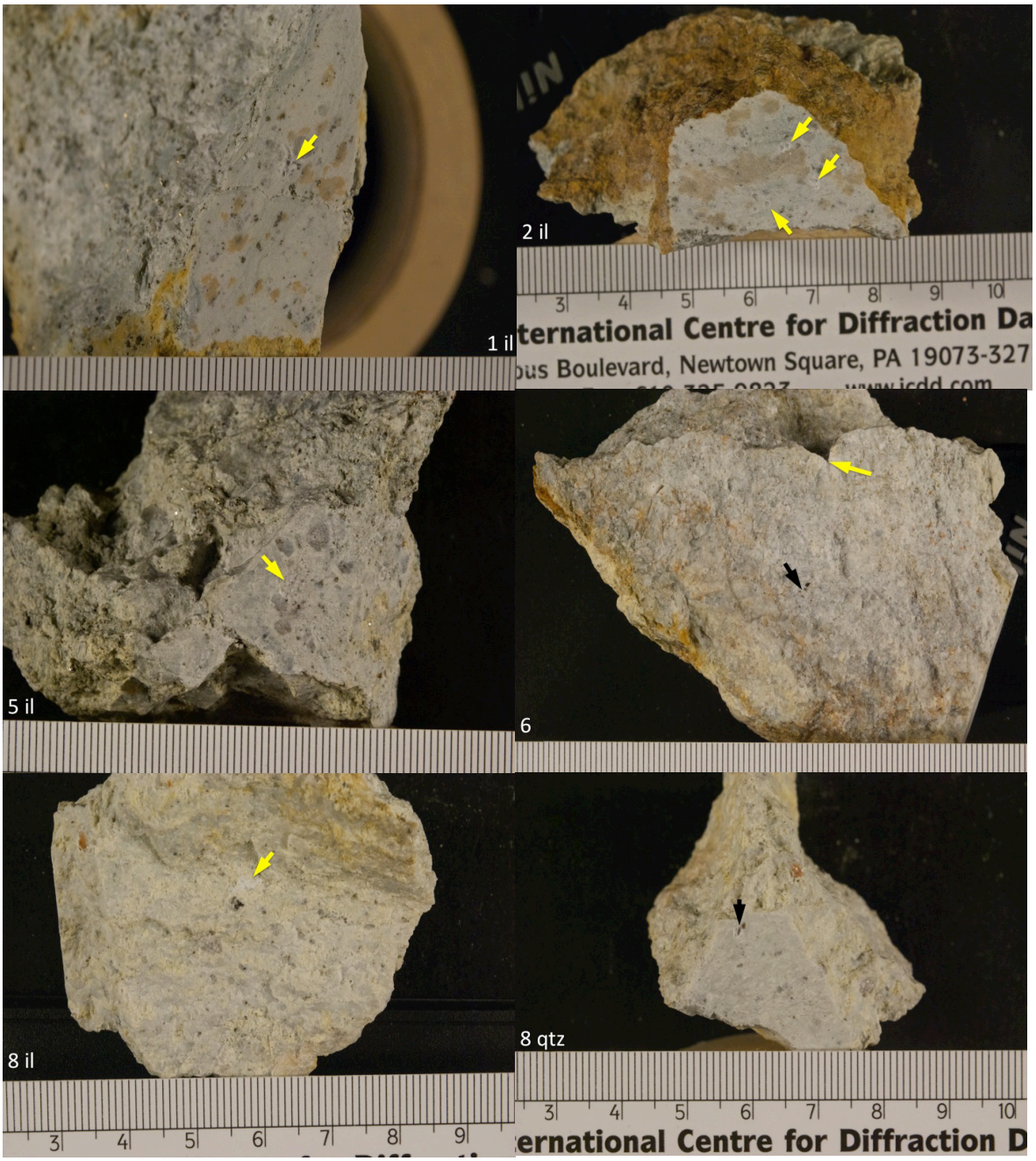
1 il
2 il
ternational Centre for Diffraction Da
us Boulevard, Newtown Square, PA 19073-327
5 il
6
8 il
8 qtz
ernational Centre for Diffraction D

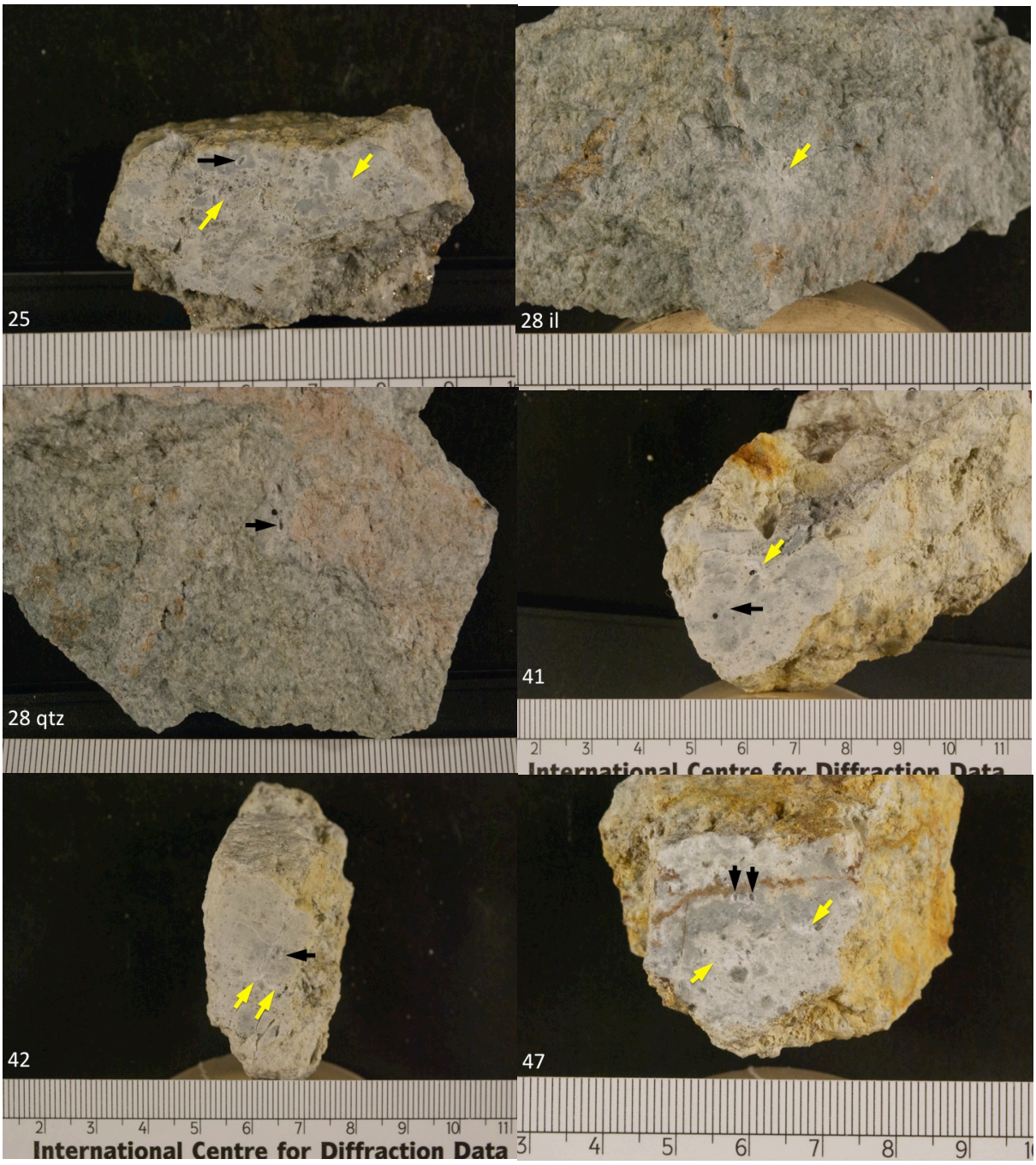
25
28 il
28 qtz
41
42
47
International Centre for Diffraction Data

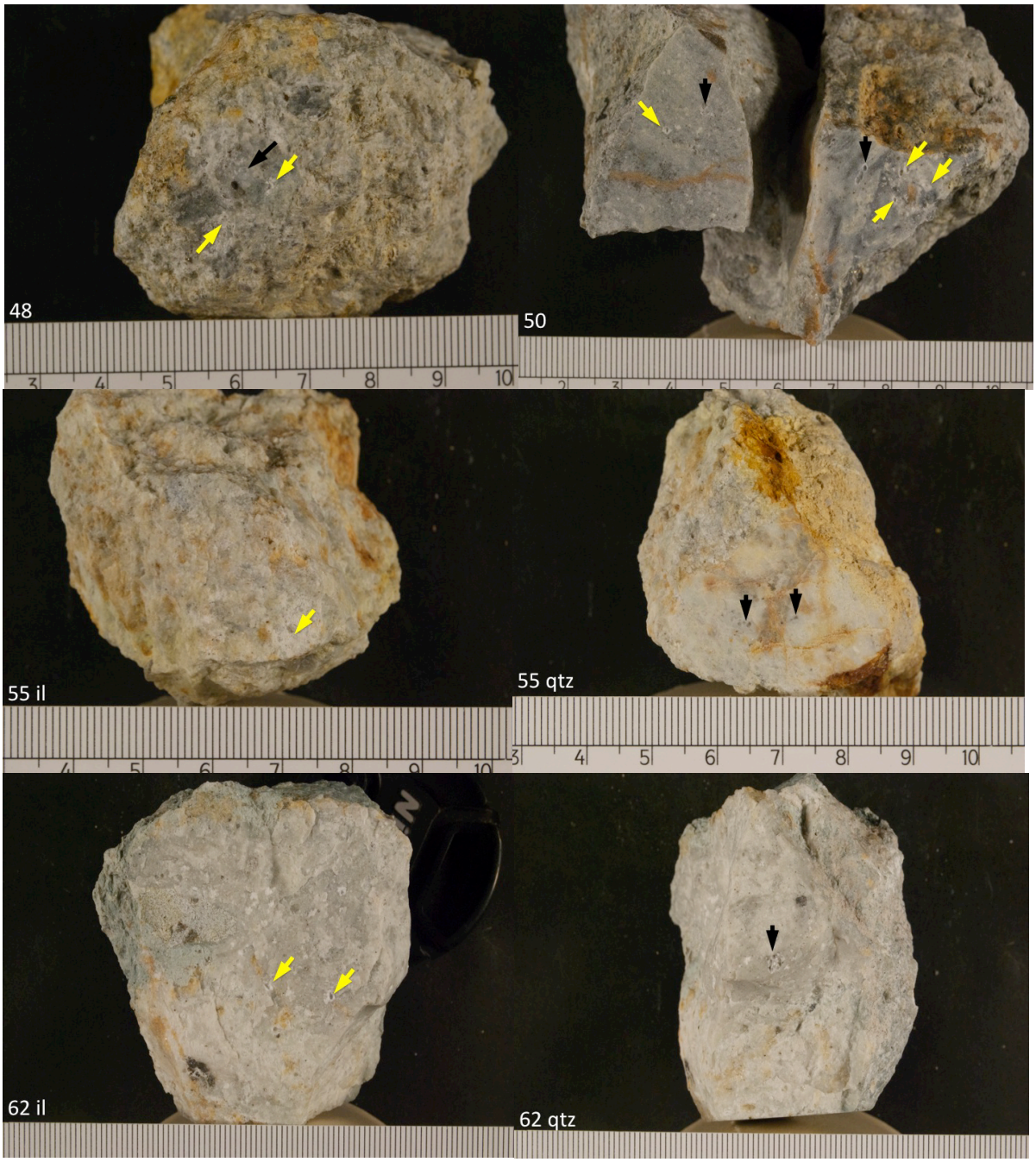
48
50
55 il
55 qtz
62 il
62 qtz

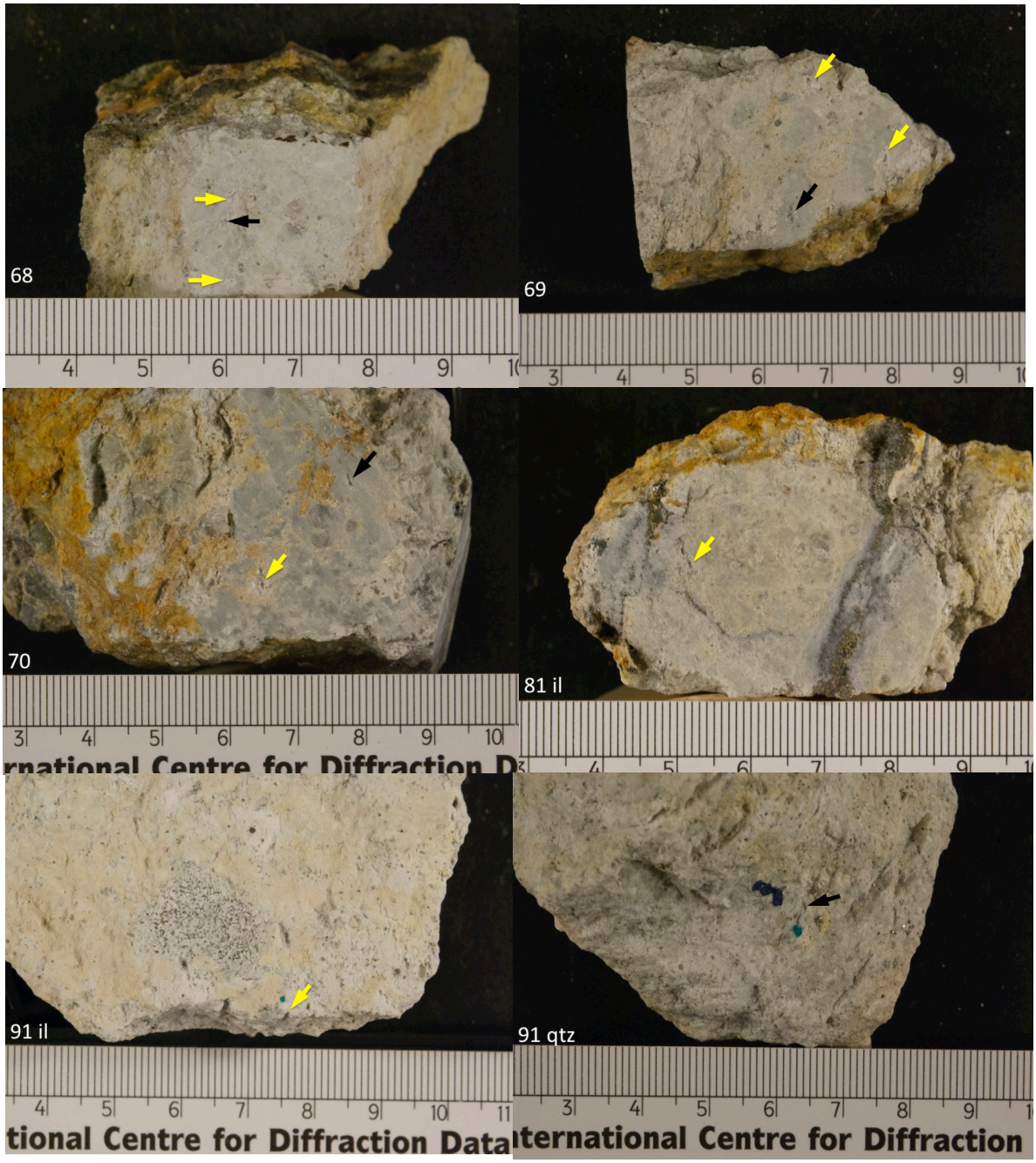
68
69
70
81 il
91 il
91 qtz
rnational Centre for Diffraction D
tional Centre for Diffraction Data
ternational Centre for Diffraction

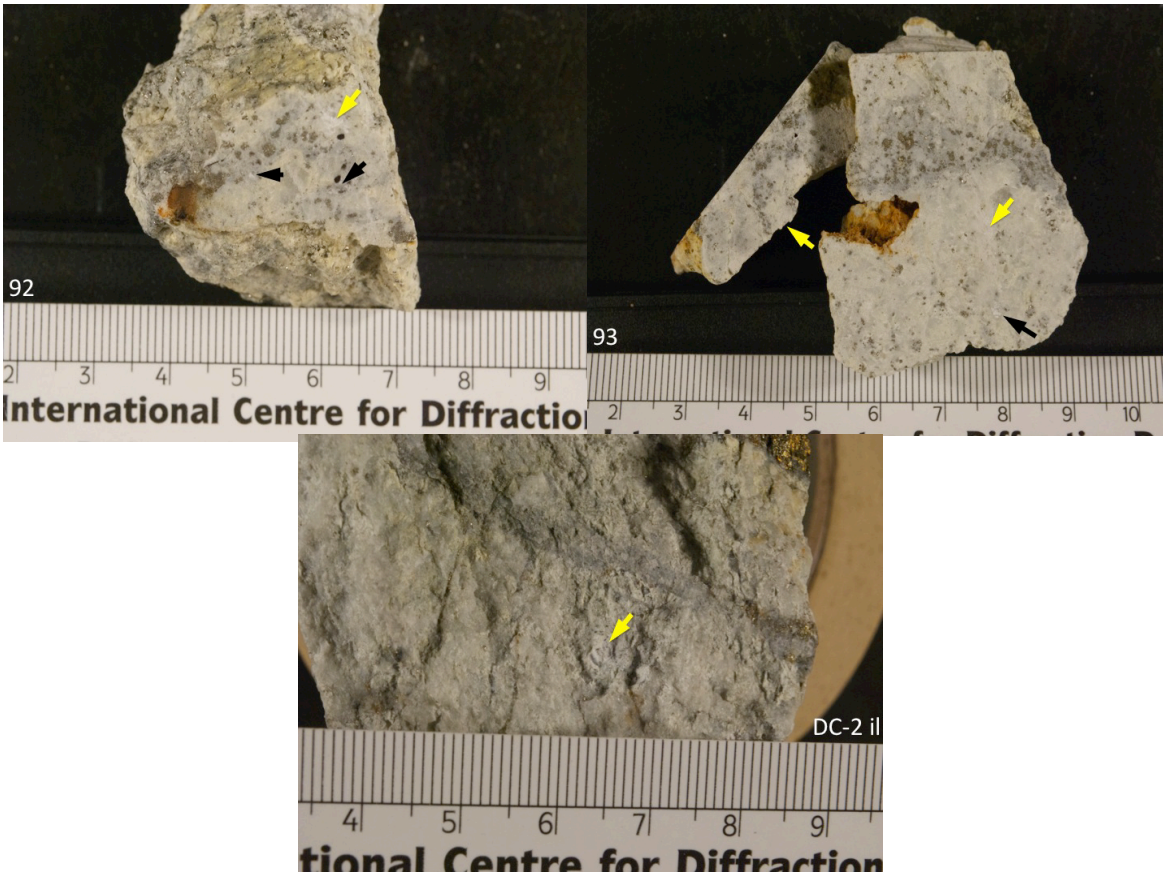
92
93
DC-2 il

Sulfides

Scale bar is in cm, broken into mm. Orange arrows point to chalcopyrite locations, red arrows point to pyrite locations.

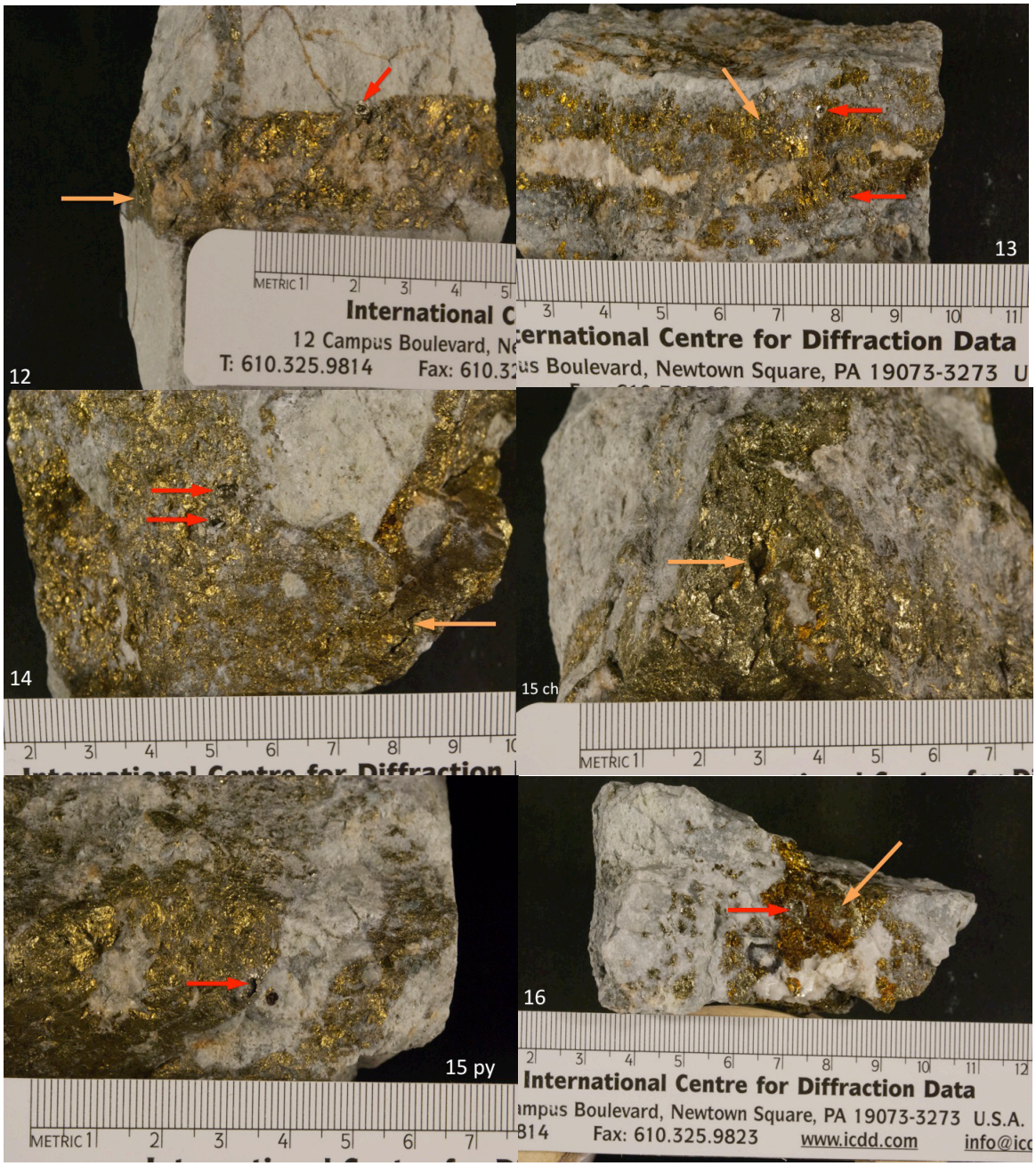

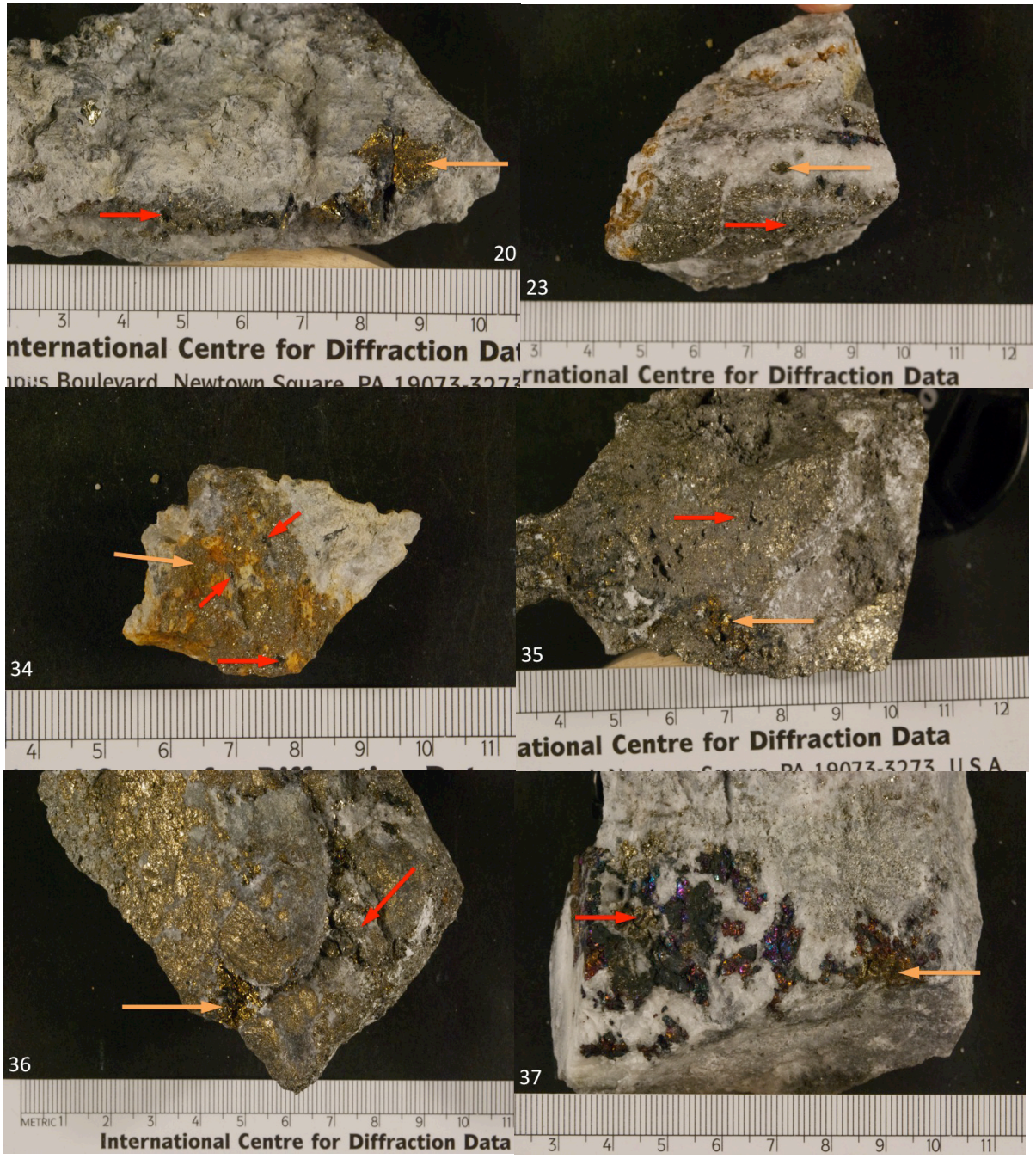
20
23
34
35
36
37
International Centre for Diffraction Data

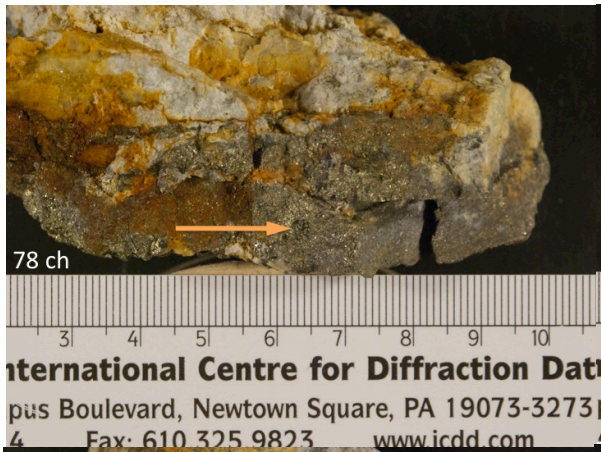
78 ch
3 4 5 6 7 8 9 10
ternational Centre for Diffraction Dat
pus Boulevard, Newtown Square, PA 19073-3273
Fax: 610 325 9823 www.icdd.com

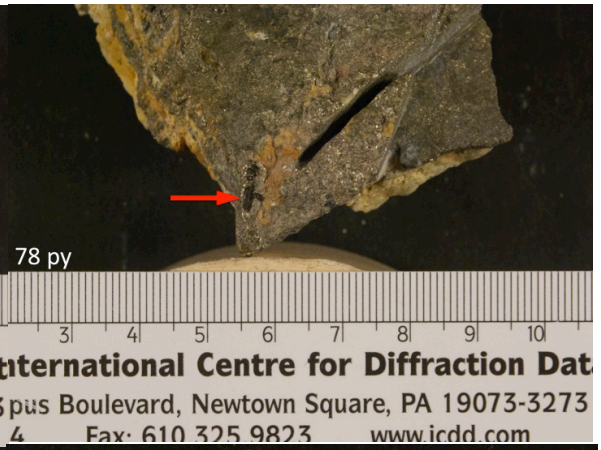
78 py
3 4 5 6 7 8 9 10
ternational Centre for Diffraction Dat
pus Boulevard, Newtown Square, PA 19073-3273
Fax: 610 325 9823 www.icdd.com

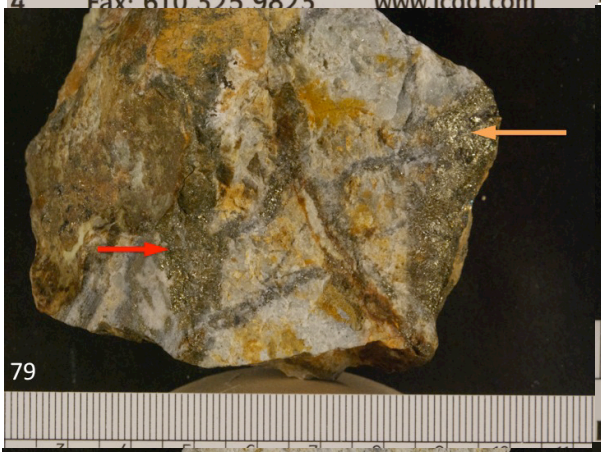
79


80
3 4 5 6 7 9 10
rnational Centre for Diffraction Da

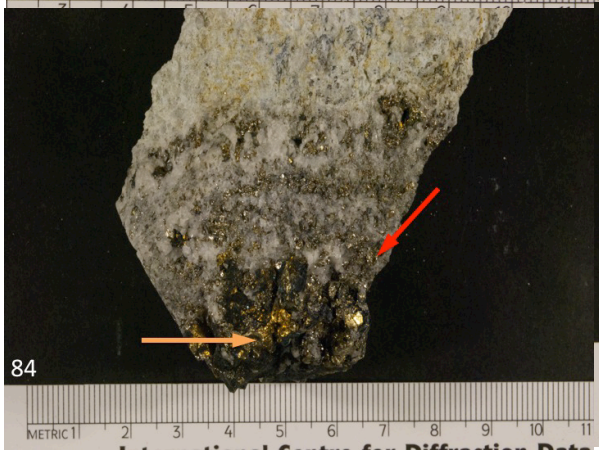
84
METRIC 1 2 3 4 5 6 7 8 9 10 11

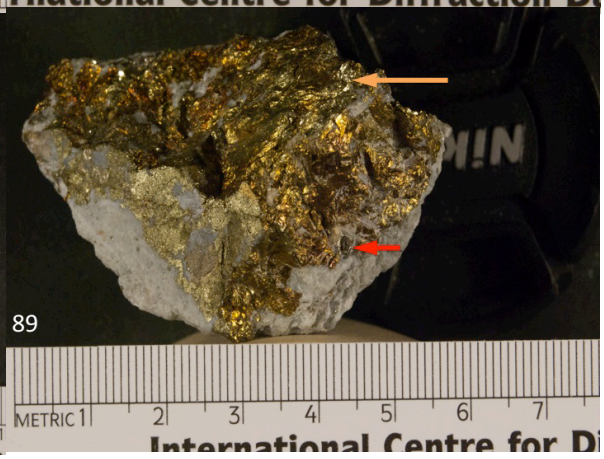
89
METRIC 1 2 3 4 5 6 7
International Centre for Di

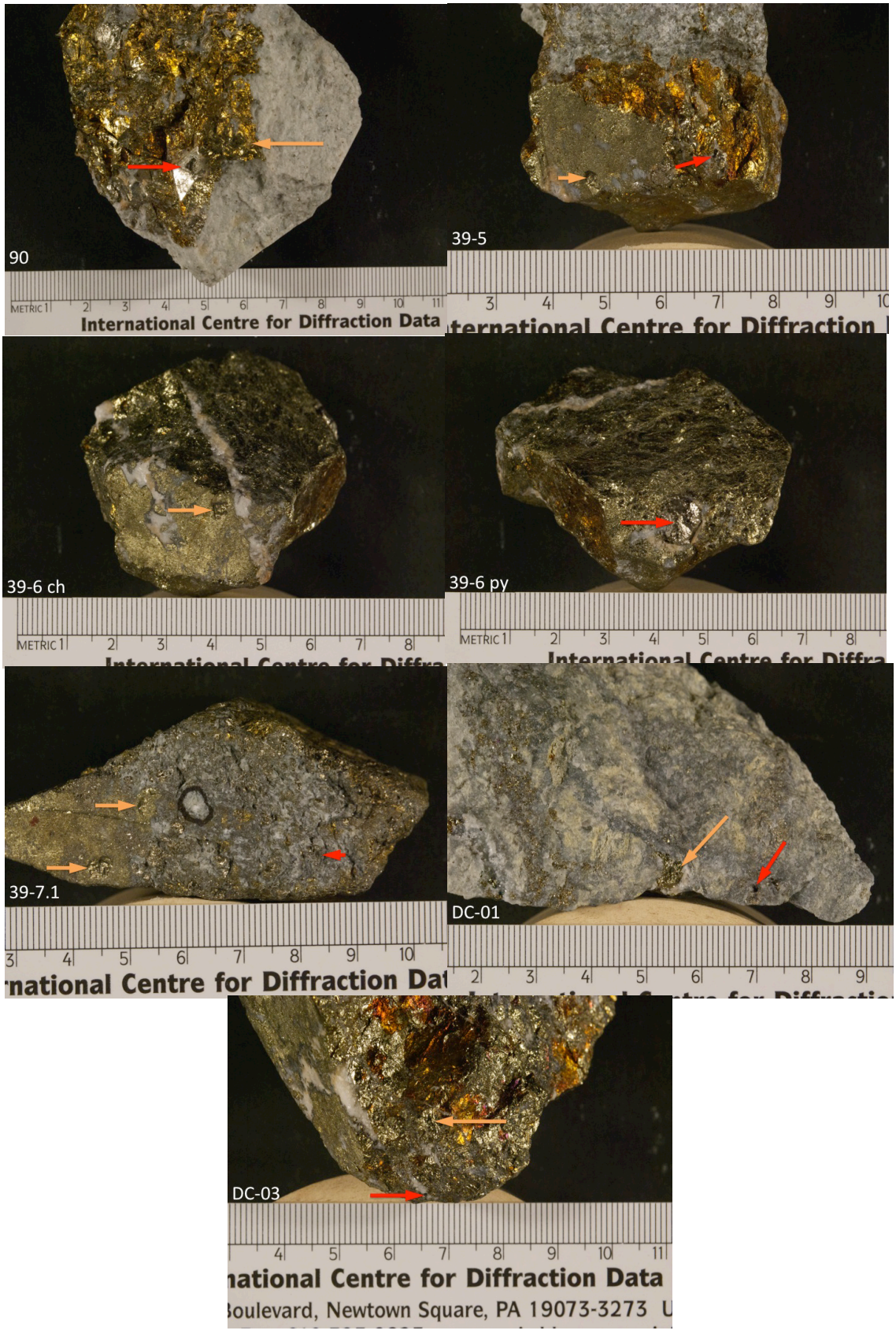
90
39-5
39-6 ch
39-6 py
39-7.1
DC-01
DC-03
International Centre for Diffraction Data